Top-Quark Pair Production at Hadron Colliders

Dissertation

zur Erlangung des Grades "Doktor der Naturwissenschaften"
am Fachbereich Physik, Mathematik und Informatik
der Johannes Gutenberg-Universität in Mainz

Valentin Ahrens
Geboren in Mainz

Mainz, September 2011

Tag der Promotion

8 Dezember 2011

Gutachter

Abstract

In this thesis we investigate several phenomenologically important properties of top-quark pair production at hadron colliders. We calculate double differential cross sections in two different kinematical setups, pair invariant-mass (PIM) and single-particle inclusive (1PI) kinematics. In pair invariant-mass kinematics we are able to present results for the double differential cross section with respect to the invariant mass of the top-quark pair and the top-quark scattering angle. Working in the threshold region, where the pair invariant mass M is close to the partonic center-of-mass energy $\sqrt{\hat{s}}$, we are able to factorize the partonic cross section into different energy regions. We use renormalization-group (RG) methods to resum large threshold logarithms to next-to-next-to-leading-logarithmic (NNLL) accuracy. On a technical level this is done using effective field theories, such as heavy-quark effective theory (HQET) and soft-collinear effective theory (SCET). The same techniques are applied when working in 1PI kinematics, leading to a calculation of the double differential cross section with respect to transverse-momentum p_T and the rapidity of the top quark. We restrict the phase-space such that only soft emission of gluons is possible, and perform a NNLL resummation of threshold logarithms.

The obtained analytical expressions enable us to precisely predict several observables, and a substantial part of this thesis is devoted to their detailed phenomenological analysis. Matching our results in the threshold regions to the exact ones at next-to-leading order (NLO) in fixed-order perturbation theory, allows us to make predictions at NLO+NNLL order in RG-improved, and at approximate next-to-next-to-leading order (NNLO) in fixed order perturbation theory. We give numerical results for the invariant mass distribution of the top-quark pair, and for the top-quark transverse-momentum and rapidity spectrum. We predict the total cross section, separately for both kinematics. Using these results, we analyze subleading contributions to the total cross section in 1PI and PIM originating from power corrections to the leading terms in the threshold expansions, and compare them to previous approaches. We later combine our PIM and 1PI results for the total cross section, this way eliminating uncertainties due to these corrections. The combined predictions for the total cross section are presented as a function of the top-quark mass in the pole, the minimal-subtraction ($\overline{\text{MS}}$), and the $1S$ mass scheme. In addition, we calculate the forward-backward (FB) asymmetry at the Tevatron in the laboratory, and in the $t\bar{t}$ rest frames as a function of the rapidity and the invariant mass of the top-quark pair at NLO+NNLL. We also give binned results for the asymmetry as a function of the invariant mass and the rapidity difference of the $t\bar{t}$ pair, and compare those to recent measurements. As a last application we calculate the charge asymmetry at the LHC as a function of a lower rapidity cut-off for the top and anti-top quarks.

Time flies like an arrow. Fruit flies like a banana.
Croucho Marx

Contents

Part I.

Introduction

1. Preface

At the moment the probable most complicated machine ever build by mankind has been in operation for about 2 years, the large hadron collider (LHC). Starting construction in 1995 it is also one of the biggest, most expensive scientific instruments ever made. This machine represents the enormous effort to understand nature, explicitly particle physics, in more detail. The fact that physicists have to go to such great length, may it be the at LHC or at the Tevatron, to obtain new data, and observe unknown phenomena can be seen as a sign of an already deep understanding of vast areas of nature. Concerning particle physics, past generations of physicists have been astonishingly successful describing experimental data better and better. After the big steps at the beginning of the 20th century, when quantum physics and general relativity changed drastically our view of the world, came an time were a refinement of the theoretical and experimental tools lead to a discovery of an abundance of new particles. In the time until the late 70s of the last century the observed forces, and the apparent zoo of particles were more and more understood. At present we know about four forces, gravity, electromagnetism, the weak and the strong force. For the main part of particle physics only the latter three are of importance. In the beginning of the 1970s it became clear that the electromagnetic and weak force could be unified into the so called electroweak force. The combination of theses two forces is build upon the gauge group $SU(2)_L \times U(1)_Y$, which is then broken down to $U(1)_{em}$, and the weak force which is mediate by the massive gauge bosons $W^{\pm}$ and Z. The concept of gauge theory to describe interactions is one of the most fruitful realizations of theoretical physics in the 20th century. In combination with the Higgs mechanism to spontaneously break a given gauge-symmetry, it is the base on which the *standard model* (SM) of particle physics is founded. This standard model is a $SU(3)_C \times SU(2)_L \times U(1)_Y$ gauge group. The $SU(3)_C$ is the non-abelian gauge group describing the strong interaction, the theory of which is called *quantum chromodynamics* (QCD). The form of the QCD Lagrangian is

$$\mathcal{L}_{\mathrm{QCD}} = -\frac{1}{4} F^{(a)}_{\mu\nu}\, F^{(a)\mu\nu} + i \sum_q \bar{\Psi}^i_q \gamma^\mu (D_\mu)_{ij} \Psi^j_q - \sum_q m_q \bar{\Psi}^i_q \Psi_{q\,i}\ , \tag{1.1}$$

where

$$F^{(a)}_{\mu\nu} = \partial_\mu A^a_\nu - \partial_\nu A^a_\mu - g_s f_{abc} A^b_\mu A^c_\nu\ , \tag{1.2}$$

and the covariant derivative is

$$(D_\mu)_{ij} = \delta_{ij}\partial_\mu + i g_s \sum_a \frac{t^a_{ij}}{2} A^a_\mu\ . \tag{1.3}$$

This Lagrangian describes the interaction of the gauge fields of QCD, the gluon fields A^a_μ, with the Dirac spinor of a quark field Ψ^i_q with flavor q, and color i. A complication, due to the non-abelian structure of QCD, is caused by the third term in (1.2), which represents an interaction among the gauge bosons themselves. This interaction is governed by the structure constant of the $SU(3)_C$ algebra f_{abc}, which is connected to the color generators t^a through $[t^a, t^b] = if^{abc}$, and the QCD coupling constant g_s. As the process we are investigating is to a large extend governed by the interaction of quarks and gluons, we will be mainly concerned with QCD.

In this thesis we want to calculate and present numerical results for several aspects of the production process of top-quark pairs. The top-quark is the heaviest elementary particle know today, with a current measured mass of about 173 GeV [1]. This fact leads to a number of consequences. Because of its large mass, the top quark has a very short lifetime of the order of $10^{-25}s$, and it decays before any strong interaction can take place. It is the only quark which does not hadronize before its decay, this makes it possible to talk about a bare quark, which is otherwise not found in nature due to the concept of confinement in QCD. On the other hand, the top-quark mass is close to the scale where one assumes that the breaking of the electroweak symmetry takes place. Because of this, the top-quark is expected to couple strongly to the fields responsible for the breaking. As a consequence, the measurement of top-quark related properties at the Tevatron and LHC are one of the main goals at these facilities. In different spectra, as the p_T or invariant mass distribution, signals of new physics are hoped to show up. In order to find these new signals one has to have a precise understanding of already known phenomena. Thus, calculating properties of top-quark pairs at hadron colliders is a crucial input to the search for new physics. At the Tevatron, where the top-quark was first discovered, thousands of top-events have been observed, and since some time the LHC is recording more and more events. As experiments increase data and refine their techniques, theoretical predictions have to be done with similar precision. This is the motivation of this thesis, in which we calculate several important observables connected to top-quark pair production to the highest available accuracy yet. The work presented here is based on our publications [2–6].

1.1. $t\bar{t}$ Production: Theory Overview and Extensions Presented in this Thesis

Increasing experimental precision asks for a matching accuracy from theoretical predictions. In the following we give a short overview of the efforts made on the theory side and how we extend this in the work presented here.

Theoretical calculations in QCD rely on the factorization formula for the differential cross section, which is of the form [7]

$$d\sigma = \sum C_{ij} \otimes f_{i/N_1} \otimes f_{j/N_2} \ , \tag{1.4}$$

where $\otimes$ stands for a convolution. The hard-scattering kernel C_{ij} can be calculated as a series in α_s and is related to the partonic cross section. The parton distribution functions

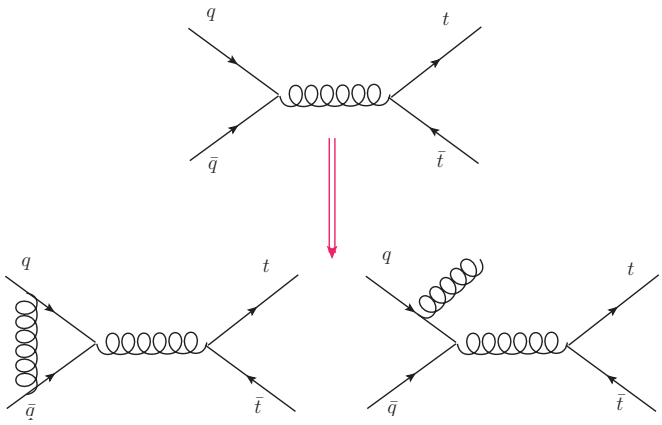

Figure 1.1.: The partonic quark-antiquark channel in $t\bar{t}$ production. First line shows a LO diagram. The lower line shows a subset of corresponding NLO diagrams, virtual correction (left) and real emission (right).

(PDFs) $f_{i/N_{1,2}}$, where $i = q, \bar{q}, g$, contain the information about the parton i in an incoming hadron $N_{1,2}$[1] and are taken from experiment. A large amount of theoretical work is concerned with the calculation of the partonic cross section C_{ij}[2]. Predictions for the total cross section are based on NLO calculations [8–11] and have been known for over two decades. Some time later also differential distributions [12–14] and the FB asymmetry [15, 16] were calculated to the same accuracy. The NLO computations suffer from theory uncertainties larger than 10%, both for Tevatron and LHC center-of-mass energies. These uncertainties are due to our imperfect knowledge of the parton distribution functions, and also to the truncation of the perturbative series in the strong coupling constant, which introduces a dependence on the unphysical renormalization and factorization scales into physical predictions. This theoretical uncertainty is typically reduced by including more terms in the perturbative series, and for this reason the calculation of the differential partonic cross section to NNLO has been an area of active research. Full NNLO predictions require the calculation of two sets of corrections: *i) virtual corrections*, which can be split into genuine two-loop diagrams [17–22] and one-loop interference terms [23–25]; *ii) real radiation*, which involves one-loop diagrams with the emission of one extra parton in the final state, and tree-level diagrams with two extra partons in the final state [26–29]. In spite of progress made by several groups on different aspects of the NNLO calculations in the last few years, especially in developing a new subtraction scheme and calculating the contributions from double real radiation [30, 31], a significant amount of work is still required to assemble all the elements.

Another way to improve on the fixed-order NLO calculation (and also the NNLO one,

[1]The $N_{1,2}$ are in our case protons or anti-protons.
[2]In Fig. 1.1 we show a small subset of diagrams in $t\bar{t}$ production up to NLO order.

upon its completion) is to supplement it with threshold resummation [32, 33][3]. More precisely, one identifies a threshold parameter which vanishes in the limit where real gluon emission is soft, expands the result to leading power in this parameter, and uses renormalization-group methods to resum logarithmic corrections in this parameter to all orders in the strong coupling constant. For the total cross section, one such approach is to work in the threshold limit $\beta \to 0$, where $\hat{s}$ is the partonic center-of-mass energy squared, and β is approximately the velocity of the top (or anti-top) quark. In this production threshold limit the top quarks are produced nearly at rest and there are logarithmic terms of the form $\alpha_s^n \ln^m \beta$ (with $m \leq 2n$), which can be resummed to all orders. This has been done to leading-logarithmic (LL) order [34–39], next-to-leading-logarithmic (NLL) order [40], and NNLL order [41–46]. Note that in this case not only logarithmic corrections, but also Coulomb corrections involving inverse powers of β occur. An approach to all-orders resummation of Coulomb terms can be found in [47].

A drawback of this method is that it performs resummation of terms that become important in the region $\beta \to 0$, which however gives a very small contribution to the total cross section. We will see in Section 8.2 that, at the Tevatron and LHC, typical values of β are in the range between 0.4 and 0.9. An alternative approach is to perform the threshold expansion and resummation at the level of differential distributions, and to obtain the total cross section by integrating the results. One such method works with the top-pair invariant mass distribution $d\sigma/dM$, where M is the invariant mass of the $t\bar{t}$ pair. The threshold limit for this case of PIM kinematics is defined as $z = M^2/\hat{s} \to 1$, and the corresponding threshold logarithms are of the form $\alpha_s^n \left[\ln^m(1-z)/(1-z)\right]_+$ (with $m \leq 2n-1$). In this limit only soft gluons can be emitted, but β is a generic $\mathcal{O}(1)$ parameter, and the top-quark velocity need not be small. Systematic resummation and fixed-order expansions of these logarithms has been studied in Mellin moment space at NLL order [48–55]. Using techniques from soft-collinear effective theory we extend this to NNLL order in momentum space in this thesis. Furthermore we include formally subleading terms in the threshold limit which have been known to be present in the analytical results of the fixed-order expanded hard scattering kernels of other processes. We will call this scheme PIM_{SCET}.

In general, it can be imagined that the approach based on differential distributions captures more contributions than the approach based on the small-β expansion, and therefore gives more reliable predictions for the total cross section. Later in this thesis, we will argue that this is indeed the case.

In addition to the invariant-mass distribution of the top-quark pair, the transverse-momentum and rapidity distributions of the top quark (or anti-top quark) are also interesting. In the case of distributions of the top quark, one collects the anti-top quark and extra radiation into an inclusive hadronic state $X[\bar{t}]$ with total momentum p_X, and defines the threshold limit as $p_X^2 \to m_t^2$ [4]. In this limit of 1PI kinematics, only soft radiation is allowed, but as in PIM kinematics the parameter β is an $\mathcal{O}(1)$ quantity. Soft gluon resummation for this case has been developed in Mellin moment space [56] and applied to

[3] We will elaborate on the concept of resummation in Section 2.3.

[4] m_t represents the top-quark mass.

the top-quark transverse-momentum distribution at NLL order [52] and recently also at NNLL order [57], in the form of approximate NNLO predictions. Starting from these distributions, it is possible to obtain the total cross section by integrating over the kinematic variables. This approach has been taken in [53–55, 57]. In principle, in the threshold limit PIM and 1PI kinematics encode the same soft gluon physics. Any differences between the two cases are due to power-suppressed corrections. At realistic collider energies, however, subleading terms are in general non-negligible, and one should study them carefully before drawing any definite conclusions. We calculate the p_T and rapidity distribution of the top-quark to NNLL order in momentum space in this thesis and present NLO+NNLL predictions for the first time. As for PIM kinematics we include formally subleading terms in the threshold limit. We will show that this "1PI_{SCET}" scheme is an improvement compared to traditional approaches.

1.2. Chapter Outline

This work is splitted into four parts, *Introduction*, *Theoretical setup*, *Phenomenology* and *Conclusions*. The first part deals with introductions to different areas in connection with the topic of this thesis. This includes a short overview of the current status of top-physics on the experimental in Sections 1.3. In addition to this several field theory concepts, such as SCET and HQET, important for later parts of the thesis, are introduced in Chapter 2. At the end of this chapter the idea of resummation is discussed.

In Part II, *Theoretical setup*, we present in detail the derivation of our analytical results. We describe the factorization of the differential cross sections separately for the case of PIM and 1PI kinematics. Working in PIM kinematics we present the factorization of the double differential cross section with respect to the invariant mass of the $t\bar{t}$ pair M and the top-quark scattering angle θ in Chapter 4. We first define the kinematical setup and then proceed to describe how we achieve to factorize the partonic cross section in the threshold limit $M^2/\hat{s} \to 1$. Following this we give details about the important building blocks, the hard and soft matrices, which are presented in Sections 4.2.3 and 4.2.4. We then derive formulas for the resummed cross section in momentum space using RG methods. This, and the the evaluation at NNLL order can be found in Section 4.2.5. In Chapter 5 we proceed similar to the above for the case of 1PI kinematics. In this chapter we present results for the factorized double differential cross section with respect to the transverse-momentum and the rapidity of the top-quark. After the definition of the relevant kinematics, we show how we apply our SCET formalism to the case of 1PI kinematics. We give the relevant perturbative ingredients as the 1PI soft matrices in Section 5.2.1, and present our resummed result for the cross section in Section 5.2.2. In Chapter 6 of the first part we explain how approximate NNLO results can be obtained from our resummed formulas. This again will be done separately for the case of PIM and 1PI kinematics. We finish this chapter by comparing certain aspects of RG-improved perturbation theory (RG-improved PT) to approximate NNLO.

Following the analytical calculations, in Part III we make use of our results to do detailed

phenomenological studies. Working in PIM kinematics we give in Chapter 8 numerical results for the invariant mass distribution in Section 8.1, and for the total cross section in Section 8.3. This is done at NLO+NNLL in RG-improved PT, and also at approximate NNLO. At the end of this chapter, in Section 8.3.1, we compare our results to previous calculations at the level of $\beta = \sqrt{1 - 4m_t^2/\hat{s}}$ distributions. In Chapter 9 we use our 1PI results to make phenomenological predictions for the rapidity and the transverse-momentum distributions of the top-quark at the LHC and Tevatron. These predictions, again both at NLO+NNLL and approximate NNLO order, can be found in Section 9.3. Integrating the distributions, we present in Section 9.4 results for the total cross sections coming from 1PI with the same accuracy. In Chapter 10 we use of our combined knowledge of PIM and 1PI kinematics. In Section 10.1.1 the total cross section coming from the different kinematics is analyzed. This is followed by giving combined numerical results for this observable as a function of the top-quark mass, working in the pole mass (Section 10.1.2) or the $\overline{\text{MS}}$ and $1S$ mass scheme (Section 10.1.3). The last part of this chapter, Section 10.2, deals with the FB asymmetry at the Tevatron and the charge asymmetry at the LHC. We give results for the FB asymmetry at the Tevatron in the laboratory frame as a function of the rapidity of the top-quark. In the $t\bar{t}$ rest frame the FB asymmetry is presented as a function of the rapidity difference and the invariant mass of the top-quark pair. Following this we compare our binned results to recent measurements. At the end of this section we calculate the charge asymmetry at the LHC as a function of a lower rapidity cut-off for the top and anti-top quarks.

We end with a summary of this work and an outlook on future extensions in Part IV.

1.3. Top-Quark Production: A Short Experimental Overview

We now give a short overview about the experimental status of top-quark physics. Having been postulated in 1973 by Kobayashi and Maskawa [58] the top-quark was first found at the Tevatron in 1995 [59], where many of its properties have been studied.

The current world average given for the top mass is $172.9 \pm 0.6 \pm 0.9\,\text{GeV}$[5] [1]. The top quark has a decay width of around 2 GeV, which leads to a lifetime of roughly 5×10^{-25}s. As already mentioned this time is too short for strong interactions to take place and no hadronization occurs. Due to this fact one is able to analyze the properties of a bare quark. There are two production modes, single-top and top-quark pair production. Single-top production at the Tevatron is about half of the rate as for $t\bar{t}$ pairs, and has been observed by the two experiments CDF and D0 [60–62]. At the LHC this cross section has also been measured [63, 64], and the value is again about half as much as for pair production. In both cases the t-channel, as shown in Figure 1.2, is numerically dominant. An important feature of single-top production is that the cross section is proportional to the absolute square of the V_{tb} entry in the Cabibbo-Kobayashi-Maskawa (CKM) quark-mixing matrix.

[5] Given with statistical and systematic errors.

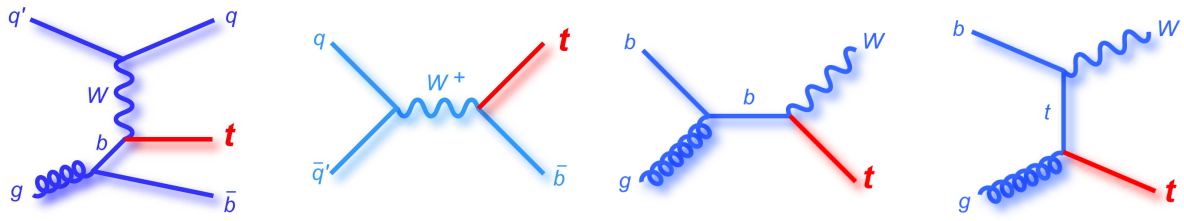

Figure 1.2.: Four possible partonic production channels for single-top production. First two: LO t-channel and s-channel process. Last two: LO diagrams for tW production.

This makes single-top production an important process for the extraction of V_{tb}.

In this thesis we are concerned with the second production mode, $t\bar{t}$ pair production, therefore we will discuss this mode in more detail. The top quark decays nearly to 100% into a W boson and a bottom quark. Other channels as $t \to W^+ + d$ or $t \to W^+ + s$ are relatively small due to the suppression of off-diagonal entries in the CKM quark-mixing matrix. The $W^\pm$ itself decays roughly to 33% into a lepton and a neutrino and to about 67% into quarks and antiquarks. This leads to the three $t\bar{t}$ decay structures for $t\bar{t}$ production shown in Fig. 1.3, the dilepton channel, lepton + jets channel and the all-hadronic channel. In the following we will give some information about recent measurements connected to $t\bar{t}$ production relevant for this work.

Until recently all information about the top-quark and its properties did come from CDF and D0 at the Tevatron, and still most of what we know about this particle comes from these experiments. At the moment however two experiments at the LHC, CMS and ATLAS are taking more and more data, and in the near future millions of top events will be recorded by them. At the Tevatron there are several recent measurements dedicated to the total cross section of $t\bar{t}$ production, using the dilepton channel [65,66], the lepton + jets channel [67,68] and the all-hadronic channel [69, 70]. The results of CDF of $\sigma_{t\bar{t}} = 7.50 \pm 0.48$ pb [71] and D0 $\sigma_{t\bar{t}} = 7.56\,^{+0.63}_{-0.56}$ pb [65][6] are compatible with each other and with the standard model prediction for the total cross section.

The total cross section was very recently measured for the first time at the LHC by the CMS [72] and the ATLAS collaboration [73], yielding $194 \pm 72(\text{stat.}) \pm 24(\text{syst.})$ and $145 \pm 31(\text{stat.})\,^{+42}_{-27}(\text{syst.})$ respectively. The two published measurements were done with 3.1pb^{-1} and 2.9pb^{-1} of integrated luminosity. There are already preliminary results with up to 0.7fb^{-1} from ATLAS [74], and CMS has many preliminary results with up to 1.09fb^{-1} as for the total cross section [75,76]. At the time of this writing, LHC data is increasing rapidly by the week, and results for more differential observables are expected to be published soon.

Besides the total cross section there are many other important properties of the top-quark which are of interest. At the Tevatron, differential properties as the invariant mass distribution of top-quark pairs [77] and the p_T distribution of the top-quark [78] have been

[6]Both assuming $m_t = 175$ GeV.

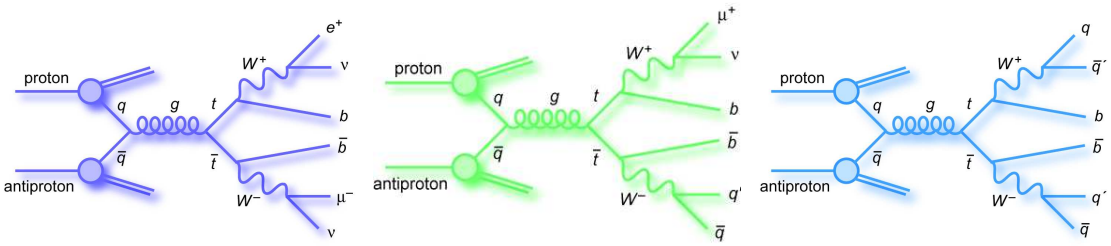

Figure 1.3.: The three possible decay structures in $t\bar{t}$ production. From the left: dilepton-channel, lepton + jets channel and all-hadronic channel.

studied. The analysis of the different spectra of the top-quark have been used to give results for the FB asymmetry at the Tevatron [79–82]. The measurements obtained by the CDF collaboration [82] using 5.3fb^{-1} of data are $A_{FB}^{p\bar{p}} = (15.0 \pm 5.5)\%$ in the $p\bar{p}$ frame, and $A_{FB}^{t\bar{t}} = (15.8 \pm 7.5)\%$ in the $t\bar{t}$ frame. Those results agree with theoretical predictions within about 1σ in the $t\bar{t}$ frame, and within about 2σ in the $p\bar{p}$ frame. In [82] a measurement of the FB asymmetry in the $t\bar{t}$ frame as a function of the invariant mass of the top-pair was presented. The results were grouped in two bins, $M_{t\bar{t}} < 450\text{GeV}$ and $M_{t\bar{t}} \geq 450\text{GeV}$, and they found for the latter bin $A_{FB}^{t\bar{t}}(M_{t\bar{t}} \geq 450\text{GeV}) = (47.5 \pm 11.4)\%$. This, much noticed, result is more than 3σ higher than the standard model NLO prediction presented in the same paper.

As the LHC has a symmetric initial condition there is no overall FB asymmetry but, by applying cuts, one is able to measure a charge asymmetry which probes the same structures also responsible for the FB asymmetry at the Tevatron. Preliminary results for this observable have been published by ATLAS [83] and CMS [84]. In contrast to the FB asymmetry at the Tevatron, the charge asymmetry at the LHC shows so far no deviation from the standard model. It should be noted however, that this observable is still dominated by statistical and systematical uncertainties, for instance the results of [83] are $A_C = 0.024 \pm 0.023(\text{stat.}) \pm 0.016(\text{syst.})$.

As already mentioned the top quark is especially interesting because its mass is close to the scale where new physics is expected to occur. New resonances coming from Kaluza-Klein-gluon decays [85], axigluons [86] or a new Z' boson [87] and many other beyond standard model theories can lead to an excess in various channels connected to top samples. Several searches for new phenomena have been undertaken by CDF (for example [88–90]) and by D0 (for example [91–93]). Except the FB asymmetry, which has a deviation from the standard model, there has been no clear sign of new physics in top samples. At the LHC only preliminary results for new physics searches are available at the moment. Several searches for new resonances have been made. At ATLAS searches for a narrow Z' [94, 95] and for FCNCs [96] have been done, and CMS presents preliminary results for heavy boson searches [97]. Both experiments do not see new resonances at the moment.

The above shows that top-quark physics is an active area of research and is very important for the search for new physics.

2. Effective Field Theories

Without realizing it we are often using effective theories when analyzing physical problems. For instance, atomic spectra can be described by a theory which does not know anything about the internal structure of the nucleus, or orbitals can be calculated without taking the earths structure into account. In both cases this can be done because there is a very distinct separation of scales. In the case of the atomic spectrum there is the size of the atom and the one of the nucleus, with a relative difference of the order of 10^5.

In nature we generally observe phenomena with distinct energies or lengths scales. When explicitly applying scale separation in quantum field theories one talks of effective field theories (EFTs), for a detailed introduction see for instance [98–100]. It should be noted that the current view we have about the standard model of particle physics is that it is itself an EFT.

In EFTs one makes use of the fact that large energy scales are suppressed by powers of the ratio of the scales involved in the problem at hand. A prominent example in particle physics is the Fermi coupling which is describing a four fermion interaction, leading to an explanation of the beta decay of a neutron. Today on the other hand, we know that the fermions are coupled through the exchange of a W boson. The large mass of the W boson leads to the fact that the interaction is very good described by a contact force. In general, when dealing with light degrees of freedom ϕ and some heavy fields Φ, one is able to integrate out the heavy modes Φ to obtain an effective actions. This is done by performing a path integral over the heavy states only [1]

$$\int \mathcal{D}\Phi \; e^{i\int \mathcal{L}(\phi,\Phi)} = e^{i\int \mathcal{L}_{eff}(\phi)} \; . \tag{2.1}$$

As it turns out, the effective Lagrangian $\mathcal{L}_{eff}$ can be expressed in terms of an expansion in local operators

$$\mathcal{L}_{eff} = \mathcal{L}_{d\leq 4} + \sum_i \frac{\mathcal{O}_i}{\Lambda^{dim(\mathcal{O}_i)-4}} \; , \tag{2.2}$$

where $dim(\mathcal{O}_i)$ stands for the dimension of the operator $\mathcal{O}_i$. In (2.2) we broke the Lagrangian into two pieces, one containing the usual renormalizable terms with dimension 4 or less, and an infinite sum containing higher dimensional operators. Even though we now have to deal with a infinite tower of operators these are suppressed due to increasing powers of Λ. Here Λ characterizes the scale of short distance physics. By truncating the series in (2.2) one is still able to make predictions with a certain accuracy at some lower

[1] In practices, integrating out the heavy degrees of freedom is performed using Feynman diagrams.

energy ω, as higher order operators are suppressed by powers of ω/Λ. This structure of encoding low energy physics in $\mathcal{L}_{eff}$ is referred to as decoupling, a concept which is based on the work of K.Wilson [101]. In the following we will discuss two EFTs, soft-collinear effective theory and heavy-quark effective theory, both will be used in the later part of this thesis.

2.1. Soft-Collinear Effective Theory

Many processes in collider physics have very special kinematical conditions. For instance in the case of $t\bar{t}$ production the initial partons have a very high energy but nearly or no invariant mass. To describe processes with such collinear partons and their interaction with soft gluons, soft-collinear effective theory (SCET) [102–105] is an appropriate framework. In the case of collider physics SCET has become one of the most successful frameworks within factorization theorems can be established. SCET was first used in combination with $\bar{B} \to X_s\gamma$ calculations. In recent years it has been applied to a wide range of different processes. For example the concept of dynamical threshold enhancement found in [106], improved predictions for Higgs production [107, 108], and event shapes in e^+e^- annihilations [109]. Also using SCET in connection with parton showers was and is an active area of research [110–112]. In the following we will give a brief introduction to SCET.

We introducing two light-like reference vectors n^ν and $\bar{n}^\nu$

$$n^\nu = (1, 0, 0, -1) \quad \bar{n}^\nu = (1, 0, 0, 1) \,, \tag{2.3}$$

with $n \cdot \bar{n} = 2$ and $n^2 = \bar{n}^2 = 0$. One can decompose any fourvector p^ν as

$$p^\nu = \frac{n^\nu}{2}\bar{n} \cdot p + \frac{\bar{n}^\nu}{2} n \cdot p + p_\perp^\nu \equiv (p^-, p^+, p_\perp) \,, \tag{2.4}$$

where $p^+ = n \cdot p$ and $p^- = \bar{n} \cdot p$. If now the particle is collinear in the "+" direction the momentum component in this direction will be big, the '-' component small. Using a small expansion parameter λ the momentum can be assumed to scales as follows[2]

$$(p^-, p^+, p_\perp) \sim Q(\lambda^2, 1, \lambda) \,, \tag{2.5}$$

where Q is a large scale intrinsic to the process being studied. Furthermore we can identify the general momentum regions

$$\begin{aligned} &\text{hard} && p^\nu \sim Q(1, 1, 1) \\ &\text{collinear '-'} && p^\nu \sim Q(1, \lambda^2, \lambda) \\ &\text{collinear '+'} && p^\nu \sim Q(\lambda^2, 1, \lambda) \end{aligned} \tag{2.6}$$

[2] In the literature one also finds a different expansion $(p^-, p^+, p^\perp) \sim Q(\lambda, 1, \lambda^{1/2})$, which leads to the same relative contributions.

$$\text{soft} \qquad p^\nu \sim Q(\lambda^2, \lambda^2, \lambda^2)$$

By considering a collinear quark we are able to extract the SCET Lagrangian by expanding the QCD Lagrangian in terms of λ. Let's assume $p^\nu \sim Q(1, \lambda^2, \lambda)$, being the momentum of an incoming quark at a collider for instance, and decompose

$$\begin{aligned} \Psi^\mu(x) &= \Psi_c^\mu(x) + \Psi_s^\mu(x) \\ A^\mu(x) &= A_c^\mu(x) + A_s^\mu(x) \ . \end{aligned} \tag{2.7}$$

In general, for a collinear (anti)particle $u(v)$ in the n direction one can show that

$$\begin{aligned} u_n &= 1/\sqrt{2}(\mathbf{u}, \sigma^3\mathbf{u}) \ , \\ v_n &= 1/\sqrt{2}(\sigma^3\mathbf{v}, \mathbf{v}) \ , \end{aligned} \tag{2.8}$$

where $\mathbf{u}$ and $\mathbf{v}$ are the spinors of the particles. The particle u_n has the following properties

$$\not{n} u_n = 0 \ ; \qquad \frac{\not{n}\not{\bar{n}}}{4} u_n = u_n \ ^3 \tag{2.9}$$

We now split the collinear fermion field into $\Psi_c(x) = \xi(x) + \eta(x)$ where

$$\xi = P_+ \Psi_c = \frac{\not{n}\not{\bar{n}}}{4}\Psi_c \ , \quad \eta = P_- \Psi_c = \frac{\not{\bar{n}}\not{n}}{4}\Psi_c \ .^4 \tag{2.10}$$

In this way we have split the fields into a collinear part ξ and soft part η, which fulfill $\not{n}\xi = \not{\bar{n}}\eta = 0$, By looking at the different propagators we can say something about the scaling of the fields with respect to λ, we start with the fermion propagator

$$\begin{aligned} \langle 0| \, T[\xi(x)\bar{\xi}(0)] \, |0\rangle &= \frac{\not{n}\not{\bar{n}}}{4} \langle 0| \, T[\Psi_c(x)\bar{\Psi}_c(0)] \, |0\rangle \frac{\not{\bar{n}}\not{n}}{4} \\ &= \int \frac{d^4p}{(2\pi)^4} \frac{i}{p^2 + i\epsilon} e^{-ip\cdot x} \frac{\not{n}\not{\bar{n}}}{4} \not{p} \frac{\not{\bar{n}}\not{n}}{4} \sim \lambda^4 \frac{1}{\lambda^2} \ , \end{aligned} \tag{2.11}$$

where we used for instance that $p^2 = \bar{n}\cdot p \ n\cdot p + p_\perp^2 = \lambda^0\lambda^2 + \lambda\lambda$ and $d^4p \sim \lambda^4$. This implies that $\xi \sim \lambda$, and similar arguments show $\eta \sim \lambda^2$. For the soft quark field one obtains

$$\Psi_s(x)\bar{\Psi}_s(0) \sim (\lambda^2)^4 \frac{1}{\lambda^4}\lambda^2 \sim \lambda^6 \tag{2.12}$$

which shows that $\Psi_s(x) \sim \lambda^3$.
Now we look at the gluon propagator

$$\langle 0| \, T[A_c^\mu(x) A_c^\nu(0)] \, |0\rangle = \int \frac{d^4p}{(2\pi)^4} \frac{i}{p^2 + i\epsilon} e^{-ip\cdot x} [-g^{\mu\nu} + \tau \, \frac{p^\mu p^\nu}{p^2}] \ . \tag{2.13}$$

---

3 $\frac{\not{n}\not{\bar{n}}}{4} = \frac{1}{2}\begin{pmatrix} \mathbb{1} & \sigma^3 \\ \sigma^3 & \mathbb{1} \end{pmatrix}$

4 Note that $P_+ + P_- = 1$.

Here τ is a gauge parameter and we have

$$\begin{aligned} g_\perp^{\mu\nu} &\sim \frac{k_\perp^\mu k_\perp^\nu}{k^2} \sim \lambda^0 \,, \\ g^{+-} &\sim \frac{k^+ k^-}{k^2} \sim \lambda^0 \,, \\ n_\mu n_\nu : \quad g^{++} &= 0 \,; \quad \frac{(n\cdot k)^2}{k^2} \sim \lambda^2 \,, \end{aligned} \tag{2.14}$$

thus $A_c^\mu \sim p^\mu \sim (1, \lambda^2, \lambda)$.
Using the above power counting we now write down the collinear quark Lagrangian.

$$\begin{aligned} \mathcal{L}_c &= \bar\Psi_c i\not{D}_c \Psi_c = (\bar\xi + \bar\eta)[\frac{\not{n}}{2} i\bar n\cdot D + \frac{\not{\bar n}}{2} in\cdot D + i\not{D}_\perp](\xi+\eta) \\ &= \bar\xi[\frac{\not{n}}{2} in\cdot D]\xi + \bar\xi[i\not{D}_\perp]\eta + \bar\eta[i\not{D}_\perp]\xi + \bar\eta[\frac{\not{n}}{2} i\bar n\cdot D]\eta \,. \end{aligned} \tag{2.15}$$

With the help of the equations of motions we eliminate η to obtain

$$\eta = -\frac{1}{i\bar n\cdot D}\frac{\not{\bar n}}{2}[i\not{D}_\perp]\xi \,. \tag{2.16}$$

With this one gets

$$\mathcal{L}_c = \bar\xi[\frac{\not{n}}{2} i\bar n\cdot D \;-\; i\not{D}_\perp \frac{\not{\bar n}}{2}\frac{1}{i\bar n\cdot D} i\not{D}_\perp]\xi \,. \tag{2.17}$$

The collinear gluon and the soft Lagrangian are just the normal QCD ones with $A^\mu, \Psi \to A_s^\mu, \Psi_s$, thus

$$\mathcal{L}_s = \bar\Psi_s i\not{D}_s \Psi_s - \frac{1}{4}\left(F_{\mu\nu}^{s\,a}\right)^2 \,, \tag{2.18}$$

where $iD_s^\mu = i\partial^\mu + gA_s^\mu$ and $igF_{\mu\nu}^{s\,a} t^a = -[D_s^\mu, D_s^\nu]$. At this stage we have the form of the collinear-collinear and soft-soft interactions, the only remaining piece of the leading SCET Lagrangian is the soft-collinear interaction. To construct this Lagrangian we note the following:

- Ψ_s is power suppressed ($\sim \lambda^3$) compared to $\xi(\sim \lambda^2)$. so it does not appear at leading power.

- $n\cdot A_s$ does appear, other components are power suppressed.

- Starting from the collinear Lagrangian we obtain the soft-collinear one by making the replacement $A_c^\mu \to A_c^\mu(x) + n \cdot A_s(x_-)\frac{\bar{n}^\mu}{2}$

  We obtain the following leading-power SCET Lagrangian

$$\mathcal{L}_{\rm SCET} = \bar{\xi}\frac{\bar{\not{n}}}{2}[in\cdot D + i\not{D}_{c\perp}\frac{1}{i\bar{n}\cdot D_c}i\not{D}_{c\perp}]\xi - \frac{1}{4}\left(F_{\mu\nu}^{c\,a}\right)^2 + \bar{\Psi}_s i\not{D}_s\Psi_s - \frac{1}{4}\left(F_{\mu\nu}^{s\,a}\right)^2 \ , \quad (2.19)$$

  where

$$\begin{aligned} iD_s^\mu &= i\partial^\mu + gA_s^\mu(x) && (2.20)\\ iD_c^\mu &= i\partial^\mu + gA_c^\mu(x) \\ iD^\mu &= i\partial^\mu + gA_c^\mu(x) + gn\cdot A_s(x_-)\frac{\bar{n}^\mu}{2} \\ igF_{\mu\nu}^{c\,a}t^a &= -[D^\mu, D^\nu] \ . && (2.21)\end{aligned}$$

In the replacement $A_c^\mu \to A_c^\mu(x) + n \cdot A_s(x_-)\frac{\bar{n}^\mu}{2}$ we have used the concept of "light-front multipole expansion" [113]. In contrast to earlier approaches to SCET we are working with the position space formulation of SCET, and we do not make use of momentum "label" operators. In position space however, we have to Taylor-expand the fields in the directions where they vary according to their counting in λ. For a generic soft field we write

$$\begin{aligned}\phi_s(x) &= \exp[x_+\cdot\partial_- + x_\perp\cdot\partial_\perp]\exp[x_-\cdot\partial_+]\phi_s(0) \\ &= \phi_s(x_-) + [x_\perp\cdot\partial_\perp\phi_s](x_-) + 1/2x_+\cdot[\partial_-\phi_s](x_-) + 1/2[x_\perp^\mu x_\perp^\nu\partial_\mu\partial_\nu\phi_s](x_-) + \mathcal{O}(\lambda^3\phi_s) \ . \end{aligned} \quad (2.22)$$

2.1.1. Gauge Transformation

Having reached the leading SCET Lagrangian by analyzing power counting we are also forced to respect the scaling of the fields when doing gauge transformations. We are interested in those transformations which do not alter the scaling of the transformed field. We consider two gauge transformations

$$V_s(x) = \exp[i\alpha_s^a(x)t^a] \ , \quad V_c(x) = \text{epx}[i\alpha_c^a(x)t^a] \ . \quad (2.23)$$

The field $\alpha_s(x)$ fulfills $\partial\alpha_s(x) \sim \lambda^2\alpha_s(x)$ whereas $\partial\alpha_c(x) \sim \lambda^0\alpha_c(x)$, thus they have soft or collinear scaling.

- **Soft Gauge Transformation**

Clearly soft fields can not transform under collinear gauge transformation, as this would turn them into collinear fields. Otherwise, under soft gauge transformation soft fields transform in the normal way

$$\Psi_s(x) \to V_s(x)\Psi_s(x) \text{ and } A_s^\mu(x) \to V_s(x)A_s^\mu(x)V_s^\dagger(x) + \frac{i}{g}V_s(x)[\partial^\mu, V_s^\dagger] \ . \quad (2.24)$$

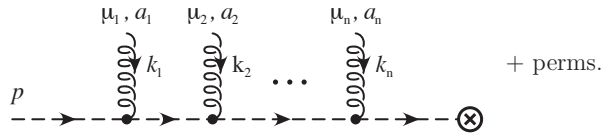

Figure 2.1.: Attachments of soft gluons to a collinear quark field.

For collinear fields a soft gauge transformation does not alter the character. One has the following transformation properties

$$\xi(x) \to V_s(x_-)\xi(x) \text{ and } A_c^\mu(x) \to V_s(x_-)A_c^\mu(x)V_s^\dagger(x_-) \; . \tag{2.25}$$

- **Collinear Gauge Transformation**

In this case the soft fields are unchanged

$$\Psi_s(x) \to \Psi_s(x) \quad \text{and} \quad A_s^\mu(x) \to A_s^\mu(x) \; , \tag{2.26}$$

whereas the collinear fields transform as

$$\xi(x) \to V_c(x)\xi(x) \text{ and } A_c^\mu(x) \to V_c(x)A_c^\mu(x)V_c^\dagger(x) + \frac{1}{g}V_c(x)[i\partial^\mu + \frac{\bar{n}^\mu}{2} n\cdot A_s(x_-), V_c^\dagger] \; . \tag{2.27}$$

2.1.2. Decoupling Transformation

Until now soft and collinear interactions are entangled. We now want to decouple those two types of interactions by means of field redefinition and the use of Wilson lines. In Figure 2.1 we show a collinear quark field in a soft gluon background. One can write the sum of these emissions as

$$\xi = S\,\xi^{(0)} \; , \tag{2.28}$$

where

$$S = 1 + \sum_{m=1}^{\infty} \sum_{\text{perms}} \frac{(-g)^m}{m!} \frac{n\cdot A_s^{a_1} \ldots n\cdot A_s^{a_m}}{n\cdot k_1 n\cdot (k_1+k_2)\ldots n\cdot (\sum_{i=1}^m k_i)}\, T^{a_m}\ldots T^{a_1} \; . \tag{2.29}$$

We can express (2.28) also with the help of the Fourier transform of a path ordered exponential

$$S_n(x) = P\exp[\,ig\int_{-\infty}^{0} ds n\cdot A_s(x+s\,n)]^5 \; . \tag{2.30}$$

The path ordering P ensures that gauge fields closer (farther) to the point x are moved to the left (right). A collinear gluon in a soft gluon background leads to the same structure as in (2.30) but with $A_s = A_s^c\, t_{ab}^c$ replaced by $(-i)A_s^c\, f^{abc}$. We will suppress the information

[5]Here we abbriviate $A_s = A_s^a T^a$ and similar for the adjoint representation.

about fundamental or adjoint representation in this section and use the general expression (2.30) for both.

With the above in mind we make the following field redefinitions

$$\xi(x) \to S_n(x_-)\xi^{(0)}(x)\ , \quad A_c^\mu(x) \to S_n(x_-)A_c^{(0)\,\mu}S_n^\dagger(x_-)\ . \tag{2.31}$$

The new fields $\xi^{(0)}$ and $A_c^{(0)\,\mu}$ do not interact with soft gluons anymore. All those interactions have been summed into the $S_n(x_-)$. The path ordered exponential of (2.30) is an example of a Wilson line. An important property of this operator is that it can be used to make products of fields at different points gauge invariant. Taking for example

$$P\exp[\,ig\int_0^s ds' n\cdot A(x+s'\,n)\,] \equiv [x+s\,n, x]\ , \tag{2.32}$$

one can make the object $\Psi(x+s\,n)\Psi(x)$ gauge invariant by connecting it with (2.32). Thus, $\Psi(x+s\,n)\Psi(x) \to \Psi(x+s\,n)\,[x+s\,n,x]\,\Psi(x)$ where the last expression is indeed gauge invariant. We now insert the decoupling transformation (2.31) into the coupled part of (2.19)

$$\begin{aligned}
\mathcal{L}_{\rm int} &= \bar\xi\frac{\bar{n}\!\!\!/}{2}i\bar n\cdot D\xi \qquad (2.33)\\
&\to \bar\xi^{(0)}S_n^\dagger(x_-)\frac{\bar{n}\!\!\!/}{2}[i\bar n\cdot\partial + gS_n(x_-)\bar n\cdot A_c^{(0)}S_n^\dagger(x_-) + g\bar n\cdot A_s(x_-)]S_n(x_-)\xi^{(0)}\\
&= \bar\xi^{(0)}\frac{\bar{n}\!\!\!/}{2}\bar n\cdot A_c^{(0)}\xi^{(0)} + \bar\xi^{(0)}S_n^\dagger(x_-)\frac{\bar{n}\!\!\!/}{2}n\cdot D_s S_n(x_-)\xi^{(0)}\\
&= \bar\xi^{(0)}\frac{\bar{n}\!\!\!/}{2}\bar n\cdot A_c^{(0)}\xi^{(0)} + \bar\xi^{(0)}\frac{\bar{n}\!\!\!/}{2}n\cdot\partial\,\xi^{(0)}\\
&= \bar\xi^{(0)}\frac{\bar{n}\!\!\!/}{2}n\cdot D_c\xi^{(0)}
\end{aligned}$$

As one can see from the end of (2.33) all sof-collinear interactions have decoupled through the field redefinitions (2.31). It should be noted that this decoupling presented here is valid at leading power in the SCET power counting, of course at subleading power soft-collinear interactions still remain. To see a detailed analysis of the subleading Lagrangian see [105].

2.1.3. Matching Example

We now will discuss an example of matching a current onto a Wilson coefficient and an effective operator in SCET. For this we choose the current $J^\mu = \bar\Psi\gamma^\mu\Psi$ (see for instance [106]). At tree level, and at leading power in the SCET power counting, we exchange Ψ with the collinear fields ξ such that

$$\bar\Psi\gamma^\mu\Psi\,(x) \to \bar\xi_n\gamma^\mu\xi_{\bar n}\,(x)\ . \tag{2.34}$$

With the help of Wilson lines, in a next step we make the above explicitly gauge invariant

$$\bar{\xi}_n \gamma^\mu \xi_{\bar{n}}(x) \to \bar{\xi}_n W_n \gamma^\mu W_{\bar{n}}^\dagger \xi_{\bar{n}}(x) ,$$

$$\text{where} \quad W_n(x) = P \exp[ig \int_{-\infty}^{0} ds\bar{n} \cdot A_{\bar{n}}(x + s\bar{n})] . \tag{2.35}$$

Furthermore we can absorb the soft eikonal interactions into a field redefinition as mentioned before

$$\bar{\xi}_n W_n \gamma^\mu W_{\bar{n}}^\dagger \xi_{\bar{n}}(x) \to \left(\bar{\xi}_n W_n\right)^{(0)} S_n^\dagger \gamma^\mu S_{\bar{n}} \left(W_{\bar{n}}^\dagger \xi_{\bar{n}}\right)^{(0)}(x) \equiv \chi_n^{(0)} S_n^\dagger \gamma^\mu S_{\bar{n}} \chi_{\bar{n}}^{(0)}(x) ,$$

$$\text{where} \quad S_n(x) = P \exp[ig \int_{-\infty}^{0} ds\bar{n} \cdot A_{\bar{n}}(x + s\bar{n})] . \tag{2.36}$$

Again the superscript (0) means that the object does not interact with soft degrees of freedom. The above matching has to be changed when radiative corrections are taken into account. In that case the current can mix with analogous ones along the light cones [114–116]

$$\chi_n^{(0)} S_n^\dagger \gamma^\mu S_{\bar{n}} \chi_{\bar{n}}^{(0)}(x) \to \int dsdt\, \tilde{C}(s,t,\mu)\, \chi_n^{(0)}(x + sn) \left[S_n^\dagger \gamma^\mu S_{\bar{n}} \right](x)\, \chi_{\bar{n}}^{(0)}(x + t\bar{n}) , \tag{2.37}$$

here $\tilde{C}$ is the Wilson coefficient to ensure the right matching, factored out at the scale μ. We can simplify the above expression to be

$$C(n \cdot p_1, \bar{n} \cdot p_2, \mu) \left[\chi_n^{(0)} S_n^\dagger \gamma^\mu S_{\bar{n}} \chi_{\bar{n}}^{(0)} \right](x) , \tag{2.38}$$

where

$$C(n \cdot p_1, \bar{n} \cdot p_2, \mu) = \int dsdt\, e^{-i(sn \cdot p_1 + t\bar{n} \cdot p_2)} \tilde{C}(s,t,\mu) \tag{2.39}$$

is the Fourier transform of the position-space Wilson coefficient.
The Wilson coefficient C has to be calculated order by order in perturbation theory. In (2.38) we have explicitly factored different regions, a collinear and a soft one, both regions do not communicate with each other anymore.

For our derivation of the differential cross section in Chapters 4 and 5 we will make use of some of the techniques presented in the above sections.

2.2. Heavy-Quark Effective Theory

In the derivation of the factorization theorem of $t\bar{t}$ production we are using a second effective approach common in the field of heavy quark physics, heavy-quark effective theory. This theory uses the fact that the energy scale of the mass of the heavy quark, in our case the top quark, is much bigger than the scale of soft interaction, for a detailed review see

[117, 118]. The starting point is easy to understand, the heavy quark mass m_Q is in many processes much larger than an occurring soft scale, $m_Q \gg \Lambda_{soft}$. This soft scale depends on the process at hand, in b-physics there is the hierarchy $m_b \gg \Lambda_{QCD}$, whereas for $t\bar{t}$ production in PIM kinematics we will have $m_t \gg M_{t\bar{t}}(1-z)$. In any case, this leads to a natural separation of scales. The momentum of a softly interacting heavy quark can be written as

$$p_Q^\mu = m_Q v^\mu + k^\mu \,, \tag{2.40}$$

where v^μ ($v^2 = 1$) is the velocity of the quark and k^μ is the so called residual momentum ($k \sim \Lambda_{soft}$). As the quark is only interacting softly k^μ is a measure of its offshellness. In the limit $m_Q \to \infty$ certain Feynman rules simplify. For instance the propagator

$$\frac{i(\not{p} + m_Q)}{p_Q^2 - m_Q + i\epsilon} = \frac{i}{v\cdot k + i\epsilon}\frac{1+\not{v}}{2} + \mathcal{O}(k/m_Q) \to \frac{i}{v\cdot k + i\epsilon} P_+ \,, \tag{2.41}$$

where we defined the projection operators $P_\pm = (1 \pm \not{v})/2$ which fulfill

$$P_+ + P_- = 1 \,, \quad P_\pm^2 = P_\pm \,, \quad P_\pm P_\mp = 0 \,. \tag{2.42}$$

We now decompose the quark field with the help of the projection operators

$$\begin{aligned} Q(x) &= P_+\, Q(x) + P_-\, Q(x) \\ &= e^{-im_Q v\cdot x}[h_v(x) + H_v(x)] \,, \end{aligned} \tag{2.43}$$

where

$$h_v(x) = e^{im_Q v\cdot x} P_+\, Q(x) \;\text{ and }\; H_v(x) = e^{im_Q v\cdot x} P_-\, Q(x) \,. \tag{2.44}$$

The phase factor in front of $Q(x)$ in (2.43) subtracts the large part of the heavy quark momentum and only fluctuations of the order k^μ are present in $h_v(x)$.
The fields in (2.44) clearly fulfill

$$P_+ h_v(x) = \not{v} h_v(x) = h_v(x) \quad \text{and} \quad P_- H_v(x) = -\not{v} H_v(x) = H_v(x) \,. \tag{2.45}$$

In addition to these properties it is possible to make the replacement $\gamma^\mu \to v^\mu(-v^\mu)$ between two h_v (H_v), due to the fact that for each coupling $igT_a\gamma^\mu$ two propagators as in (2.41) appear. We now insert (2.43) into the Lagrangian for a heavy field and make use of the relations mentioned above.

$$\begin{aligned} \mathcal{L}_Q &= \bar{Q}(i\not{D} - m_Q)Q \qquad (2.46)\\ &= \bar{h}_v i\not{D} h_v + \bar{H}_v(i\not{D} - 2m_Q)H_v + \bar{h}_v i\not{D} H_v + \bar{H}_v i\not{D} h_v \\ &= \bar{h}_v iv\cdot D h_v - \bar{H}_v(iv\cdot D + 2m_Q)H_v + \bar{h}_v i\vec{\not{D}} H_v + \bar{H}_v i\vec{\not{D}} h_v \,, \end{aligned}$$

where $iD^\mu = \vec{D} + iv^\mu v\cdot D$, thus $\vec{\not{D}}$ represents the spatial covariant derivative. We will now integrate out the heavy field H_v by solving the equations of motion for this field. One arrives at

$$H_v = \frac{1}{2m_Q + iv\cdot D} i\not{D} h_v = \frac{1}{2m_Q}\sum_{k=0}^{\infty} \frac{(-iv\cdot D)^k}{2m_Q} i\not{D} h_v \,, \tag{2.47}$$

and the leading term in this series is $\propto 1/m_Q \not{D} h_v$. By looking at (2.46) we see that h_v describes a massless fermion and given that the residual momentum k^μ is not large we get $H_v = \mathcal{O}(\Lambda_{soft}/m_Q)h_v$. Because of this one sometimes refers to h_v as the large and to H_v as the small components of Q. We can now write down the leading order effective Lagrangian as

$$\mathcal{L}_{HQET} = \bar{h}_v iv \cdot D h_v + \mathcal{O}(1/m_Q) \; . \tag{2.48}$$

As in SCET we will do a scaling analysis in order to assign the right scaling to the different fields. The goal again is to decouple soft gluon interactions by means of field redefinition. We already set the scaling of the residual momentum to $k^\mu \sim \Lambda_{soft}$ and in (2.48) we applied an expansion of the form Λ_{soft}/m_Q. In the following we will count the different scales in relation to the hard scale m_Q with the help of $\lambda = \sqrt{\Lambda_{soft}/m_Q}$ [6]. With this $\Lambda_{soft} \sim \lambda^2$, and derivatives on soft fields $\partial^\mu \sim \lambda^2$. Again we look at the fermion propagator in order to get information about the scaling behavior of the heavy-quark field h_v. We have

$$\langle 0| \, T[h_v(x)\bar{h}_v(0)] \, |0\rangle = \int \frac{d^4p}{(2\pi)^4} \, \frac{i}{v \cdot k + i\epsilon} e^{-ip\cdot x} \sim \lambda^4 \frac{1}{\lambda} \; , \tag{2.49}$$

thus $h_v \sim \lambda^{3/2}$. For the soft gluon propagator one obtains

$$\langle 0| \, T[A_s^\mu(x) A_s^\nu(0)] \, |0\rangle = \int \frac{d^4p}{(2\pi)^4} \frac{i}{p^2 + i\epsilon} e^{-ip\cdot x} \sim \lambda^4 \frac{1}{\lambda^2} [-g^{\mu\nu} + \tau \frac{p^\mu p^\nu}{p^2}] \; , \tag{2.50}$$

leading to $A_s^\mu \sim \lambda$.
Similar to chapter 2.1.1 we can now decouple soft interactions by means of field redefinition.

$$h_v(x) = S_v(x) h_v^{(0)}(x) \tag{2.51}$$

with

$$S_v(x) = P \exp[ig \int_\infty^0 dt v \cdot A_s(x + tv)] \; . \tag{2.52}$$

Where now $h_v^{(0)}(x)$ does not interact with soft gluons anymore.

2.3. Factorization and Resummation

In the following we want to discuss two topics closely related to this thesis, the concept of resummation and its connection to factorization.

In (2.38) we had factorized the current $J^\mu(x)$ into a Wilson coefficient and an effective operator. In general one can write an amplitude as follows

$$A = \sum_{i=1}^{n} C_i(\mu) \, \langle Q_i(\mu) \rangle \; , \tag{2.53}$$

[6] The counting above corresponds to the one in Section 2.1, but one often finds in the literature the counting $\lambda = \Lambda_{soft}/m_Q$.

where μ is the scale where one has renormalized the operator matrix element. Of course the whole amplitude is independent of that scale, leading to

$$\begin{aligned} &\frac{d}{d\ln\mu}\sum_{i=1}^{n} C_i(\mu)\,\langle Q_i(\mu)\rangle = 0 \\ \Longrightarrow &\sum_{i=1}^{n}\left[\left(\frac{d}{d\ln\mu}C_i(\mu)\right)\langle Q_i(\mu)\rangle + C_i(\mu)\left(\frac{d}{d\ln\mu}\langle Q_i(\mu)\rangle\right)\right] = 0 \end{aligned} \tag{2.54}$$

Assuming a complete set of linear independent operators $Q_i(\mu)$ we are able to write

$$\frac{d}{d\ln\mu}\langle Q_i(\mu)\rangle = -\sum_{j=1}^{n}\gamma_{ij}(\mu)\,\langle Q_j(\mu)\rangle \ , \tag{2.55}$$

with γ_{ij} being the anomalous dimension, which is a measure of change under scale variation. From the fact that we are dealing with linear independent operators now follows

$$\frac{d}{d\ln\mu}C_j(\mu) = \sum_{i=1}^{n}\gamma_{ij}C_i(\mu) \quad \Rightarrow \quad \frac{d}{d\ln\mu}\vec{C}(\mu) = \hat{\gamma}^T(\mu)\vec{C}(\mu)\ . \tag{2.56}$$

The anomalous dimension matrix $\hat{\gamma}$ of the Wilson coefficient is directly connected to the remormalization matrix $\mathbf{Z}$ of the operators. This is due to the fact that the bare matrix elements of the operators are scale independent:

$$\left\langle Q_i^{bare}\right\rangle = Z_{ij}(\mu)Q_j(\mu) \quad \Rightarrow \quad Z_{ij}^{-1}(\mu)\left\langle Q_i^{bare}\right\rangle = Q_j(\mu) \tag{2.57}$$

From the above in combination with (2.55) one obtains

$$\gamma_{ij} = (Z)_{ik}\frac{d}{d\ln\mu}Z_{kj}\ . \tag{2.58}$$

Given an expansion of $\mathbf{Z}$ in terms of the coefficients of the different poles, $\mathbf{Z} = \sum_{k=1}^{\infty} 1/\epsilon^k\ \mathbf{Z}^{(k)}$, one finds [119]

$$\gamma_{ij} = -2\alpha_s\frac{d}{d\alpha_s}Z_{ij}^{(1)}\ . \tag{2.59}$$

Knowing how to calculate the anomalous dimension matrix we can now solve (2.58) which leads to the formal expression

$$\begin{aligned} \vec{C}(\mu) &= \mathbf{U}(\mu,\mu_0)\,\vec{C}(\mu_0) \\ &= \left[\mathcal{P}\exp\int_{\mu_0}^{\mu}\frac{d\mu'}{\mu'}\,\hat{\gamma}^T(\mu')\right]\ \vec{C}(\mu_0)\ . \end{aligned} \tag{2.60}$$

In the above equation $\mathcal{P}$ is ordering the integrand such that the ones with larger values of α stand to the left of those with smaller values. This ordering procedure is a remnant of the fact that in general the different $\hat{\gamma}(\mu)$ do not commute. The evolution matrix $\mathbf{U}$ runs the Wilson coefficient from a scale μ_0 to the scale μ. To see how (2.60) can help to resum potentially large logs let us examine the form of $\vec{C}(\mu)$. In general one encounters Wilson coefficient of the following form[7]

$$C(\mu) = \sum_{n=0}^{\infty} c_n \left(\frac{\alpha_s}{4\pi}\right)^n \; ; \quad c_n = \sum_{k=0}^{2n} c_n^{(k)} L_\mu^k \; ; \quad L_\mu = \ln(Q_c^2/\mu^2) \; , \tag{2.61}$$

where Q_c^2 is a scale related to the kinematics occurring in C. Similar expansions hold for $\langle O(\mu)\rangle$. At the n-th order in α_s one has terms of the structure $\alpha_s^n L_\mu^m$, $m = 0, ..., 2n$ for a double logarithmic series. Assuming that $L_\mu \sim 1/\alpha_s$ this structure would spoil the perturbative expansion, which can be "cured" by setting $\mu = Q_c$. But by factorizing the amplitude in (2.53) we have separated different energy scales. To understand this we explicitly write

$$A = C(\mu, Q_c) \langle Q(\mu, Q_q)\rangle \; , \tag{2.62}$$

where we have made clear that the Wilson coefficient is associated to the scale Q_c and the operator matrix element to the scale Q_q. In a situation were $\ln(Q_c^2/Q_q^2)$ is a large number no setting of μ in (2.53) will get rid of all large logs. Having solved the evolution equation for $C(\mu)$ we are able to give an expression were all large logs have been resummed. Using (2.60) we write

$$\begin{aligned} A &= C(\mu, Q_c) \langle Q(\mu, Q_q)\rangle \\ &= U(Q_q, Q_c)\, C(Q_c, Q_c)\, \langle Q(Q_q, Q_q)\rangle \; , \end{aligned} \tag{2.63}$$

where the Wilson coefficient and the operator matrix element are free of large logs. We will now show how $U(Q_q, Q_c)$ resums the logs $L = \ln(Q_c^2/Q_q^2)$.

In Higgs [107], Drell-Yan [106] and in $t\bar{t}$ production one encounters Wilson coefficients which have the following anomalous dimension structure

$$\gamma(\mu) = \Gamma_{\text{cusp}}(\alpha_s)\; \ln(Q_c/\mu) + \gamma_s(\alpha_s) \; . \tag{2.64}$$

The above form of γ is an example of a double logarithmic series, and the double logs are governed by the so called cusp anomalous dimension Γ_{cusp}. The general form of (2.60) now is

$$U(Q_q, Q_c) = \exp\left[2S(Q_c, Q_q) - a_{\gamma^s}(Q_c, Q_q)\right] . \tag{2.65}$$

[7] For the sake of simplicity we will work with a single Wilson coefficient and operator matrix element from now on.

RG-improved PT	Log. approx.	$\alpha_s^n L^k$	C, $\langle Q \rangle$
—	LL	$k = 2n$	tree-level
LO	NLL	$2n-1 \leq k \leq 2n$	tree-level
NLO	NNLL	$2n-3 \leq k \leq 2n$	1-loop
NNLO	NNNLL	$2n-5 \leq k \leq 2n$	2-loop

Table 2.1.: Different orders in RG-improved PT., the matching logarithmic accuracy needed and the terms $\alpha_s^n L^k$ contained.

The RG exponents in the square brackets of the exponential factor are given by

$$S(Q_c, Q_q) = -\int\limits_{\alpha_s(Q_c)}^{\alpha_s(Q_q)} d\alpha \, \frac{\Gamma_{\text{cusp}}(\alpha)}{\beta(\alpha)} \int\limits_{\alpha_s(Q_c)}^{\alpha} \frac{d\alpha'}{\beta(\alpha')}\,, \qquad a_{\gamma^s}(Q_c, Q_q) = -\int\limits_{\alpha_s(Q_c)}^{\alpha_s(Q_q)} d\alpha \, \frac{\gamma^s(\alpha)}{\beta(\alpha)}\,. \quad (2.66)$$

The above integrals can be calculated order by order in perturbation theory and can be found in the Appendix, $\beta(\alpha_s) = d\alpha_s(\mu)/d\ln\mu$ is the QCD β-function. We are not interested in the explicit forms right now but rather state the general structure of the result, which can be written as[8]

$$U(Q_q, Q_c) = \exp\Bigg[\underbrace{\underbrace{\underbrace{L\, a_{-1}\left(\alpha_s L\right)}_{\text{LL}} + a_0\left(\alpha_s L\right)}_{\text{NLL}} + \alpha_s a_1\left(\alpha_s L\right) + \cdots}_{\text{NNLL}}\Bigg]\,. \quad (2.67)$$

In (2.67) the a_i are coefficients depending on the various anomalous dimensions, here Γ_{cusp}, γ^s and β. In the above we count $L \sim 1/\alpha_s$ and the exponent is a reorganization of the fixed order[9] series in which higher order terms are *resummed*. The term in the exponent which we marked as leading-logarithmic order clearly reproduces terms to *all* orders of the form $\alpha_s^n L^{2n}$. Similarly, by including the second term in the exponent marked as next-to-leading-logarithmic order, we are able to get all terms $\alpha_s^n L^k$ with $2n-1 \leq k \leq 2n$. As $L \sim 1/\alpha_s$ all terms $\alpha_s^n L^n$ are counted as $\mathcal{O}(1)$, similarly $\alpha_s^n L^{n-1} \sim \mathcal{O}(\alpha_s)$ and so on. Applying this counting is referred to as renormalization-group improved perturbation theory. In Table 2.1 we show the different order in RG-improved PT, what logarithmic accuracy is needed for each order and what terms of the form $\alpha_s^n L^k$ are reproduced. It should be made clear that these logarithmic terms would also occur in a fixed order calculation. The method we just discussed enables one to calculate higher oder terms with a drastic reduction of the calculational complexity. The terms produced in this way can but need not be

[8] We have already used $L \sim 1/\alpha_s$ and expanded $r \approx 1 + \beta_0 \frac{\alpha_s}{4\pi} L$.

[9] Standard calculations have an expansion in α_s, thus each order has a *fixed* power in α_s.

numerically important. Large logs, and thus numerically important ones, are connected to the occurrence of largely separated scales in the process.

In the following we will use the above methods of renormalization group improved perturbation theory. We will specify what are the different scales in our process and analyze if the logs connected to them are numerically important.

Part II.

$t\bar{t}$ Production: Theoretical Setup

3. Introduction

In this part of the thesis we present details of our $t\bar{t}$ production calculation. This part is split up into three chapters. In the first chapter we show the derivation of the differential cross section using PIM kinematics. In this kinematics we calculate the double differential cross section with respect to the invariant mass M, and the scattering angle θ of the top-quark. As a first step in this chapter we define the kinematical setup in Section 4.1, where the partonic process and kinematical variables are explained. Furthermore we set out the threshold in which we will work. In Section 4.2 we then use the methods explained in the introduction part to establish a factorization theorem for the cross section. We explain in detail how the matching is done, and how matrix elements of operators and Wilson coefficients are calculated. In our calculation we use the so called *color-space formalism* which is an effective method to organize color algebra, in Section 4.2.1 we give an introduction to this formalism.

Having set up the different calculational inputs, we proceed in Section 4.2.2 to give explicit expressions of the cross section in terms of Wilson coefficients and matrix elements. The double differential cross section will be written as a product of a hard and a soft function. In Sections 4.2.3 and 4.2.4 we give a a description of how we derive these two functions. We present the RG equations and solve them for the hard and soft functions in Section 4.2.5. The resummed expression for the hard scattering kernel at the end of Section 4.2.5 is the main results of this chapter.

Chapter 5 is concerned with our calculation in 1PI kinematics, it proceeds along the lines of the previous one. In this kinematics we calculate the double differential cross section with respect to rapidity, and p_T of the top-quark . Details of the kinematical setup of 1PI is given in Section 5.1, where we define the kinematical variables used, and the differential form of the cross section is given. As for PIM we first explain the threshold in which we work before proceeding. In this chapter we do not again present details about the factorization procedure, as most of the discussion can be carried over from PIM kinematics. A major new input is the 1PI soft function which has been calculated by us to NLO order for the first time. In Section 5.2.1 we give details about the derivation of this function. We end this chapter by stating, and solving the RG equations for the partonic cross section in 1PI kinematics in Section 5.2.2. Similar to the PIM chapter we present the resummed expression of the hard scattering kernel at the end of this section.

In Chapter 6 we present details about the extraction of approximate NNLO results starting from our resummed calculations. We do this separately for PIM and 1PI kinematics in Sections 6.1 and 6.2 respectively. In Section 6.3 we compare certain aspects of resummation to approximate NNLO.

4. Pair Invariant-Mass Kinematics

In this chapter we focus on the pair invariant-mass kinematics. Working in PIM we are able to derive results for the double differential cross section with respect to the invariant mass of the $t\bar{t}$ pair and the scattering angle θ of the top-quark. The following work will be done in the threshold limit where $(1-z) = 1 - M^2/\hat{s} \to 1$, with M being the invariant mass of the $t\bar{t}$ pair. This approach will allow us to resum logarithms of $\ln(1-z)$ to full next-to-next-to-leading-logarithmic order. This is an extension of similar studies done in NLL order [48–50] and approximate NNLL calculations [52–55].

The analytical results obtained in this chapter will enable us to make predictions for the total cross section and the invariant mass distribution for $t\bar{t}$ production. Furthermore it allows us to give numerical results for the FB asymmetry at the Tevatron. As this chapter is concerned with the analytical calculation, we refrain from a detailed numerical analysis here.

4.1. Kinematics

We consider the process

$$N_1(P_1) + N_2(P_2) \to t(p_3) + \bar{t}(p_4) + X(p_X)\,, \tag{4.1}$$

where X is an inclusive hadronic final state and N_1, N_2 are the hadronic initial states, which are either proton-proton (LHC) or proton-antiproton (Tevatron). We will treat the top-quarks as on-shell partons and neglect their decay. The large mass of the top quark results in a decay width of $0.3\,\mathrm{GeV} < \Gamma_t < 4.4\,\mathrm{GeV}$ [120]. Corrections to the above treatment scale like $\Gamma_t/m_t \ll 1$ and are thus numerically subleading.
As shown in Figure 4.1, at Born level the production proceeds through the $q\bar{q}$ annihilation and gluon-fusion channels

$$q(p_1) + \bar{q}(p_2) \to t(p_3) + \bar{t}(p_4)\,,$$

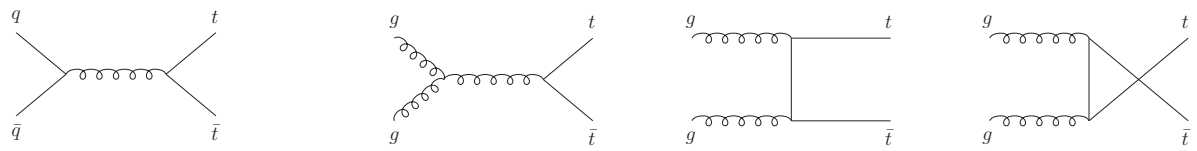

Figure 4.1.: The Born level channels for $t\bar{t}$ production: $q\bar{q}$ inicial state and gg initial state.

$$g(p_1) + g(p_2) \to t(p_3) + \bar{t}(p_4)\,, \tag{4.2}$$

where $p_1 = x_1 P_1$ and $p_2 = x_2 P_2$. We define the kinematic invariants

$$\begin{aligned} s &= (P_1 + P_2)^2\,, \quad \hat{s} = (p_1 + p_2)^2\,, \quad M^2 = (p_3 + p_4)^2\,, \\ \hat{t}_1 &= (p_1 - p_3)^2 - m_t^2\,, \quad \hat{u}_1 = (p_2 - p_3)^2 - m_t^2\,, \end{aligned} \tag{4.3}$$

and momentum conservation at Born level implies $\hat{s} + \hat{t}_1 + \hat{u}_1 = 0$. As one can see $\hat{s}$ is the invariant mass of the partonic initial state whereas M^2 the the invariant mass of the partonic final state. In the following the ratio $z = M^2/\hat{s}$ will play a key role. It is clear the at LO $z = 1$, due to momentum conservation, but at higher orders, real radiation can lead to $z < 1$. We will analyze the above process in the following in the limit $z \to 1$ which we call partonic threshold. In this limit the phase space is restricted such that only soft radiation is possible. Furthermore we are mainly interested in the doubly differential cross section expressed in terms of the invariant mass M of the $t\bar{t}$ pair and the scattering angle θ between $\vec{p}_1$ and $\vec{p}_3$ in the partonic center-of-mass frame[1]. To describe this distribution we need the variables

$$\tau = \frac{M^2}{s}\,, \qquad \beta_t = \sqrt{1 - \frac{4m_t^2}{M^2}} \quad \text{and} \quad z = \frac{M^2}{\hat{s}} = \frac{\tau}{x_1 x_2}\,. \tag{4.4}$$

We already had defined z, τ is the equivalent of z on a hadronic scale. The limit $\tau \to 1$ is often considered as the machine threshold.
The quantity β_t gives the 3-velocity of the top quarks in the $t\bar{t}$ rest frame. Another common related variable is $\beta = \sqrt{1 - 4m_t^2/\hat{s}}$, which coincides with β_t in the limit $z \to 1$. To describe the total inclusive cross section, one often considers the limit $\beta \to 0$ [40–46]. It should be noted that in our approach the numerical values for β and β_t are supposed to be close to each other. Working in the limit $z \to 1$ leaves β_t a generic $\mathcal{O}(1)$ parameter and in that case the top quarks are not produced at rest, nor are they highly boosted, and the emitted partons in the final state X are constrained to be soft. This threshold limit is often referred to in the literature as the pair-invariant-mass kinematics, and the theoretical framework to deal with this situation was developed in [48, 49, 121, 122]. According to the QCD factorization theorem [7], the differential cross section in M and $\cos\theta$ can be written as

$$\frac{d^2\sigma}{dM\, d\cos\theta} = \frac{8\pi\beta_t}{3sM} \sum_{i,j} \int \frac{dx_1}{x_1} \frac{dx_2}{x_2}\, f_{i/N_1}(x_1, \mu_f) f_{j/N_2}(x_2, \mu_f)\, C_{ij}(z, M, m_t, \cos\theta, \mu_f)\,. \tag{4.5}$$

Equation (4.5) shows the general scheme of factorizing the cross section into the partonic process, captured in the hard scattering kernel C_{ij}, and the information about the hadronic initial state shown as f_{i/N_j}, μ_f is the factorization scale. Again, the $f_{i/N}$ are universal non-perturbative parton distribution functions, which are extracted from experimental data.

[1] The fully differential cross section depends on three kinematic variables.

One can see from (4.4) that the integration region in (4.5) is restricted to $x_1 x_2 \geq \tau$. From this it is possible to write (4.5) as follows

$$\frac{d^2\sigma}{dM\, d\cos\theta} = \frac{8\pi\beta_t}{3sM} \sum_{i,j} \int_\tau^1 \frac{dz}{z}\, \mathit{fff}_{ij}(\tau/z, \mu_f)\, C_{ij}(z, M, m_t, \cos\theta, \mu_f)\,, \tag{4.6}$$

where the parton luminosity functions fff_{ij} are defined by

$$\mathit{fff}_{ij}(y, \mu_f) = \int_y^1 \frac{dx}{x}\, f_{i/N_1}(x, \mu_f)\, f_{j/N_2}(y/x, \mu_f)\,. \tag{4.7}$$

The hard-scattering kernels C_{ij} are related to the partonic cross sections and can be calculated as a power series in α_s. We shall write their expansion as

$$C_{ij} = \alpha_s^2 \left[C_{ij}^{(0)} + \frac{\alpha_s}{4\pi} C_{ij}^{(1)} + \left(\frac{\alpha_s}{4\pi}\right)^2 C_{ij}^{(2)} + \ldots \right]. \tag{4.8}$$

At leading order in α_s, only $C_{q\bar{q}}$ and C_{gg} are non-zero. They are proportional to $\delta(1-z)$ and read

$$\begin{aligned} C_{q\bar{q}}^{(0)} &= \delta(1-z)\, \frac{3}{8N}\, C_F \left(\frac{\hat{t}_1^2 + \hat{u}_1^2}{M^4} + \frac{2m_t^2}{M^2} \right), \\ C_{gg}^{(0)} &= \delta(1-z)\, \frac{3}{8(N^2-1)} \left(C_F \frac{M^4}{\hat{t}_1 \hat{u}_1} - C_A \right) \left[\frac{\hat{t}_1^2 + \hat{u}_1^2}{M^4} + \frac{4m_t^2}{M^2} - \frac{4m_t^4}{\hat{t}_1 \hat{u}_1} \right], \end{aligned} \tag{4.9}$$

where $N = 3$ is the number of colors in QCD, and $\hat{t}_1$ and $\hat{u}_1$ can be expressed in terms of M and $\cos\theta$ as

$$\hat{t}_1 = -\frac{M^2}{2}(1 - \beta_t \cos\theta)\,, \qquad \hat{u}_1 = -\frac{M^2}{2}(1 + \beta_t \cos\theta)\,. \tag{4.10}$$

Note that for the doubly differential cross section the coefficient $C_{\bar{q}q}$ is also needed. It can be obtained from the expression for $C_{q\bar{q}}$ by replacing $\cos\theta \to -\cos\theta$, which is a symmetry at tree level but not beyond.

At higher orders in α_s the hard-scattering kernels receive corrections from virtual loop diagrams and real gluon emissions in the $q\bar{q}$ and gg channels, as well as from other partonic channels such as $gq \to t\bar{t}q$. The calculation of these corrections near threshold is greatly simplified. For $z \to 1$ there is no phase-space available for hard gluon emission, which is thus suppressed by powers of $(1-z)$. Moreover, contributions from channels such as $gq \to t\bar{t}q$, which involve external soft-quark fields, are also suppressed. The partonic scattering process is thus dominated by virtual corrections and the real emission of soft gluons. The phase-space for such processes is effectively that for a two-body final state, so the hard-scattering kernels can be written in terms of the kinematic invariants from the

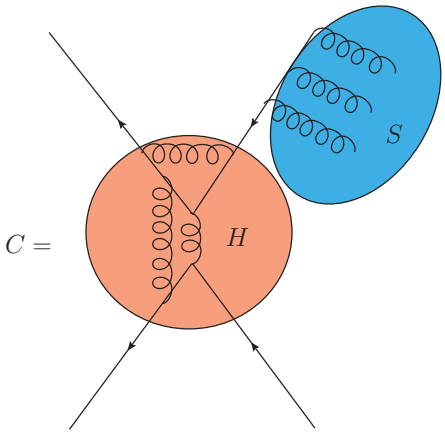

Figure 4.2.: Illustration of the contributions to the hard and soft function.

Born-level processes. Therefore, up to corrections of order $(1-z)$, we can rewrite (4.6) in the threshold region as

$$\frac{d^2\sigma}{dM\,d\cos\theta} = \frac{8\pi\beta_t}{3sM}\int_\tau^1 \frac{dz}{z}\Big[ff_{gg}(\tau/z,\mu_f)\,C_{gg}(z,M,m_t,\cos\theta,\mu_f) + ff_{q\bar{q}}(\tau/z,\mu_f)\,C_{q\bar{q}}(z,M,m_t,\cos\theta,\mu_f) + ff_{\bar{q}q}(\tau/z,\mu_f)\,C_{q\bar{q}}(z,M,m_t,-\cos\theta,\mu_f)\Big]\,, \tag{4.11}$$

where $ff_{q\bar{q}}$ is understood to be summed over all light quark flavors.

At partonic threshold the hard-scattering kernels C_{ij} are governed by two distinct scales, a hard scale related to the virtual corrections and a soft one related to soft-gluon emission. We have illustrated the contributions to these functions schematically in Figure 4.2. In what follows we will factorize C_{ij} into these two different regions. In detail we will find that

$$C_{ij}(z,M,m_t,\cos\theta,\mu_f) = \mathrm{Tr}\left[\boldsymbol{H}_{ij}(M,m_t,\cos\theta,\mu_f)\,\boldsymbol{S}_{ij}(\sqrt{\hat{s}}(1-z),m_t,\cos\theta,\mu_f)\right] + \mathcal{O}(1-z)\,. \tag{4.12}$$

The boldface indicates that the hard functions $\boldsymbol{H}_{ij}$ and soft functions $\boldsymbol{S}_{ij}$ are matrices in color space, with respect to which the trace is taken. We will derive this formula in the next section, using techniques from SCET. (A similar factorization formula in Mellin moment space was derived in [49].)

As we already mentioned the hard functions are related to the virtual corrections, while the soft functions are related to the real emission of soft gluons. These soft functions contain singular distributions in $(1-z)$, terms proportional to $\delta(1-z)$ and, in the n-th order

corrections in α_s, plus distributions of the form

$$\left[\frac{\ln^m(1-z)}{1-z}\right]_+ ; \qquad m = 0, \ldots, 2n-1\,. \tag{4.13}$$

These so called plus-distributions are defined as

$$\int_\tau^1 dz \left[\frac{\ln^m(1-z)}{1-z}\right]_+ g(z) = \int_\tau^1 dz\, \frac{\ln^m(1-z)}{1-z}\,[g(z)-g(1)] - g(1)\int_0^\tau dz\, \frac{\ln^m(1-z)}{1-z} \tag{4.14}$$

for an arbitrary function $g(z)$. These singular distributions make the perturbative series badly convergent near threshold and must be resummed to all orders in perturbation theory. In this thesis we perform such a resummation directly in momentum space [123], up to NNLL order. To this end, we extend the procedure for deep-inelastic scattering [124], Drell-Yan process [106], Higgs production [107, 108], and direct photon production [125] to processes with four colored external particles. The formalism will be described in Section 4.2.5.

4.2. Factorization in SCET and HQET

As mentioned above in this section we will derive the factorization formula (4.12) for the hard-scattering kernels in the threshold region using SCET and HQET. Derivation of similar factorizations have been achieved in [106, 124, 125]. Due to the fact that we are dealing with colored final states, the derivation presented here is more involved. The derivation of factorization in the effective theory relies on a two-step matching procedure. In the first step, fluctuations at the hard scale from virtual corrections are integrated out by matching QCD onto an effective-theory with collinear and soft degrees of freedom. The Wilson coefficients from this matching step give the hard function when squaring the amplitude. In the second step, the soft degrees of freedom are integrated out, giving rise to a soft function, which is defined as the vacuum expectation value of a Wilson loop operator.

Fields

The scattering amplitude for $t\bar{t}$ production involves several scales, which we assume to satisfy

$$\hat{s}, M^2, |\hat{t}_1|, |\hat{u}_1|, m_t^2 \gg \hat{s}(1-z)^2 \gg \Lambda^2_{\rm QCD} \tag{4.15}$$

in the threshold region. The elements of the first set of scales are taken to be of the same order and shall be collectively referred to as hard scales, whereas $\hat{s}(1-z)^2$ defines the soft scale. The small quantity $\lambda = (1-z) \ll 1$ then serves as the expansion parameter in the effective theory. Note that we treat M and m_t as of the same order, which means that the

top quarks are not highly boosted[2]. However, given that even for M as large as 1.5 TeV the ratio $2m_t/M \approx 0.23$ is still a reasonable $\mathcal{O}(1)$ parameter, we see no need to adopt it for the present work. The topic of highly boosted tops is very interesting and we will comment in the outlook on how this work might be extended to this kinematical region.

The formalism for SCET applied to a generic n-body scattering process involving both heavy and light partons was set up in [110, 126]. In our case, the effective theory contains two sets of collinear fields to describe the degrees of freedom in the incoming hadrons, two sets of HQET fields to describe the outgoing heavy quarks, and a single set of soft fields describing the final state X and the soft interactions among particles. In classifying the collinear fields we define two light-like vectors n and $\bar{n}$ in the directions of the colliding partons, which satisfy $n \cdot \bar{n} = 2$. The collinear quark fields are related to the QCD fields by

$$\xi_n(x) = \frac{\not{n}\bar{\not{n}}}{4}\,\psi(x)\,, \qquad \xi_{\bar{n}}(x) = \frac{\bar{\not{n}}\not{n}}{4}\,\psi(x)\,. \tag{4.16}$$

The collinear gluon fields in a single collinear sector are identical to those in QCD, with their momenta restricted to be collinear to the given direction. As we have seen in Section 2.1 it is convenient to introduce manifestly gauge-invariant combinations of fields

$$\chi_n(x) = W_n^\dagger(x)\,\xi_n(x)\,, \qquad \mathcal{A}_{n\perp}^\mu(x) = W_n^\dagger(x)\,[iD_\perp^\mu W_n(x)]\,, \tag{4.17}$$

where the n-collinear Wilson line is

$$W_n(x) = \mathcal{P}\exp\left(ig\int_{-\infty}^0 ds\,\bar{n}\cdot A_n(x+s\bar{n})\right)\,. \tag{4.18}$$

The corresponding objects for the $\bar{n}$-collinear fields are obtained by interchanging n and $\bar{n}$. Similar to section 2.2 we label the HQET fields h_{v_3} and h_{v_4} by the velocities of the top quark and anti-quark, which are related to their momenta as

$$p_3^\mu = m_t v_3^\mu + k_3^\mu\,, \qquad p_4^\mu = m_t v_4^\mu + k_4^\mu\,. \tag{4.19}$$

We remind ourselves that the residual momenta k_i scale as soft momenta and are set to zero for on-shell quarks. As shown in (2.44), in terms of the QCD top-quark fields, the HQET fields are defined as

$$h_{v_i}(x) = \frac{1+\not{v}}{2}\,e^{-im_t v_i\cdot x}\,t(x)\,. \tag{4.20}$$

$$\tag{4.21}$$

A crucial property of the leading-order SCET Lagrangian is that the interactions of soft

[2]To describe the invariant mass spectrum in the region where $M \gg 2m_t$, a more appropriate treatment would require a different effective theory to separate these two scales, and two jet functions have to be introduced for the top and anti-top quarks.

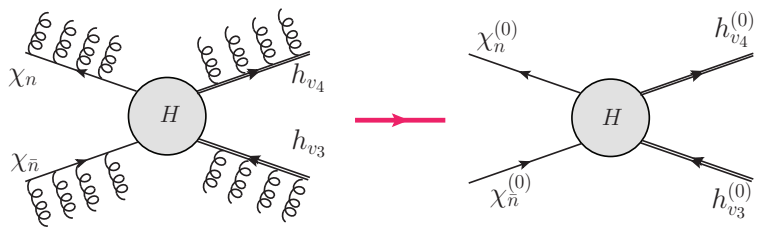

Figure 4.3.: Illustration of the field redefinition mentioned in (4.23). The fields $\chi_{n,\bar{n}}(h_{v_{3,4}})$ have been "stripped" from soft interaction, and the remaining fields are $\chi^{(0)}_{n,\bar{n}}$ $(h^{(0)}_{v_{3,4}})$.

gluon fields with collinear and heavy-quark fields are described by eikonal vertices. The explicit form of the interaction terms for soft gluons with the fermion fields is

$$\begin{aligned}\mathcal{L}_{\rm int} &= \bar{\xi}_n(x)\,\frac{\bar{n}\!\!\!/}{2}\,g\,n\cdot A_s(x)\,\xi_n(x) + \bar{\xi}_{\bar{n}}(x)\,\frac{n\!\!\!/}{2}\,g\,\bar{n}\cdot A_s(x)\,\xi_{\bar{n}}(x)\\ &\quad + \bar{h}_{v_3}(x)\,g\,v_3\cdot A_s(x)\,h_{v_3}(x) + \bar{h}_{v_4}(x)\,g\,v_4\cdot A_s(x)\,h_{v_4}(x)\,,\end{aligned} \tag{4.22}$$

and those between collinear and soft gluon fields can be deduced by making the substitution $A_n \to A_n + n\cdot A_s\,\bar{n}/2$ (and similarly for the $\bar{n}$-collinear fields) in the Yang-Mills Lagrangian. We now make use of the fact that these eikonal interactions can be absorbed into Wilson lines via the field redefinitions [104, 127]

$$\chi_n^a(x) \to \big[S_n(x)\big]^{ab}\,\chi_n^{b(0)}(x)\,,\quad \mathcal{A}^a_{n\mu}(x) \to \big[S_n^{\rm adj}(x)\big]^{ab}\,\mathcal{A}^{b(0)}_{n\mu}(x)\,,\quad h^a_{v_3}(x) \to \big[S_{v_3}(x)\big]^{ab}\,h^{b(0)}_{v_3}(x)\,, \tag{4.23}$$

with

$$\begin{aligned}\big[S_n(x)\big]^{ab} &= \mathcal{P}\exp\left(ig\int_{-\infty}^0 dt\,n\cdot A_s^c(x+tn)\,t^c_{ab}\right),\\ \big[S_n^{\rm adj}(x)\big]^{ab} &= \mathcal{P}\exp\left(ig\int_{-\infty}^0 dt\,n\cdot A_s^c(x+tn)\,(-if^{cab})\right),\\ \big[S_{v_3}(x)\big]^{ab} &= \mathcal{P}\exp\left(-ig\int_0^\infty dt\,v_3\cdot A_s^c(x+tv_3)\,t^c_{ab}\right),\end{aligned} \tag{4.24}$$

and similarly for the $\bar{n}$-collinear and h_{v_4} fields. We have used the superscript "adj" to indicate Wilson lines in the adjoint representation. The fields with the superscript (0) no longer interact with soft gluon fields, we have illustrated this field redefinition in Figure 4.3.

One must supplement the effective Lagrangian with a set of operators describing the

$(q\bar{q}, gg) \to t\bar{t}$ scattering processes. Similar to the matching example in Section 2.1.3 these operators appear in convolution with perturbative Wilson coefficients along light-like directions. As there are two collinear fields we have to have a twofold integration in the case of $t\bar{t}$ production, we write the effective Hamiltonian as

$$\mathcal{H}_{\text{eff}}(x) = \sum_{I,m} \int dt_1 dt_2 \, e^{im_t(v_3+v_4)\cdot x} \left[\tilde{C}^{q\bar{q}}_{Im}(t_1,t_2)\, O^{q\bar{q}}_{Im}(x,t_1,t_2) + \tilde{C}^{gg}_{Im}(t_1,t_2)\, O^{gg}_{Im}(x,t_1,t_2) \right], \tag{4.25}$$

where I labels color structures and m labels Dirac structures. The operators can be written as

$$O^{q\bar{q}}_{Im}(x,t_1,t_2) = \sum_{\{a\}} \left(c^{q\bar{q}}_I\right)_{\{a\}} \bar{\chi}^{a_2}_{\bar{n}}(x+t_2 n)\, \Gamma'_m\, \chi^{a_1}_n(x+t_1\bar{n})\, \bar{h}^{a_3}_{v_3}(x)\, \Gamma''_m\, h^{a_4}_{v_4}(x)\,,$$

$$O^{gg}_{Im}(x,t_1,t_2) = \sum_{\{a\}} \left(c^{gg}_I\right)_{\{a\}} \mathcal{A}^{a_1}_{n\mu\perp}(x+t_1\bar{n})\, \mathcal{A}^{a_2}_{\bar{n}\nu\perp}(x+t_2 n)\, \bar{h}^{a_3}_{v_3}(x)\, \Gamma^{\mu\nu}_m\, h^{a_4}_{v_4}(x)\,, \tag{4.26}$$

where $\Gamma^{\mu\nu}_m$, Γ'_m, and Γ''_m are combinations of Dirac matrices and the external vectors n, $\bar{n}$, v_3, and v_4 (note that there can be contractions of Lorentz indices between Γ'_m and Γ''_m). The $c^{q\bar{q}}_I$ and c^{gg}_I are tensors in color space, whose indices $\{a\} \equiv \{a_1, a_2, a_3, a_4\}$ can be in either the fundamental or adjoint representation. For each channel, they are chosen to be the independent color singlet (e.g. gauge-invariant) structures needed to describe the scattering amplitude. We will choose the color structures to be in the singlet-octet bases

$$\left(c^{q\bar{q}}_1\right)_{\{a\}} = \delta_{a_1 a_2}\delta_{a_3 a_4}\,, \qquad \left(c^{q\bar{q}}_2\right)_{\{a\}} = t^c_{a_2 a_1} t^c_{a_3 a_4}\,,$$

$$\left(c^{gg}_1\right)_{\{a\}} = \delta^{a_1 a_2}\delta_{a_3 a_4}\,, \qquad \left(c^{gg}_2\right)_{\{a\}} = i f^{a_1 a_2 c}\, t^c_{a_3 a_4}\,, \qquad \left(c^{gg}_3\right)_{\{a\}} = d^{a_1 a_2 c}\, t^c_{a_3 a_4}\,. \tag{4.27}$$

When squaring the amplitude and summing over colors, one must evaluate products of the color structures with their indices contracted. In the absence of soft gluon emissions, these are of the form $\left(c^{q\bar{q}}_I\right)_{a_1 a_2 a_3 a_4} \left(c^{q\bar{q}}_J\right)^*_{a_1 a_2 a_3 a_4}$ (and similarly for the gluon fusion channel) and are equal to an N-dependent factor multiplying δ_{IJ}. In this sense the color structures are orthogonal, but not orthonormal.

Time-ordered products of the operators (4.26) with the SCET and HQET Lagrangians describe the collinear and soft contributions to the $(q\bar{q}, gg) \to t\bar{t}X$ scattering amplitudes in QCD, where the final state X contains any number of soft gluons from real emissions. In the formulation used so far, the final state X is built up through insertions of the interaction Lagrangian (4.22) into the SCET operators. To account explicitly for soft gluon emission to all orders in the strong coupling constant, it is convenient to use the decoupling relations (4.23) and represent the soft gluon interactions by Wilson lines. Performing this decoupling and dropping the superscripts on the new fields, the operators factorize into products of collinear, heavy-quark, and soft-gluon operators in the form of Wilson loops. The resulting operators in the $q\bar{q}$ channel read

$$O_{Im}(x,t_1,t_2) = \sum_{\{a\},\{b\}} \left(c_I\right)_{\{a\}} \left[O^h_m(x)\right]^{b_3 b_4} \left[O^c_m(x,t_1,t_2)\right]^{b_1 b_2} \left[O^s(x)\right]^{\{a\},\{b\}}, \tag{4.28}$$

where

$$\big[O_m^h(x)\big]^{b_3b_4} = \bar{h}_{v_3}^{b_3}(x)\,\Gamma''_m\,h_{v_4}^{b_4}(x)\,, \qquad \big[O_m^c(x,t_1,t_2)\big]^{b_1b_2} = \bar{\chi}_{\bar{n}}^{b_2}(x+t_2n)\,\Gamma'_m\,\chi_n^{b_1}(x+t_1\bar{n})\,,$$
$$\big[O^s(x)\big]^{\{a\},\{b\}} = \big[S_{v_3}^\dagger(x)\big]^{b_3a_3}\,\big[S_{v_4}(x)\big]^{a_4b_4}\,\big[S_{\bar{n}}^\dagger(x)\big]^{b_2a_2}\,\big[S_n(x)\big]^{a_1b_1}\,. \tag{4.29}$$

Those in the gluon-fusion channel are obtained by making the obvious replacements in Dirac structure and the collinear operators, and by changing the Wilson lines S_n and $S_{\bar{n}}$ to the corresponding ones in the adjoint representation.

In the form shown above, the different sectors no longer interact with each other. After squaring the amplitude, this property leads to the factorized form (4.11) for the hard-scattering kernels. A complication is that the color indices on the Wilson lines representing the soft-gluon interactions act on the color structures (4.27) and can mix them into each other. Consider, for example, the calculation of an $\mathcal{O}(\alpha_s)$ correction due to soft gluon exchange between partons 1 and 3 in the squared amplitude in the $q\bar{q}$ channel. This could either be from the product of diagrams involving the real emission of one soft gluon, or from a virtual diagram with a soft loop (which would be scaleless for on-shell quarks, but appears in the calculation of the anomalous-dimension matrix). After summing over colors one must evaluate contractions of the form

$$\big(c_I^{q\bar{q}}\big)_{\{b_1a_2b_3a_4\}}\,t^c_{b_1a_1}\,t^c_{a_3b_3}\big(c_J^{q\bar{q}}\big)^*_{\{a_1a_2a_3a_4\}}\,. \tag{4.30}$$

In general, this contraction is not proportional to δ_{IJ}, and must be worked out case by case. This mixing of the different color structures due to soft gluon exchange is responsible for the non-trivial matrix structure of the hard and soft functions. To organize this color algebra, it is convenient to use the color-space formalism [128, 129]. Before moving on to the calculation of the differential cross section in Section 4.2.2, we briefly pause to review this formalism.

4.2.1. Color-Space Formalism

Consider the on-shell scattering amplitudes for $(q\bar{q}, gg) \to t\bar{t}$, for a given color configuration of the external particles. We write this in the quark channel as

$$\mathcal{M}^{q\bar{q}}_{\{a\}} = \langle t^{a_3}(p_3)\,\bar{t}^{a_4}(p_4)\,|\,\mathcal{H}_{\rm eff}(0)\,|\,q^{a_1}(p_1)\,\bar{q}^{a_2}(p_2)\rangle\,, \tag{4.31}$$

and also define the object $\mathcal{M}^{gg}_{\{a\}}$ in the obvious way. In what follows, we will drop the superscript indicating the channel, and work with a single amplitude which can represent either $\mathcal{M}^{q\bar{q}}$ or $\mathcal{M}^{gg}$. As in [128, 129], we introduce an orthonormal basis of vectors $\{|a_1,a_2,a_3,a_4\rangle\}$, where the indices $\{a\}$ refer to the colors of the external particles. The amplitude can then be written as

$$\mathcal{M}_{\{a\}} = \langle a_1,a_2,a_3,a_4\,|\,\mathcal{M}\rangle\,, \tag{4.32}$$

where the object $|\mathcal{M}\rangle$ is an abstract vector in color space. Since we only consider color-singlet amplitudes, we can decompose the QCD amplitude into the set of color structures (4.27). In the color-space formalism, this is done by writing

$$|\mathcal{M}\rangle = \sum_I \mathcal{M}_I \sum_{\{a\}} \big(c_I\big)_{\{a\}} |\{a\}\rangle \equiv \mathcal{M}_I \, |c_I\rangle \;, \tag{4.33}$$

where the coefficients $\mathcal{M}_I$ are combinations of Dirac matrices, external vectors, spinors, and polarization vectors. Note that with this definition the basis vectors $|c_I\rangle$ are orthogonal but not normalized, so to project out the $\mathcal{M}_I$ one must use

$$\mathcal{M}_I = \frac{1}{\langle c_I \,|\, c_I\rangle} \langle c_I \,|\, \mathcal{M}\rangle \;. \tag{4.34}$$

The square of the amplitude summed over colors is then given by the inner product of $|\mathcal{M}\rangle$:

$$\sum_{\text{colors}} |\mathcal{M}|^2 = \langle \mathcal{M} \,|\, \mathcal{M}\rangle = \sum_I \mathcal{M}_I^* \mathcal{M}_I \, \langle c_I \,|\, c_I\rangle = \sum_I \sum_{\{a\}} \mathcal{M}_I^* \mathcal{M}_I \big(c_I\big)^*_{a_1 a_2 a_3 a_4} \big(c_I\big)_{a_1 a_2 a_3 a_4} \,. \tag{4.35}$$

Following [128, 129], we introduce color generators $\boldsymbol{T}_i$ to describe the color algebra associated with the emission of a soft gluon from parton $i = 1, 2, 3, 4$. These matrices act on the color indices of the i-th parton as

$$\boldsymbol{T}_i^c \, |\ldots, a_i, \ldots\rangle = (\boldsymbol{T}_i^c)_{b_i a_i} \, |\ldots, b_i, \ldots\rangle \;. \tag{4.36}$$

If the i-th parton is a final-state quark or an initial-state anti-quark we set $(\boldsymbol{T}_i^c)_{ba} = t^c_{ba}$, for a final-state anti-quark or an initial-state quark we have $(\boldsymbol{T}_i^c)_{ba} = -t^c_{ab}$, and for a gluon we use $(\boldsymbol{T}_i^c)_{ba} = i f^{abc}$. We also use the notation $\boldsymbol{T}_i \cdot \boldsymbol{T}_j \equiv \boldsymbol{T}_i^c \, \boldsymbol{T}_j^c$, and $\boldsymbol{T}_i^2$ denotes the quadratic Casimir operator in the representation of the i-th parton, with eigenvalues C_F for quarks and C_A for gluons. Since we consider color-singlet amplitudes, color conservation implies the relation

$$(\boldsymbol{T}_1 + \boldsymbol{T}_2 + \boldsymbol{T}_3 + \boldsymbol{T}_4) \, |\mathcal{M}\rangle = 0 \,. \tag{4.37}$$

We will be particularly interested in products of color generators acting on the scattering amplitudes, which appear in the calculation of perturbative corrections to the differential cross section. We write such products as, for instance,

$$\langle \mathcal{M} \,|\, \boldsymbol{T}_2 \cdot \boldsymbol{T}_4 \,|\, \mathcal{M}\rangle = \mathcal{M}^*_{a_1 b_2 a_3 b_4} (\boldsymbol{T}_2^c)_{b_2 a_2} (\boldsymbol{T}_4^c)_{b_4 a_4} \mathcal{M}_{a_1 a_2 a_3 a_4} \,. \tag{4.38}$$

Rather than evaluating such expressions for each amplitude $\mathcal{M}$, it is more convenient to work out how the products $\boldsymbol{T}_i \cdot \boldsymbol{T}_j$ act on the basis vectors $|c_I\rangle$:

$$\boldsymbol{T}_i \cdot \boldsymbol{T}_j \, |c_J\rangle = [\boldsymbol{T}_i \cdot \boldsymbol{T}_j]_{IJ} \, |c_I\rangle \;, \tag{4.39}$$

where the matrix elements are given by

$$[\boldsymbol{T}_i \cdot \boldsymbol{T}_j]_{IJ} = \frac{1}{\langle c_I \,|\, c_I \rangle} \langle c_I \,|\, \boldsymbol{T}_i \cdot \boldsymbol{T}_j \,|\, c_J \rangle \ . \tag{4.40}$$

It is worth emphasizing that while the generators themselves act in the abstract color space, on the left-hand side of the above equation they are just labels to identify a matrix acting in the space of color-singlet structures. This matrix is thus a 2×2 matrix for the $q\bar{q}$ channel, and a 3×3 matrix for the gg channel.

We now consider the SCET representation of the amplitude $\mathcal{M}_{\{a\}}$. For the $q\bar{q}$ channel, this is equal to

$$\begin{aligned} &\sum_{I,m} \int dt_1 dt_2 \, \tilde{C}_{Im}(t_1, t_2) \, \big(c_I\big)_{\{a\}} \\ &\qquad \times \Big\langle t^{b_3}(p_3) \, \bar{t}^{b_4}(p_4) \Big| \, \big[O_m^h\big]^{b_3 b_4} \big[O_m^c\big]^{b_1 b_2} \big[O^s\big]^{\{a\},\{b\}}(0, t_1, t_2) \Big| \, q^{b_1}(p_1) \, \bar{q}^{b_2}(p_2) \Big\rangle \ , \end{aligned} \tag{4.41}$$

where no summation over the set of indices $\{b\}$ is performed. We have made clear that for the amplitude to be non-zero, the colors of the heavy-quark and collinear fields must coincide with those of the external partons. The reason is that after the decoupling of soft gluons, the heavy-quark fields are effectively free fields, while collinear exchanges take place only within O_m^c itself and are diagonal in color space. We can therefore suppress the color indices on O_m^h and O_m^c as well as on the external states, and keep in mind that we shall sum over the color indices of O^s when we square the amplitude. Color correlations such as (4.38) are mediated by the exchange of soft gluons, which are represented by the Wilson lines in the soft operator O_s. To describe these exchanges in the color-space formalism we use the operator

$$\boldsymbol{O}_s(x) = \big[\boldsymbol{S}_n \boldsymbol{S}_{\bar{n}}^\dagger \boldsymbol{S}_{v_3}^\dagger \boldsymbol{S}_{v_4}\big](x) \, , \tag{4.42}$$

where the Wilson lines $\boldsymbol{S}_i$ are defined as in (4.24), with the color generators promoted to the abstract ones $\boldsymbol{T}_i$ according to the rules stated below in (4.36). The decoupling relations (4.23) are of the same form for quarks and gluons when expressed in terms of the $\boldsymbol{S}_i$ [130], so this operator is used for both the $q\bar{q}$ and gg channels. Its action on the basis vectors $|c_I\rangle$ is then defined according to (4.38). We define the full SCET operator as $\boldsymbol{O}_m = O_m^h O_m^c \boldsymbol{O}^s$.

To evaluate the partonic matrix elements of the collinear fields we use

$$\begin{aligned} \big\langle 0 \,\big|\, \big(\chi_n\big)_\alpha^a(t\bar{n}) \,\big|\, p_i; a_i, s_i \big\rangle &= \delta_{aa_i} \, e^{-it\bar{n}\cdot p} \, u_\alpha(p_i, s_i) \, , \\ \big\langle 0 \,\big|\, \big(\mathcal{A}_{n\perp}\big)_\alpha^a(t\bar{n}) \,\big|\, p_i; a_i, s_i \big\rangle &= \delta_{aa_i} \, e^{-it\bar{n}\cdot p} \, \epsilon_\alpha(p_i, s_i) \, . \end{aligned} \tag{4.43}$$

The heavy-quark fields are always taken to be on-shell, so their partonic matrix elements are equal to HQET spinors multiplied by Kronecker delta symbols in the spin and color indices. Upon taking the partonic matrix elements, the integrals over t_1 and t_2 produce the Fourier-transformed Wilson coefficients

$$C_{Im}(M, m_t, \cos\theta, \mu) = \int dt_1 dt_2 \, e^{-it_1 \bar{n}\cdot p_1 - it_2 n\cdot p_2} \, \tilde{C}_{Im}(t_1, t_2) \, , \tag{4.44}$$

where we have made the full dependence of the momentum space Wilson coefficients on the kinematic variables explicit. Defining a vector of Wilson coefficients as

$$|C_m\rangle \equiv \sum_I C_{Im}\,|c_I\rangle\ , \tag{4.45}$$

and introducing the symbol $\langle\!\langle \ldots \rangle\!\rangle$ for partonic matrix elements as in [131], i.e.,

$$\langle\!\langle \boldsymbol{O}_m \rangle\!\rangle = \langle t(p_3)\,\bar{t}(p_4)\,|\,\boldsymbol{O}_m(0,0,0)\,|\,q(p_1)\,\bar{q}(p_2)\rangle\ , \tag{4.46}$$

we can write the color-space representation of the SCET scattering amplitude as

$$|\mathcal{M}\rangle = \sum_m \langle\!\langle \boldsymbol{O}_m \rangle\!\rangle\,|C_m\rangle\ . \tag{4.47}$$

4.2.2. Factorization of the Differential Cross Section

We now return to the derivation of the factorization formula (4.11) by calculating the partonic cross sections. The hadronic cross section is then obtained by convoluting these results with the PDFs. Below we will discuss the $q\bar{q}$ case in detail; the gg channel can be analyzed in an analogous way.

The differential cross section is given by the phase-space integral of the squared amplitude

$$\begin{aligned} d\hat{\sigma} = {}& \frac{1}{2\hat{s}}\frac{d^3\vec{p}_3}{(2\pi)^3 2E_3}\frac{d^3\vec{p}_4}{(2\pi)^3 2E_4}\sum_{X_s}(2\pi)^4\delta^{(4)}(p_s+p_3+p_4-p_1-p_2) \\ & \times\frac{1}{4d_R^2}\left|\sum_m \langle t(p_3)\,\bar{t}(p_4)\,X_s(p_s)\,|\,\boldsymbol{O}_m(0)\,|\,q(p_1)\,\bar{q}(p_2)\rangle\,|C_m\rangle\right|^2, \end{aligned} \tag{4.48}$$

where $\boldsymbol{O}_m(x) \equiv \boldsymbol{O}_m(x,0,0)$, and we have used translational invariance to write the result in terms of the Fourier-transformed coefficients C_m from (4.44). The cross section is implicitly summed over the external colors and spins, and the factor $d_R = N$ for quarks and $d_R = N^2-1$ for gluons arises from averaging over the colors of the initial-state partons. The factor $1/4$ accounts for the averaging over the polarizations of the initial-state partons. Since the different types of effective-theory fields do not interact with each other, we can factorize the matrix element into soft, heavy-quark, and collinear pieces. The partonic matrix elements of the heavy-quark and collinear pieces just give the usual products of spinors, which we combine into the tree-level matrix element

$$\langle\!\langle O_m \rangle\!\rangle_{\text{tree}} \equiv \langle\!\langle O_m^h(0)O_m^c(0) \rangle\!\rangle_{\text{tree}} = \big\langle t(p_3)\,\bar{t}(p_4)\,\big|\,O_m^h(0)O_m^c(0)\,\big|\,q(p_1)\,\bar{q}(p_2)\big\rangle_{\text{tree}}\ . \tag{4.49}$$

Summed over spins, these give rise to the usual Dirac traces. The matrix element of the soft operator is taken using the vacuum as the initial state and is of the form $|\,\langle X_s(p_s)\,|\,\boldsymbol{O}_s(0)\,|\,0\rangle\,|^2$. This can be evaluated directly, but we prefer instead to sum over the final states X_s and

convert it into a forward matrix element using the formalism explained in Appendix C of [106]. Written in this form, the differential cross section reads

$$d\hat{\sigma} = \frac{1}{2\hat{s}} \frac{d^3\vec{p}_3}{(2\pi)^3 2E_3} \frac{d^3\vec{p}_4}{(2\pi)^3 2E_4} \int d^4x\, e^{i(p_1+p_2-p_3-p_4)\cdot x} \times \frac{1}{4d_R^2} \sum_{m,m'} \left[\langle\!\langle O_m \rangle\!\rangle^\dagger_{\text{tree}} \langle\!\langle O_{m'} \rangle\!\rangle_{\text{tree}} \times \langle C_m | \left\langle 0 \,\middle|\, \bar{\mathbf{T}}[\boldsymbol{O}^{s\dagger}(x)]\, \mathbf{T}[\boldsymbol{O}^s(0)] \,\middle|\, 0 \right\rangle | C_{m'} \rangle \right], \quad (4.50)$$

where $\mathbf{T}$ and $\bar{\mathbf{T}}$ represent time and anti-time ordering [106]. Since we treat the soft scale as perturbative, the soft fields can be integrated out by evaluating the vacuum matrix element. We now define a hard matrix and a position-space soft function as

$$\boldsymbol{H}(M, m_t, \cos\theta, \mu) = \frac{3}{8} \frac{1}{(4\pi)^2} \frac{1}{4d_R} \sum_{m,m'} \langle\!\langle O_{m'} \rangle\!\rangle_{\text{tree}} \, |C_{m'}\rangle \langle C_m| \, \langle\!\langle O_m \rangle\!\rangle^\dagger_{\text{tree}} ,$$

$$\boldsymbol{W}(x, \mu) = \frac{1}{d_R} \left\langle 0 \,\middle|\, \bar{\mathbf{T}}[\boldsymbol{O}^{s\dagger}(x)]\, \mathbf{T}[\boldsymbol{O}^s(0)] \,\middle|\, 0 \right\rangle , \quad (4.51)$$

where we have chosen the prefactors to match the overall normalization of (4.11). The elements of these matrices in the chosen color basis are defined as

$$H_{IJ} \equiv \frac{1}{\langle c_I | c_I \rangle \langle c_J | c_J \rangle} \langle c_I \,|\, \boldsymbol{H} \,|\, c_J \rangle , \qquad W_{IJ} \equiv \langle c_I \,|\, \boldsymbol{W} \,|\, c_J \rangle , \quad (4.52)$$

so that the term in square brackets in the second line of (5.14) is proportional to

$$\mathrm{Tr}\big[\boldsymbol{H}\, \boldsymbol{W}\big] = \sum_{I,J} H_{IJ} W_{JI} . \quad (4.53)$$

In order to compute the invariant mass spectrum for the $t\bar{t}$ pair, we define $q = p_3 + p_4$ and insert

$$1 = \int d^4q\, dM\, \delta^{(4)}(q - p_3 - p_4)\, 2M\, \delta(M^2 - q^2) \quad (4.54)$$

into (5.14). After performing the $\vec{p}_4$ integral using the first δ-function, the q^0 integration using the second, and carrying out the trivial angular integration in the $\vec{p}_3$ integral, we arrive at

$$\frac{d^2\hat{\sigma}}{dM\, d\cos\theta} = \frac{16M}{3\hat{s}} \frac{1}{(2\pi)^3} \int \frac{d^3\vec{q}}{2q^0} \int dE_3 |\vec{p}_3| \; \delta(M^2 - 2q\cdot p_3) \times \int d^4x\, e^{i(p_1+p_2-q)\cdot x}\, \mathrm{Tr}\big[\boldsymbol{H}(M, m_t, \cos\theta, \mu_f)\, \boldsymbol{W}(x, \mu_f)\big] , \quad (4.55)$$

where $|\vec{p}_3| = \sqrt{E_3^2 - m_t^2}$ and $q_0 = \sqrt{M^2 + \vec{q}^2}$. In the partonic center-of-mass frame, we have $|\vec{q}| = \mathcal{O}(\sqrt{\hat{s}}(1-z))$, so we can set $q_0 = M$ and drop $\vec{q}$ in the δ-function. Then the

integral over $\vec{q}$ produces a factor $\delta^3(\vec{x})$ from the exponential, and after a few manipulations we find

$$\frac{d^2\hat{\sigma}}{dM\,d\cos\theta} = \frac{8\pi\beta_t}{3\hat{s}M}\mathrm{Tr}\big[\boldsymbol{H}(M,m_t,\cos\theta,\mu_f)\,\boldsymbol{S}(\sqrt{\hat{s}}(1-z),M,m_t,\cos\theta,\mu_f)\big]\,, \tag{4.56}$$

where the momentum-space soft function is defined by [106]

$$\boldsymbol{S}(\sqrt{\hat{s}}(1-z),M,m_t,\cos\theta,\mu) = \sqrt{\hat{s}}\int\frac{dx_0}{4\pi}\,e^{i\sqrt{\hat{s}}(1-z)x_0/2}\,\boldsymbol{W}(x_0,\vec{x}=0,\mu)\,. \tag{4.57}$$

The hadronic cross section (4.5) is now obtained by convoluting the partonic cross sections in (4.55) with the parton luminosities. Comparing with (4.11), we finally arrive at the factorized form of the hard-scattering kernel

$$C(z,M,m_t,\cos\theta,\mu_f) = \mathrm{Tr}\big[\boldsymbol{H}(M,m_t,\cos\theta,\mu_f)\,\boldsymbol{S}(\sqrt{\hat{s}}(1-z),M,m_t,\cos\theta,\mu_f)\big]\,, \tag{4.58}$$

where we have set $\hat{s}=M^2$ everywhere except in the first argument of the soft function.

PIM$_{\mathrm{SCET}}$ scheme

It should be noted that at leading power in $(1-z)$ the argument of the soft function could have been simplified as $\sqrt{\hat{s}}(1-z) = M(1-z)/\sqrt{z} \approx M(1-z)$. However, in the case of Drell-Yan [106] and Higgs production [107,108] near threshold it was found that by keeping the exact dependence $\omega = 2E_g$ in the SCET soft functions as in (4.57), one can reproduce a set of logarithmic power corrections involving $\ln[z/(1-z)]$, which are indeed present in the analytic results for the fixed-order expansions of the hard-scattering kernels. Keeping such terms improved agreement of the threshold-expanded hard-scattering kernels with the exact results in QCD. Results in this "PIM$_{\mathrm{SCET}}$" scheme include the same type of logarithmic corrections found in Drell-Yan and Higgs production. Later in the phenomenological part in Section 10.1.1, we will find that the numerical results for the threshold expansion at NLO in this scheme are indeed significantly improved compared to the traditional PIM approach, which does not include such corrections.

4.2.3. The Hard Functions

The hard functions are related to products of Wilson coefficients, as shown in (4.51). To obtain the Wilson coefficients C_{Im}, one matches renormalized Green's functions in QCD with those in SCET. The matching can be done with any choice of external states and infrared (IR) regulators. It is by far simplest to use on-shell partonic states for $(q\bar{q},gg)\to t\bar{t}$ scattering and dimensional regularization in $d=4-2\epsilon$ dimensions to regularize both the ultraviolet (UV) and IR divergences. With this choice, the loop graphs in SCET are scaleless and vanish, so the effective-theory matrix elements are equal to their tree-level expressions multiplied by a UV renormalization matrix $\boldsymbol{Z}$. The matrix elements in QCD, on

the other hand, are just the virtual corrections to the $(q\bar{q}, gg) \to t\bar{t}$ scattering amplitudes. The matching condition then reads [126, 130, 131]

$$\lim_{\epsilon\to 0} \boldsymbol{Z}^{-1}(\epsilon, M, m_t, \cos\theta, \mu)\, |\mathcal{M}(\epsilon, M, m_t, \cos\theta)\rangle = \sum_m \langle\!\langle O_m \rangle\!\rangle_{\text{tree}}\, |C_m(M, m_t, \cos\theta, \mu)\rangle \,, \tag{4.59}$$

where $\mathcal{M}$ is the UV-renormalized virtual QCD amplitude expressed in terms of α_s with $n_l = 5$ active flavors. We have moved the SCET renormalization matrix $\boldsymbol{Z}$ to act on the QCD amplitude, so that both sides of the equation are finite in the limit $\epsilon \to 0$. The explicit results for the matrix elements $\boldsymbol{Z}_{IJ}$ in our color basis for the $q\bar{q}$ and gg channels can be found in [131].

In practice, we are not interested in the Wilson coefficients themselves, but rather the hard matrix H_{IJ}. To calculate this, we first define

$$|\mathcal{M}_{\text{ren}}\rangle \equiv \lim_{\epsilon\to 0} \boldsymbol{Z}^{-1}(\epsilon)\, |\mathcal{M}(\epsilon)\rangle = 4\pi\alpha_s \left[\left|\mathcal{M}^{(0)}_{\text{ren}}\right\rangle + \frac{\alpha_s}{4\pi} \left|\mathcal{M}^{(1)}_{\text{ren}}\right\rangle + \ldots \right], \tag{4.60}$$

and expand the hard function as

$$\boldsymbol{H} = \alpha_s^2 \frac{3}{8 d_R} \left(\boldsymbol{H}^{(0)} + \frac{\alpha_s}{4\pi} \boldsymbol{H}^{(1)} + \ldots \right). \tag{4.61}$$

Using (4.59) and (4.60) to express the SCET matrix element in terms of the finite, IR-subtracted QCD amplitudes in the definition of the hard function (4.51), the matrix elements (4.52) can be written as

$$\begin{aligned} H^{(0)}_{IJ} &= \frac{1}{4} \frac{1}{\langle c_I | c_I\rangle \langle c_J | c_J\rangle} \left\langle c_I \,\middle|\, \mathcal{M}^{(0)}_{\text{ren}} \right\rangle \left\langle \mathcal{M}^{(0)}_{\text{ren}} \,\middle|\, c_J \right\rangle , \\ H^{(1)}_{IJ} &= \frac{1}{4} \frac{1}{\langle c_I | c_I\rangle \langle c_J | c_J\rangle} \left[\left\langle c_I \,\middle|\, \mathcal{M}^{(0)}_{\text{ren}} \right\rangle \left\langle \mathcal{M}^{(1)}_{\text{ren}} \,\middle|\, c_J \right\rangle + \left\langle c_I \,\middle|\, \mathcal{M}^{(1)}_{\text{ren}} \right\rangle \left\langle \mathcal{M}^{(0)}_{\text{ren}} \,\middle|\, c_J \right\rangle \right]. \end{aligned} \tag{4.62}$$

The leading-order result for the $q\bar{q}$ channel follows from a simple calculation and reads

$$\boldsymbol{H}^{(0)}_{q\bar{q}} = \begin{pmatrix} 0 & 0 \\ 0 & 2 \end{pmatrix} \left[\frac{\hat{t}_1^2 + \hat{u}_1^2}{M^4} + \frac{2m_t^2}{M^2} \right], \tag{4.63}$$

while that for the gg channel is

$$\boldsymbol{H}^{(0)}_{gg} = \begin{pmatrix} \frac{1}{N^2} & \frac{1}{N}\frac{\hat{t}_1-\hat{u}_1}{M^2} & \frac{1}{N} \\ \frac{1}{N}\frac{\hat{t}_1-\hat{u}_1}{M^2} & \frac{(\hat{t}_1-\hat{u}_1)^2}{M^4} & \frac{\hat{t}_1-\hat{u}_1}{M^2} \\ \frac{1}{N} & \frac{\hat{t}_1-\hat{u}_1}{M^2} & 1 \end{pmatrix} \frac{M^4}{2\hat{t}_1\hat{u}_1} \left[\frac{\hat{t}_1^2 + \hat{u}_1^2}{M^4} + \frac{4m_t^2}{M^2} - \frac{4m_t^4}{\hat{t}_1\hat{u}_1} \right]. \tag{4.64}$$

To calculate the NLO hard function requires the one-loop virtual corrections to the partonic scattering amplitudes, decomposed into the singlet-octet basis. Although results

for the NLO virtual corrections interfered with the Born-level amplitudes exist in the literature [8–10], results for the one-loop amplitude decomposed into our color basis are not available and must be calculated from scratch. For this purpose in-house routines written in the computer algebraic system FORM [132] were used in our group[3].

We have been able to perform several checks on our results. First, we have verified that applying the renormalization factor $\boldsymbol{Z}$ to the tree-level amplitude indeed absorbs the IR poles in the UV-renormalized QCD amplitudes at one-loop order. Second, we have checked that inserting the results for the products of one-loop hard functions and tree-level soft functions, given in (4.67) below, into the formula for the differential cross section, we reproduce the results of [8–10], as required. Finally, using the one-loop hard functions, we were able to calculate the IR singularities of the two-loop amplitudes in [131], which agree with all the available results in the literature [17–19].

4.2.4. The Soft Functions

The soft functions are given by the vacuum expectation values of the soft Wilson-loop operators, as defined in (4.51). In what follows we will calculate the one-loop corrections to these objects directly in position space. When performing the resummation in the next section, it will be more convenient to work with the Laplace-transformed functions. They are defined as

$$\begin{aligned}\tilde{\boldsymbol{s}}(L, M, m_t, \cos\theta, \mu) &= \frac{1}{\sqrt{\hat{s}}}\int_0^\infty d\omega\, \exp\left(-\frac{\omega}{e^{\gamma_E}\mu e^{L/2}}\right)\boldsymbol{S}(\omega, M, m_t, \cos\theta, \mu)\\ &= \boldsymbol{W}\left(x_0 = \frac{-2i}{e^{\gamma_E}\mu e^{L/2}}, \mu\right),\end{aligned} \tag{4.65}$$

where the second equality was shown in [106] and follows from the functional form of position-space Wilson loops [133].

We expand the soft functions in power of α_s as

$$\tilde{\boldsymbol{s}} = \tilde{\boldsymbol{s}}^{(0)} + \frac{\alpha_s}{4\pi}\tilde{\boldsymbol{s}}^{(1)} + \left(\frac{\alpha_s}{4\pi}\right)^2\tilde{\boldsymbol{s}}^{(2)} + \dots\,. \tag{4.66}$$

At leading order, the Wilson loop is just the unit matrix, so $\tilde{s}^{(0)}_{IJ} = \langle c_I \,|\, c_J\rangle / d_R$, and it is easy to show that

$$\tilde{\boldsymbol{s}}^{(0)}_{q\bar{q}} = \begin{pmatrix} N & 0 \\ 0 & \frac{C_F}{2}\end{pmatrix}, \qquad \tilde{\boldsymbol{s}}^{(0)}_{gg} = \begin{pmatrix} N & 0 & 0 \\ 0 & \frac{N}{2} & 0 \\ 0 & 0 & \frac{N^2-4}{2N}\end{pmatrix}. \tag{4.67}$$

At NLO, the soft functions receive contributions from the diagrams depicted in Figure 4.4. The calculation is similar to that in [133]. To evaluate the diagrams we associate an

[3]The calculation of the hard function was not part of this thesis, explicit results provided by our co-authors could be used.

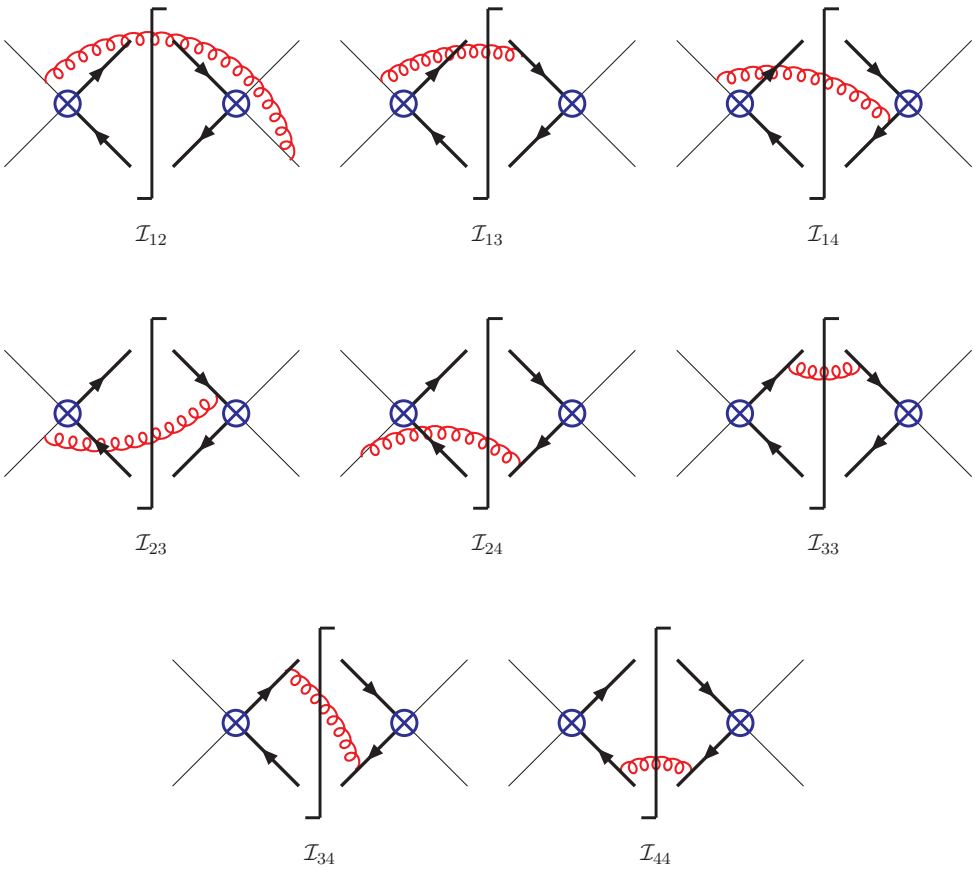

Figure 4.4.: Diagrams contributing to the soft functions at NLO. The thick lines represent Wilson lines in the time-like directions v_3 and v_4, the thin lines Wilson lines in the light-like directions n and $\bar{n}$, and the cut curly lines represent the cut gluon propagator (4.68).

eikonal factor $v_i^\mu / k \cdot v_i$ multiplied by a color generator $\boldsymbol{T}_i$ for each attachment of a gluon to a particle with velocity v_i (we define $v_1 = n$ and $v_2 = \bar{n}$), and contract with the cut gluon propagator in position space, which in Feynman gauge reads

$$D_+^{\mu\nu}(x) = -g^{\mu\nu} \int \frac{d^d k}{(2\pi)^d} \, e^{-ik\cdot x} \, (2\pi) \, \delta(k^2) \, \theta(k^0) \, . \tag{4.68}$$

We can then write the bare soft function in position space as

$$\boldsymbol{W}^{(1)}_{\text{bare}}(\epsilon, x_0, \mu) = \sum_{i,j} \boldsymbol{w}_{ij} \, \mathcal{I}_{ij}(\epsilon, x_0, \mu) \, , \tag{4.69}$$

where the matrices $\boldsymbol{w}_{ij}$ are related to products of color generators and will be given in (4.74) and (4.75) below. The integrals $\mathcal{I}_{ij}$ are defined as

$$\mathcal{I}_{ij}(\epsilon, x_0, \mu) = -\frac{(4\pi\mu^2)^\epsilon}{\pi^{2-\epsilon}} \, v_i \cdot v_j \int d^d k \, \frac{e^{-ik^0 x_0}}{v_i \cdot k \, v_j \cdot k} \, (2\pi) \, \delta(k^2) \, \theta(k^0) \, , \tag{4.70}$$

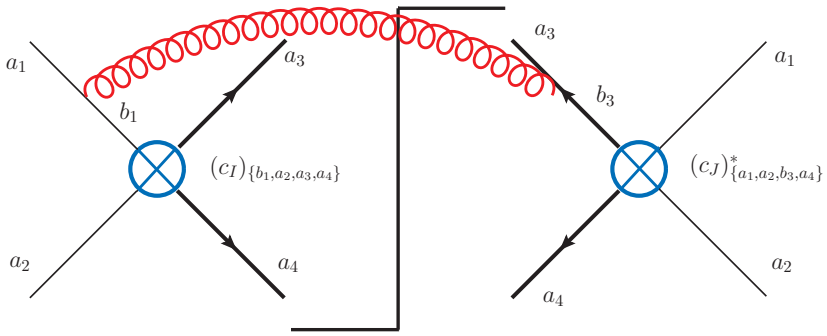

Figure 4.5.: Example of the calculation of $\boldsymbol{w}_{ij}$. The diagram represents the structure for $\boldsymbol{w}_{13}$.

which are obviously symmetric in the indices i and j. In Section .2 of the appendix we give details about the calculation of these integrals. The integrals $\mathcal{I}_{11} = \mathcal{I}_{22} = 0$, and the non-vanishing integrals are

$$\mathcal{I}_{12} = -\left(\frac{2}{\epsilon^2} + \frac{2}{\epsilon}L_0 + L_0^2 + \frac{\pi^2}{6}\right),$$

$$\mathcal{I}_{33} = \mathcal{I}_{44} = \frac{2}{\epsilon} + 2L_0 - \frac{2}{\beta_t}\ln x_s\,,$$

$$\mathcal{I}_{34} = -\frac{1+x_s^2}{1-x_s^2}\left[\left(\frac{2}{\epsilon} + 2L_0\right)\ln x_s - \ln^2 x_s + 4\ln x_s \ln(1-x_s) + 4\mathrm{Li}_2(x_s) - \frac{2\pi^2}{3}\right],$$

$$\mathcal{I}_{13} = \mathcal{I}_{24} = -\left[\frac{1}{2}\left(L_0 - \ln\frac{(1+y_t)^2 x_s}{(1+x_s)^2}\right)^2 + \frac{\pi^2}{12} + 2\mathrm{Li}_2\left(\frac{1-x_s y_t}{1+x_s}\right) + 2\mathrm{Li}_2\left(\frac{x_s - y_t}{1+x_s}\right)\right],$$

$$\mathcal{I}_{14} = \mathcal{I}_{23} = \mathcal{I}_{13}(y_t \to z_u)\,, \tag{4.71}$$

where $x_s = (1-\beta_t)/(1+\beta_t)$, $y_t = -\hat{t}_1/m_t^2 - 1$, $z_u = -\hat{u}_1/m_t^2 - 1$, and

$$L_0 = \ln\left(-\frac{\mu^2 x_0^2 e^{2\gamma_E}}{4}\right). \tag{4.72}$$

The renormalized soft functions $\boldsymbol{W}^{(1)}$ can then be obtained by subtracting the divergent part from $\boldsymbol{W}^{(1)}_{\text{bare}}$. Later on we will need the Laplace-transformed function $\tilde{\boldsymbol{s}}$, which according to (4.65) is obtained by replacing $L_0 \to -L$. To finish the calculation, we must also determine the matrix elements of

$$\left(\boldsymbol{w}_{ij}\right)_{IJ} = \frac{1}{d_R}\,\langle c_I \,|\, \boldsymbol{T}_i \cdot \boldsymbol{T}_j \,|\, c_J\rangle\,. \tag{4.73}$$

In Figure 4.5 we show as an example the diagram leading to $\boldsymbol{w}_{13}$. For the $q\bar{q}$ channel, the results are

$$\begin{aligned}
\boldsymbol{w}_{12}^{q\bar{q}} &= \boldsymbol{w}_{34}^{q\bar{q}} = -\frac{C_F}{4N}\begin{pmatrix} 4N^2 & 0 \\ 0 & -1 \end{pmatrix}, \\
\boldsymbol{w}_{33}^{q\bar{q}} &= \boldsymbol{w}_{44}^{q\bar{q}} = \frac{C_F}{2}\begin{pmatrix} 2N & 0 \\ 0 & C_F \end{pmatrix}, \\
\boldsymbol{w}_{13}^{q\bar{q}} &= \boldsymbol{w}_{24}^{q\bar{q}} = -\frac{C_F}{2}\begin{pmatrix} 0 & 1 \\ 1 & 2C_F - \frac{N}{2} \end{pmatrix}, \\
\boldsymbol{w}_{14}^{q\bar{q}} &= \boldsymbol{w}_{23}^{q\bar{q}} = -\frac{C_F}{2N}\begin{pmatrix} 0 & -N \\ -N & 1 \end{pmatrix},
\end{aligned} \tag{4.74}$$

while for the gg channel we obtain

$$\begin{aligned}
\boldsymbol{w}_{12}^{gg} &= -\frac{1}{4}\begin{pmatrix} 4N^2 & 0 & 0 \\ 0 & N^2 & 0 \\ 0 & 0 & N^2-4 \end{pmatrix}, \\
\boldsymbol{w}_{34}^{gg} &= -\begin{pmatrix} C_F N & 0 & 0 \\ 0 & -\frac{1}{4} & 0 \\ 0 & 0 & -\frac{N^2-4}{4N^2} \end{pmatrix}, \\
\boldsymbol{w}_{33}^{gg} &= \boldsymbol{w}_{44}^{gg} = \frac{C_F}{2N}\begin{pmatrix} 2N^2 & 0 & 0 \\ 0 & N^2 & 0 \\ 0 & 0 & N^2-4 \end{pmatrix}, \\
\boldsymbol{w}_{13}^{gg} &= \boldsymbol{w}_{24}^{gg} = -\frac{1}{8}\begin{pmatrix} 0 & 4N & 0 \\ 4N & N^2 & N^2-4 \\ 0 & N^2-4 & N^2-4 \end{pmatrix}, \\
\boldsymbol{w}_{14}^{gg} &= \boldsymbol{w}_{23}^{gg} = -\frac{1}{8}\begin{pmatrix} 0 & -4N & 0 \\ -4N & N^2 & -(N^2-4) \\ 0 & -(N^2-4) & N^2-4 \end{pmatrix}.
\end{aligned} \tag{4.75}$$

The NLO contributions to the cross section from real emissions in the soft limit have been known for some time [13]. Transforming our results to momentum space, we have checked that the integrals (4.70) are consistent with those given in Appendix A of that paper (after taking into account some misprints in [13] later corrected in [134]). As another

check, we have used our results along with the one-loop hard functions from the previous section to calculate the total partonic cross sections at NLO in the limit $\beta \to 0$ (see Section 8.3.1), reproducing the analytic expressions from [11]. Finally, using the RG invariance of the cross section we will derive the RG equation for $\tilde{\boldsymbol{s}}$ in the next section. We have checked that our one-loop result satisfies this equation, which also justifies our procedure of simply subtracting the $1/\epsilon$ poles in the bare function to get the renormalized results.

4.2.5. Threshold Resummation

In the region where the cross section is dominated by the threshold terms, one needs to resum the leading singular terms in $(1-z)$ to all orders in perturbation theory. This is accomplished by deriving and solving RG equations for the hard and soft functions in the effective theory, which will be described in what follows. Since these equations contain information on the logarithmic structure of the hard-scattering kernels at higher-orders in perturbation theory, they can also be used to derive an approximate NNLO formula for the differential cross section in the threshold region. We will discuss this further in Section 6.1.

RG evolution and resummation at NNLL

The hard function satisfies the evolution equation

$$\frac{d}{d\ln\mu}\boldsymbol{H}(M,m_t,\cos\theta,\mu) = \boldsymbol{\Gamma}_H(M,m_t,\cos\theta,\mu)\,\boldsymbol{H}(M,m_t,\cos\theta,\mu) + \boldsymbol{H}(M,m_t,\cos\theta,\mu)\,\boldsymbol{\Gamma}_H^\dagger(M,m_t,\cos\theta,\mu)\,. \tag{4.76}$$

Using (4.52), we can write the above equation in a matrix form, where the matrix elements of $\boldsymbol{\Gamma}_H$ are defined according to (4.40), and can be obtained from the matrices $\boldsymbol{\Gamma}_{q\bar{q}}$ or $\boldsymbol{\Gamma}_{gg}$ in [131]. The form of the evolution equation follows from (4.60) and (4.62), along with the defining relation

$$\boldsymbol{Z}^{-1}\frac{d}{d\ln\mu}\boldsymbol{Z} = -\boldsymbol{\Gamma}_H \tag{4.77}$$

for the anomalous dimension. The explicit results to two-loop order are

$$\begin{aligned}\boldsymbol{\Gamma}_{q\bar{q}} &= \left[C_F\,\gamma_{\rm cusp}(\alpha_s)\,\left(\ln\frac{M^2}{\mu^2}-i\pi\right)+C_F\,\gamma_{\rm cusp}(\beta_{34},\alpha_s)+2\gamma^q(\alpha_s)+2\gamma^Q(\alpha_s)\right]\mathbf{1}\\ &\quad+\frac{N}{2}\left[\gamma_{\rm cusp}(\alpha_s)\,\left(\ln\frac{\hat{t}_1^2}{M^2m_t^2}+i\pi\right)-\gamma_{\rm cusp}(\beta_{34},\alpha_s)\right]\begin{pmatrix}0&0\\0&1\end{pmatrix}\\ &\quad+\gamma_{\rm cusp}(\alpha_s)\,\ln\frac{\hat{t}_1^2}{\hat{u}_1^2}\left[\begin{pmatrix}0&\frac{C_F}{2N}\\1&-\frac{1}{N}\end{pmatrix}+\frac{\alpha_s}{4\pi}\,g(\beta_{34})\begin{pmatrix}0&\frac{C_F}{2}\\-N&0\end{pmatrix}\right],\end{aligned} \tag{4.78}$$

and

$$\begin{aligned}\mathbf{\Gamma}_{gg} = &\left[N\,\gamma_{\rm cusp}(\alpha_s)\,\left(\ln\frac{M^2}{\mu^2} - i\pi\right) + C_F\,\gamma_{\rm cusp}(\beta_{34},\alpha_s) + 2\gamma^g(\alpha_s) + 2\gamma^Q(\alpha_s)\right]\mathbf{1}\\ &+\frac{N}{2}\left[\gamma_{\rm cusp}(\alpha_s)\,\left(\ln\frac{\hat{t}_1^2}{M^2 m_t^2} + i\pi\right) - \gamma_{\rm cusp}(\beta_{34},\alpha_s)\right]\begin{pmatrix}0&0&0\\0&1&0\\0&0&1\end{pmatrix}\\ &+\gamma_{\rm cusp}(\alpha_s)\,\ln\frac{\hat{t}_1^2}{\hat{u}_1^2}\left[\begin{pmatrix}0&\frac{1}{2}&0\\1&-\frac{N}{4}&\frac{N^2-4}{4N}\\0&\frac{N}{4}&-\frac{N}{4}\end{pmatrix} + \frac{\alpha_s}{4\pi}\,g(\beta_{34})\begin{pmatrix}0&\frac{N}{2}&0\\-N&0&0\\0&0&0\end{pmatrix}\right],\end{aligned} \tag{4.79}$$

where the various anomalous-dimension functions can be found in the Appendix, and the cusp angle $\beta_{34} = i\pi - \ln(1+\beta_t)/(1-\beta_t)$. The solution to the evolution equation can be written as

$$\boldsymbol{H}(M, m_t, \cos\theta, \mu) = \boldsymbol{U}(M, m_t, \cos\theta, \mu_h, \mu)\,\boldsymbol{H}(M, m_t, \cos\theta, \mu_h)\,\boldsymbol{U}^\dagger(M, m_t, \cos\theta, \mu_h, \mu)\,, \tag{4.80}$$

where the unitary matrix $\boldsymbol{U}$ satisfies the equation

$$\frac{d}{d\ln\mu}\boldsymbol{U}(M, m_t, \cos\theta, \mu_h, \mu) = \mathbf{\Gamma}_H(M, m_t, \cos\theta, \mu)\,\boldsymbol{U}(M, m_t, \cos\theta, \mu_h, \mu)\,. \tag{4.81}$$

The matching scale μ_h must be chosen of order a typical hard scale, so that the matching condition for the hard function is free of large logarithms. With the help of the evolution matrix $\boldsymbol{U}$, the hard function can then be evolved to an arbitrary scale μ. The formal solution to this equation is

$$\boldsymbol{U}(M, m_t, \cos\theta, \mu_h, \mu) = \mathcal{P}\exp\int_{\mu_h}^{\mu}\frac{d\mu'}{\mu'}\,\mathbf{\Gamma}_H(M, m_t, \cos\theta, \mu')\,, \tag{4.82}$$

where the path-ordering is necessary because $\mathbf{\Gamma}_H$ is a matrix. To evaluate the path-ordered exponential, it is convenient to separate the explicit logarithmic dependence on the scale μ, which is related to Sudakov double logarithms, from the remaining piece, which is related to single logarithmic evolution. We thus write the anomalous dimension as

$$\mathbf{\Gamma}_H(M, m_t, \cos\theta, \mu) = \Gamma_{\rm cusp}(\alpha_s)\left(\ln\frac{M^2}{\mu^2} - i\pi\right)\mathbf{1} + \boldsymbol{\gamma}^h(M, m_t, \cos\theta, \alpha_s)\,, \tag{4.83}$$

where $\Gamma_{\rm cusp}$ is equal to $C_F\,\gamma_{\rm cusp}$ for $q\bar{q}$ and $N\,\gamma_{\rm cusp}$ for gg, and the matrices $\boldsymbol{\gamma}^h$ are defined through a comparison with (4.78) and (4.79). Since the term proportional to $\Gamma_{\rm cusp}$ multiplies the unit matrix, we can factor this piece out of the path-ordering and evaluate it

using standard techniques. The result for the evolution matrix is then

$$\boldsymbol{U}(M, m_t, \cos\theta, \mu_h, \mu) = \exp\left[2S(\mu_h, \mu) - a_\Gamma(\mu_h, \mu)\left(\ln\frac{M^2}{\mu_h^2} - i\pi\right)\right]\boldsymbol{u}(M, m_t, \cos\theta, \mu_h, \mu)\,. \tag{4.84}$$

The RG exponents in the square brackets of the exponential factor are, as already mentioned in Section 2.3,

$$S(\mu_h, \mu) = -\int_{\alpha_s(\mu_h)}^{\alpha_s(\mu)} d\alpha\,\frac{\Gamma_{\rm cusp}(\alpha)}{\beta(\alpha)}\int_{\alpha_s(\mu_h)}^{\alpha}\frac{d\alpha'}{\beta(\alpha')}\,, \qquad a_\Gamma(\mu_h, \mu) = -\int_{\alpha_s(\mu_h)}^{\alpha_s(\mu)} d\alpha\,\frac{\Gamma_{\rm cusp}(\alpha)}{\beta(\alpha)}\,. \tag{4.85}$$

The quantity $\boldsymbol{u}$ contains the non-trivial matrix evolution due to $\boldsymbol{\gamma}^h$ and reads

$$\boldsymbol{u}(M, m_t, \cos\theta, \mu_h, \mu) = \mathcal{P}\exp\int_{\alpha_s(\mu_h)}^{\alpha_s(\mu)}\frac{d\alpha}{\beta(\alpha)}\,\boldsymbol{\gamma}^h(M, m_t, \cos\theta, \alpha)\,. \tag{4.86}$$

The perturbative solutions to the above equations are reviewed in the Appendix.

We now turn to the evolution of the soft function. We derive its evolution equation by using the RG invariance of the cross section,

$$\frac{d}{d\ln\mu}\mathrm{Tr}\left[\boldsymbol{H}\boldsymbol{S}\right]\otimes \text{ff} = 0\,, \tag{4.87}$$

along with the evolution equations for the hard function and parton luminosities. The evolution equation for the hard function was given above, and the parton luminosity functions satisfy the DGLAP equations [135–137]. While the full DGLAP equations involve flavor mixing, what we need here is the $x \to 1$ limit of them, which is flavor-diagonal and can be written as

$$\frac{d}{d\ln\mu}\text{ff}(y, \mu) = 2\int_y^1\frac{dx}{x}\,P(x)\,\text{ff}(y/x, \mu)\,, \tag{4.88}$$

where $P(x)$ is given by

$$P(x) = \frac{2\Gamma_{\rm cusp}(\alpha_s)}{(1-x)_+} + 2\gamma^\phi(\alpha_s)\,\delta(1-x)\,. \tag{4.89}$$

The evolution for the momentum-space soft function is then

$$\frac{d}{d\ln\mu}\boldsymbol{S}(\omega, M, m_t, \cos\theta, \mu) = -\left[2\Gamma_{\rm cusp}(\alpha_s)\ln\frac{\omega}{\mu} + \boldsymbol{\gamma}^{s\dagger}(M, m_t, \cos\theta, \alpha_s)\right]\boldsymbol{S}(\omega, M, m_t, \cos\theta, \mu)$$
$$-\boldsymbol{S}(\omega, M, m_t, \cos\theta, \mu)\left[2\Gamma_{\rm cusp}(\alpha_s)\ln\frac{\omega}{\mu} + \boldsymbol{\gamma}^{s}(M, m_t, \cos\theta, \alpha_s)\right]$$

$$- 4\Gamma_{\rm cusp}(\alpha_s) \int_0^\omega d\omega' \, \frac{\boldsymbol{S}(\omega', M, m_t, \cos\theta, \mu) - \boldsymbol{S}(\omega, M, m_t, \cos\theta, \mu)}{\omega - \omega'} \,, \tag{4.90}$$

where we have defined

$$\boldsymbol{\gamma}^s(M, m_t, \cos\theta, \alpha_s) = \boldsymbol{\gamma}^h(M, m_t, \cos\theta, \alpha_s) + 2\gamma^\phi(\alpha_s)\, \mathbf{1} \,. \tag{4.91}$$

As in [106], the non-local evolution equation for the soft function can be turned into a local one by the Laplace transformation (4.65). The evolution equation for the Laplace-transformed function reads

$$\begin{aligned} \frac{d}{d\ln\mu}\, \tilde{\boldsymbol{s}} \left(\ln\frac{M^2}{\mu^2}, M, m_t, \cos\theta, \mu \right) = \\ - \left[\Gamma_{\rm cusp}(\alpha_s) \ln\frac{M^2}{\mu^2} + \boldsymbol{\gamma}^{s\dagger}(M, m_t, \cos\theta, \alpha_s) \right] \tilde{\boldsymbol{s}} \left(\ln\frac{M^2}{\mu^2}, M, m_t, \cos\theta, \mu \right) \\ - \tilde{\boldsymbol{s}} \left(\ln\frac{M^2}{\mu^2}, M, m_t, \cos\theta, \mu \right) \left[\Gamma_{\rm cusp}(\alpha_s) \ln\frac{M^2}{\mu^2} + \boldsymbol{\gamma}^{s}(M, m_t, \cos\theta, \alpha_s) \right] . \end{aligned} \tag{4.92}$$

This can be solved using the same methods as for the hard function. Transforming the results back to momentum space, we find

$$\begin{aligned} \boldsymbol{S}(\omega, M, m_t, \cos\theta, \mu_f) = \sqrt{\hat{s}}\, \exp\left[-4S(\mu_s, \mu_f) + 4a_{\gamma^\phi}(\mu_s, \mu_f) \right] \\ \times \boldsymbol{u}^\dagger(M, m_t, \cos\theta, \mu_f, \mu_s)\, \tilde{\boldsymbol{s}}(\partial_\eta, M, m_t, \cos\theta, \mu_s)\, \boldsymbol{u}(M, m_t, \cos\theta, \mu_f, \mu_s)\, \frac{1}{\omega} \left(\frac{\omega}{\mu_s} \right)^{2\eta} \frac{e^{-2\gamma_E \eta}}{\Gamma(2\eta)} \,, \end{aligned} \tag{4.93}$$

where $\eta = 2a_\Gamma(\mu_s, \mu_f)$. The soft scale μ_s should be chosen such that the contribution from the soft function to the cross section is perturbatively well-behaved, and will be discussed in detail in Section 8.1.2.

Combining the results for the hard and soft functions, our final resummed expression for the hard-scattering kernel is

$$\begin{aligned} C(z, M, m_t, \cos\theta, \mu_f) = \exp\left[4a_{\gamma^\phi}(\mu_s, \mu_f) \right] \\ \times {\rm Tr} \Bigg[\boldsymbol{U}(M, m_t, \cos\theta, \mu_h, \mu_s)\, \boldsymbol{H}(M, m_t, \cos\theta, \mu_h)\, \boldsymbol{U}^\dagger(M, m_t, \cos\theta, \mu_h, \mu_s) \\ \times \tilde{\boldsymbol{s}} \left(\ln\frac{M^2}{\mu_s^2} + \partial_\eta, M, m_t, \cos\theta, \mu_s \right) \Bigg] \frac{e^{-2\gamma_E\eta}}{\Gamma(2\eta)} \frac{z^{-\eta}}{(1-z)^{1-2\eta}} \,. \end{aligned} \tag{4.94}$$

For values $\mu_s < \mu_f$ the parameter $\eta < 0$, and one must use a subtraction at $z = 1$ and analytic continuation to express integrals over z in terms of star (or plus) distributions [138].

Formula (4.94) can be evaluated order-by-order in RG-improved perturbation theory, using the standard counting $\ln \mu_h/\mu_s \sim \ln(1-z) \sim 1/\alpha_s$. The perturbative solutions for the RG factors needed to evaluate the evolution matrix $\boldsymbol{U}$ to NLO in this counting scheme are given in (A.2), (A.3), and (A.5) of the Appendix. The correspondence between this counting and the standard counting of logarithms (e.g. NLL, NNLL), along with the accuracy of the anomalous dimensions and matching functions needed at a given order, can be summarized as follows:

RG-improved PT	log accuracy	$\Gamma_{\rm cusp}$	$\boldsymbol{\gamma}^h$, γ^ϕ	$\boldsymbol{H}$, $\tilde{\boldsymbol{s}}$
LO	NLL	2-loop	1-loop	tree-level
NLO	NNLL	3-loop	2-loop	1-loop

In the remainder of the paper we will use the logarithmic counting (e.g. NNLL) when referring to the resummed results obtained in this section. These results are valid for the leading-order term in the threshold expansion in $(1-z)$, whereas the full result at NLO in fixed-order perturbation theory also contains information on subleading terms. In phenomenological applications we can match the resummed results with the NLO fixed-order results to achieve an NLO+NNLL precision. The method for doing this is described in Section 8.

5. Single-Particle Inclusive Kinematics

In the following we calculate the double differential cross section with respect to the transverse momentum p_T and the rapidity y of the top-quark using 1PI kinematics. We work in the threshold limit $p_X^2 \to m_t^2$, where p_X is the momentum of the inclusive hadronic state $X[\bar{t}]$ which contains also the anti-top quark. This limit forces the real radiation to be soft. The derivation of the analytical results is close to the one presented for the case of PIM kinematics, and not all details described there will be repeated here. Important ingredients, for instance the hard function, can be taken over from PIM. The 1PI soft function was previously unknown, and had to be calculated from scratch. We present results for this matching function at NLO in perturbation theory. The analytical results obtained here will enable us to make predictions for p_T and y distributions, the FB asymmetry at the Tevatron and the charge-asymmetry at the LHC at NLO+NNLL. As for the case of PIM kinematics we refrain from a numerical analysis here. Detailed phenomenological studies will be presented in Chapter 9.

5.1. Kinematics

As in Section 4 we consider the scattering process

$$N_1(P_1) + N_2(P_2) \to t(p_3) + \bar{t}(p_4) + X\,, \tag{5.1}$$

where N_1 and N_2 indicate the incoming protons (LHC) or proton and anti-proton (Tevatron), while X represents an inclusive hadronic final state.

The partonic processes which we will analyze in detail are thus

$$\begin{aligned} q(p_1) + \bar{q}(p_2) &\to t(p_3) + \bar{t}(p_4) + \hat{X}(k)\,, \\ g(p_1) + g(p_2) &\to t(p_3) + \bar{t}(p_4) + \hat{X}(k)\,. \end{aligned} \tag{5.2}$$

Note that the hadronic state $\hat{X}$ in the above equations is different than the state X in (5.1): $\hat{X}$ contains only the products of the hard-scattering, while X contains also the beam remnants from the initial hadrons. The relations between the hadronic and partonic momenta are the same as in Section 4, $p_1 = x_1 P_1$ and $p_2 = x_2 P_2$ and we define the same hadronic variables

$$s = (P_1 + P_2)^2\,, \quad t_1 = (P_1 - p_3)^2 - m_t^2\,, \quad u_1 = (P_2 - p_3)^2 - m_t^2\,, \tag{5.3}$$

while the corresponding quantities at the partonic level are given by

$$\hat{s} = x_1 x_2 s\,, \quad \hat{t}_1 = x_1 t_1\,, \quad \hat{u}_1 = x_2 u_1\,, \quad M^2 = (p_3 + p_4)^2\,. \tag{5.4}$$

Besides the above variables which are the same as in PIM kinematics we define

$$s_4 = \hat{s} + \hat{t}_1 + \hat{u}_1 = (p_4 + k)^2 - m_t^2\,. \tag{5.5}$$

Momentum conservation implies that at Born level (for $k = 0$) we have $\hat{s} = M^2$ and $s_4 = 0$. In Section 4 we had considered the threshold $\hat{s} \to M^2$. In the case of 1PI observables such as the transverse-momentum or rapidity distribution of a single top quark, it is natural to define the threshold region as $s_4 \to 0$. This threshold limit was first studied in [56]. It should be stressed again that as in PIM, the top and anti-top quarks are not forced to be nearly at rest.

Similar to PIM the double-differential cross section in the transverse momentum p_T and the rapidity y can be written in the factorized form

$$\frac{d\sigma}{dp_T dy} = \frac{16\pi p_T}{3s} \sum_{i,j} \int_{x_1^{\min}}^1 \frac{dx_1}{x_1} \int_{x_2^{\min}}^1 \frac{dx_2}{x_2}\, f_{i/N_1}(x_1,\mu_f)\, f_{j/N_2}(x_2,\mu_f)\, C_{ij}(s_4,\hat{s},\hat{t}_1,\hat{u}_1,m_t,\mu_f)\,. \tag{5.6}$$

The hadronic Mandelstam variables are related to p_T and y in the laboratory frame via

$$t_1 = -\sqrt{s}\, m_\perp\, e^{-y}\,, \quad u_1 = -\sqrt{s}\, m_\perp e^{y}\,, \tag{5.7}$$

where $m_\perp = \sqrt{p_T^2 + m_t^2}$. Together with (5.4) and (5.5), the kinematic variables entering C_{ij} can be expressed as functions of p_T, y, x_1 and x_2. The lower limits of integrations in (5.6) are

$$x_1^{\min} = \frac{-u_1}{s + t_1}\,, \quad x_2^{\min} = \frac{-x_1 t_1}{x_1 s + u_1}\,.$$

Finally, the total cross section can be calculated by integrating the double-differential distribution over the ranges

$$0 \le |y| \le \frac{1}{2} \ln \frac{1 + \sqrt{1 - 4m_\perp^2/s}}{1 - \sqrt{1 - 4m_\perp^2/s}}\,, \quad 0 \le p_T \le \sqrt{\frac{s}{4} - m_t^2}\,. \tag{5.8}$$

In this chapter we will mainly discuss the distributions of the top quark, but our results can also be applied to the transverse momentum $\bar{p}_T$ and rapidity $\bar{y}$ distributions of the anti-top quark after appropriate replacements[1]. At the Tevatron, charge-conjugation invariance of the strong interactions implies that within QCD we have the simple relation

$$\frac{d\sigma}{d\bar{p}_T d\bar{y}} = \frac{d\sigma}{dp_T dy}\Big|_{p_T \to \bar{p}_T,\, y = \to -\bar{y}}\,, \tag{5.9}$$

[1]We will make use of this fact later in Section 10.2.4.

which we will use in Section 10.2 in interpreting the charge asymmetry in terms of a forward-backward asymmetry.

As for $z \to 1$, the limit $s_4 \to 0$ greatly simplifies the calculation, since one effectively deals with a two-body final state. The hard-scattering kernels can be factorized into a hard function $\boldsymbol{H}_{ij}$ and a soft function $\boldsymbol{S}_{ij}$ as

$$C_{ij}(s_4, \hat{s}, \hat{t}_1, \hat{u}_1, m_t, \mu_f) = \mathrm{Tr}\left[\boldsymbol{H}_{ij}(\hat{s}', \hat{t}_1', \hat{u}_1', m_t, \mu_f)\, \boldsymbol{S}_{ij}(s_4, \hat{s}', \hat{t}_1', \hat{u}_1', m_t, \mu_f)\right] + \mathcal{O}(s_4)\,. \tag{5.10}$$

The notation above is meant to emphasize that there are ambiguities in the choice of $\hat{s}'$, $\hat{t}_1'$ and $\hat{u}_1'$, which can in general differ from the exact Mandelstam variables $\hat{s}$, $\hat{t}_1$ and $\hat{u}_1$ by power corrections that vanish at $s_4 = 0$. For instance, given an explicit result for the hard and soft functions, one can always rewrite it using $\hat{s}' + \hat{t}_1' + \hat{u}_1' = 0$ or $\hat{s}' + \hat{t}_1' + \hat{u}_1' = s_4$. Although the difference is suppressed by positive powers of s_4, the two choices give different numerical results upon integration. In Section 9.1, we will explain in detail our method for dealing with this ambiguity.

As in Section 4, the use of boldface in (5.10) indicates that the hard and soft functions are matrices in color space. The hard function originates from virtual corrections and is the same as that in the PIM case once the variables $\hat{s}'$, $\hat{t}_1'$, $\hat{u}_1'$ are expressed in terms of M and $\cos\theta$. Analog to PIM, the soft function captures contributions arising from the emission of soft real radiation. It depends on the details of the phase-space integrals and is different in 1PI and PIM kinematics. The 1PI soft function contains singular distributions in s_4, which are of the form

$$P_n(s_4) \equiv \left[\frac{1}{s_4} \ln^n \frac{s_4}{m_t^2}\right]_+, \tag{5.11}$$

where the plus-distributions are defined by

$$\int_0^{m_t^2} ds_4 \left[\frac{1}{s_4} \ln^n \frac{s_4}{m_t^2}\right]_+ g(s_4) = \int_0^{m_t^2} ds_4\, \frac{1}{s_4} \ln^n\left(\frac{s_4}{m_t^2}\right) [g(s_4) - g(0)]\,. \tag{5.12}$$

With this definition

$$\int_0^{s_4^{\max}} \left[\frac{1}{s_4} \ln^n \frac{s_4}{m_t^2}\right]_+ g(s_4) = \int_0^{s_4^{\max}} ds_4\, \frac{1}{s_4} \ln^n\left(\frac{s_4}{m_t^2}\right) [g(s_4) - g(0)] + \frac{g(0)}{n+1} \ln^{n+1}\left(\frac{s_4^{\max}}{m_t^2}\right). \tag{5.13}$$

Near threshold, these singular distributions lead to a bad convergence of the perturbation series. More generally, they give rise to the dominant higher-order corrections to the hadronic cross section if the product of PDFs in (5.6) falls off very quickly away from values of x_1, x_2 where $s_4 \to 0$. In either case, resumming such terms to all orders can lead to improved theoretical predictions. This is the topic of the next section.

5.2. Factorization in SCET and HQET

Most of the discussion about factorization and resummation can be carried from PIM over directly to the case of 1PI kinematics. In fact, the differences between 1PI and PIM kinematics arise solely from the structure of real emission in the two cases and therefore affect only the soft function, which must be modified in two essential ways. First, the phase-space integrals for real emission in the soft limit change, so the fixed-order expansion of the soft function is different from its PIM counterpart and must be calculated from scratch. Second, the RG equation for the soft function, derived using the RG invariance of the cross section along with the evolution equations of the hard function and PDFs, also differs slightly from its expression in PIM kinematics. In what follows we focus on how to deal with these two differences with respect to PIM kinematics and otherwise just quote results from Chapter 4 for the pieces which remain unchanged. In particular, we derive the explicit one-loop soft function and the RG equation needed for NNLL resummation in 1PI kinematics. We also discuss the structure of power corrections to the leading-order term in the threshold expansion and explain how a certain set of subleading corrections in s_4 appears naturally within the SCET formalism. Later, in Section 6.2 we present results for approximate NNLO formulas in fixed-order perturbation theory.

5.2.1. The Soft Functions in 1PI

In general, the soft function is related to the vacuum expectation value of a soft Wilson-loop operator. To calculate it explicitly, we first generalize the derivation of the differential cross section at partonic threshold given for PIM kinematics in 4.2.4 to the 1PI case.

In the limit where extra gluon radiation is soft, the differential cross section can be factorized as[2]

$$d\hat{\sigma} = \frac{1}{2\hat{s}}\frac{d^3\vec{p}_3}{(2\pi)^3 2E_3}\int\frac{d^3\vec{p}_4}{(2\pi)^3 2E_4}\int d^4x\, e^{i(p_1+p_2-p_3-p_4)\cdot x} \times \frac{128\pi^2}{3}\mathrm{Tr}\big[\boldsymbol{H}(\hat{s}',\hat{t}_1',\hat{u}_1',m_t,\mu_f)\,\boldsymbol{W}(x,\hat{s}',\hat{t}_1',\hat{u}_1',m_t,\mu_f)\big]\,, \tag{5.14}$$

where $\boldsymbol{W}$ is the expectation value of the Wilson-loop operator in position space. Since the integrand depends on $\vec{p}_4$ only through $E_4 = \sqrt{|\vec{p}_4|^2+m_t^2}$ and in the exponent, its calculation is simplified by going to the rest frame of the inclusive final state $\bar{t}+\hat{X}$ in (5.2), which consists of the anti-top-quark plus additional soft radiation. In this frame $|\vec{p}_4| = \mathcal{O}(s_4/m_t)$, and we can drop the dependence on it in $E_4 \sim m_t$. The integral over $\vec{p}_4$ then produces a factor of $(2\pi)^3\delta^{(3)}(\vec{x})$, and the exponent depends only on $E_s \equiv (p_1+p_2-p_3-p_4)^0 = s_4/(2\sqrt{s_4+m_t^2})$, which is the energy of the soft radiation in this particular frame. Using the δ-function to perform the integral over $d^3\vec{x}$, and converting the result to

[2]The functions $\boldsymbol{H}$ and $\boldsymbol{W}$ are summed over the channel indices ij. In order to keep the notation as simple as possible, in the remainder of this section we suppress the sum and indices.

a differential cross section in $\hat{t}_1$ and $\hat{u}_1$, we obtain

$$\frac{d\hat{\sigma}}{d\hat{t}_1 d\hat{u}_1} = \frac{8\pi}{3\hat{s}^2}\frac{1}{m_t}\int \frac{dx^0}{4\pi}\,\exp\left(\frac{ix^0 s_4}{2\sqrt{s_4+m_t^2}}\right) \times \mathrm{Tr}\big[\boldsymbol{H}(\hat{s}',\hat{t}_1',\hat{u}_1',m_t,\mu_f)\,\boldsymbol{W}\big((x^0,\vec{x}=0),\hat{s}',\hat{t}_1',\hat{u}_1',m_t,\mu_f\big)\big]\,. \tag{5.15}$$

We now introduce the momentum-space soft function according to

$$\hat{\boldsymbol{W}}(\omega,\hat{s}',\hat{t}_1',\hat{u}_1',m_t,\mu) = \int \frac{dx^0}{4\pi}\exp\left(\frac{i\omega x^0}{2}\right)\boldsymbol{W}\big((x^0,\vec{x}=0),\hat{s}',\hat{t}_1',\hat{u}_1',m_t,\mu\big)\,. \tag{5.16}$$

The soft function entering the factorization formula is then given by

$$\boldsymbol{S}(s_4,\hat{s}',\hat{t}_1',\hat{u}_1',m_t,\mu) = \frac{1}{m_t}\hat{\boldsymbol{W}}\left(\frac{s_4}{\sqrt{s_4+m_t^2}},\hat{s}',\hat{t}_1',\hat{u}_1',m_t,\mu\right). \tag{5.17}$$

Using the results above, one recovers the factorization formula (5.10) for the hard-scattering kernels by noting that

$$C_{ij}(s_4,\hat{s},\hat{t}_1,\hat{u}_1,m_t,\mu_f) = \frac{3\hat{s}^2}{8\pi}\frac{d\hat{\sigma}_{ij}}{d\hat{t}_1 d\hat{u}_1}\,. \tag{5.18}$$

1PI$_{\mathsf{SCET}}$ scheme

It is instructive to compare this derivation with that given in 4.2.4 for PIM kinematics. In both cases, the calculations are simplified by working in a frame where the soft function depends only on the time component x^0, or in momentum space, on the energy of the extra soft radiation (although of course the final results are Lorentz invariant and do not depend on the frame). In PIM kinematics this is the partonic center-of-mass frame, while in 1PI kinematics it is the center-of-mass frame of the unobserved partonic final state, consisting of the anti-top-quark plus additional soft radiation. The difference between these two cases comes from which combinations of the momenta are counted as "small": in PIM kinematics it is $(p_3+p_4)\cdot k$ against $(p_3+p_4)^2 = M^2$, while in 1PI kinematics it is $p_4\cdot k$ against $p_4^2 = m_t^2$. This difference has important implications for the structure of power corrections in the two types of kinematics. Such power corrections come both from time-ordered products involving the subleading SCET Lagrangian and operators, which before phase-space integrations are the same in both cases, and from the approximations in the phase-space integrals, e.g. $E_4 = \sqrt{|\vec{p}_4|^2+m_t^2} \sim m_t$ in 1PI and $E_3+E_4 = \sqrt{|\vec{p}_3+\vec{p}_4|^2+M^2} \sim M$ in PIM kinematics. The corrections from the latter source can be quite different: for 1PI kinematics they involve the expansion parameter $|\vec{p}_4|/m_t = s_4/(2m_t\sqrt{m_t^2+s_4})$, while for PIM kinematics they involve the expansion parameter $|\vec{p}_3+\vec{p}_4|/M = \sqrt{\hat{s}}(1-z)/(2M) = (1-z)/(2\sqrt{z})$.

In Chapter 4, we followed the procedure, using the exact form $\omega = 2E_g = M(1-z)/\sqrt{z}$ instead of $\omega = M(1-z)$ in the first argument of the soft function in PIM kinematics. In

1PI kinematics, the equivalent procedure is to use $\omega = 2E_g = s_4/\sqrt{m_t^2 + s_4}$, as we have already indicated explicitly in (5.17). We will refer to numerical results obtained with this choice as being calculated in the "1PI_{SCET}" scheme. Since the factorization formula (5.15) is derived in the limit $s_4 \ll m_t^2$, it would be equally valid to use $\omega = s_4/m_t$ in the first argument of the soft function (5.17). This is in fact the choice that has been made in previous calculations in 1PI kinematics [56], and later on we will refer to this as the "1PI" scheme. When expanded in fixed-order perturbation theory, the two schemes differ through terms involving $\ln(1 + s_4/m_t^2)/s_4$, which are power suppressed in the limit $s_4 \to 0$. However, in our analysis in Sections 9.2.1 and 9.3 we will see that these power-suppressed effects can be numerically important, and that the agreement with the exact numerical results at NLO is improved in the 1PI_{SCET} scheme. Furthermore, although in this case we do not have explicit analytic results to compare with, we note that the logarithms of $\ln(1 + s_4/m_t^2)$ appear naturally in the fixed-order NLO calculations of hard gluon corrections through terms of the form $\ln(2E_g/\mu)$, see for instance Eqs. (4.16) and (4.17) of [9].

We now present the calculation of the soft function in 1PI kinematics at one-loop order. The results can be written as

$$\boldsymbol{W}^{(1)}_{\text{bare}}(\epsilon, x^0, \mu) = \sum_{i,j} \boldsymbol{w}_{ij}\, \mathcal{I}'_{ij}(\epsilon, x^0, \mu)\,, \tag{5.19}$$

where the matrices $\boldsymbol{w}_{ij}$ are related to products of color generators and can be found in Section 4.2.4. The integrals $\mathcal{I}'_{ij}$ are again defined as

$$\mathcal{I}'_{ij}(\epsilon, x^0, \mu) = -\frac{(4\pi\mu^2)^\epsilon}{\pi^{2-\epsilon}}\, v_i \cdot v_j \int d^dk\, \frac{e^{-ik^0x^0}}{v_i \cdot k\, v_j \cdot k}\, (2\pi)\, \delta(k^2)\, \theta(k^0)\,. \tag{5.20}$$

Again, in Section .2 of the appendix we give details about the calculation of these integrals. As results for these objects in the rest frame of the heavy anti-top quark, we find for the non-vanishing integrals

$$\begin{aligned}
\mathcal{I}'_{12} &= -\left[\frac{2}{\epsilon^2} + \frac{2}{\epsilon}\left(L_0 - \ln\frac{\hat{s}' m_t^2}{\hat{t}'_1 \hat{u}'_1}\right) + \left(L_0 - \ln\frac{\hat{s}' m_t^2}{\hat{t}'_1 \hat{u}'_1}\right)^2 + \frac{\pi^2}{6} + 2\text{Li}_2\left(1 - \frac{\hat{s}' m_t^2}{\hat{t}'_1 \hat{u}'_1}\right)\right], \\
\mathcal{I}'_{33} &= \frac{2}{\epsilon} + 2L_0 - \frac{2(1+\beta_t^2)}{\beta_t} \ln x_s\,, \\
\mathcal{I}'_{44} &= \frac{2}{\epsilon} + 2L_0 + 4\,, \\
\mathcal{I}'_{14} = \mathcal{I}'_{24} &= -\frac{1}{\epsilon^2} - \frac{1}{\epsilon} L_0 - \frac{1}{2} L_0^2 - \frac{\pi^2}{12}\,, \\
\mathcal{I}'_{13} &= -\left[\frac{1}{\epsilon^2} + \frac{1}{\epsilon}\left(L_0 - 2\ln\frac{\hat{t}'_1}{\hat{u}'_1}\right) + \frac{1}{2}\left(L_0 - 2\ln\frac{\hat{t}'_1}{\hat{u}'_1}\right)^2 + \frac{\pi^2}{12}\right.
\end{aligned} \tag{5.21}$$

$$+ 2\mathrm{Li}_2\left(1-\frac{\hat{t}_1'}{\hat{u}_1' x_s}\right) + 2\mathrm{Li}_2\left(1-\frac{\hat{t}_1' x_s}{\hat{u}_1'}\right)\Bigg],$$

$$\mathcal{I}_{23}' = \mathcal{I}_{13}'\left(\hat{t}_1' \leftrightarrow \hat{u}_1'\right),$$

$$\mathcal{I}_{34}' = \frac{1+\beta_t^2}{2\beta_t}\left[-\frac{2}{\epsilon}\ln x_s - 2L_0 \ln x_s + 2\ln^2 x_s - 4\ln x_s \ln(1-x_s^2) - 2\mathrm{Li}_2(x_s^2) + \frac{\pi^2}{3}\right],$$

where $\beta_t = \sqrt{1-4m_t^2/\hat{s}'}$, $x_s = (1-\beta_t)/(1+\beta_t)$ and

$$L_0 = \ln\left(-\frac{\mu^2 (x^0)^2 e^{2\gamma_E}}{4}\right). \tag{5.22}$$

The renormalized function is obtained by subtracting the $1/\epsilon^n$ poles in the bare function. When performing resummation it is more convenient to introduce the Laplace transform of this object, which is defined as

$$\begin{aligned}\tilde{\boldsymbol{s}}(L, \hat{s}', \hat{t}_1', \hat{u}_1', m_t, \mu) &= \int_0^\infty d\omega \exp\left(-\frac{\omega}{e^{\gamma_E}\mu e^{L/2}}\right) \hat{\boldsymbol{W}}(\omega, \hat{s}', \hat{t}_1', \hat{u}_1', m_t, \mu), \\ &= \boldsymbol{W}\left(\left(x^0 = -\frac{2i}{e^{\gamma_E}\mu e^{L/2}}, \vec{x}=0\right), \hat{s}', \hat{t}_1', \hat{u}_1', m_t, \mu\right).\end{aligned} \tag{5.23}$$

From the second line it is clear that the Laplace-transformed function $\tilde{\boldsymbol{s}}$ is determined directly from the position-space soft function through the replacement $L_0 \to -L$ [106].

The above expression for the one-loop soft function is new, but we have been able to perform two important checks. First, we have verified that our results are consistent with the results for real emission in the soft limit given in [9] for the gg channel and in [10] for the $q\bar{q}$ channel. Second, we have made sure that the divergence structure of the one-loop soft function is consistent with the RG equation derived in the following section.

5.2.2. Threshold Resummation

The physical cross section should be independent of the factorization scale, which implies

$$\begin{aligned}0 = \int_{x_1^{\min}}^1 \frac{dx_1}{x_1}\int_{x_2^{\min}}^1 \frac{dx_2}{x_2}\Bigg\{&\left[\frac{d}{d\ln\mu_f}\left[f_{i/N_1}(x_1,\mu_f)\, f_{j/N_2}(x_2,\mu_f)\right]\right] C_{ij}(s_4,\hat{s},\hat{t}_1,\hat{u}_1,m_t,\mu_f) \\ &+ f_{i/N_1}(x_1,\mu_f)\, f_{j/N_2}(x_2,\mu_f)\frac{d}{d\ln\mu_f} C_{ij}(s_4,\hat{s},\hat{t}_1,\hat{u}_1,m_t,\mu_f)\Bigg\}.\end{aligned} \tag{5.24}$$

Compared to the PIM case, the terms arising from the derivatives acting on the PDFs are slightly different. To understand their structure, first consider the term where the derivative acts on $f_{j/N_2}(x_2,\mu_f)$. Analog to (4.88) and (4.89), under the dynamical assumption of

steeply falling PDFs, the DGLAP evolution equations can be simplified by keeping only the leading terms for $x \to 1$ in the Altarelli-Parisi splitting functions, in which case the evolution becomes diagonal and reads

$$\frac{d}{d\ln\mu} f_{j/N_2}(y,\mu) = \int_y^1 \frac{dx}{x}\, P_{jj}(x)\, f_{j/N_2}(y/x,\mu)\,, \tag{5.25}$$

with $P_{jj}(x)$ given by

$$P_{jj}(x) = \frac{2\Gamma^j_{\rm cusp}(\alpha_s)}{(1-x)_+} + 2\gamma^\phi_j(\alpha_s)\,\delta(1-x)\,. \tag{5.26}$$

We then obtain (up to power-suppressed terms)

$$\int_{x_1^{\rm min}}^1 \frac{dx_1}{x_1} f_{i/N_1}(x_1,\mu_f) \left[\int_{x_2^{\rm min}}^1 \frac{dx_2}{x_2} \int_{x_2}^1 \frac{d\xi}{\xi}\, f_{j/N_2}(x_2/\xi,\mu_f) P_{jj}(\xi)\, C_{ij}(s_4,\hat{s},\hat{t}_1,\hat{u}_1,m_t,\mu_f)\right]. \tag{5.27}$$

To derive the evolution equation for the soft function, we arrange the integrations such that the Altarelli-Parisi kernel acts on the C_{ij} rather than on the PDF. After some manipulations, the term in the square brackets above can be written as

$$\int_{x_2^{\rm min}}^1 \frac{dx_2}{x_2}\, f_{j/N_2}(x_2,\mu_f) \int_{x_2^{\rm min}/x_2}^1 \frac{d\xi}{\xi} P_{jj}(\xi)\, C_{ij}(s_4',\xi\hat{s},\hat{t}_1,\xi\hat{u}_1,m_t,\mu_f) \tag{5.28}$$

with $s_4' = \hat{t}_1 + \xi(\hat{s}+\hat{u}_1)$. Changing the integration variable from ξ to s_4', taking the threshold limit $s_4 \to 0$, and using the identity

$$\int_0^{s_4} ds_4' \,\frac{f(s_4')}{(-\hat{t}_1)[(s_4-s_4')/(-\hat{t}_1)]_+} = \int_0^{s_4} ds_4' \,\frac{f(s_4')-f(s_4)}{s_4-s_4'} + f(s_4)\ln\frac{s_4}{-\hat{t}_1}\,, \tag{5.29}$$

we can convert this term into a form from which the RG equation for the soft function is more easily derived. The analogous procedure is then used for the term where the derivative acts on the other PDF. Finally, we use the RG equation for the hard function

$$\begin{aligned}\frac{d}{d\ln\mu}\boldsymbol{H}(\hat{s}',\hat{t}_1',\hat{u}_1',m_t,\mu) &= \boldsymbol{\Gamma}_H(\hat{s}',\hat{t}_1',\hat{u}_1',\mu)\,\boldsymbol{H}(\hat{s}',\hat{t}_1',\hat{u}_1',m_t,\mu)\\ &\quad + \boldsymbol{H}(\hat{s}',\hat{t}_1',\hat{u}_1',m_t,\mu)\,\boldsymbol{\Gamma}_H^\dagger(\hat{s}',\hat{t}_1',\hat{u}_1',m_t,\mu)\,,\end{aligned} \tag{5.30}$$

with

$$\boldsymbol{\Gamma}_H(\hat{s}',\hat{t}_1',\hat{u}_1',m_t,\mu) = \Gamma_{\rm cusp}(\alpha_s)\left(\ln\frac{\hat{s}'}{\mu^2} - i\pi\right)\mathbf{1} + \boldsymbol{\gamma}^h(\hat{s}',\hat{t}_1',\hat{u}_1',m_t,\alpha_s)\,, \tag{5.31}$$

Assembling the different pieces and enforcing (5.24), the evolution equation for the momentum-space soft function reads

$$\begin{aligned}\frac{d}{d\ln\mu}\boldsymbol{S}(s_4,\hat{s}',\hat{t}_1',\hat{u}_1',m_t,\mu) = &-\left[2\Gamma_{\rm cusp}(\alpha_s)\ln\frac{s_4}{m_t\mu}+\boldsymbol{\gamma}^{s\dagger}(\hat{s}',\hat{t}_1',\hat{u}_1',m_t,\alpha_s)\right]\boldsymbol{S}(s_4,\hat{s}',\hat{t}_1',\hat{u}_1',m_t,\mu)\\ &-\boldsymbol{S}(s_4,\hat{s}',\hat{t}_1',\hat{u}_1',m_t,\mu)\left[2\Gamma_{\rm cusp}(\alpha_s)\ln\frac{s_4}{m_t\mu}+\boldsymbol{\gamma}^{s}(\hat{s}',\hat{t}_1',\hat{u}_1',m_t,\alpha_s)\right]\\ &-4\Gamma_{\rm cusp}(\alpha_s)\int_0^{s_4}ds_4'\,\frac{\boldsymbol{S}(s_4',\hat{s}',\hat{t}_1',\hat{u}_1',m_t,\mu)-\boldsymbol{S}(s_4,\hat{s}',\hat{t}_1',\hat{u}_1',m_t,\mu)}{s_4-s_4'},\end{aligned} \tag{5.32}$$

where we have defined

$$\boldsymbol{\gamma}^s(\hat{s}',\hat{t}_1',\hat{u}_1',m_t,\alpha_s)=\boldsymbol{\gamma}^h(\hat{s}',\hat{t}_1',\hat{u}_1',m_t,\alpha_s)+\left(2\gamma^\phi(\alpha_s)+\Gamma_{\rm cusp}(\alpha_s)\ln\frac{\hat{s}'m_t^2}{\hat{t}_1'\hat{u}_1'}\right)\mathbf{1}\,. \tag{5.33}$$

This evolution equation is of the same form as for the PIM case, but the soft anomalous dimension is modified by the logarithmic term in (5.33), which can be traced back to the different form of the collinear evolution terms after arranging the integrations as appropriate for 1PI kinematics (this extra term vanishes in the production threshold limit $\beta\to 0$, where PIM and 1PI kinematics agree). Therefore, we can use the expression for the resummed soft function derived for PIM kinematics, taking into account the changes in the anomalous dimension and soft matching function, and the fact that now $\omega = s_4/\sqrt{s_4+m_t^2}$ sets the mass scale in the soft logarithms. The resummed soft function is then given by

$$\begin{aligned}\boldsymbol{S}(s_4,\hat{s}',\hat{t}_1',\hat{u}_1',m_t,\mu_f) = &\exp\left[-4S(\mu_s,\mu_f)+2a_\Gamma(\mu_s,\mu_f)\ln\frac{\hat{s}'m_t^2}{\hat{t}_1'\hat{u}_1'}+4a_{\gamma^\phi}(\mu_s,\mu_f)\right]\\ &\times\boldsymbol{u}^\dagger(\hat{s}',\hat{t}_1',\hat{u}_1',m_t,\mu_f,\mu_s)\,\tilde{\boldsymbol{s}}(\partial_\eta,\hat{s}',\hat{t}_1',\hat{u}_1',m_t,\mu_s)\,\boldsymbol{u}(\hat{s}',\hat{t}_1',\hat{u}_1',m_t,\mu_f,\mu_s)\\ &\times\frac{1}{s_4}\left(\frac{s_4}{\sqrt{m_t^2+s_4\mu_s}}\right)^{2\eta}\frac{e^{-2\gamma_E\eta}}{\Gamma(2\eta)}\,\Bigg|_{\eta=2a_\Gamma(\mu_s,\mu_f)},\end{aligned} \tag{5.34}$$

and combining this with the solution for the hard function, the final result for the resummed hard-scattering kernels in 1PI is

$$\begin{aligned}C(s_4,\hat{s}',\hat{t}_1',\hat{u}_1',m_t,\mu_f) = &\exp\left[2a_\Gamma(\mu_s,\mu_f)\ln\frac{m_t^2\mu_s^2}{\hat{t}_1'\hat{u}_1'}+4a_{\gamma^\phi}(\mu_s,\mu_f)\right]\\ &\times{\rm Tr}\Bigg[\boldsymbol{U}(\hat{s}',\hat{t}_1',\hat{u}_1',m_t,\mu_h,\mu_s)\,\boldsymbol{H}(\hat{s}',\hat{t}_1',\hat{u}_1',m_t,\mu_h)\,\boldsymbol{U}^\dagger(\hat{s}',\hat{t}_1',\hat{u}_1',m_t,\mu_h,\mu_s)\\ &\times\tilde{\boldsymbol{s}}(\partial_\eta,\hat{s}',\hat{t}_1',\hat{u}_1',m_t,\mu_s)\Bigg]\frac{1}{s_4}\left(\frac{s_4}{\sqrt{m_t^2+s_4\mu_s}}\right)^{2\eta}\frac{e^{-2\gamma_E\eta}}{\Gamma(2\eta)}\,\Bigg|_{\eta=2a_\Gamma(\mu_s,\mu_f)}.\end{aligned} \tag{5.35}$$

The result (5.35) is the same as in Chapter 4, and the the RG exponents a_Γ and a_{γ^ϕ} as the evolution factors $\boldsymbol{U}$ and $\boldsymbol{u}$ can again be found in the Appendix. The notation is such that one must first take the derivatives with respect to η appearing in the first argument of the Laplace-transformed soft function $\tilde{\boldsymbol{s}}$, defined in (5.23), and then set $\eta = 2a_\Gamma(\mu_s, \mu_f)$. Again, for values of the scale where $\eta < 0$, one must use analytic continuation to interpret the formula in terms of plus-distributions.

Our result for the resummed hard-scattering kernels is equivalent to the Mellin-space resummation formula from [56] when expanded to any fixed order in α_s, if we approximate $\sqrt{m_t^2 + s_4} \sim m_t$. However, the scale choices used in Mellin-space resummation are typically such that the one encounters a Landau-pole ambiguity in the evaluation of the all-orders formula, upon inverting the Mellin transform and integrating over s_4. One way of dealing with this, as done in [53–55,57], is to instead use the resummation formula only to construct approximate fixed-order expansions at NNLO. Another way is to instead view μ_s as a function of the observables p_T and y, and choose it in such a way that the perturbative expansion of the soft function at μ_s is well behaved. With such a choice of μ_s, one can still evaluate the all-orders resummation formula, but without encountering Landau-pole ambiguities. We will describe how to construct the fixed-order expansion to NNLO in Section 6.2, and then compare the two methods in more detail in Section 6.3.

6. Approximate NNLO

The goal of this Section is to present a subset of the NNLO corrections to the hard-scattering kernels for the $t\bar{t}$ invariant mass, and the rapidity and p_T distribution of the top-quark at hadron colliders. The leading-order terms in the threshold expansions $z \to 1$ (in the PIM case) or $s_4 \to 0$ (in the 1PI case) for the differential cross section are equivalent to the virtual-soft approximation, and are written in terms of singular plus distributions and delta functions in the variable $(1-z)$ and s_4 respectively. Those have been shown at the end of Sections 4.1 and 5.1. Our results determine the coefficients of all plus distributions of the form $[\ln^n(1-z)/(1-z)]_+$ (PIM) and $[1/s_4 \ln^n(s_4/m_t^2)]_+$ (1PI), as well as all μ-dependent pieces multiplying the $\delta(1-z)$ term and the $\delta(s_4)$ term respectively. Remaining pieces of the delta-function coefficients are left undetermined. The basis for our calculations are the factorization formulas for the hard-scattering kernels in the partonic threshold regions given in Section 4.2.5 and Section 5.2.2. As we have shown, the hard and soft functions contained in the hard-scattering kernels satisfy certain renormalization-group equations, which determine their dependence on the scale μ. By knowing the hard and soft functions at one-loop order, and using results for the two-loop anomalous dimensions also mentioned in Sections 4.2.5 and 5.2.2, the μ-dependent logarithms in the hard and soft functions can be determined exactly to NNLO using the renormalization group. The logarithms in the soft functions are of the form $\ln[\hat{s}(1-z)^2/\mu^2]$ (PIM) and $\ln[s_4/(\sqrt{s_4+m_t^2}\,\mu)]$ (1PI), and they uniquely determine the coefficients of the different plus-distributions mentioned above.

Concerning the case of PIM kinematics this is similar in spirit to the calculations of [54] for the soft corrections to the NNLO differential cross section using threshold resummation techniques in Mellin space, but goes beyond those results by completely determining the coefficient of the $[1/(1-z)]_+$ distribution, which is sensitive to process-dependent two-loop anomalous dimensions. In the case of 1PI kinematics, the analytic expressions for D_i $(i = 1, 2, 3)$ were first derived in [54] starting from resummed formulas in Mellin moment space. We have compared with those results and found agreement. In a recent paper the coefficient D_0 was also determined [57], but its explicit form was not reported there.

6.1. Approximate NNLO: PIM

In the Chapter 4 we derived a formula for the resummed differential cross section, which is valid up to NNLL order. Starting from (4.94), we will now obtain expressions for the differential cross section which are valid in fixed-order perturbation theory. As mentioned in the introduction, our results allow one to obtain analytic expression for all of the co-

efficients multiplying singular plus distributions in the variable $(1-z)$ appearing in the hard-scattering kernels up to NNLO. With the same method, which is outlined below, it is also possible to determine analytically, up to $\mathcal{O}(\alpha_s^4)$, the scale-dependent parts of the coefficient multiplying $\delta(1-z)$.

In order to derive fixed-order formulas from (4.94), we first set $\mu_h = \mu_s = \mu_f = \mu$. In that case the evolution matrix $\boldsymbol{U}$ is equal to unity, and $\eta = 2a_\Gamma(\mu_f, \mu_s) \to 0$. The formula for the hard-scattering kernels then becomes

$$C(z, M, m_t, \cos\theta, \mu) = \tilde{c}(\partial_\eta, M, m_t, \cos\theta, \mu) \left(\frac{M}{\mu}\right)^{2\eta} \frac{e^{-2\gamma_E \eta}}{\Gamma(2\eta)} \frac{z^{-\eta}}{(1-z)^{1-2\eta}}\bigg|_{\eta=0}, \tag{6.1}$$

where

$$\tilde{c}(\partial_\eta, M, m_t, \cos\theta, \mu) = \mathrm{Tr}\Big[\boldsymbol{H}(M, m_t, \cos\theta, \mu)\, \tilde{\boldsymbol{s}}(\partial_\eta, M, m_t, \cos\theta, \mu)\Big]. \tag{6.2}$$

From the above, we conclude that it is sufficient to focus on the calculation of $\widetilde{c}$ at NNLO. Using the perturbative expansion of the hard (4.62) and soft function (4.66), the result at NNLO reads

$$\begin{aligned}\widetilde{c}^{(2)}(\partial_\eta, M, m_t, \cos\theta, \mu) &= \mathrm{Tr}\left[\boldsymbol{H}^{(2)}\, \widetilde{\boldsymbol{s}}^{(0)}\right] + \mathrm{Tr}\left[\boldsymbol{H}^{(0)}\, \widetilde{\boldsymbol{s}}^{(2)}\right] + \mathrm{Tr}\left[\boldsymbol{H}^{(1)}\, \widetilde{\boldsymbol{s}}^{(1)}\right] \\ &= \sum_{j=0}^{4} c_j^{(2)}(M, m_t, \cos\theta, \mu)\, \partial_\eta^j\,.\end{aligned} \tag{6.3}$$

By using (4.76) and (4.92) in combination with the analytic expressions for the hard and soft functions at NLO, it is possible to determine all terms proportional to $\ln\mu$ in the two-loop hard function $\boldsymbol{H}^{(2)}(M, m_t, \cos\theta, \mu)$, as well as all terms proportional to L in the two-loop soft function $\tilde{\boldsymbol{s}}^{(2)}(L, M, m_t, \cos\theta, \mu)$. This information allows us to derive an approximate expression for $\tilde{c}$ at NNLO. By inserting that formula for $\tilde{c}$ into (6.1), we obtain the corresponding NNLO expression for the hard-scattering kernel C. The results are conventionally written in terms of the plus distributions

$$P_n(z) = \left[\frac{\ln^n(1-z)}{1-z}\right]_+. \tag{6.4}$$

However, the right-hand side of (6.1) is more conveniently expressed in terms of the distributions

$$P_n'(z) = \left[\frac{1}{1-z}\ln^n\left(\frac{M^2(1-z)^2}{\mu^2 z}\right)\right]_+. \tag{6.5}$$

It is possible to show that taking the derivatives with respect to η and the limit $\eta \to 0$ in (6.1) is equivalent to making the following set of replacements in $\tilde{c}(L, M, m_t, \cos\theta, \mu)$:

$$1 \to \delta(1-z)\,,$$

$$L \to 2P_0'(z) + \delta(1-z)\ln\left(\frac{M^2}{\mu^2}\right),$$

$$L^2 \to 4P_1'(z) + \delta(1-z)\ln^2\left(\frac{M^2}{\mu^2}\right),$$

$$L^3 \to 6P_2'(z) - 4\pi^2 P_0'(z) + \delta(1-z)\left[\ln^3\left(\frac{M^2}{\mu^2}\right) + 4\zeta_3\right],$$

$$L^4 \to 8P_3'(z) - 16\pi^2 P_1'(z) + 128\zeta_3 P_0'(z) + \delta(1-z)\left[\ln^4\left(\frac{M^2}{\mu^2}\right) + 16\zeta_3\ln\left(\frac{M^2}{\mu^2}\right)\right]. \quad (6.6)$$

In order to translate the P_n' into the conventional P_n distributions, we employ the general relation

$$P_n'(z) = \sum_{k=0}^{n}\binom{n}{k}\ln^{n-k}\left(\frac{M^2}{\mu^2}\right)\left[2^k P_k(z)\right. \quad (6.7)$$
$$\left. + \sum_{j=0}^{k-1}\binom{k}{j}2^j(-1)^{k-j}\left(\frac{\ln^j(1-z)\ln^{k-j}z}{1-z} - \delta(1-z)\int_0^1 dx\frac{\ln^j(1-x)\ln^{k-j}x}{1-x}\right)\right].$$

The final result for the hard-scattering kernels at NNLO can be written as

$$C^{(2)}(z, M, m_t, \cos\theta, \mu) = D_3\left[\frac{\ln^3(1-z)}{1-z}\right]_+ + D_2\left[\frac{\ln^2(1-z)}{1-z}\right]_+$$
$$+ D_1\left[\frac{\ln(1-z)}{1-z}\right]_+ + D_0\left[\frac{1}{1-z}\right]_+ + C_0\,\delta(1-z) + R(z). \quad (6.8)$$

The coefficients $D_0, \ldots, D_3$ and C_0 are functions of the variables $M, m_t, \cos\theta$, and μ. The analytic expression for D_i $(i = 1, 2, 3)$ were first derived in [54] starting from resummed formulas in Mellin moment space. Here we determine the coefficients $D_0, \ldots, D_3$ completely. D_0 can be calculated in this way because the process-dependent anomalous-dimension matrices in (4.78) and (4.79) are now known up to NNLO. With the same method, it is possible to calculate the scale dependence of δ-function coefficient C_0. The function $R(z)$ is finite for $z \to 1$, dropping it recovers the traditional PIM scheme. The computation of the scale-independent part of C_0 requires the knowledge of the hard and soft functions at two-loop order. As long as these are missing, there is an ambiguity in C_0. We will comment on this in more detail after the derivation of the approximate NNLO formulas in 1PI.

The coefficients c_n^{A} and c_n^{B} $(n = 1, 2, 3)$ are known, while c_0^{A} and c_0^{B} are unknown. In our publication [4], the explicit expressions for the coefficients $D_0, \ldots, D_3$ and C_0 were collected in a `Mathematica` file, which can be downloaded from the arXiv version of that work.

6.2. Approximate NNLO: 1PI

We now proceed to obtain approximate NNLO expressions for the case of 1PI kinematics. We derive those analog to the previous section, this time starting from 5.35. Setting all scales equal we arrive at

$$C(s_4,\hat{s}',\hat{t}_1',\hat{u}_1',m_t,\mu)=\tilde{c}(\partial_\eta,\hat{s}',\hat{t}_1',\hat{u}_1',m_t,\mu)\,\frac{e^{-2\gamma_E\eta}}{\Gamma(2\eta)}\,\frac{1}{s_4}\left(\frac{s_4}{\sqrt{m_t^2+s_4\mu_s}}\right)^{2\eta}\Bigg|_{\eta=0}, \tag{6.9}$$

where now

$$\tilde{c}(\partial_\eta,\hat{s}',\hat{t}_1',\hat{u}_1',m_t,\mu)=\mathrm{Tr}\Big[\boldsymbol{H}(\hat{s}',\hat{t}_1',\hat{u}_1',m_t,\mu)\,\tilde{\boldsymbol{s}}(\partial_\eta,\hat{s}',\hat{t}_1',\hat{u}_1',m_t,\mu)\Big]\,. \tag{6.10}$$

Using the same methods as in the last section, we determine at NNLO the coefficients of all powers of L in $\tilde{c}$ and again the μ-dependent part of the constant piece. We convert the derivatives with respect to the auxiliary parameter η into distributions in s_4 defined in (5.11), which can be easily done by using the following replacement rules:

$$\begin{aligned}
1 &\longrightarrow \delta(s_4)\,,\\
L &\longrightarrow 2P_0(s_4)-\delta(s_4)\,L_m\,,\\
L^2 &\longrightarrow 8P_1(s_4)-4L_mP_0(s_4)+\delta(s_4)\left(L_m^2-\frac{2\pi^2}{3}\right)-\frac{4L_4}{s_4}\,,\\
L^3 &\longrightarrow 24P_2(s_4)-24L_mP_1(s_4)+\left(6L_m^2-4\pi^2\right)P_0(s_4)+\delta(s_4)\left(-L_m^3+2\pi^2L_m+16\zeta_3\right)\\
&\quad-\frac{6L_4}{s_4}\left[-L_4+2\ln\frac{s_4^2}{m_t^2\mu^2}\right],\\
L^4 &\longrightarrow 64P_3(s_4)-96L_mP_2(s_4)+\left(48L_m^2-32\pi^2\right)P_1(s_4)\\
&\quad+\left(-8L_m^3+16\pi^2L_m+128\zeta_3\right)P_0(s_4)+\delta(s_4)\left(L_m^4-4\pi^2L_m^2-64\zeta_3L_m+\frac{4\pi^4}{15}\right)\\
&\quad-\frac{8L_4}{s_4}\left[L_4^2-3L_4\ln\frac{s_4^2}{m_t^2\mu^2}+3\ln^2\frac{s_4^2}{m_t^2\mu^2}-2\pi^2\right],
\end{aligned} \tag{6.11}$$

where $L_m=\ln(\mu^2/m_t^2)$ and $L_4=\ln(1+s_4/m_t^2)$.

The final result for the hard-scattering kernels at NNLO can be written as

$$\begin{aligned}
C^{(2)}(s_4,\hat{s}',\hat{t}_1',\hat{u}_1',m_t,\mu)=&D_3\,P_3(s_4)+D_2\,P_2(s_4)+D_1\,P_1(s_4)+D_0\,P_0(s_4)\\
&+C_0\,\delta(s_4)+R(s_4)\,,
\end{aligned} \tag{6.12}$$

where the coefficients $D_0,\ldots,D_3$ and C_0 are functions of the variables $\hat{s}'$, $\hat{t}_1'$, $\hat{u}_1'$, m_t and μ. The explicit results are quite lengthy and are contained in a computer program which can

be downloaded together with the arXiv version of our paper [3]. The regular piece $R(s_4)$ collects terms involving L_4, which arise from choosing $\omega = s_4/\sqrt{m_t^2 + s_4}$ in the argument of the soft function. As noted in Section 5.2.1, dropping $R(s_4)$ recovers the 1PI scheme used in earlier work, for instance [57].

6.2.1. C_0 Term

In both kinematics, the C_0 term is ambiguous since only its scale-dependent part is exactly determined. We want to specify which terms are contributing. One contribution to C_0 comes from the conversions of powers of L in $\tilde{c}^{(2)}$ according to (6.11) or (6.6) respectively, which are determined exactly, therefore the ambiguity comes from the constant term of $\tilde{c}^{(2)}$, which is

$$\tilde{c}^{(2)}(0) = \mathrm{Tr}\Big[\boldsymbol{H}^{(1)}\,\tilde{\boldsymbol{s}}^{(1)}(0) + \boldsymbol{H}^{(0)}\,\tilde{\boldsymbol{s}}^{(2)}(0) + \boldsymbol{H}^{(2)}\,\tilde{\boldsymbol{s}}^{(0)}(0)\Big]\,, \tag{6.13}$$

where we have suppressed the dependence on different variables for convenience. In the three terms above, the first term is known exactly, while the constant term of the two-loop soft function in the second term is unknown. As for the two-loop hard function in the third term, one can determine its scale-dependent part and include it in the formula.

For the case of PIM kinematics we chose the following:
We include the two-loop hard function, associated with this fact is the possibility to normalize the scale-dependent logarithms in an arbitrary way, i.e.

$$\ln\left(\frac{\mu_0^2}{\mu^2}\right) = \ln\left(\frac{\mu_1^2}{\mu^2}\right) + \ln\left(\frac{\mu_0^2}{\mu_1^2}\right). \tag{6.14}$$

Scale-independent terms proportional to the second logarithm on the right-hand side can be absorbed into the unknown μ-independent part of the coefficient function C_0. Therefore, the numerical results for C_0 depend on the choice of the second mass scale, which appears in the scale-dependent logarithms; we indicate this second scale by μ_0. In Chapter 8 we shall consider two different choices for μ_0: $\mu_0 = M$ (scheme A), and $\mu_0 = m_t$ (scheme B). The situation is summarized in the following formula:

$$C_0 = \begin{cases} \displaystyle\sum_{i=0}^{4} c_n^{\mathrm{A}} \ln^n \frac{M^2}{\mu^2} & \text{(scheme A)} \\ \displaystyle\sum_{i=0}^{4} c_n^{\mathrm{B}} \ln^n \frac{m_t^2}{\mu^2} & \text{(scheme B)} \end{cases} \tag{6.15}$$

For the case of 1PI kinematics we focus on the terms exactly known, and instead drop the contributions of the two-loop hard function. Later, in Section 10.1 when we combine the numerical results for the total cross section derived using PIM and 1PI kinematics, the PIM numbers will also be computed in the equivalent way, i.e., by dropping the two-loop hard function completely.

6.3. Resummation vs. NNLO Expansion

In our numerical studies later on we will typically give results from both resummed perturbation theory and the approximate NNLO formulas. Although the perturbative information used in these formulas is the same – the NLO matching functions and the NNLO anomalous dimensions – the implementation and philosophy is different.

In resummed perturbation theory, one views the soft function as depending on the distributions

$$P_n'(z) = \left[\frac{1}{1-z}\ln^n\left(\frac{M^2(1-z)^2}{\mu_s^2 z}\right)\right]_+, \quad P_n'(s_4) = \left[\frac{1}{s_4}\ln^n\left(\frac{s_4}{\sqrt{s_4+m_t^2}\mu_s}\right)\right]_+, \quad (6.16)$$

as well as $\delta(1-z)$ and $\delta(s_4)$ respectively. The logarithmic corrections are in general considered large compared to the δ-function term (and of course subleading terms in z or s_4), but it is assumed that with a proper choice of μ_s they can be treated on the same footing, so that the soft function at this scale can be reliably calculated in fixed-order perturbation theory. Considering the case of 1PI kinematics as an example, here it would obviously be the case if we chose $\mu_s = s_4/\sqrt{s_4+m_t^2}$, since then the logarithmic corrections would vanish, but in that case the running coupling in the soft corrections would, for some value of s_4, be evaluated at the Landau pole, which would spoil the clear separation between perturbative and non-perturbative physics accomplished by using the effective field-theory formalism. Therefore, as usually done in momentum-space resummation [106–108,123,124], we will view the soft scale as a function of the observables p_T and y, and choose it based on the convergence of the physical cross section. A similar procedure will be applied to the case of PIM kinematics where instead the μ_s is a function of the invariant mass distribution. In both kinematics, we study corrections from the soft function to the cross section as a function of μ_s, and choose the numerical value of the scale as the point where the correction is minimized. The formulas then sum logarithms of the numerical ratio μ_s/μ_f, where μ_s is the dynamically generated soft scale. The same reasoning applies to the choice of the hard and factorization scales, and an advantage of the resummation formalism is that the three scales can be varied independently as a way of estimating perturbative uncertainties.

This approach should be contrasted with that based on approximate NNLO formulas. In using such an approximation, one assumes that the logarithmic corrections from the P_n' distributions account for the bulk of the NNLO corrections in fixed order at an arbitrary factorization scale μ_f, and at the same time that the corrections at NNNLO and beyond, evaluated at that scale, are small enough that the perturbative series is well behaved. From this point of view, the resummation formalism is just a useful tool for constructing the approximate fixed-order expansion, and no physical significance is given to the soft scale μ_s, on which the final answer does not depend.

It is worth emphasizing that the fixed-order expansion of the NLO+NNLL formulas to NNLO in α_s is not exactly equivalent to the approximate NNLO formulas from the previous sections. The direct expansion of the NLO+NNLL formulas to NNLO contains explicit dependence on the scale μ_s and also a different pattern of plus-distributions compared to

the approximate NNLO formulas. For instance, the approximate NNLO formula contains P_3 distributions, but the expansion of the NLO+NNLL formula to NNLO in fixed order contains at most P_2 distributions, as required by the Altarelli-Parisi equations. This aspect of the calculation is discussed in greater detail in the Section .3 of the appendix.

Dynamical Threshold Enhancement

The optimal method for including the higher-order perturbative effects is not entirely clear without further information. The reason is that it is not possible to tell whether the logarithmic corrections from the partonic threshold region can be considered large, or how to minimize them with a proper choice of μ_s, until *after* the integration over z or s_4 respectively. After that integration, they give large perturbative corrections to the differential cross section if the PDFs fall off very quickly away from the region where $z \to 1$ (PIM) or $s_4 \to 0$ (1PI), an effect referred to as "*dynamical threshold enhancement*" [106] . Since the PDFs are not known analytically, it is only possible to assess the extent to which the corrections in the partonic threshold region are dynamically enhanced through a numerical study. We will do so for the case of PIM in Section 8.1.1, and for 1PI in Section 9.2.1.

Part III.

$t\bar{t}$ Production: Phenomenology

7. Introduction

In this part we use our theoretical results to make phenomenological predictions for various observables at the LHC and the Tevatron at NLO+NNLL and at approximate NNLO order. The analysis is split into three chapters, *Studies in PIM*, *Studies in 1PI* and *Combined studies*.

The first chapter starts by studying the importance of threshold terms in PIM kinematics in Section 8.1.1. We then define our scale setting scheme in PIM in Section 8.1.2, which is followed by a detailed analysis of the invariant mass distribution in Section 8.2. Using these results, we make predictions for the total cross section in Section 8.3. By studying the differential cross section with respect to $\beta = \sqrt{1 - 4m_t^2/\hat{s}}$, we do a comparison with previous calculations in Section 8.3.1. Throughout this first chapter we apply the PIM_{SCET} scheme, and specify it specifically when necessary.

In *Studies in 1PI* we begin by making our numerical implementation concrete in Section 9.1. This is then followed by an examination of the threshold terms in 1PI kinematics, Section 9.2.1. Similar to PIM we first have to choose a scale setting scheme before giving resummed results, this is done in Section 9.2.2. Phenomenological predictions for the rapidity and transverse-momentum distributions are then presented in Section 9.3. We finish again by using our differential results to make detailed predictions for the total cross section in Section 9.4.

Both types of kinematics, PIM and 1PI, can be used to calculate the total cross section at the LHC and Tevatron, and they both yield results for the FB asymmetry at the Tevatron. In the sections mentioned above we make predictions for the total cross section separately, for PIM and 1PI kinematics. As the numerical difference between the two predictions can be seen as a theoretical uncertainty we make a joined analysis in Chapter 10. We start by comparing the different approaches on the level of the β spectrum in Section 10.1.1, where we also investigate subleading contributions to the different threshold terms. In Section 10.1.2 we give combined results for the total cross section as a function of the top-quark mass using the pole mass scheme. Finally we end the discussion about the total cross section by making combined prediction for this quantity using the $\overline{\text{MS}}$ and 1S mass scheme in Section 10.1.3.

We give results for the FB asymmetry in the laboratory frame using our 1PI results and in the $t\bar{t}$ frame using the PIM ones. In the laboratory frame we give numbers for the total asymmetry in Section 10.2.2 and we present the differential asymmetry with respect to the rapidity of the top quark y_t in the same section. Predictions for the total asymmetry in the $t\bar{t}$ frame can be found in Section 10.2.3. The differential asymmetry with respect to the invariant mass is also presented in Section 10.2.3, where we use our binned results to make a comparison to recent measurements. Using PIM kinematics we calculate the

$\Delta y = y_t - y_{\bar{t}}$ dependent asymmetry, results for this quantity can be found at the end of Section 10.2.3. We again use binned results of the Δy dependent asymmetry to compare to experimental measurements.

The LHC has a symmetric initial condition which leads to the fact that there one does not observe an inclusive asymmetry, a charge asymmetry on the other hand is observable at the LHC. We will investigate such an asymmetry in Section 10.2.4 by imposing lower cuts on the top and anti-top rapidities.

In the following we specify some of the inputs we use for our calculation in PIM and 1PI kinematics. Those will be applied in the upcoming sections if not specified otherwise.

Our results obtained in resummed perturbation theory would require PDF sets extracted from data using resummed predictions for the relevant cross sections; however, such PDF sets do not exist at present. Since our resummed expressions include the bulk of the perturbative corrections appearing one order higher in α_s, we use NLO parton densities for the NLO and NLL approximations, and NNLO parton densities for the approximate NNLO and matched NLO+NNLL approximations, as summarized in Table 7.1. The associated running couplings $\alpha_s(\mu)$ are taken in the $\overline{\text{MS}}$ scheme with five active flavors, using one-loop running at LO, two-loop running at NLO, and three-loop running at NNLO. As can be seen we use MSTW2008 PDF sets [139] for our numerical calculations . It will be specified when we differ from the above.

For some of our analysis we are using a fixed set of MSTW2008NNLO PDFs. The reason

Order	PDF set	$\alpha_s(M_Z)$
LO	MSTW2008LO	0.139
NLO, NLL	MSTW2008NLO	0.120
NNLO approx, NLO+NNLL	MSTW2008NNLO	0.117

Table 7.1.: Order of the PDFs [139] and the corresponding values of the strong coupling used for the different perturbative approximations.

is that it helps to elucidate more clearly the behavior of the perturbative expansion of the hard-scattering kernels in higher orders of perturbation theory.

In general we employ the value $m_t = 173.1\,\text{GeV}$ for the top-quark mass defined in the pole scheme. It will be made clear in the relevant sections when we differ from that, due to making mass dependent predictions or changing the mass scheme.

We do not consider the theoretical uncertainty induced by the error on $\alpha_s(M_Z)$ in general. In Section 10.1 however we give results for the total cross section with α_s and combined PDF+α_s errors. From this we conclude that the additional α_s theoretical uncertainty can be as big as 4% for the total top-quark pair production cross section at the LHC and the Tevatron. Such an uncertainty is therefore not negligible in comparison to the residual scale uncertainty in NNLO and NNLL calculations, and it will need to be considered when

comparing data and theoretical predictions.

To not repeat ourself we specify our standard scale uncertainty estimation scheme (SUES) when giving RG-improved numbers. In SUES we vary each of the three scales μ_f, μ_h and μ_s separately by a factor of two about their individually defined default values, and add the uncertainties in quadrature. Thus, for a default setting $\mu_f = m_t$, μ_f would be varied in the range $m_t/2 \leq \mu_f \leq 2m_t$ whilst holding the other scales fixed at their default values.

The higher-order corrections computed in this thesis are limited to leading order in the threshold expansions, whereas the exact NLO results in fixed order also contain subleading terms in $(1-z)$ or s_4 respectively. To make optimal use of our results, we match them onto the NLO fixed-order expressions in such a way that these subleading corrections are fully taken into account. For the resummed results, NLO+NNLL accuracy can be achieved by evaluating differential cross sections according to[1]

$$\begin{aligned} d\sigma^{\text{NLO+NNLL}} &\equiv d\sigma^{\text{NNLL}}\Big|_{\mu_h,\mu_s,\mu_f} + d\sigma^{\text{NLO, subleading}}\Big|_{\mu_f} \\ &\equiv d\sigma^{\text{NNLL}}\Big|_{\mu_h,\mu_s,\mu_f} + \left(d\sigma^{\text{NLO}}\Big|_{\mu_f} - d\sigma^{\text{NLO, leading}}\Big|_{\mu_f} \right), \end{aligned} \tag{7.1}$$

where $d\sigma^{\text{NLO}}$ is the exact result in fixed order, and $d\sigma^{\text{NLO,leading}}|_{\mu_f} \equiv d\sigma^{\text{NNLL}}|_{\mu_h=\mu_s=\mu_f}$ captures the leading singular terms in the threshold limits $z \to 1$ (PIM) or $s_4 \to 0$ (1PI) at NLO. The term $d\sigma^{\text{NLO, subleading}}$ is of subleading order in the equivalent threshold, and ensures that the total result reduces to the exact fixed-order result when all the scales are set equal. It also makes the result invariant under variations of the factorization scale, up to terms at NNLO in the perturbative expansion, even at subleading order in $(1-z)$ or s_4 respectively. To obtain approximate NNLO results in fixed order, we simply add the NNLO correction onto the exact NLO results, i.e.,

$$d\sigma^{\text{NNLO, approx}} = d\sigma^{\text{NLO}} + d\sigma^{(2),\text{ approx}}, \tag{7.2}$$

where $d\sigma^{(2),\text{ approx}}$ is the NNLO correction to the differential cross section obtained using the coefficient function (6.8) respectively (6.12).

For convenience we present in Table 7.2 a list of the different calculation schemes and their definitions which will be used in the following sections. The table is meant as a quick overview and reminder, the information containing it has been explained in previous sections.

[1] This matching procedure is general valid for results in PIM and in 1PI kinematics.

	scheme	ω	differences	observables
PIM	PIM	$M(1-z)$	$\ln(z)/(1-z)$	Invariant mass distribution Total cross section FB asymmetry dependent on M and Δy
	PIM_{SCET}	$M(1-z)/\sqrt{z}$		
1PI	1PI	s_4/m_t	$\ln(1+s_4/m_t^2)/s_4$	Rapidity and p_T distributions Total cross section FB asymmetry dependent on y_t Charge asymmetry at the LHC
	1PI_{SCET}	$s_4/\sqrt{m_t^2+s_4}$		

Table 7.2.: Listing of the different calculation schemes. Here ω is the argument of the soft-functions. The column *differences* refers to the difference in subleading terms between the two schemes on the left. Column *observables* shows the different observables which are calculable in the relevant kinematics.

8. Studies in PIM

8.1. Systematic Studies

8.1.1. Threshold Enhancement

It is important to examine the relative size of the leading and subleading terms in (7.1). If the subleading terms were comparable in size to the leading ones, it would make little sense to resum the logarithms in $(1-z)$, which we have discussed so far, or to construct approximate fixed-order formulas at NNLO which capture only the effects of the singular terms. The naive expectation would be that the singular terms are dominant only when $\tau = M^2/s \to 1$, since then the integrand in (4.6) is needed only in the $z \to 1$ limit and the less singular terms are clearly subleading. However, the most interesting region for phenomenology ranges from $M \sim 2m_t$ to around 1 TeV at the Tevatron and up to several TeV at the LHC, which corresponds to $\tau < 0.3$ (at most). For the leading-order singular terms to be dominant, it is necessary that the parton luminosity functions $ff_{ij}(\tau/z, \mu)$ fall off sufficiently fast for $\tau/z \to 1$ that only the largest values of z give significant contributions to the integrand, an effect we already referred to as dynamical threshold enhancement. This is illustrated in Figure 8.1, which shows the invariant mass distributions at the Tevatron and LHC predicted using different approximations in fixed-order perturbation theory. The difference between the boundaries of the dark NLO bands and the dashed lines is due to the small contributions from the subleading terms $d\sigma^{\text{NLO,subleading}}$ in (7.1). The fact that, even at these relatively low values of M, the leading terms provide a very good approximation to the full NLO result provides a strong motivation to study within our formalism higher-order corrections to integrated quantities such as the total cross section and FB asymmetry, which receive their dominant contributions from low values of the invariant mass.

We will always do the matching onto fixed-order results as in (7.1) and (7.2), when the goal is to provide quantitative phenomenological predictions. Such a matching is straightforward for integrated quantities such as the total cross section and FB asymmetry, since the NLO results in fixed order are available in analytic form. For the invariant mass distribution, on the other hand, the fixed-order NLO results are available in the form of Monte Carlo programs such as MCFM [140]. This makes it difficult to get accurate values of the top-quark pair invariant mass spectrum at high M, where the differential cross section is small, and makes it impractical to calculate the spectrum with the scale choice $\mu_f = M$ used in the next section, since doing so would require to run the program separately at each point in μ_f. (Monte Carlo programs generate the invariant mass spectrum by first producing a set of events for a given μ_f, and then grouping them into bins in M). When we

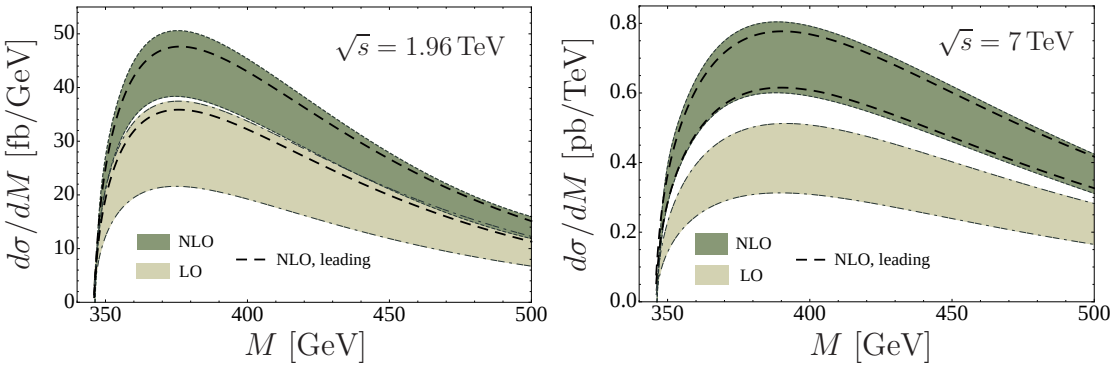

Figure 8.1.: Fixed-order predictions for the invariant mass spectrum at LO (light bands) and NLO (dark bands) for the Tevatron (left) and LHC (right). We use MSTW2008NLO PDFs [139] with $\alpha_s(M_Z) = 0.120$. The width of the bands reflects the uncertainty of the spectrum under variations of the matching and factorization scales. The dashed lines refer to the leading terms in the threshold expansion.

study certain aspects of the invariant mass distribution in the next sections, we will take the NLO correction in the threshold approximation, so that (7.1) and (7.2) are evaluated with $d\sigma^{\text{NLO}} \to d\sigma^{\text{NLO, leading}}$. This is still a good approximation to the full NLO result, and allows us to study the qualitative behavior of the invariant mass spectrum with $\mu_f = M$ over a large range of M, as well as PDF uncertainties, in a simple way. For this purpose, we also define an NNLO approximation which includes only the singular terms at threshold in the NLO correction:

$$d\sigma^{\text{NNLO, leading}} = d\sigma^{\text{NLO, leading}} + d\sigma^{(2),\text{ approx}}\,. \tag{8.1}$$

8.1.2. Scale Setting

The invariant mass distribution is obtained by integrating the doubly differential rate over the range $-1 < \cos\theta < 1$. The resummed results (4.94) depend on the three scales μ_s, μ_h, and μ_f, and to give a numerical result we must first specify how to choose them. In the similar cases of Drell-Yan [106] and Higgs production [107, 108] at threshold, the soft and hard scales were chosen by examining the contributions of the one-loop soft and hard matching coefficients as functions of the scales μ_s and μ_h, and then choosing default values of the scales in such a way as to minimize these corrections. We shall use this approach here, a small complication being the extra dependence on the kinematic variable $\cos\theta$ in (4.94). For the analysis in this section we use the default set of MSTW2008NNLO PDFs [139] and take $\alpha_s(M_z) = 0.117$ with three-loop running.

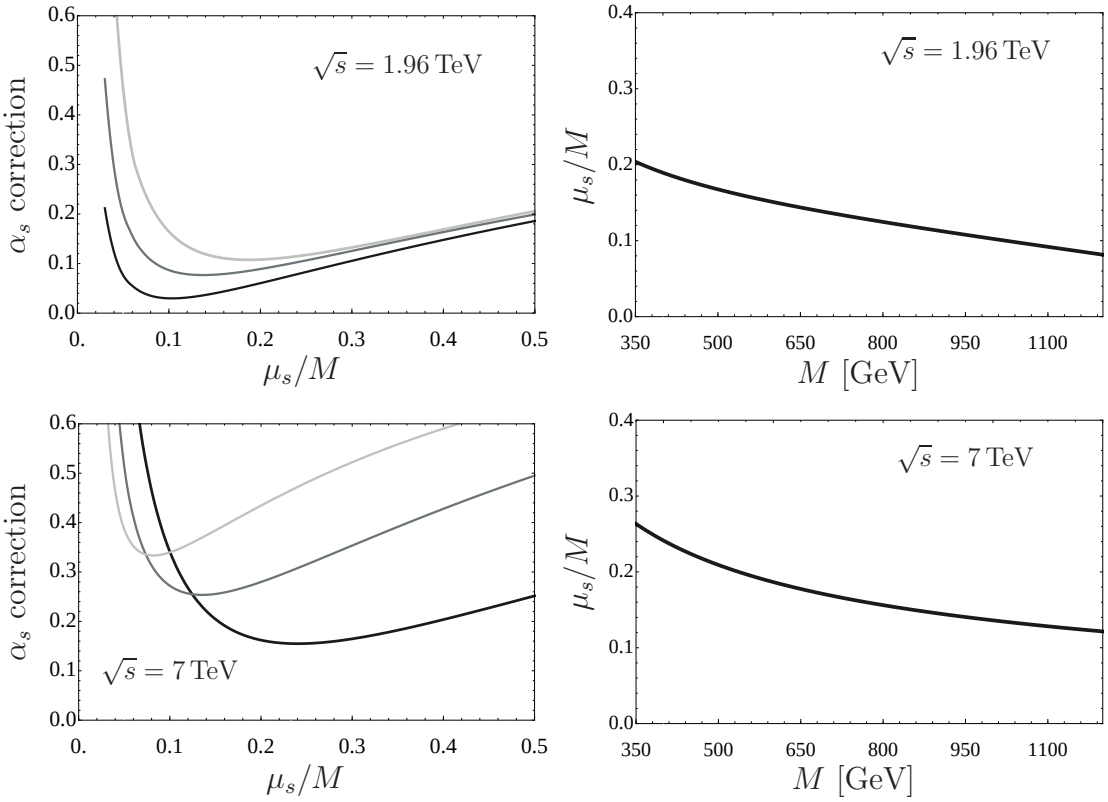

Figure 8.2.: Top left: Ratio of the one-loop correction from the soft function over the leading-order result for top pair production at the Tevatron, as a function of μ_s/M, for $M = 400\,\text{GeV}$ (dark), $M = 700\,\text{GeV}$ (medium), and $M = 1000\,\text{GeV}$ (light). Top right: The scale μ_s/M determined by the point where the one-loop correction from the soft function is minimal, as a function of the invariant mass M. Bottom: Analogous plots for the LHC, but with $M = 400\,\text{GeV}$ (dark), $M = 1000\,\text{GeV}$ (medium), and $M = 2000\,\text{GeV}$ (light).

Determination of the Matching and Factorization Scales

We begin by examining the corrections from the NLO soft matching coefficient as a function of μ_s. We isolate this contribution by picking out the piece of the NNLL approximation to (4.94) proportional to $\widetilde{\boldsymbol{s}}^{(1)}$, evaluating the differential cross section using only this piece, and dividing the result by that at NLL, for the choice $\mu_f = \mu_h = M$. The results are shown in the left-hand plots of Figure 8.2 for the Tevatron and the LHC with $\sqrt{s} = 7\,\text{TeV}$, for several different values of M. We note that the corrections are larger at the LHC than at the Tevatron, especially at high values of M. This behavior appears to be a property of the gluon channel, which gives the dominant contribution at the LHC. The correction is generally at its minimum between $M/4$ and $M/10$, and moves to lower values of μ_s at higher values of M. The exact position of the minimum as a function of M is shown in the right-hand plots of Figure 8.2. To a good approximation, the numerical results for μ_s

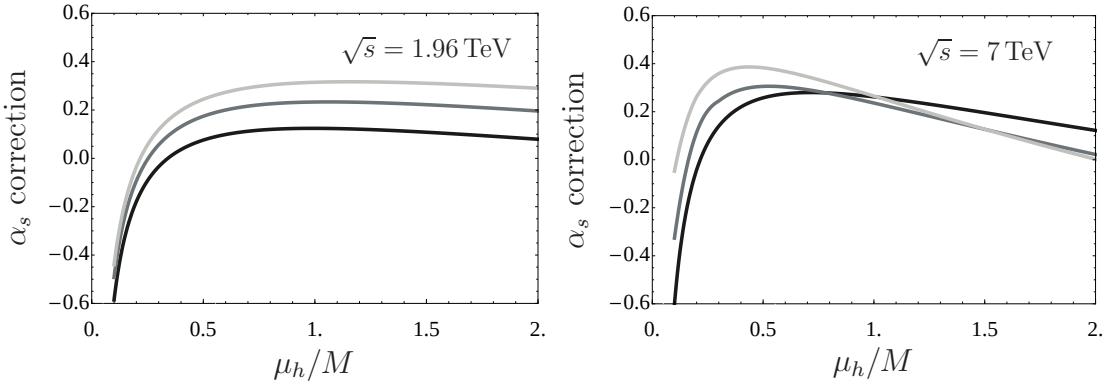

Figure 8.3.: Left: Ratio of the one-loop correction the from hard function over the leading-order result at the Tevatron, as a function of μ_h/M, at $M = 400\,\text{GeV}$ (dark), $M = 700\,\text{GeV}$ (medium), and $M = 1000\,\text{GeV}$ (light). Right: Analogous plot for the LHC, with $M = 400\,\text{GeV}$ (dark), $M = 1000\,\text{GeV}$ (medium), and $M = 2000\,\text{GeV}$ (light).

can be fitted by the function

$$\mu_s^{\text{def}} = \frac{M(1-\tau)}{(a + b\,\tau^{1/4})^c} \tag{8.2}$$

with $a = -33$, $b = 150$, and $c = 0.46$ for the Tevatron, and $a = -1.3$, $b = 23$, and $c = 0.98$ for the LHC at $\sqrt{s} = 7\,\text{TeV}$. Finally for the LHC with $\sqrt{s} = 10,\, 14\,\text{TeV}$, we use $a = 0.95$, $b = 6.7$, and $c = 1.6$.

The most appropriate choice of the hard scale μ_h is not immediately apparent, since the invariant mass spectrum depends on the two hard scales m_t and M. As a guide to an appropriate choice we look at the size of the correction from the hard matching function for different choices of μ_h. We show in Figure 8.3 the correction obtained by isolating the contribution of $\boldsymbol{H}^{(1)}$ to the differential cross section at NNLL, and dividing it by the NLL result, for the choice $\mu_f = M$ and μ_s determined according to (8.2). We see that at lower values of μ_h closer to m_t the correction typically gets smaller and can even become negative. In this lower range of μ_h, however, the correction depends very strongly on the scale. The results are more stable in the range $M/2 < \mu_h < 2M$, where the correction is generally below 30% at the Tevatron and between $20-40\%$ at the LHC. In what follows we shall choose $\mu_h = M$ by default, in order to avoid the instability at lower μ_h. In the case of Higgs production, a negative hard scale squared $\mu_h^2 \sim -m_H^2 - i\epsilon$ was chosen to minimize the logarithms arising from time-like kinematics [107, 108]. In the $t\bar{t}$ case, however, there are both time-like and space-like momentum invariants, and it is not straightforward to tell which point in the complex plane should be chosen to minimize the logarithms. We have thus investigated the choice $\mu_h^2 = M^2 e^{i\phi_h}$ with ϕ_h varied between $-\pi$ and π. The results show that at the LHC, the correction is smallest for $\phi_h \sim -\pi$, and is about 10% compared to 20% at $\phi_h \sim 0$. At the Tevatron, however, the minimal correction is obtained for values close to $\phi_h \sim 0$. In view of this, and since the corrections are in any case not

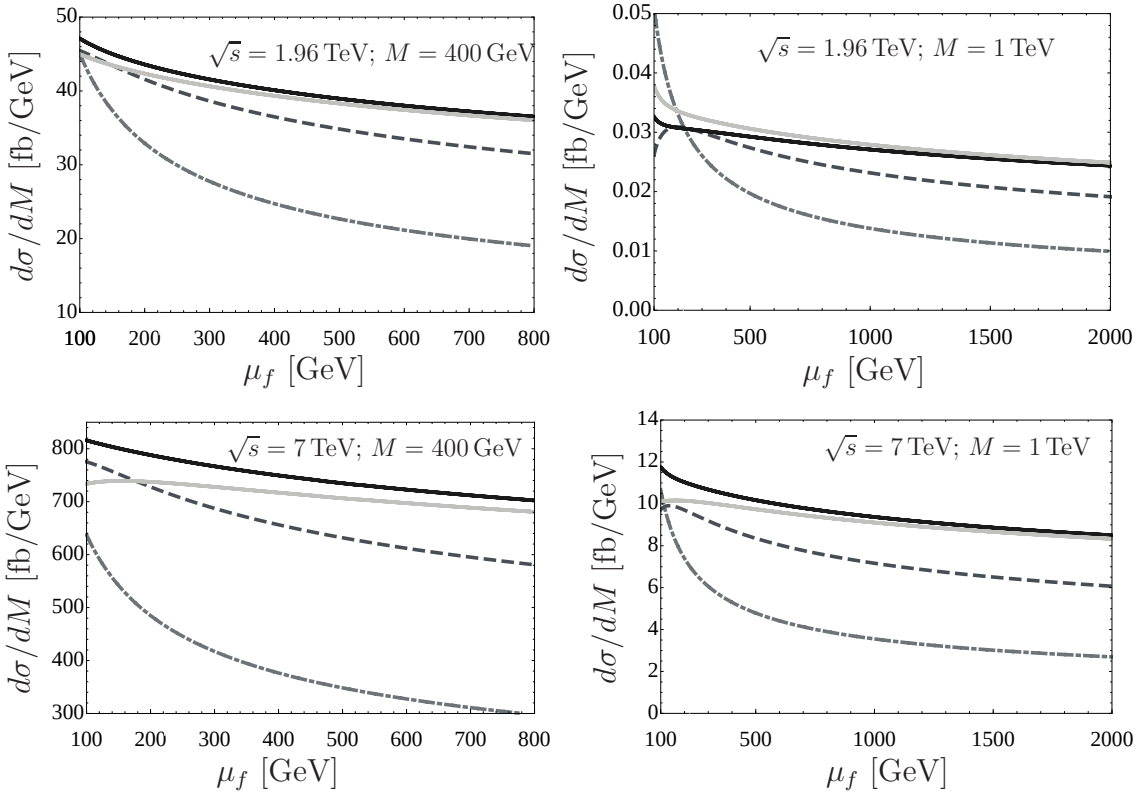

Figure 8.4.: Dependence of $d\sigma/dM$ at the Tevatron (left) and LHC (right) on the scale μ_f in fixed-order perturbation theory. The dashed-dotted lines show $d\sigma^{\text{LO}}$, the dashed lines $d\sigma^{\text{NLO, leading}}$, and the dark (light) solid lines the approximate threshold expansion (8.1) at NNLO in scheme A (scheme B).

very large, we will not go into this complication in our numerical analyses below.

Finally, we must choose a default value for the factorization scale μ_f in both the resummed and fixed-order results. To do so, we study the behavior of the cross sections as a function of this scale. For the fixed-order results, the invariant mass spectrum as a function of μ_f at $M = 400\,\text{GeV}$ and $M = 1\,\text{TeV}$ is shown in Figure 8.4. For the moment we do *not* match the results onto fixed-order perturbation theory at NLO, using instead the threshold expansion $d\sigma^{\text{NLO, leading}}$ and $d\sigma^{\text{NNLO, leading}}$. As a result, our predictions are not strictly independent of the scale μ_f, but a slight scale dependence enters via subleading terms in $(1-z)$. At $M = 400\,\text{GeV}$ the approximate NNLO formulas differ from each other less at $\mu_f \sim 400\,\text{GeV}$ than at $\mu_f \sim m_t$. The same is true at $M = 1\,\text{TeV}$, but in this case the results become very unstable at $\mu_f \sim m_t$. It therefore seems more appropriate to make the choice $\mu_f \sim M$ when studying the invariant mass spectrum. The resummed results at $M = 400\,\text{GeV}$ and $M = 1\,\text{TeV}$ as a function of μ_f, with $\mu_h = M$ and μ_s as in (8.2), are shown in the upper two plots of Figure 8.5, for the case of the Tevatron (plots for the LHC would look very similar). Again, the results at $\mu_f \sim M$ are more stable than at $\mu_f \sim m_t$,

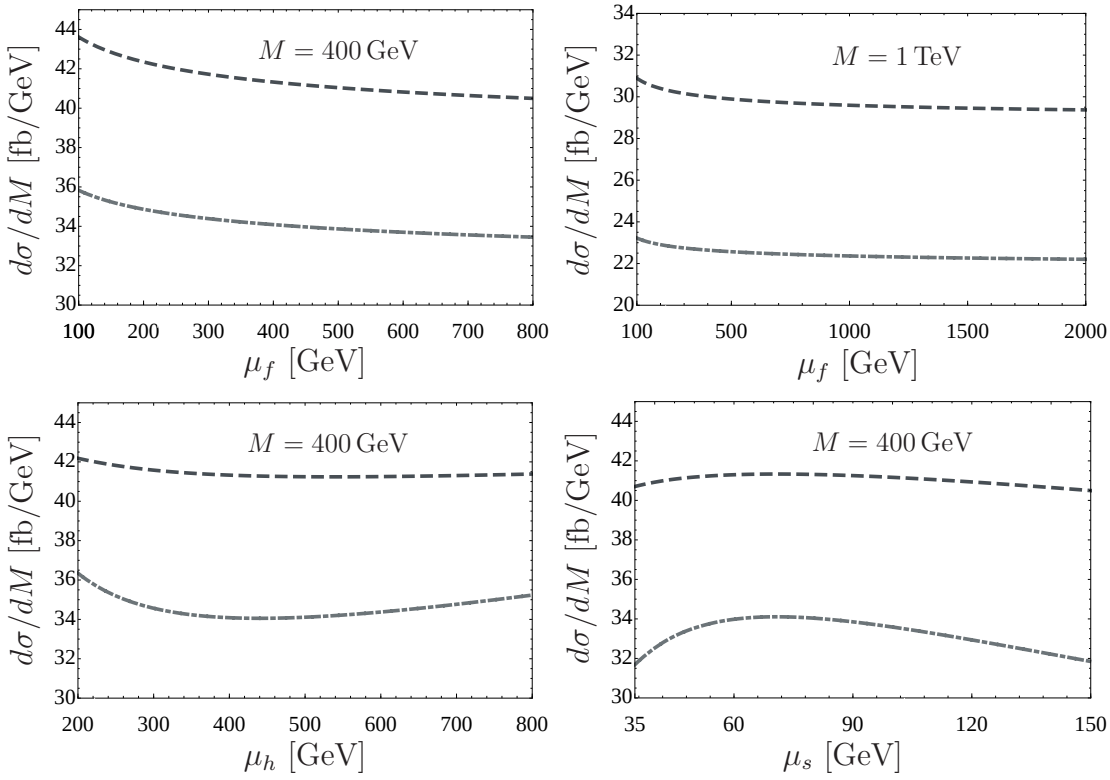

Figure 8.5.: Dependence of $d\sigma/dM$ at the Tevatron on the scales μ_h, μ_s, and μ_f in resummed perturbation theory. The default choices are $\mu_h = \mu_f = M$, and μ_s according to (8.2). The dashed-dotted lines refer to NLL, the dashed to NNLL.

although compared to the fixed-order results the difference is less pronounced. We will thus make the choice $\mu_f = M$ by default in the resummed result.

Having chosen default values for the scales, we now discuss in more detail the behavior of the fixed-order and resummed predictions for the invariant mass distribution. We have already seen how the results depend on the scale μ_f. In the lower two plots of Figure 8.5, we show the dependence of the resummed results at $M = 400\,\text{GeV}$ on the scales μ_h and μ_s. The results as a function of these two scales are significantly more stable at NNLL than at NLL.

Convergence of the Perturbation Series

An interesting difference between the fixed-order and resummed results is that the perturbative uncertainties and the size of the higher-order corrections in the resummed results depend much less on the value of M. This is seen in Figure 8.6, where we show the K factors and uncertainties in the invariant mass spectrum as a function of M, comparing fixed-order results with the resummed ones. The bands in fixed order reflect the uncertainty associated with varying the factorization scale around its default value $\mu_f = M$ by

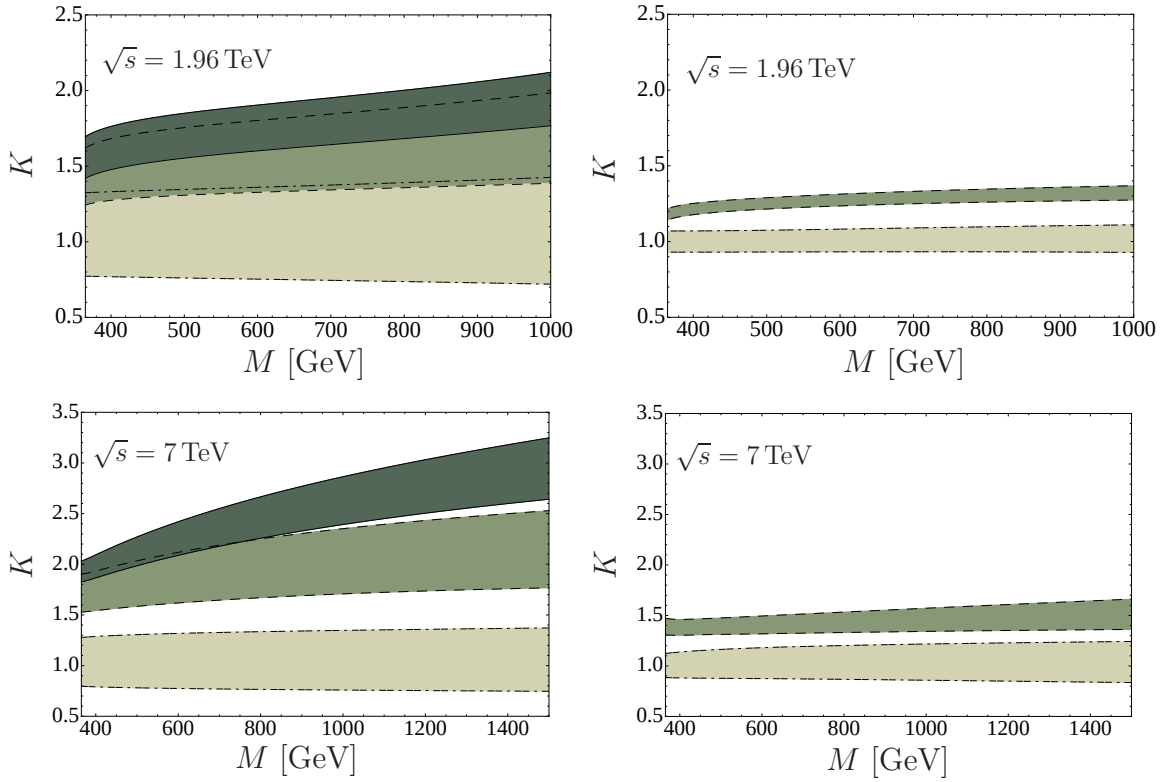

Figure 8.6.: K factors $(d\sigma/dM)/(d\sigma^{\text{LO, def}}/dM)$ in fixed-order perturbation theory (left) and $(d\sigma/dM)/(d\sigma^{\text{NLL, def}}/dM)$ in resummed perturbation theory (right), for the Tevatron (top) and LHC (bottom). The light bands in the fixed-order (resummed) results show LO (NLL) results, the medium bands show NLO leading (NNLL) results, and the dark bands in the fixed-order results refer to the approximate threshold expansion (8.1) at NNLO in scheme A. The width of the bands reflects the uncertainties associated with variations of the scales, as described in the text.

a factor of two. Here and in the following figures, for the approximate NNLO formulas we show results only in scheme A; those in scheme B look very similar. We apply SUES to make the bands in resummed perturbation theory at each point in M. At the Tevatron, the K factors in resummed perturbation theory have smaller uncertainties and depend only weakly on M, compared to fixed order. The same is true at the LHC, although at small M the approximate NNLO results and the resummed ones have comparable uncertainties.

To illustrate more precisely the quantitative differences between the various perturbative approximations to the invariant mass spectrum, we show in Table 8.1 the exact numerical values of the spectrum at the points $M = 400\,\text{GeV}$ and $M = 1000\,\text{GeV}$. We have assigned uncertainties associated with variations of the various scales by factors of two up and down from their default values. To obtain a total scale uncertainty for the resummed results, we have added the uncertainties associated with variations of μ_h, μ_s, and μ_f in

Tevatron	$M = 400\,\text{GeV}$ [fb/GeV]	$M = 1\,\text{TeV}$ [fb/GeV]
NLL	$34.1^{+2.4+1.7}_{-2.4-1.2}$	$(22.4^{+2.5+1.7}_{-1.6-1.3}) \cdot 10^{-3}$
NLO, leading	$36.5^{+5.1+1.9}_{-5.0-1.4}$	$(23.2^{+4.2+1.9}_{-4.0-1.4}) \cdot 10^{-3}$
NNLL	$41.3^{+1.3+1.9}_{-1.2-1.4}$	$(29.6^{+1.0+2.2}_{-1.1-1.6}) \cdot 10^{-3}$
NNLO, leading (scheme A)	$40.1^{+3.5+1.9}_{-3.6-1.4}$	$(27.1^{+2.2+2.1}_{-2.7-1.6}) \cdot 10^{-3}$
NNLO, leading (scheme B)	$39.3^{+3.0+1.9}_{-3.3-1.4}$	$(27.9^{+2.7+2.2}_{-3.0-1.6}) \cdot 10^{-3}$
LHC ($\sqrt{s} = 7\,\text{TeV}$)	$M = 400\,\text{GeV}$ [fb/GeV]	$M = 1\,\text{TeV}$ [fb/GeV]
NLL	558^{+78+20}_{-68-21}	$7.43^{+1.61+0.69}_{-1.07-0.70}$
NLO, leading	656^{+72+26}_{-76-27}	$7.17^{+1.19+0.69}_{-1.10-0.69}$
NNLL	775^{+39+30}_{-47-31}	$10.83^{+0.84+1.01}_{-0.87-1.03}$
NNLO, leading (scheme A)	750^{+38+29}_{-47-30}	$9.38^{+0.82+0.90}_{-0.87-0.90}$
NNLO, leading (scheme B)	717^{+20+28}_{-36-29}	$9.11^{+0.63+0.86}_{-0.78-0.86}$

Table 8.1.: Values for $d\sigma/dM$ for $M = 400\,\text{GeV}$ and $M = 1\,\text{TeV}$ at the Tevatron and the LHC at $\sqrt{s} = 7\,\text{TeV}$. The first error refers to perturbative scale uncertainties, the second to PDF uncertainties, see text for a detailed explanation.

quadrature. We have also included uncertainties associated with the PDFs, by using the set of MSTW2008NNLO PDFs from at 90% confidence level (CL). The perturbative scale uncertainties are smaller or comparable than those from the PDFs only once the NNLL or approximate NNLO corrections are taken into account. For the practical reasons explained earlier, we have not matched the higher-order results with the fixed-order NLO results. However, the threshold approximation works rather well. For reference, at the Tevatron the exact NLO results are $(38.6^{+5.1}_{-5.2})\,\text{fb/GeV}$ for $M = 400\,\text{GeV}$ and $(24.8^{+4.5}_{-4.8}) \cdot 10^{-3}\,\text{fb/GeV}$ for $M = 1000\,\text{GeV}$, while at the LHC they are $(654^{+98}_{-89})\,\text{fb/GeV}$ for $M = 400\,\text{GeV}$ and $(6.84^{+1.40}_{-1.11})\,\text{fb/GeV}$ for $M = 1000\,\text{GeV}$. The deviations from the leading NLO terms shown in the second line in both parts of the table are smaller than 7% for the Tevatron and 5% for the LHC.

8.2. Invariant Mass Distributions

After these systematic studies, we now present our final results for the $t\bar{t}$ invariant mass distributions at the Tevatron and LHC. Here and below, we will use different sets of PDFs, as appropriate for the order of the perturbative approximation employed as advertised in Table 7.1.

We begin by studying in more detail the invariant mass spectrum at relatively low values of M, where it is the largest, in fixed-order and resummed perturbation theory. Contrary to the previous section, we now match the results in resummed perturbation theory with the exact fixed-order results at NLO using the MCFM program, according to (7.1). In

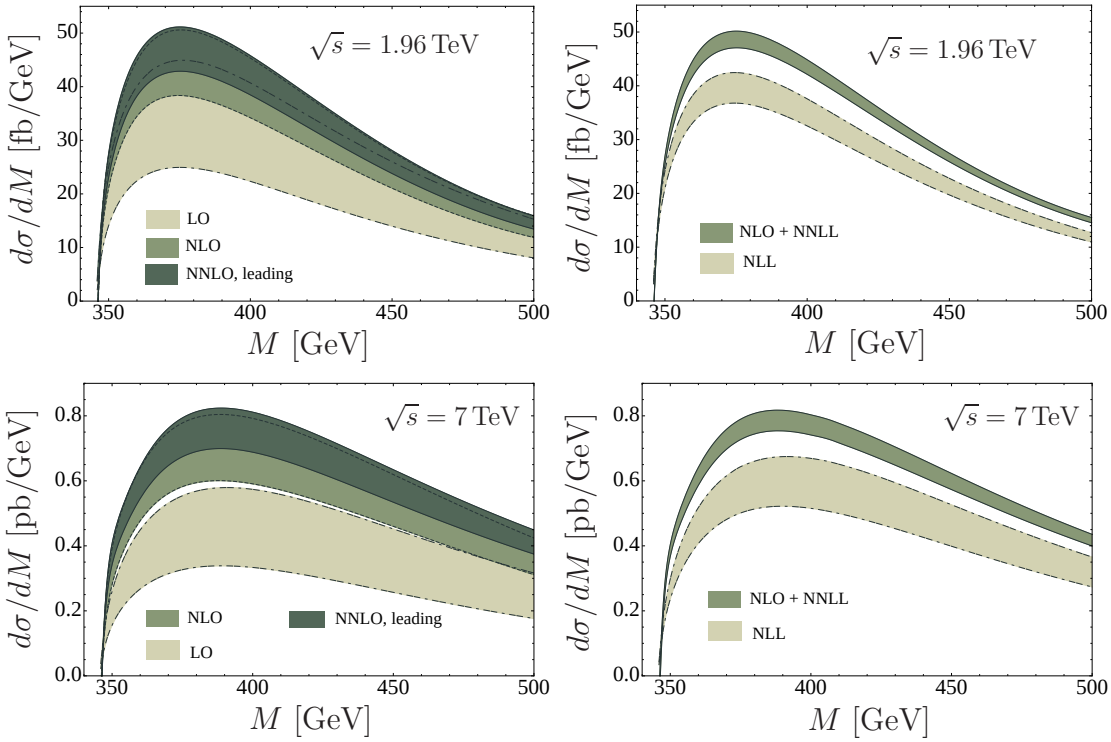

Figure 8.7.: Left: Fixed-order predictions for the invariant mass spectrum at LO (light), NLO (darker), and approximate NNLO (dark bands) for the Tevatron (top) and LHC (bottom). Right: Corresponding predictions at NLL (light) and NLO+NNLL (darker bands) in resummed perturbation theory. The width of the bands reflects the uncertainty of the spectrum under variations of the matching and factorization scales, as explained in the text.

this way we obtain state-of-the-art predictions, which include everything known about the perturbative series for the spectrum. Our results are shown in Figure 8.7. The bands reflect uncertainties in scale variations according to the same procedure explained in the previous paragraph, but in this case with $\mu_f = 400\,\text{GeV}$ by default. For the range of M in the plot, this choice is very close to our preferred scheme $\mu_f = M$, but allows for a simple matching with the fixed-order results from MCFM. One sees that the perturbative uncertainty estimated by scale variations is by far the smallest at NLO+NNLL order.

We now consider the region of higher invariant masses, for which the dominance of the threshold terms is even more pronounced, as indicated by the convergence of the dark bands and dashed lines in Figure 8.1 toward higher M values. Figure 8.8 shows our results for the Tevatron, both in fixed-order and resummed perturbation theory. Figure 8.9 shows the corresponding results for the LHC. It is impractical to match onto fixed-order results obtained using the MCFM program in this case; however, the differences compared with the shown curves are so small that they would hardly be visible on the scales of the plots. The upper two plots show K factors, which are defined as the ratio of the cross section

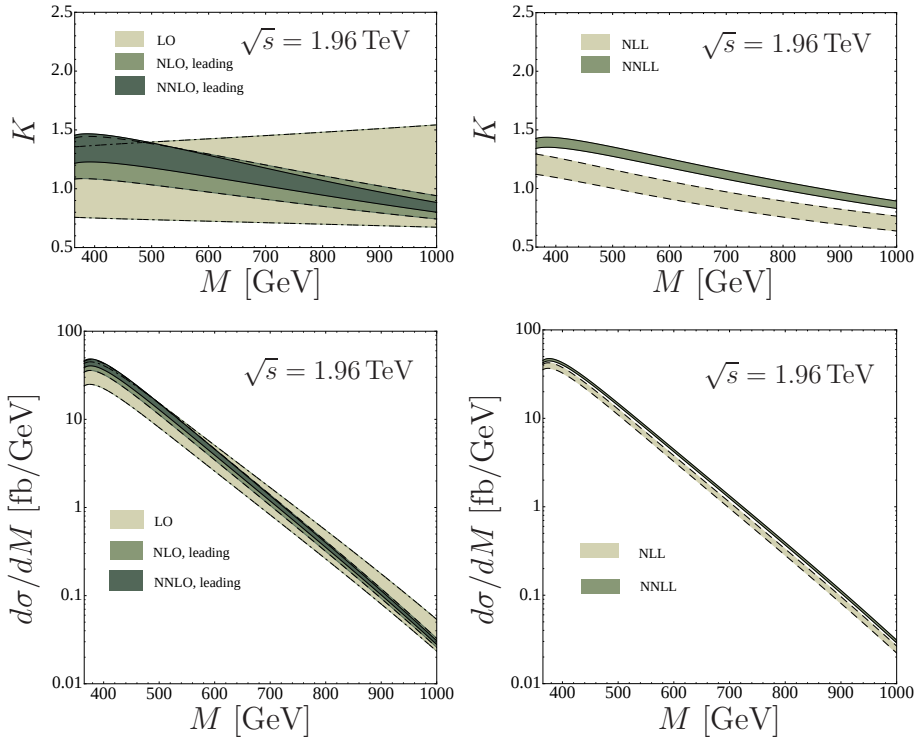

Figure 8.8.: Left: Fixed-order predictions for the K factor and invariant mass spectrum at LO (light), NLO (darker), and approximate NNLO (dark bands) for the Tevatron. Right: Corresponding predictions at NLL (light) and NLO+NNLL (darker bands) in resummed perturbation theory. The width of the bands reflects the uncertainty of the spectrum under variations of the matching and factorization scales, as explained in the text.

to the default lowest-order prediction $d\sigma^{\text{LO,def}}/dM$. Contrary to Figure 8.6, we now use the same normalization in both fixed-order and resummed perturbation theory, so that the two spectra can more readily be compared to each other. The lower plots show the corresponding spectra directly. We observe similar behavior as in the low-mass region. The bands obtained in fixed-order perturbation theory become narrower in higher orders and overlap. The bands obtained in resummed perturbation theory are narrower than the corresponding ones at fixed order. The leading-order resummed prediction is already close to the final result.

The information contained in Figures 8.7–8.9 can be represented differently in terms of the very useful distribution $d\sigma/d\beta_t$, with β_t defined as in (4.4). A simple change of variables yields

$$\frac{d\sigma}{d\beta_t} = \frac{2m_t\beta_t}{(1-\beta_t^2)^{\frac{3}{2}}}\,\frac{d\sigma}{dM}\,. \tag{8.3}$$

The resulting spectra for the Tevatron and LHC, obtained using RG-improved perturbation theory, are shown in Figure 8.10. As before, the distributions are normalized such that

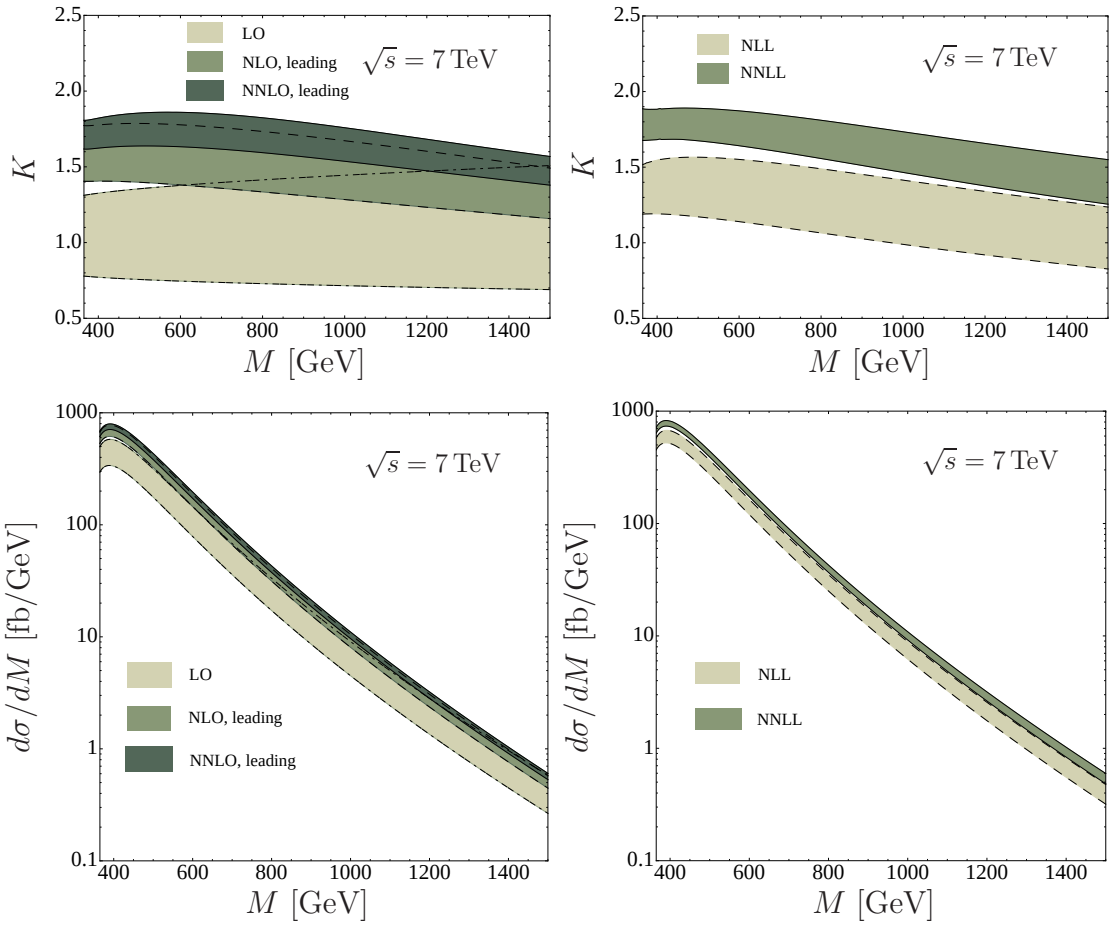

Figure 8.9.: Left: Fixed-order predictions for the K factor and invariant mass spectrum at LO (light), NLO (darker), and approximate NNLO (dark bands) for the LHC. Right: Corresponding predictions at NLL (light) and NLO+NNLL (darker bands) in resummed perturbation theory. The width of the bands reflects the uncertainty of the spectrum under variations of the matching and factorization scales, as explained in the text.

the area under the curves corresponds to the total cross section. Recall that the physical meaning of the variable β_t is that of the 3-velocity of the top quarks in the $t\bar{t}$ rest frame. The distributions show that the dominant contributions to the cross section arise from the region of relativistic top quarks, with velocities of order 0.4–0.8 at the Tevatron and 0.5–0.9 at the LHC. We will come back to the significance of this observation in the Section 8.3.1.

In Figure 8.11, we compare our RG-improved prediction for the invariant mass spectrum to a measurement of the CDF collaboration obtained using the "lepton + jets" decay mode of the top quark [77]. We observe an overall good agreement between our prediction and the measurement, especially for higher values of M. Apparently, there is no evidence of non-standard resonances in the spectrum. The only small deviation from our prediction

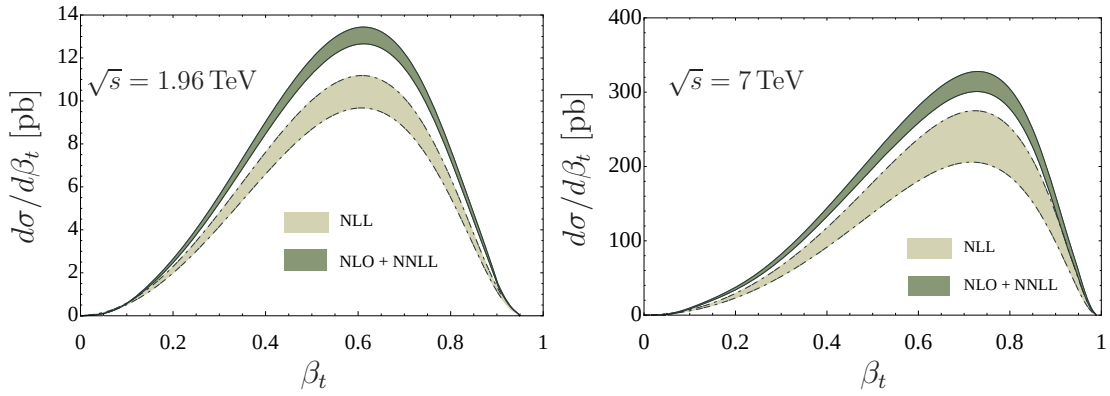

Figure 8.10.: Distributions $d\sigma/d\beta_t$ at the Tevatron (left) and LHC (right).

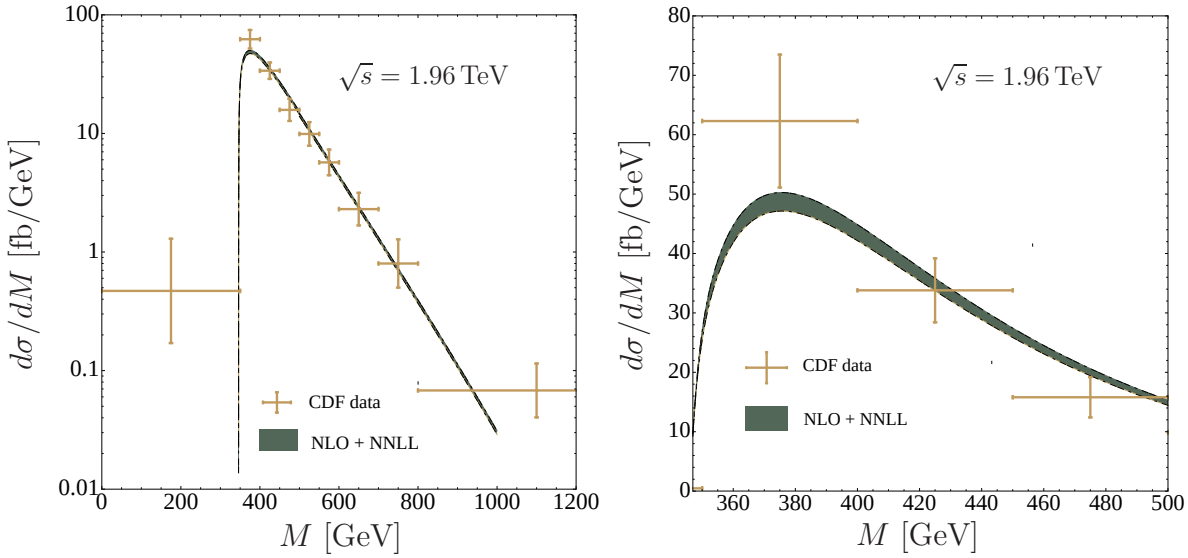

Figure 8.11.: Comparison of the RG-improved predictions for the invariant mass spectrum with CDF data [77]. The value $m_t = 173.1\,\text{GeV}$ has been used. No fit to the data has been performed.

concerns the peak region of the distribution, shown in more details in the right plot. This deviation has also been observed in [77], where a Monte Carlo study of the SM expectation has been performed.

8.3. Total Cross Section

The total cross section is obtained in our approach by integrating numerically the doubly differential cross section in the ranges $-1 < \cos\theta < 1$ and $2m_t < M < \sqrt{s}$. In this case it is a simple matter to match onto NLO in fixed-order perturbation theory, using the analytic results of [11]. To do this, however, we can no longer correlate the factorization scale μ_f with M, as we did when studying the invariant mass spectrum. Instead, we should resort to representative average values of M, which characterize the spectrum in the region yielding sizable contributions to the total cross section. One possibility is to take the location of the peak in the $d\sigma/dM$ distributions, which is $M_{\text{peak}} \approx 375\,\text{GeV}$ for the Tevatron and $M_{\text{peak}} \approx 388\,\text{GeV}$ for the LHC (see Figure 8.7). Another possibility is to take the average value $\langle M \rangle$ of the distributions, for which we find $\langle M \rangle \approx 445\,\text{GeV}$ for the Tevatron and $\langle M \rangle \approx 496\,\text{GeV}$ for the LHC. As previously, we take the fixed value $\mu_f = 400\,\text{GeV}$ as our default choice. On the other hand, we are still free to choose the hard and soft scales as we have done so far and match with the fixed-order result as shown in (7.1). We display in Table 8.2 the central values and scale uncertainties for the total cross section obtained using this procedure. The results in resummed perturbation theory use $\mu_h = M$ and μ_s chosen according to (8.2) by default, and the uncertainties are obtained through SUES. The perturbative uncertainties in the fixed-order results are obtained by varying the factorization scale up and down by a factor of two from its default value. In addition to the perturbative uncertainties, we also list the PDF uncertainties obtained by evaluating the cross section with the appropriate set of MSTW2008 PDFs at 90% CL. Again we use PDFs according to Table 7.1. In the following tables, these different classes of predictions are separated by horizontal lines.

A few comments are in order concerning the results shown in the table. At NLO the cross sections $\sigma_{\text{NLO, leading}}$ evaluated using only the leading singular terms from the threshold expansion reproduce between 95% (for the Tevatron) to almost 100% (for the LHC) of the exact fixed-order result at the default values of the factorization scale. The subleading terms in $(1 - z)$, obtained by integrating $d\sigma_{\text{NLO, subleading}}$, contribute the remaining few percent. In other words, the singular terms capture about 85% of the NLO correction at the Tevatron and practically 100% of it at the LHC. We cannot say whether the threshold expansion works so well also at higher orders in perturbation theory, although this does not seem unreasonable. Our best prediction is obtained by matching the fixed-order result with the resummed result at NLO+NNLL accuracy and is highlight in gray. The effect of resummation is roughly a 10–15% enhancement over the fixed-order NLO result. A more important effect is that the resummation stabilizes the scale dependence significantly. Concerning the approximate NNLO schemes, the results from scheme A are noticeably higher than those from scheme B, but these differences are well inside the quoted errors.

	Tevatron	LHC (7 TeV)	LHC (10 TeV)	LHC (14 TeV)
σ_{LO}	$4.49^{+1.71+0.24}_{-1.15-0.19}$	84^{+29+4}_{-20-5}	217^{+70+10}_{-49-11}	$495^{+148+19}_{-107-24}$
σ_{NLL}	$5.07^{+0.37+0.28}_{-0.36-0.18}$	112^{+18+5}_{-14-5}	276^{+47+10}_{-37-11}	$598^{+108+19}_{-94\ -19}$
$\sigma_{\text{NLO, leading}}$	$5.49^{+0.78+0.31}_{-0.78-0.20}$	134^{+16+7}_{-17-7}	341^{+34+14}_{-38-14}	761^{+64+25}_{-75-26}
σ_{NLO}	$5.79^{+0.79+0.33}_{-0.80-0.22}$	133^{+21+7}_{-19-7}	341^{+50+14}_{-46-15}	$761^{+105+26}_{-101-27}$
$\sigma_{\text{NLO+NNLL}}$	$6.30^{+0.19+0.31}_{-0.19-0.23}$	149^{+7+8}_{-7-8}	373^{+17+16}_{-15-16}	821^{+40+24}_{-42-31}
$\sigma_{\text{NNLO, approx}}$ (scheme A)	$6.14^{+0.49+0.31}_{-0.53-0.23}$	146^{+13+8}_{-12-8}	369^{+34+16}_{-30-16}	821^{+71+27}_{-65-29}
$\sigma_{\text{NNLO, approx}}$ (scheme B)	$6.05^{+0.43+0.31}_{-0.50-0.23}$	139^{+9+7}_{-9-7}	349^{+23+15}_{-23-15}	773^{+47+25}_{-50-27}

Table 8.2.: Results for the total cross section in pb, using the default choice $\mu_f = 400\,\text{GeV}$. The first set of errors refers to perturbative uncertainties associated with scale variations, the second to PDF uncertainties. The most advanced prediction is the NLO+NNLL expansion highlighted in gray.

	Tevatron	LHC (7 TeV)	LHC (10 TeV)	LHC (14 TeV)
σ_{LO}	$6.66^{+2.95+0.34}_{-1.87-0.27}$	122^{+49+6}_{-32-7}	$305^{+112+14}_{-76\ -16}$	$681^{+228+26}_{-159-34}$
σ_{NLL}	$5.20^{+0.40+0.29}_{-0.36-0.19}$	103^{+17+5}_{-14-5}	253^{+44+10}_{-36-10}	$543^{+101+18}_{-88\ -19}$
$\sigma_{\text{NLO, leading}}$	$6.42^{+0.42+0.35}_{-0.76-0.23}$	$152^{+7\ +8}_{-15-8}$	381^{+12+16}_{-32-17}	835^{+18+29}_{-60-30}
σ_{NLO}	$6.72^{+0.36+0.37}_{-0.76-0.24}$	159^{+20+8}_{-21-9}	402^{+49+17}_{-51-18}	$889^{+107+31}_{-106-32}$
$\sigma_{\text{NLO+NNLL}}$	$6.48^{+0.17+0.32}_{-0.21-0.25}$	146^{+7+8}_{-7-8}	368^{+20+19}_{-14-15}	813^{+50+30}_{-36-35}
$\sigma_{\text{NNLO, approx}}$ (scheme A)	$6.72^{+0.45+0.33}_{-0.47-0.24}$	162^{+19+9}_{-14-9}	411^{+49+17}_{-35-20}	$911^{+111+35}_{-77\ -32}$
$\sigma_{\text{NNLO, approx}}$ (scheme B)	$6.55^{+0.32+0.33}_{-0.41-0.24}$	$149^{+10+8}_{-9\ -8}$	377^{+28+16}_{-23-18}	832^{+65+31}_{-50-29}

Table 8.3.: Same as Table 9.1, but with the "educated" scale choice $\mu_f = m_t$.

Since the two schemes differ only by terms proportional to $\delta(1-z)$, this gives an indication of the size of the unknown constant terms.

To some extent, the enhancement effect resulting from the resummation of the leading threshold terms can be mimicked using fixed-order results evaluated at a significantly lower factorization and renormalization scale μ_f. Such an "educated" scale choice, which is often adopted in the literature on fixed-order calculations, is $\mu_f = m_t$. Table 8.3 shows the cross-section predictions obtained in this case. The fixed-order results are indeed significantly enhanced with this scale choice. The resummed predictions, on the other hand, do not change much compared to those shown in Table 8.2.

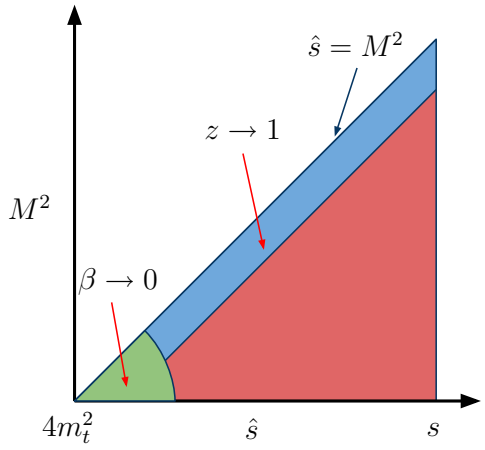

Figure 8.12.: Phase space in the $(\hat{s}, M^2)$ plane. In the blue region along the diagonal threshold singularities arise, and the cross sections receives its main contributions. In the small green region near the origin Coulomb singularities appear and the small-β expansion applies.

8.3.1. Comparison with Previous Calculations

Small-β expansion

The approach pursued here offers an alternative to the direct threshold expansion of the total partonic cross section in the limit $\beta \to 0$, corresponding to $\hat{s} \to 4m_t^2$. In this case not only the phase-space for real gluon emissions shrinks to zero, but in addition the top and anti-top quarks are produced at rest in the partonic center-of-mass frame, which implies that in addition to soft-gluon singularities one encounters Coulomb singularities. The leading terms in the $\beta \to 0$ limit were first calculated at NNLO in [41, 43], and later corrected in [46].

It is important to emphasize that the leading singular contributions to the total cross section arising from the $\beta \to 0$ limit do not coincide with those arising from the limit $z \to 1$, even after integrating over all kinematic variables. The reason is that after convolution with the PDFs there are no truly small scale ratios left in the process (the total center-of-mass energy $\sqrt{s}$ at the Tevatron or LHC are so large that they can be taken to infinity compared with the scale m_t). The large perturbative corrections to the cross section arise dynamically, because of the relatively strong fall-off of the parton luminosities combined with the fact that the partonic cross sections receive their dominant contributions from the region near Born-level kinematics [106,107]. One would then expect that the most accurate account of enhanced perturbative corrections should be the one that captures enhanced contributions in all relevant regions of phase space.

In terms of the variables $\hat{s}$ and M^2, the phase space is given by the triangular region $4m_t^2 \leq M^2 \leq \hat{s} \leq s$, as illustrated in Figure 8.12. The large threshold terms considered in this thesis are located along the diagonal, where the partonic cross sections are largest.

The large corrections arising in the $\beta \to 0$ limit are located near the origin of the diagram, where both $\hat{s}$ and M^2 approach $4m_t^2$. The parton luminosities are largest for small values of $\hat{s}$. It is obvious from the figure, and also by considering the invariant mass distributions shown in Figure 8.7, that the region near the origin gives only a very small contribution to the total cross section. This fact is most clearly demonstrated by the distributions in the variable β_t shown in Figure 8.10, which peak at $\beta_t \approx 0.6$ (Tevatron) and $\beta_t \approx 0.7$ (LHC). The region of small velocity, say below $\beta_t = 0.2$, obviously yields very small contributions to the total cross sections. Since the variable β is always larger than β_t, this conclusion is even more true for the small-β region. On the contrary, the approach pursued in the present work accounts for enhanced perturbative contributions in all regions of phase space giving rise to large contributions to the total cross section. It is completely analogous to threshold (or soft-gluon) resummation for Drell-Yan or Higgs production at fixed value of the lepton pair or Higgs boson mass. Even though one can never be sure how accurately the full NNLO correction to a cross sections is approximated by a subset of calculable terms, we strongly believe that our treatment provides an approximation that captures more physics than that based on the $\beta \to 0$ limit.

Having just argued that the $\beta \to 0$ limit is not of much relevance for the total cross section, it is nevertheless interesting to study how well our predictions fare in this region. Since in our case the top quarks are generically not at rest in their center-of-mass frame, we are not dealing with Coulomb singularities, and hence our approximate prediction for the NNLO corrections to the cross section misses a subset of terms involving potential-gluon exchange. We will now study in more detail which of the singular terms in the $\beta \to 0$ limit can be recovered in our approach. To this end, we write the total cross section in the form

$$\sigma(s, m_t^2) = \frac{\alpha_s^2}{m_t^2} \sum_{ij} \int_{4m_t^2}^{s} \frac{d\hat{s}}{s} \, ff_{ij}\left(\frac{\hat{s}}{s}, \mu\right) f_{ij}\left(\frac{4m_t^2}{\hat{s}}, \mu\right). \tag{8.4}$$

We can obtain an expression for the perturbative functions f_{ij} by integrating (4.6) over all of phase-space, in which case we find

$$\alpha_s^2 \, f_{ij}\left(\frac{4m_t^2}{\hat{s}}, \mu\right) = \frac{8\pi m_t^2}{3\hat{s}} \int_{2m_t}^{\sqrt{\hat{s}}} \frac{dM}{M} \int_{-1}^{1} d\cos\theta \sqrt{1 - \frac{4m_t^2}{M^2}} \, C_{ij}\left(\frac{M^2}{\hat{s}}, M, m_t, \cos\theta, \mu\right). \tag{8.5}$$

We can now evaluate the above formula in the limit $\hat{s} \to 4m_t^2$. Defining expansion coefficients for the functions f_{ij} as

$$f_{ij} = f_{ij}^{(0)} + 4\pi\alpha_s f_{ij}^{(1)} + (4\pi\alpha_s)^2 \left[f_{ij}^{(2,0)} + f_{ij}^{(2,1)} \ln\left(\frac{\mu_f^2}{m_t^2}\right) + f_{ij}^{(2,2)} \ln^2\left(\frac{\mu_f^2}{m_t^2}\right) \right] + \ldots, \tag{8.6}$$

the answer for the scale-independent pieces with $n_h = 1$, $n_l = 5$, and $N = 3$ can be written as

$$f_{q\bar{q}}^{(2,0)} = \frac{1}{(16\pi^2)^2} \frac{\pi\beta}{9} \Big[910.22 \ln^4\beta - 1315.5 \ln^3\beta + 592.29 \ln^2\beta + 452.52 \ln\beta$$

$$- \frac{1}{\beta}\left(140.37\ln^2\beta + 18.339\ln\beta - 72.225\right) + f_{q\bar{q}}^{\text{potential}}\Big] + \ldots,$$

$$f_{gg}^{(2,0)} = \frac{1}{(16\pi^2)^2}\frac{7\pi\beta}{192}\Big[4608.0\ln^4\beta - 1894.9\ln^3\beta - 912.35\ln^2\beta + 2747.5\ln\beta$$

$$+ \frac{1}{\beta}\left(496.30\ln^2\beta + 400.41\ln\beta - 236.22\right) + f_{gg}^{\text{potential}}\Big] + \ldots, \tag{8.7}$$

where the dots refer to $\mathcal{O}(\beta\ln^0\beta)$ terms, which are yet unknown. We have split the answer into the piece recovered from the expansion of our results, which we have written explicitly, and a piece related to NNLO effects from potential gluons, which would be recovered from the small-β expansion of the as yet unknown μ-independent part of the NNLO coefficient C_0 in (6.12). Such potential-gluon contributions were obtained in [46] by using the two-loop calculations of [141–143], and lead to the additional terms

$$f_{q\bar{q}}^{\text{potential}} = \frac{3.6077}{\beta^2} + \frac{1}{\beta}\left(50.445\ln\beta - 68.274\right) + 76.033\ln\beta\,,$$

$$f_{gg}^{\text{potential}} = \frac{68.547}{\beta^2} + \frac{1}{\beta}\left(-79.270\ln\beta + 227.59\right) - 290.76\ln\beta\,. \tag{8.8}$$

The coefficients $f_{ij}^{(2,1)}$ and $f_{ij}^{(2,2)}$ (with $ij = q\bar{q}, gg$) in (8.6) are also recovered from the expansion of our results, up to terms of $\mathcal{O}(\beta^2)$. We have checked that they agree with the results given in [43] when expanded to that order.

It is worth noting that after obtaining the small-β expansion as in (8.7), one can replace the approximated Born prefactors, $\pi\beta/9$ in the $q\bar{q}$ case and $7\pi\beta/192$ in the gg case, with the exact Born-level results. This procedure has been adopted in the recent literature on the small-β expansion [41, 43, 46]. Therefore, we will differentiate the two versions of the small-β expansion: version 1 refers to the version where a complete expansion is carried out as in (8.7), while version 2 refers to the version with the exact Born-level results as prefactors.

We are now ready to compare our results to those obtained using the small-β expansion. We focus first on a comparison at NLO, where the exact answers are known. In the upper portion of Table 8.4, we show the results of the different approximations as well as the exact NLO cross sections. As we have mentioned in the last section, our NLO leading singular terms are always a good approximation to the exact NLO results, at both the Tevatron and the LHC. On the other hand, the small-β expansion version 1 tends to overestimate the cross section at the Tevatron by more than 2 pb. By incorporating the exact Born prefactors (version 2) the small-β expansion works better, but still it overestimates the exact results by about 1 pb. At the LHC, the small-β expansion happens to give results closer to the exact answers. However, as we will now explain, this is a coincidence. In Figure 8.13 we plot the NLO corrections to the cross sections, including the parton luminosities, as functions of β. The black solid curves show the exact results, the red solid curves our PIM_{SCET} leading singular terms, the dotted curves the results obtained using version 2 of

	Tevatron	LHC (7 TeV)	LHC (10 TeV)	LHC (14 TeV)
σ_{NLO}	$5.79^{+0.79+0.33}_{-0.80-0.22}$	133^{+21+7}_{-19-7}	341^{+50+14}_{-46-15}	$761^{+105+26}_{-101-27}$
$\sigma_{\text{NLO, leading}}$	$5.49^{+0.78+0.31}_{-0.78-0.20}$	134^{+16+7}_{-17-7}	341^{+34+14}_{-38-14}	761^{+64+25}_{-75-26}
$\sigma_{\text{NLO, }\beta\text{-exp. v1}}$	$8.22^{+0.54+0.49}_{-0.88-0.33}$	157^{+12+8}_{-16-8}	395^{+24+14}_{-36-15}	877^{+49+29}_{-73-30}
$\sigma_{\text{NLO, }\beta\text{-exp. v2}}$	$6.59^{+0.96+0.38}_{-0.95-0.25}$	151^{+15+8}_{-18-8}	386^{+30+15}_{-39-16}	863^{+49+29}_{-73-30}
$\sigma_{\text{NLO+NNLL}}$	$6.30^{+0.19+0.31}_{-0.19-0.23}$	149^{+7+8}_{-7-8}	373^{+17+16}_{-15-16}	821^{+40+24}_{-42-31}
$\sigma_{\text{NNLO, }\beta\text{-exp. v1}}$	$7.37^{+0.01+0.39}_{-0.20-0.29}$	156^{+2+8}_{-5-8}	$392^{+4\ +16}_{-11-17}$	$865^{+5\ +29}_{-17-30}$
$\sigma_{\text{NNLO, }\beta\text{-exp.+potential v1}}$	$7.30^{+0.01+0.39}_{-0.18-0.28}$	158^{+3+8}_{-6-8}	$398^{+7\ +16}_{-13-17}$	880^{+12+29}_{-22-31}
$\sigma_{\text{NNLO, }\beta\text{-exp. v2}}$	$6.98^{+0.17+0.37}_{-0.40-0.27}$	156^{+2+8}_{-6-8}	$394^{+2\ +16}_{-10-17}$	$871^{+0\ +29}_{-14-31}$
$\sigma_{\text{NNLO, }\beta\text{-exp.+potential v2}}$	$6.95^{+0.16+0.36}_{-0.39-0.26}$	159^{+3+8}_{-7-8}	$401^{+6\ +17}_{-12-17}$	$888^{+7\ +30}_{-19-32}$

Table 8.4.: Results for the total cross section in pb, using the default choice $\mu_f = 400\,\text{GeV}$. Some numbers from Table 8.2 are compared with results obtained from different implementations of the small-β expansion (see text for explanation). The errors have the same meaning as before.

the small-β expansion, and the dashed line refers to the conventional PIM approach. In the small-β region, all the approximations work rather well as expected. With increasing β, the different approximations start to deviate from one another. We observe that, at both the Tevatron and the LHC, our approximations always reproduce the shapes of the exact results quite well, which is not at all achieved by the small-β expansion. The fact that the small-β expansion overestimates the cross section at the Tevatron, where the $q\bar{q}$ channel dominates, is evident from the left plots in Figure 8.13. At the LHC, where the gg channel dominates, the small-β expansion does not reproduce the shapes of the exact results, even though it happens that the integrated cross sections are close to the exact ones due to a coincidental cancellation. However, it is unlikely that a similar cancellation will happen at NNLO.

We next compare our best prediction, NLO+NNLL, to the best prediction obtained using the small-β expansion at NNLO, which is obtained by adding the approximate NNLO corrections derived using the small-β expansion to the exact NLO cross sections. Without knowing the exact expression for the NNLO corrections, it is hard to tell which one is closer to the true answer, but we can study the validity of small-β expansion by investigating the effects of the subleading terms in β that are contained in our results. We have included in Table 8.4 the numerical results for the cross section obtained by evaluating the small-β expansion (8.7) of our approximate NNLO formula, without including the extra potential terms (labeled "β-exp." in the table), and that obtained using this expansion plus the potential terms in (8.8) (labeled "β-exp.+potential"). We notice that the NLO+NNLL resummed results and the small-β expansion differ by about 10–15% at the Tevatron and about 6% at the LHC. On the other hand, the effect of adding the potential-gluon contributions to the small-β expansion, which cannot be reproduced in our approach, is always

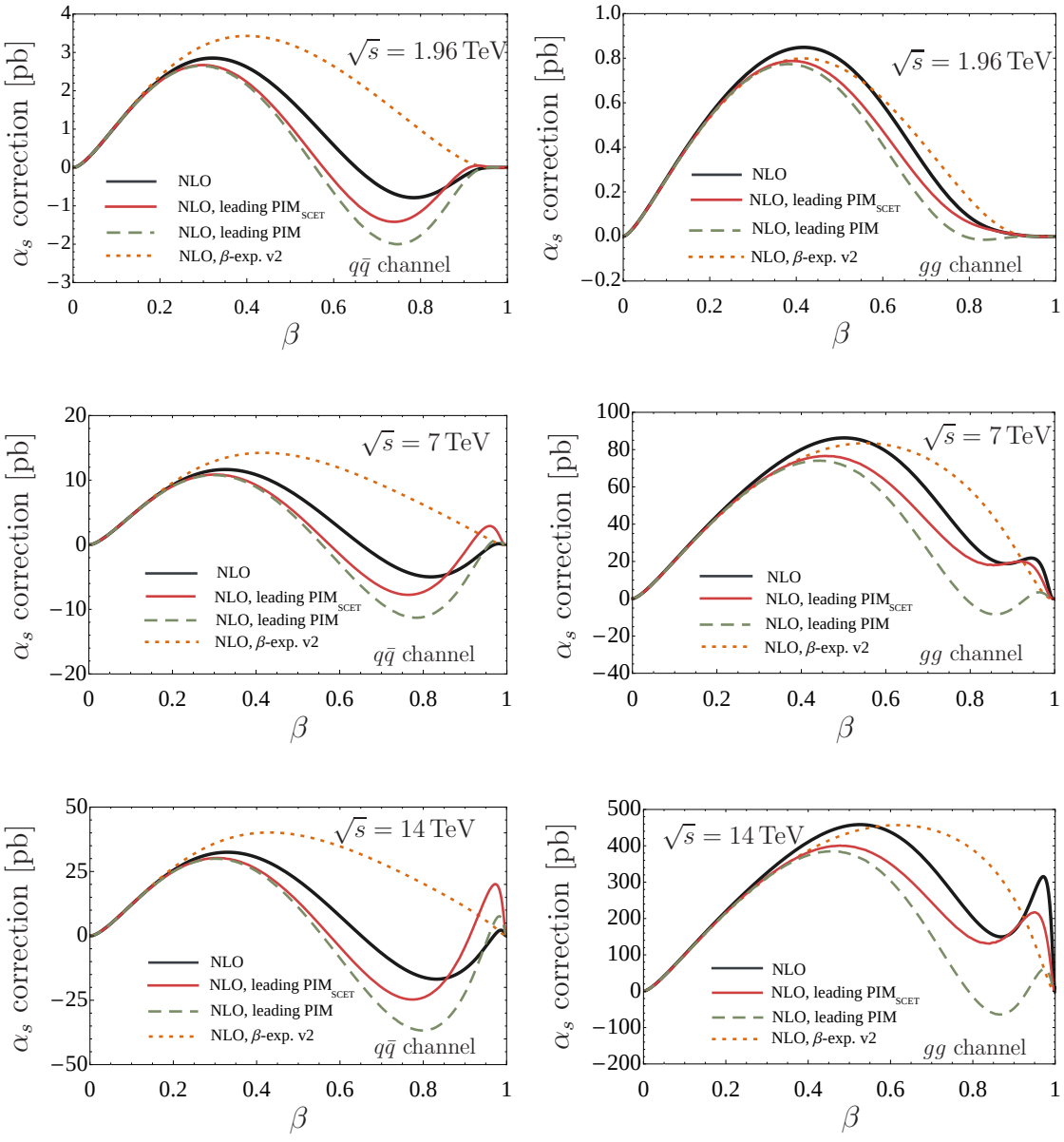

Figure 8.13.: The α_s corrections to $d\sigma/d\beta$ for the different approximations mentioned in the text at the Tevatron and LHC, with $\mu_f = m_t$. The plots on the left side show the $q\bar{q}$ channel, those on the right the gg channel.

smaller than 2%. We conclude that the bulk of the terms that become singular in the $\beta \to 0$ limit are accounted for in our approach. The reverse statement is not true. A resummation based on the $\beta \to 0$ expansion does *not* account for the bulk of the terms that become singular in the $z \to 1$ limit, and our analysis suggests that subleading terms in β are by no means generically small.

9. Studies in 1PI

9.1. Numerical Implementation

We now describe the numerical implementation of our results from Chapter 5.

As pointed out in Section 5.1, there are power-suppressed ambiguities in the choice of the variables $\hat{s}'$, $\hat{t}_1'$ and $\hat{u}_1'$ of the hard and soft functions. Apart from when it appears in the δ-function or plus-distributions, in the perturbative calculation of the hard and soft functions one can set $s_4 = 0$ everywhere and use $\hat{s}' + \hat{t}_1' + \hat{u}_1' = 0$ to rewrite the hard-scattering kernels in many different forms. While these are all formally equivalent in the threshold limit $s_4 \to 0$, they change the functional dependence of the hard-scattering kernels on x_1 and x_2, so the integration in (5.6) gives different results for the pieces multiplying plus-distributions in s_4. Moreover, since one typically trades either x_1 or x_2 in favor of s_4 as an integration variable, another obvious choice is to use $\hat{s}' + \hat{t}_1' + \hat{u}_1' = s_4$ before integration, again leading to numerically different answers which are nonetheless equivalent in the threshold limit $s_4 \to 0$.

Our method of fixing this ambiguity is as follows. First, we enforce $\hat{s}' + \hat{t}_1' + \hat{u}_1' = 0$ in the hard-scattering kernels, and use this to eliminate either $\hat{t}_1'$ or $\hat{u}_1'$ as an independent variable. We then define the two cross sections

$$\frac{d\sigma^t}{dp_T dy} = \frac{16\pi p_T}{3s} \sum_{i,j} \int_{-u_1/(s+t_1)}^1 \frac{dx_1}{x_1} \int_0^{x_1(s+t_1)+u_1} \frac{ds_4}{s_4 - x_1 t_1} \times f_{i/N_1}(x_1, \mu_f)\, f_{j/N_2}(x_2(s_4), \mu_f)\, C_{ij}(s_4, \hat{s}', \hat{t}_1', -\hat{s}' - \hat{t}_1', m_t, \mu_f)\,, \tag{9.1}$$

$$\frac{d\sigma^u}{dp_T dy} = \frac{16\pi p_T}{3s} \sum_{i,j} \int_{-t_1/(s+u_1)}^1 \frac{dx_2}{x_2} \int_0^{x_2(s+u_1)+t_1} \frac{ds_4}{s_4 - x_2 u_1} \times f_{i/N_1}(x_1(s_4), \mu_f)\, f_{j/N_2}(x_2, \mu_f)\, C_{ij}(s_4, \hat{s}', -\hat{s}' - \hat{u}_1', \hat{u}_1', m_t, \mu_f)\,. \tag{9.2}$$

We have changed variables from x_2 or x_1 to s_4 in the two equations, respectively, so that

$$x_1(s_4) = \frac{s_4 - x_2 u_1}{x_2 s + t_1}\,, \quad x_2(s_4) = \frac{s_4 - x_1 t_1}{x_1 s + u_1}\,. \tag{9.3}$$

Finally, we drop all dependence on s_4 in the hard-scattering kernels by using

$$\hat{t}_1' = \hat{t}_1 = x_1 t_1\,, \quad \hat{s}' = x_1 x_2(0) s \tag{9.4}$$

in (9.1), and

$$\hat{u}_1' = \hat{u}_1 = x_2 u_1 \,, \quad \hat{s}' = x_1(0) x_2 s \tag{9.5}$$

in (9.2). It is easy to see that with this choice σ^t and σ^u are not necessarily the same, although the difference is power suppressed. We shall take the average of the two as the final result for the differential cross section:

$$\frac{d\sigma}{dp_T dy} = \frac{1}{2}\left[\frac{d\sigma^t}{dp_T dy} + \frac{d\sigma^u}{dp_T dy}\right]. \tag{9.6}$$

In this way, the rapidity distribution in the gluon channel is invariant under $y \to -y$, as it should be, and the relation (5.9) is preserved. The scheme above specifies our procedure for the numerical evaluation of the threshold formulas for the differential distribution in p_T and y.

Having specified our procedure for evaluating the formulas in the threshold region, we next clarify how to match the results with fixed-order perturbation theory at NLO. The exact results contain the perturbative corrections to our formula which vanish in the limit $s_4 \to 0$, and to obtain solid phenomenological results it is important to include them. In resummed perturbation theory, we achieve NLO+NNLL accuracy by evaluating differential cross sections according to (7.1). Also, as in Section 8, we evaluate the approximate NNLO results as given by (7.2).

Similar to the case of PIM kinematics in Section 8 we have to examine the size of the power corrections contained in parentheses in the second term of (7.1). The power corrections are expected to be small when $\hat{s} \to 4m_\perp^2$, since in that case $s_4 \to 0$. However, experiments do not typically reconstruct $\hat{s}$ as an observable. For more interesting differential distributions the limit $s_4 \to 0$ can be enforced via a restriction to the machine threshold, for instance by requiring that $m_\perp \to \sqrt{s}/2$ for the p_T spectrum, but in this case the differential cross section would be extremely small. Away from such special kinematic regions we have to study if a dynamical enhancement occurs, because the product of PDFs appearing in the cross section falls off sharply away from the region where $s_4 \to 0$. We address the issue of threshold enhancement and power corrections to the threshold expansion in some detail in the next section.
We again will use input variables as specified in Section 7 and Table 7.1.

9.2. Systematic Studies

9.2.1. Threshold Enhancement

We now proceed to study threshold enhancement and the numerical importance of power corrections to the factorization formula (5.10). The goal is to examine under which conditions the higher-order corrections dominating in the limit $s_4 \to 0$ can be expected to give a good approximation to the full result. Given its importance, we approach this question from several different angles. In the following we compare the leading terms in the 1PI and

1PI_{SCET} threshold expansions for the p_T and rapidity distributions with the exact results at NLO in QCD.

Transverse-momentum and rapidity distributions at NLO

Our first test of the threshold expansion in 1PI kinematics is to compare its predictions for the transverse-momentum and rapidity distributions with the exact ones at NLO in QCD. In other words, we study whether the leading singular pieces in the 1PI or 1PI_{SCET} threshold expansions provide a good approximation to the exact NLO hard-scattering kernels, so that the power corrections contained in the parentheses of the second term in (7.1) are small. The results of this comparison can be found in Figure 9.1, where the transverse-momentum and rapidity distributions at the Tevatron and the LHC with $\sqrt{s} = 7$ and 14 TeV are displayed, for the choice $\mu_f = 2m_t$. To compute the exact QCD corrections we again rely on the Monte Carlo programs MCFM [140] and an internal NLO version of MadGraph/MadEvent[1] [144,145], whereas to implement the leading pieces of the threshold expansion in 1PI_{SCET} and 1PI we have used the procedure described in Section 9.1. It is obvious from the figures that the 1PI_{SCET} approximation does better than the 1PI approximation in reproducing the exact QCD results. Since the three curves differ only through the NLO corrections to the hard-scattering kernels, we can compare them much better if we isolate these pieces. We have done so for the p_T distribution in Figure 9.2, in this case for two different values of μ_f. We then see that at the Tevatron the 1PI_{SCET} approximation works remarkably well over the full range of μ_f. At the LHC, the 1PI_{SCET} approximation reasonably reproduces the correction at $\mu_f = m_t$, but does relatively poorly in reproducing the correct μ_f dependence. The 1PI approximation significantly overestimates the true result at all three values of μ_f, both at the Tevatron and at the LHC.

Given that the numerical differences between the 1PI_{SCET}, 1PI, and exact results are due solely to subleading terms as $s_4 \to 0$, we conclude that power corrections to the pure threshold expansion can be sizable at NLO. At the Tevatron, where the $q\bar{q}$ channel gives the largest contributions, the extra terms related to L_4 included in 1PI_{SCET} account for the dominant power corrections. They are also important at the LHC, where the gg channel dominates, but so are other corrections, which cannot be obtained in our formalism.

We have focused on the region of p_T where the differential cross section is largest. In principle, our results can also be used to predict the high-p_T tail of the distribution. In the limit $m_\perp \to \sqrt{s}/2$, for instance, $s_4 \to 0$, so threshold expansion is bound to work well when compared to the exact NLO result. However, in such kinematic regions the differential cross section is so small that it is essentially unobservable, and the top-quark is so highly boosted that $m_t \ll \sqrt{\hat{s}}$, so the power counting in the effective theory would need to be modified. A more interesting region would be up to around 400 GeV at the Tevatron, and up to around a TeV at the LHC. We will include the higher-p_T region for the Tevatron in the phenomenological studies. For the LHC, however, s_4 can be on average rather large at such values of p_T, so power corrections to the gg and qq channels can become significant,

[1] We are grateful to Rikkert Frederix for providing the code.

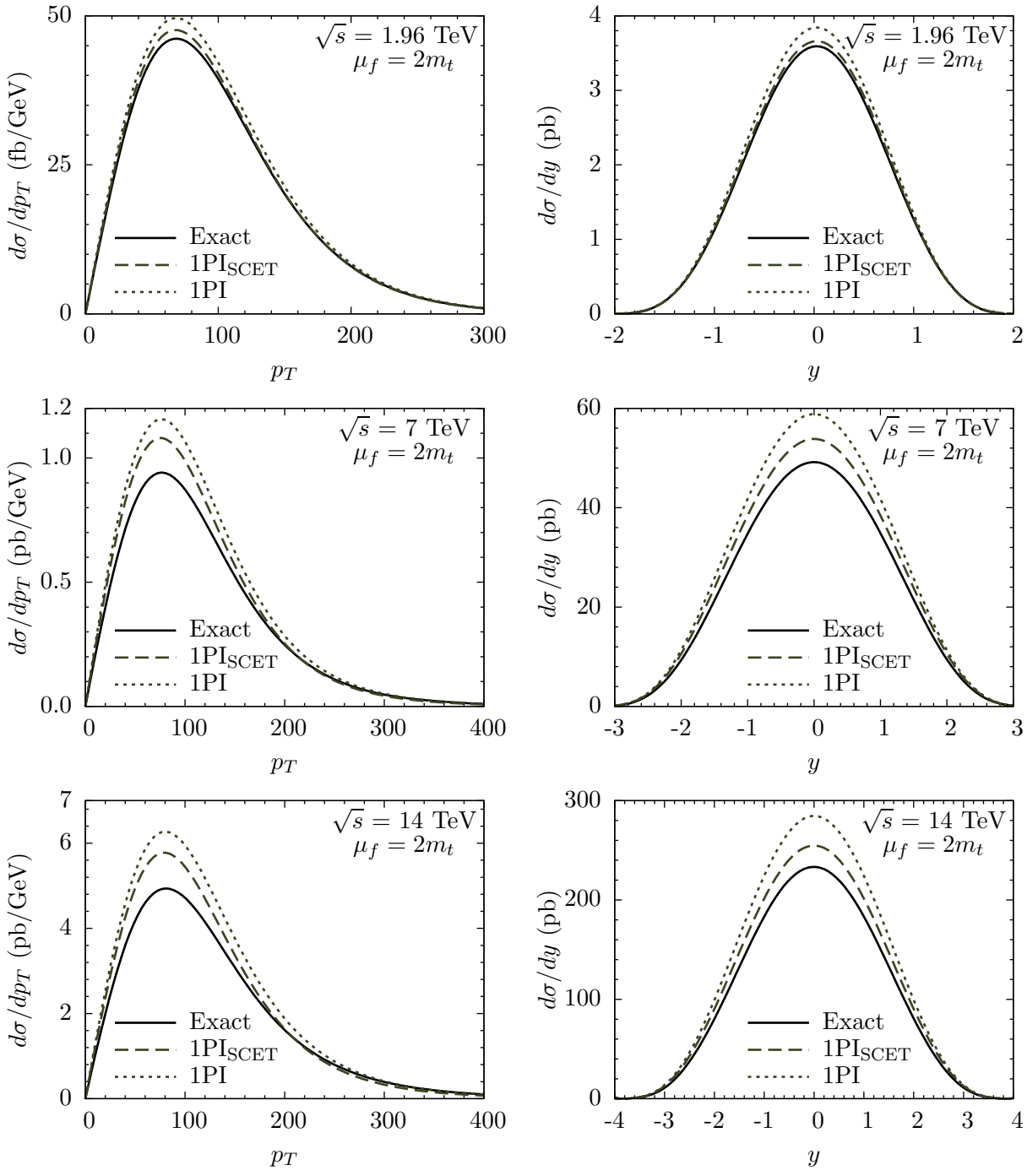

Figure 9.1.: The transverse-momentum and rapidity distributions at NLO at the Tevatron with $\sqrt{s} = 1.96$ TeV and at the LHC with $\sqrt{s} = 7$ and 14 TeV.

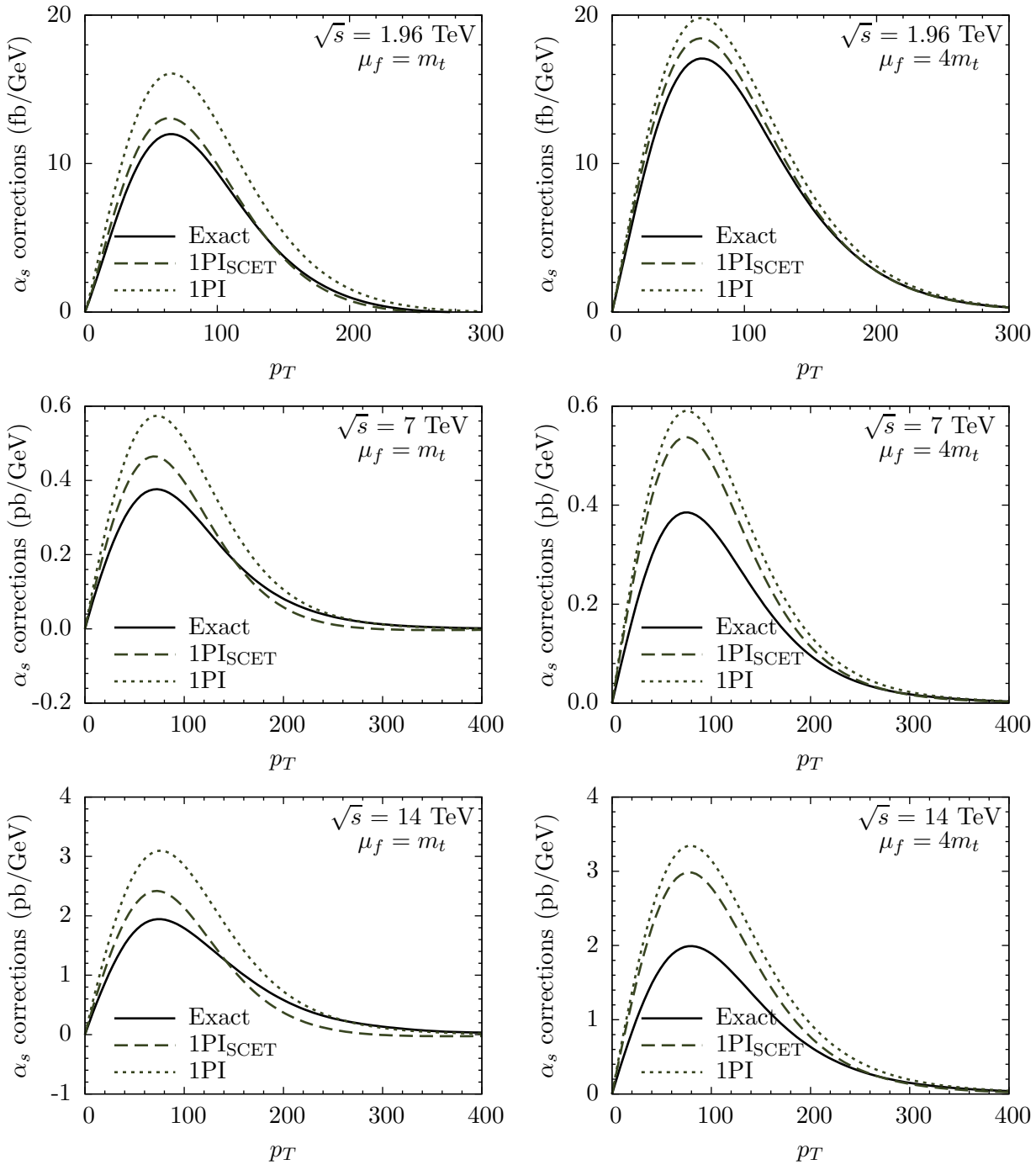

Figure 9.2.: The NLO corrections to $d\sigma/dp_T$.

and the qg channel can also give non-negligible contributions. Given these problems, we will not study the high-p_T distributions at the LHC.

This simple NLO study is instructive, but in the end the real issue is how well the threshold approximation is expected to work at NNLO. On the one hand, at NNLO one encounters plus-distributions enhanced by up to three powers of logarithms, so it is not unreasonable to expect that the power corrections are of less relative importance than at NLO. On the other hand, at NLO the coefficients multiplying both the P_n distributions and δ-function terms are known exactly, while at NNLO only those multiplying the P_n distributions are available. It is therefore difficult to anticipate the behavior of the threshold expansion at NNLO based only on its behavior at NLO. We will turn to this issue later in a Section 10.1.1.

9.2.2. Scale Setting

As for the PIM case we have to find appropriate settings for the scales μ_f, μ_h and μ_s. We begin with determining an appropriate choice of the soft scale μ_s. From theoretical arguments, we expect that the perturbative expansion of the soft function should be well-behaved at a scale characteristic of the energy of the real soft radiation, which is generally smaller than the hard scales m_t and $\sqrt{\hat{s}}$. As explained in Section 6.3, a general analysis would determine the soft scale by requiring that the corrections from the soft function to the double-differential spectrum are well behaved, after integration over the partonic variables. We have performed such an analysis for the p_T distribution and found reasonable results at the Tevatron. This is also the case for the LHC at lower values of p_T, where the differential cross section is large. As long as we study a relatively modest range in p_T, an equally valid procedure for determining the soft scale is to study the corrections to the total cross section as a function of μ_s. This automatically samples the regions of phase-space where the double-differential cross section is largest. We show the results of such an analysis in Figure 9.3. To isolate the α_s correction from the soft function shown there, we pick out the piece of the NNLL approximation to the hard scattering kernels arising from $\widetilde{\boldsymbol{s}}^{(1)}$, evaluate the total cross section using only this piece, and divide the result by that at NLL, working in the 1PI_{SCET} scheme. We furthermore make the scale choice $\mu_f = \mu_h = \mu_s$, which amounts to looking at the correction at NLO in fixed-order. As seen from the figure, a well-defined minimum in the soft correction appears for $\mu_s \sim 60$ GeV at the Tevatron, $\mu_s \sim 80$ GeV at the LHC with $\sqrt{s} = 7$ GeV, and $\mu_s \sim 90$ GeV at the LHC with $\sqrt{s} = 14$ GeV. We will use these as the default choices of μ_s in the rest of this section, both for the total cross section and for differential distributions.

One can apply this same procedure to determine an appropriate choice of the hard scale. Since the hard function is the same in PIM and 1PI kinematics, we recall that in the PIM case, we found that $\mu_h = M$ is a reasonable default value. Translated to 1PI kinematics, this would imply the choice $\mu_h = \sqrt{\hat{s}}$. The actual result for the α_s correction to the total cross section arising from the hard function as a function of μ_h is shown in the right panel of Figure 9.3. We isolate this correction as we did for the soft function, except for this time we pick out the piece of the NNLL cross section proportional to $\boldsymbol{H}^{(1)}$, and examine the

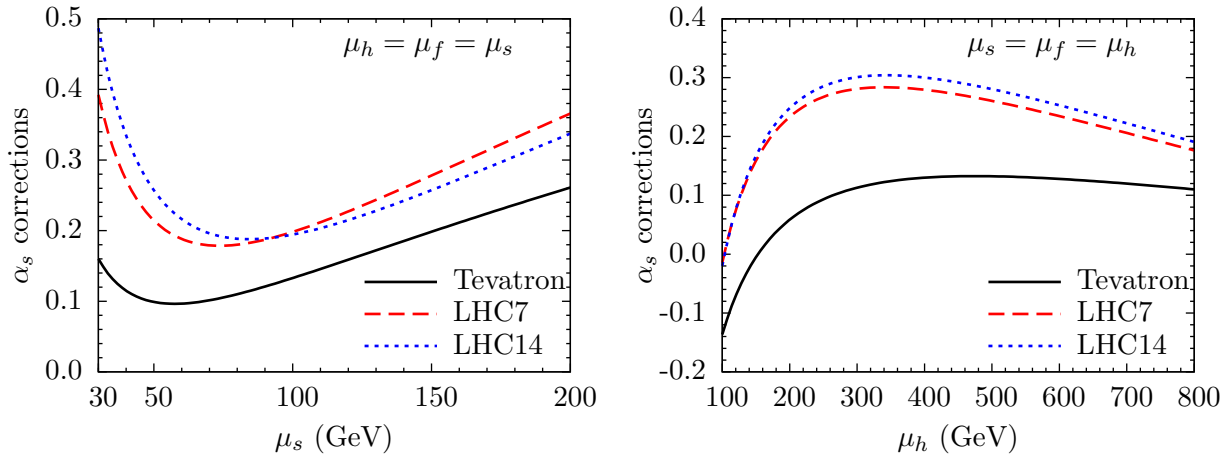

Figure 9.3.: The one-loop correction from the soft function (left) and the hard function (right) to the total cross section, divided by the leading-order result. The solid black line is for the Tevatron, the dashed red line for LHC7, and the dotted blue line for LHC14.

result as a function of μ_h. As for the analysis with the soft function, we make the choice $\mu_f = \mu_h = \mu_s$. At lower values of μ_h the correction becomes negative and depends strongly on the scale. To avoid sensitivity to that region, we will choose $\mu_h = 400$ GeV by default, which is close to the average value of $\sqrt{\hat{s}}$ for the total cross section, and in any case will be varied by a factor of two in the error analysis.

For the factorization scale, we will consider the two different choices $\mu_f = m_t$ and $\mu_f = 400$ GeV which we also used in PIM kinematics. For the differential distributions in the following subsection, on the other hand, we use $\mu_f = 2m_t$ as the central value. A more refined analysis could use other choices, such as $\mu_f = m_\perp$ for the p_T distribution, but since we do not study tails of the distributions we prefer to stick to a single value which is roughly intermediate between the two values used for the total cross section.

Another method often used to argue for a particular scale choice is to look for areas where the scale dependence of the observable is flat. As part of our analysis below, we show in Figure 9.4 the dependence of the total cross section on the scales μ_s, μ_h, and μ_f, at NLO+NNLL and approximate NNLO. We note that the scale-dependence of the cross section at NLO+NNLL order is indeed flat close to our default values of μ_s and μ_h, and also close to $\mu_f = m_t$. The approximate NNLO results, on the other hand, do not seem to favor a particular choice of μ_f based on this criteria.

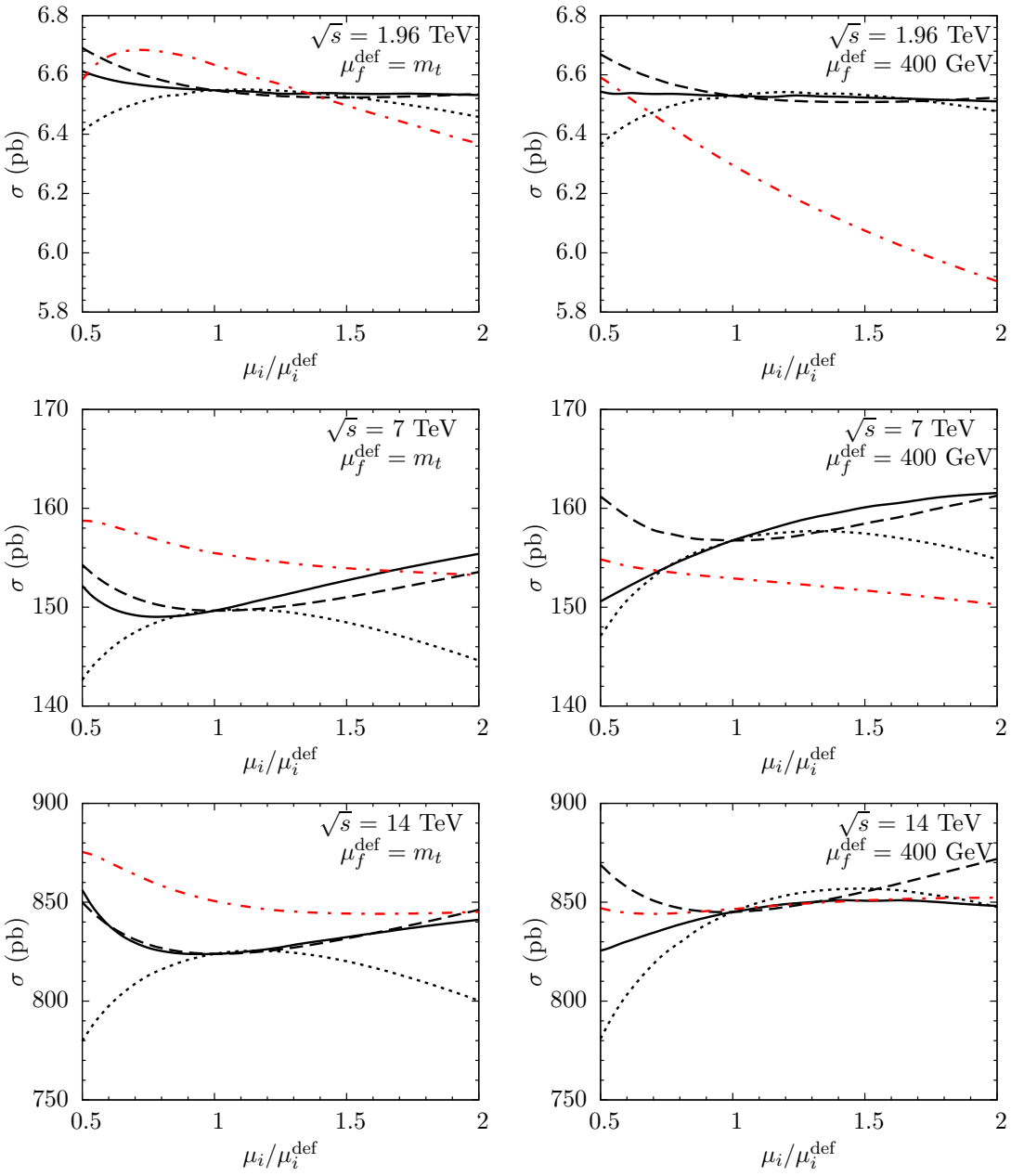

Figure 9.4.: Dependence of the cross section at NLO+NNLL and approximate NNLO in 1PI_{SCET} on the scales μ_f, μ_s, and μ_h. The dot-dashed red lines show the dependence of the cross section on μ_f in approximate NNLO. The dependence of the cross section on the scales at NLO+NNLL order is represented by the solid black lines (μ_f), the dashed black lines (μ_s), and the dotted black lines (μ_h).

9.3. Rapidity and Transverse-Momentum Distributions

We now present results for the top-quark rapidity and transverse-momentum distributions. We begin by studying rapidity distributions in Figure 9.5, where we compare results from fixed-order and resummed calculations in the 1PI_{SCET} scheme at the Tevatron and the LHC with $\sqrt{s} = 7$ and 14 TeV. The results within a given perturbative approximation are represented as bands indicating the theoretical uncertainties from scale variations. To make the bands in fixed-order perturbation theory at a given point in y, we vary the value of the factorization scale up and down from its default value at $\mu_f = 2m_t$ by a factor of two, and pick out the highest and lowest numbers at that point, in resummed perturbation we apply SUES. The results in the figure clearly show that the higher-order corrections contained in the approximate NNLO and NLO+NNLL formulas tend to reduce the uncertainties due to scale dependence, and slightly raise the central values at a given rapidity to the upper part of the fixed-order NLO band. The error bands for the NLO+NNLL and approximate NNLO results are of similar size at the Tevatron, but at the LHC the approximate NNLO bands are noticeably smaller, a result which we will quantify in more detail when we study the total cross section.

Next, we consider the top-quark transverse-momentum distribution. In this case, we focus our analysis on the Tevatron, where experimental measurements are available. In Figure 9.6 we show our predictions for this distribution within the different perturbative approximations, comparing the fixed-order and resummed results. As with the rapidity distributions, the higher-order perturbative corrections serve to decrease the scale dependence, and also to slightly raise the central values of the results at a given p_T. We compare the NLO+NNLL results for the p_T distribution with a recent measurement at the Tevatron performed by the D0 collaboration using the lepton+jets channel [78] in Figure 9.7, showing also the NLO calculation for illustration. Since the D0 analysis uses $m_t = 170$ GeV, for the purposes of this study we deviate from our default choice and also adopt this value. We observe that the slight increase in the the differential cross section due to resummation leads to a better agreement with the data compared to the NLO predictions. In general, the measured spectrum and the NLO+NNLL theory prediction agree within the errors, both in the shape and the normalization. This is true even at higher values of p_T, although one should keep in mind that our scale-setting procedure was designed to work in areas where the differential cross section is large.

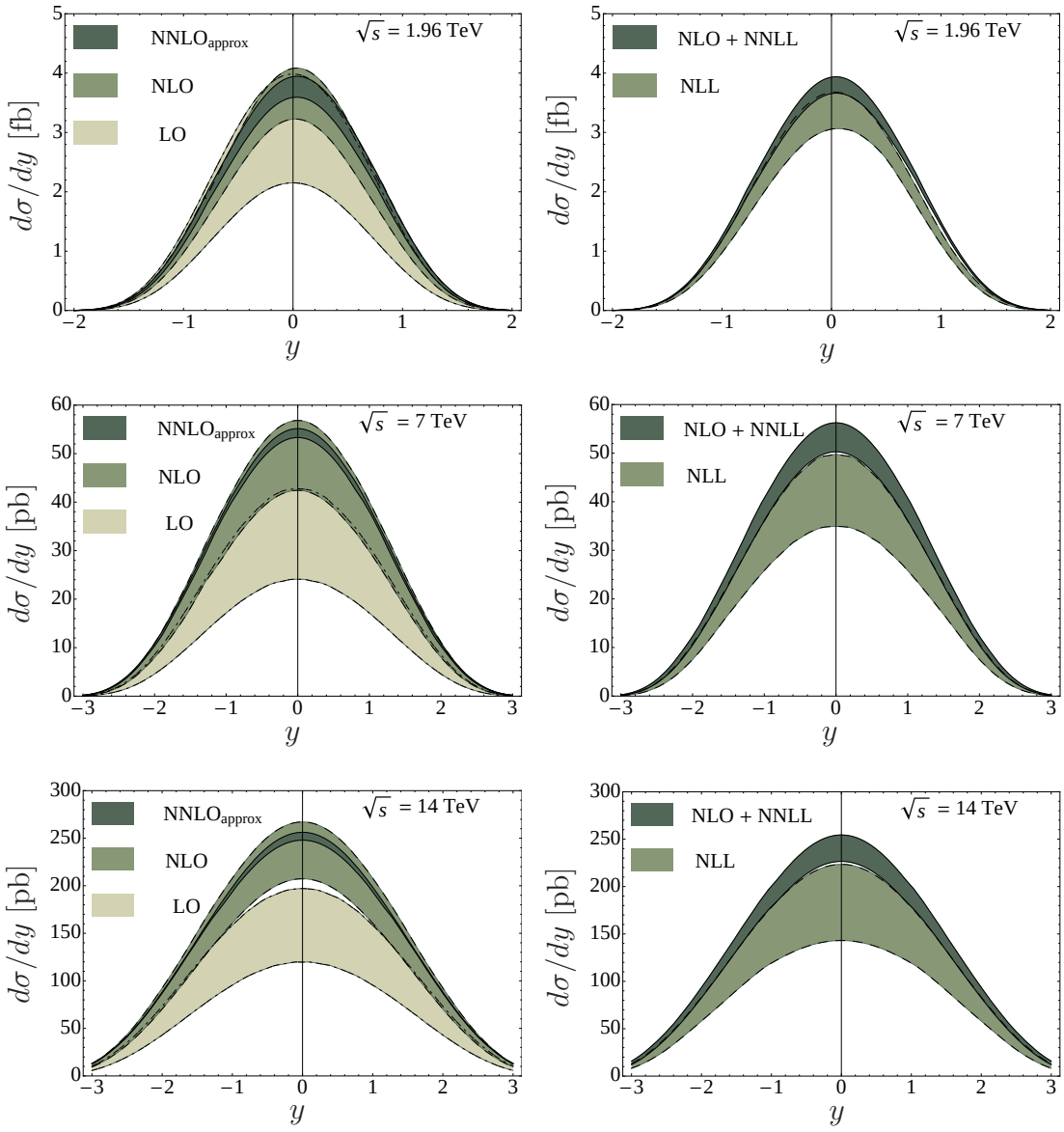

Figure 9.5.: Left: Fixed-order predictions for the rapidity distribution at LO (light), NLO (darker), and approximate NNLO (dark bands) for the Tevatron (top) and LHC (bottom). Right: Corresponding predictions at NLL (light) and NLO+NNLL (darker bands) in resummed perturbation theory. The width of the bands reflects the uncertainty of the distributions under variations of the matching and factorization scales, as explained in the text.

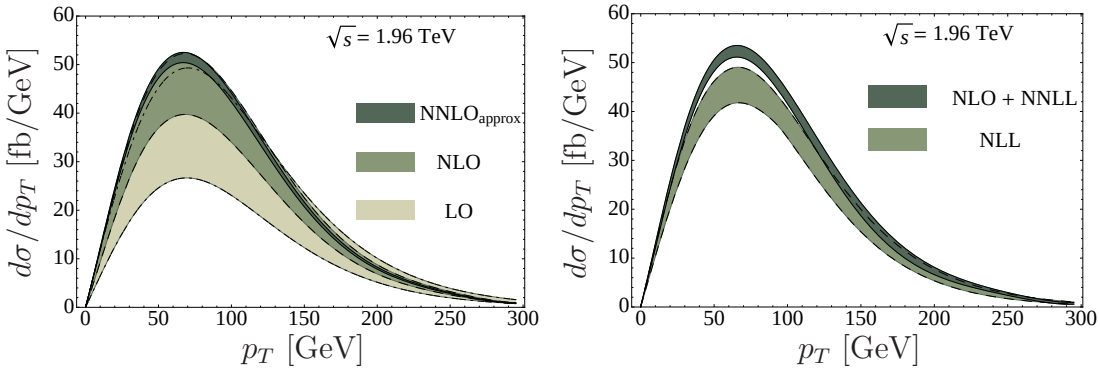

Figure 9.6.: Left: Fixed-order predictions for the p_T distribution at LO (light), NLO (darker), and approximate NNLO (dark bands) at the Tevatron. Right: Corresponding predictions at NLL (light) and NLO+NNLL (darker bands) in resummed perturbation theory. The width of the bands reflects the uncertainty of the distributions under variations of the matching and factorization scales, as explained in the text.

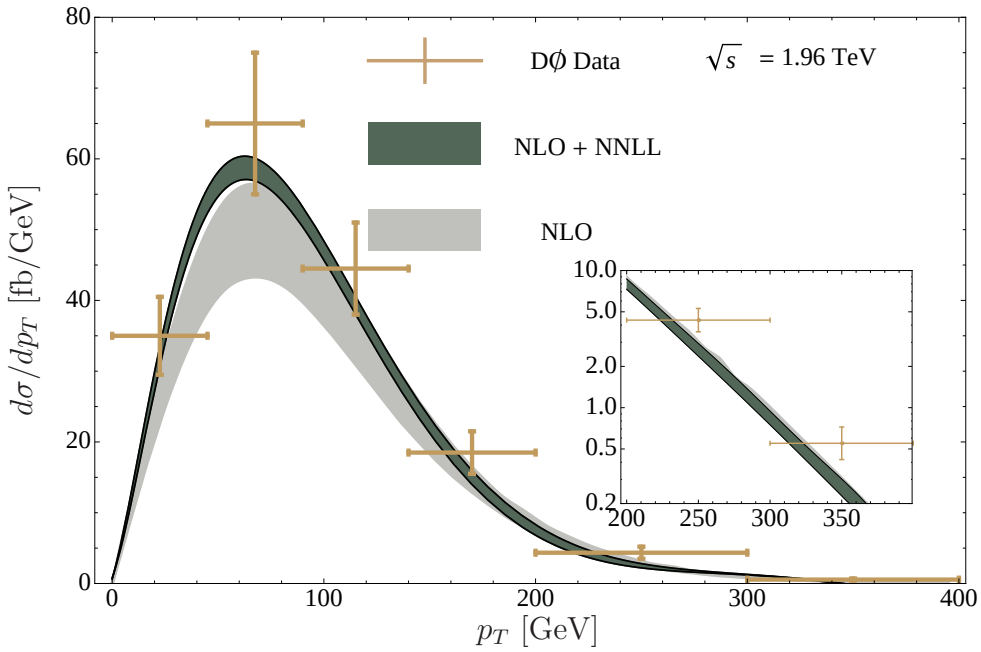

Figure 9.7.: Comparison between our NLO+NNLL predictions, NLO results and recent measurements from the D0 collaboration [78]. The error bands refers to perturbative uncertainties related to scale variations. Furthermore we have enlarged the region of bigger p_T for better comparison.

9.4. Total Cross Section

Our main new results concerning the total cross section are the NLO+NNLL and approximate NNLO expressions in the 1PI_{SCET} scheme. Our results for the total cross section within different approximations are summarized in Tables 9.1 and 9.2. We have also shown the scale dependence of the 1PI_{SCET} results at NLO+NNLL and approximate NNLO in more detail in Figure 9.4. The main phenomenological results are the NLO+NNLL and approximate NNLO numbers in the bottom half of the tables, but for comparison we also give the NLO predictions obtained within the different approximations. In that case, we also present the sum of the $q\bar{q}$ and gg channels alone, without the extra piece from the gq and $g\bar{q}$ channels; this allows for a more direct comparison with the leading-singular results in the 1PI_{SCET} scheme at NLO, which does not include those pieces. In the fixed-order results, the scale uncertainties are obtained by varying the factorization scale up and down by a factor of two. Again, in the resummed results, we apply SUES to obtain the perturbative uncertainties shown in the tables. We have included PDF uncertainties obtained by evaluating the cross section with the set of MSTW2008 PDFs at 90% CL.

	Tevatron	LHC (7 TeV)	LHC (8 TeV)	LHC (14 TeV)
$\sigma_{\text{NLO leading}}$	$5.92^{+0.74+0.33}_{-0.80-0.22}$	149^{+13+8}_{-16-8}	214^{+16+10}_{-22-10}	853^{+35+29}_{-65-30}
$\sigma_{\text{NLO, } q\bar{q}+gg}$	$5.89^{+0.77}_{-0.81}$	142^{+14}_{-17}	203^{+21}_{-23}	801^{+67}_{-77}
σ_{NLO}	$5.79^{+0.79+0.33}_{-0.80-0.22}$	133^{+21+7}_{-19-7}	192^{+30+9}_{-27-9}	$761^{+105+26}_{-96\ -27}$
$\sigma_{\text{NLO+NNLL}}$	$6.53^{+0.14+0.32}_{-0.17-0.23}$	$157^{+7\ +8}_{-11-8}$	$223^{+9\ +10}_{-15-11}$	845^{+27+27}_{-67-29}
$\sigma_{\text{NNLO approx}}$	$6.30^{+0.30+0.32}_{-0.39-0.23}$	153^{+2+8}_{-3-8}	219^{+2+10}_{-3-11}	847^{+6+28}_{-0-30}

Table 9.1.: Results for the total cross section in pb, using the default choice $\mu_f = 400\,\text{GeV}$. The first set of errors refers to perturbative uncertainties associated with scale variations, and the second to PDF uncertainties.

	Tevatron	LHC (7 TeV)	LHC (8 TeV)	LHC (14 TeV)
$\sigma_{\text{NLO leading}}$	$6.79^{+0.20+0.38}_{-0.70-0.24}$	$163^{+0\ +9}_{-11-9}$	$232^{+0\ +11}_{-14-12}$	$887^{+0\ +30}_{-66-32}$
$\sigma_{\text{NLO, } q\bar{q}+gg}$	$6.80^{+0.27}_{-0.73}$	160^{+5}_{-15}	228^{+6}_{-20}	879^{+21}_{-62}
σ_{NLO}	$6.72^{+0.36+0.37}_{-0.76-0.24}$	159^{+20+8}_{-21-9}	227^{+28+11}_{-30-12}	$889^{+107+31}_{-106-32}$
$\sigma_{\text{NLO+NNLL}}$	$6.55^{+0.16+0.32}_{-0.14-0.24}$	150^{+7+8}_{-7-8}	214^{+10+10}_{-10-11}	824^{+41+28}_{-44-30}
$\sigma_{\text{NNLO approx}}$	$6.63^{+0.00+0.33}_{-0.27-0.24}$	155^{+3+8}_{-2-9}	222^{+5+11}_{-3-11}	$851^{+25+29}_{-5\ -31}$

Table 9.2.: Same as Table 9.1, but with the scale choice $\mu_f = m_t$.

At NLO, the central value of the exact result is always lower than the leading singular pieces whereas, for smaller collider energies, the μ_f dependence is well accounted by them.

For $\mu_f = 400$, going to higher collider energies the difference between exact NLO and leading singular terms becomes bigger. This is not the case for the default choice $\mu_f = m_t$, where the relative difference stay roughly the same. The NLO+NNLL and approximate NNLO formulas include the NLO corrections from the qg and $\bar{q}g$ channels through the matching, and the fact that these higher-order approximations have a rather small scale dependence even without the NNLO corrections from the qg channel can be taken as an indication that such corrections are small, but this is a point which should nonetheless be kept in mind when applying approximate formulas to the LHC with $\sqrt{s} = 14$ TeV.

Another noticeable pattern has to do with the difference between the NLO+NNLL and approximate NNLO results: the NLO+NNLL results are higher for $\mu_f = 400$ GeV, but lower for $\mu_f = m_t$. We can learn more about the scale variations in the NLO+NNLL and approximate NNLO results in the 1PI_{SCET} scheme by examining Figure 9.4. Compared to the NLO+NNLL approximations, the approximate NNLO results in 1PI_{SCET} have very small scale uncertainties around a given μ_f, particularly at the LHC. When μ_f is considered in the entire range $m_t/2 < \mu_f < 800$ GeV, on the other hand, the approximate NNLO results are in good agreement with the resummed results in that same range. This is not an unreasonable means of comparison, since at a given μ_f the resummed results probe scales ranging from $\mu_s^{\text{def}} \sim 75$ GeV to $\mu_h \sim 400$ GeV, so in estimating errors in fixed-order one should arguably focus on a similar range instead of just using $m_t/2 < \mu_f < 2m_t$, as is often done in the literature.

As emphasized in Section 6.3, due to our method for determining the soft scale μ_s, the NLO+NNLL predictions contain slightly different information than the approximate NNLO formulas. In particular, the NNLO expansion of the resummed formulas differ in the structure of the P_n distributions. For instance, the approximate NNLO results contain P_3 distributions, but the equivalent terms in the direct NNLO expansion of the resummed formula are of the form $P_2 \ln(\mu_s/\mu_f)$. These contribute at the same order in the counting of RG-improved perturbation theory, but there are obviously numerical differences between the two forms of the expansion. This issue is discussed in more detail in Section .3 of the Appendix. Since the analysis in Figure 9.3 was done at NLO and at that order one encounters at most P_1 distributions, it is worthwhile to ask whether the choice of scale of μ_s deduced there is really appropriate to account for the mismatch between the two approximations. If this were not the case, our NLO+NNLL predictions would become unstable upon the inclusion of the higher-order matching corrections and it would make more sense to use the approximate fixed-order NNLO results. To address this issue, we have also calculated the cross section where we add the NNLO matching coefficients on top of the NLO+NNLL resummation. More precisely, we include the pieces of the matching functions specified in (6.13), but still including the NLL evolution matrices in the trace, as in (5.35). In the case where $\mu_f = \mu_h = \mu_s$, this approximation reduces to the approximate NNLO result (compared to the NLO+NNLL result, which reduces to the NLO result in this limit). We have checked that the numerical results in this "NNLO+NNLL" approximation are within the uncertainties estimated by the NLO+NNLL calculation. This provides evidence that our scale-setting procedure is indeed appropriate for effectively including the higher-order corrections.

10. Combined Studies

10.1. Total Cross Section

In this section we combine our knowledge about PIM and 1PI kinematics to analyze various aspects of the total cross section.

The different distributions, which we are able to calculate using PIM or 1PI should all lead to the same total cross section after integration over them. In the next section we will compare the total cross section using PIM or 1PI kinematics starting from a distribution in β. In Section 8.3.1 we did a detailed comparison between results in the $\beta \to 0$ limit coming from our PIM calculation and previous approaches in this limit. There we were interested in the accuracy of the $\beta \to 0$ limit, and found that subleading terms in β are not generically small. By analyzing results on the level of the β distribution coming from PIM and 1PI kinematics we are able to directly compare the threshold expansion and power corrections in these two kinematical approaches. The results must agree in the limit $\beta \to 0$, since in that case gluon emission is soft, but beyond that they receive a different set of power corrections, so the agreement of the two approximations with each other is one way of testing whether these power corrections are under control. Furthermore we are able to test if our improved PIM_{SCET} and 1PI_{SCET} schemes decrease the impact of power corrections in comparison to the standard approaches.

Having analyzed the different power corrections, we combine 1PI and PIM results in Section 10.1.2 to make predictions for the total cross section as a function of the top-quark mass in the pole scheme. Following this we also give results for the top-quark mass dependent cross section using the $\overline{\text{MS}}$ and $1S$ mass scheme.

10.1.1. The β Distribution in PIM and 1PI Kinematics

As for the case of PIM in Section 8.3.1, we can obtain the total cross section starting from a distribution in β using our results in 1PI kinematics. We calculate the distribution in β through an exact change of variables and integration orders in (9.6). With this, the total cross section in 1PI kinematics takes the form

$$\sigma(s, m_t^2) = \int_{4m_t^2}^{s} \frac{4\pi\beta}{3sm_t^2} \sum_{i,j} ff_{ij}\left(\frac{\hat{s}}{s}, \mu_f\right) \times \frac{1}{2}\Bigg[\int_{-\hat{s}(1+\beta)/2}^{-\hat{s}(1-\beta)/2} d\hat{t}_1 \int_0^{\hat{s}+\hat{t}_1+\hat{s}m_t^2/\hat{t}_1} ds_4\, C_{ij}(s_4, \hat{s}_t', \hat{t}_1', -\hat{s}_t' - \hat{t}_1', m_t, \mu_f)$$

$$+\int_{-\hat{s}(1+\beta)/2}^{-\hat{s}(1-\beta)/2} d\hat{u}_1 \int_0^{\hat{s}+\hat{u}_1+\hat{s}m_t^2/\hat{u}_1} ds_4\, C_{ij}(s_4, \hat{s}'_u, -\hat{s}'_u - \hat{u}'_1, \hat{u}'_1, m_t, \mu_f)\Bigg], \quad (10.1)$$

where $\hat{s} = 4m_t^2/(1-\beta^2)$, and

$$\hat{s}'_t = \hat{s}\,\frac{-\hat{t}_1}{s_4 - \hat{t}_1}\,, \quad \hat{t}'_1 = \hat{t}_1 \quad (10.2)$$

in the first term in the bracket, while

$$\hat{s}'_u = \hat{s}\,\frac{-\hat{u}_1}{s_4 - \hat{u}_1}\,, \quad \hat{u}'_1 = \hat{u}_1 \quad (10.3)$$

in the second. Comparing this with (8.4) gives the coefficients f_{ij} in 1PI kinematics.[1]

We now begin with a study of the NLO corrections, similar to that performed in Section 8.3.1. In Figure 10.1 we compare results for the α_s correction to (8.4) obtained within the different expansions. As in Figure 8.13, we compare the quark and gluon channels separately and look at the corrections in a kinematic range from the production threshold at $\beta = 0$ to the machine threshold at $\beta_{\max} = \sqrt{1-4m_t^2/s}$. As anticipated from the results of Section 9.3, the 1PI_{SCET} approximation works quite well in the $q\bar{q}$ channel, but somewhat worse in the gg channel, especially at the LHC. The 1PI results overestimate the exact corrections in all cases. As for the results in PIM kinematics, they are lower than the exact results in all cases, but the power-suppressed terms included in PIM_{SCET} bring the leading terms in the threshold expansion closer to the full result. The PIM_{SCET} approximation is slightly worse than 1PI_{SCET} in the $q\bar{q}$ channel, and slightly better in the gg channel, but the differences are not major.

As mentioned in the introduction to this section, all of the approximations have the same leading-order expansion in the limit $\beta \to 0$. The power-suppressed effects accounting for the differences between the curves start to become noticeable at $\beta \sim 0.2$. After that point, there is more phase space for hard gluon emission and the size of the power corrections increases. Evidently, the subleading terms included in the 1PI_{SCET} and PIM_{SCET} approximations account for these power-suppressed terms in part, although not completely. This is especially noticeable in 1PI kinematics, where the power corrections are generically more important than in PIM kinematics, a point we will return to below. The power corrections become progressively more important at higher values of the collider energy, since then the luminosities are larger at high β and the differences in the partonic cross sections in that region are magnified. This is most easily seen by comparing the LHC results at the two different collider energies, where one observes larger gaps between the approximations at 14 TeV than at 7 TeV. A careful examination of the results at the LHC with $\sqrt{s} = 14$ GeV also shows a feature not obvious in the other cases: at very high values of β close to the endpoint, the exact correction in the gg channel remains a positive number. In fact, the exact NLO correction to the partonic cross section in the gg channel tends to a positive

[1] It should be noted that, since the change of variables in (10.1) is carried out exactly, (9.6) and (10.1) give the same result for the total cross section.

constant at very high $\hat{s}$ [8], while that for the $q\bar{q}$ channel, and also the threshold approximations to the corrections in PIM and 1PI kinematics in both channels, approach zero at high $\hat{s}$. This feature is only visible at the highest collider energy, because otherwise the high-β cross section is completely damped by the luminosities. For the same reason, the qg channel, for which the partonic cross section also tends to a positive constant at high $\hat{s}$, can become important at high β. We show the α_s correction from this channel at the LHC in Figure 10.2, for three different values of μ_f (at the Tevatron, the contribution from this channel is still very small.) For higher values of β, and especially at lower values of μ_f, it can be as important as the gg channel, even though it is suppressed in the limit $s_4 \to 0$.

We can also perform some comparisons of results at NNLO. Those we can get coming from PIM or 1PI kinematics, and the agreement of these results with each other gives some information about the size of power-suppressed terms. In addition, as already mentioned, the NNLO corrections proportional to the scale-dependent logarithmic terms in (8.4) are known exactly [43]. This gives us an opportunity to also compare both types of kinematics with an exact result beyond NLO.

The NNLO corrections proportional to the scale-dependent logarithmic terms within the different approximations are shown in Figure 10.3. The results are obtained by dropping the scale-independent coefficient $f^{(2,0)}$ from (8.6). Since these contributions would vanish for $\mu_f = m_t$, we have chosen in this case $\mu_f = 2m_t$ instead. We have evaluated the exact results in QCD using the formulas from [43], and the PIM_{SCET} and PIM results using those in Section 8.3.1. To obtain the threshold expansions for this comparison, in both kinematics, we have included the μ-dependent pieces of the two-loop hard function, and wrote all μ-dependent logarithms in the form $\ln(m_t^2/\mu^2)^2$. Concerning the agreement between the 1PI approximations and the exact results, one sees the same qualitative behavior as at NLO. The 1PI_{SCET} results are consistently a better approximation than the 1PI results, especially at the LHC, where the power corrections are large at higher values of β. As for the PIM results, the PIM_{SCET} approximation fares slightly better than the PIM results in the gluon channel, but slightly worse in the quark channel. In any case, the differences between the PIM_{SCET} and PIM results are much smaller than those between the 1PI_{SCET} and 1PI results, which can be taken as an indication that the power corrections are smaller in PIM than in 1PI kinematics. However, once the extra corrections unique to the 1PI_{SCET} scheme are taken into account, the results in these two types of kinematics are very much compatible with one another and provide a good approximation to the exact results.

The NNLO corrections from the scale-independent pieces $f^{(2,0)}$ to (8.4) within the different PIM and 1PI approximations are shown in Figure 10.4, for the choice $\mu_f = m_t$. For these pieces it is not possible to make a comparison with an exact result, but we can make a couple of comments based on the agreement of the different approximations with each other. As before, the difference between the two PIM schemes is small compared to that between the two 1PI schemes, indicating that the power corrections in PIM kinematics are smaller, and the difference between the 1PI_{SCET} and PIM_{SCET} results are much reduced compared to the difference between the 1PI and PIM results. In general, the NNLO

[2] In the case of PIM we called this scheme B in Section 6.1.

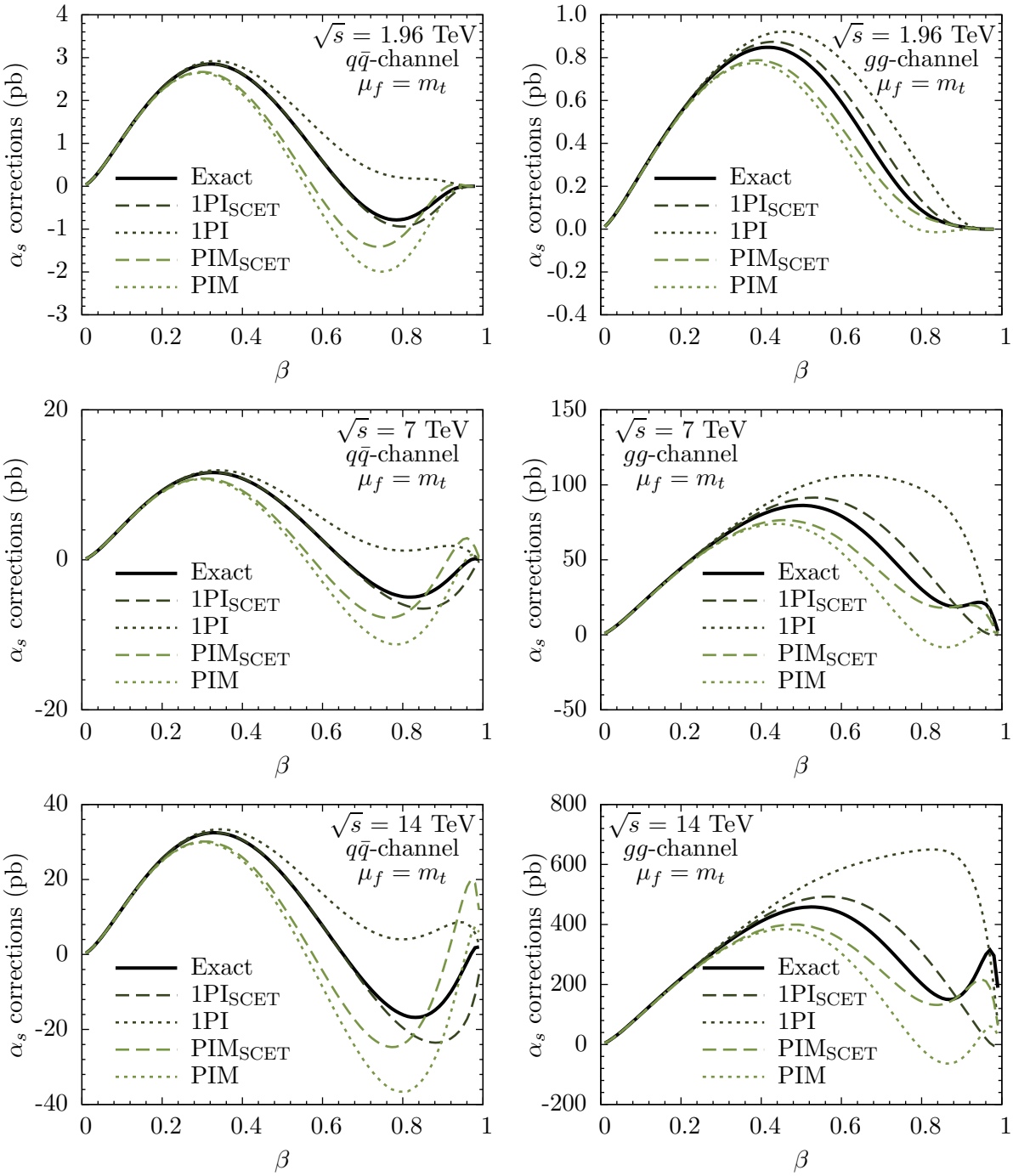

Figure 10.1.: The α_s corrections to $d\sigma/d\beta$ for the different approximations mentioned in the text, with $\mu_f = m_t$.

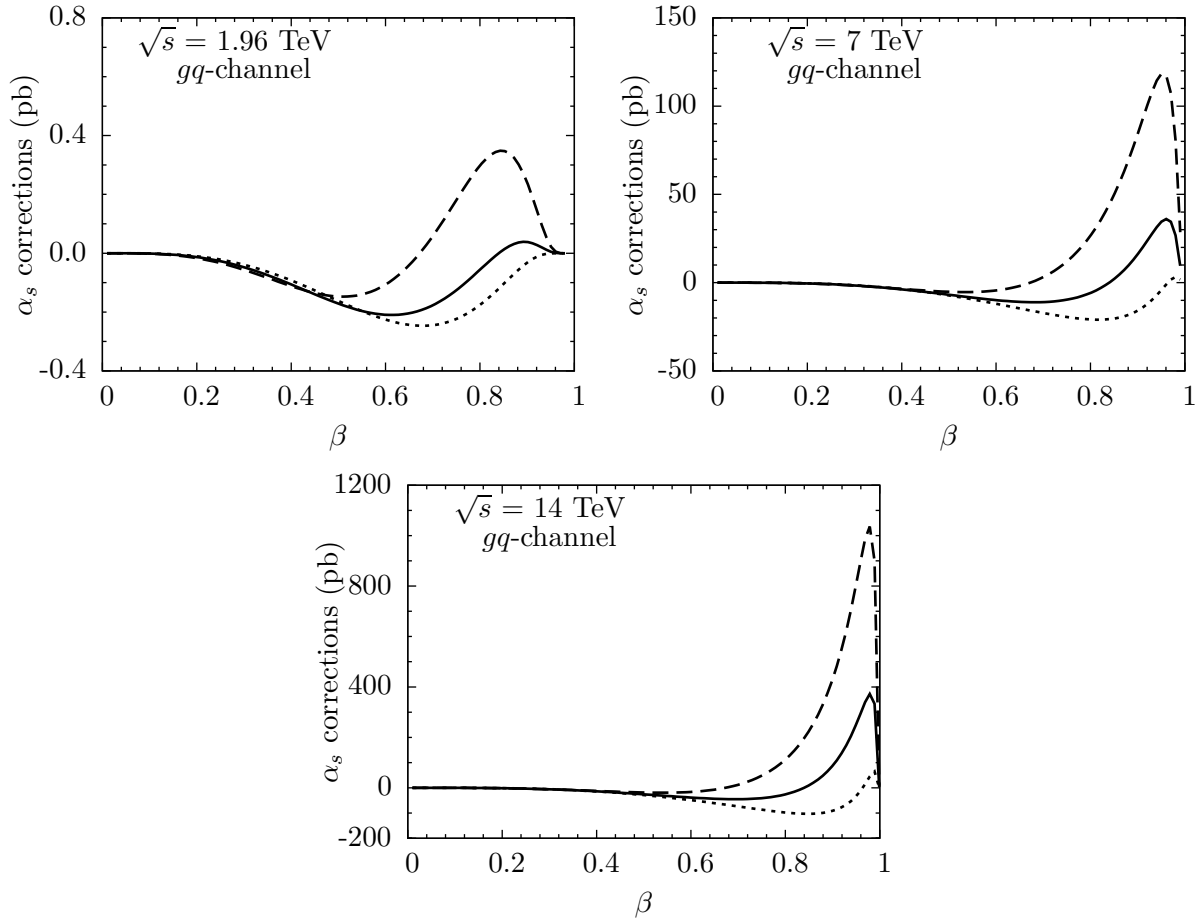

Figure 10.2.: The α_s corrections to $d\sigma/d\beta$ from the gq channel, for $\mu_f = m_t$ (solid), $\mu_f = m_t/2$ (dashed) and $\mu_f = 2m_t$ (dotted).

corrections in the 1PI approximation are much larger than any of the others.

The explicit results from these studies all point to the fact that 1PI kinematics is more susceptible to power-suppressed effects than PIM kinematics. We can gain more insight into this observation through a very simple analysis. As discussed in Section 5.2, the leading power corrections in 1PI kinematics are related to the partonic expansion parameter $\lambda = E_s/m_t$, where $2E_s \sim s_4/\sqrt{m_t^2 + s_4}$ is the energy of extra soft radiation in the partonic scattering process. For the case of PIM kinematics, as mentioned in Section 4.2, the equivalent parameter is $\lambda = E_s^{\rm PIM}/M$, where $2E_s^{\rm PIM} = M(1-z)/\sqrt{z}$. We can quantify in part the relative size of these parameters as a function of β by evaluating the mean value

$$\langle\lambda\rangle_{\rm 1PI} = \int_{t_1^{\rm min}}^{t_1^{\rm max}} d\hat{t}_1 \int_0^{s_4^{\rm max}} ds_4 \left(\frac{s_4}{2m_t\sqrt{m_t^2+s_4}}\right) \Bigg/ \int_{t_1^{\rm min}}^{t_1^{\rm max}} d\hat{t}_1 \int_0^{s_4^{\rm max}} ds_4 \qquad (10.4)$$

in 1PI kinematics, where the appropriate integration range can be read off from (10.1),

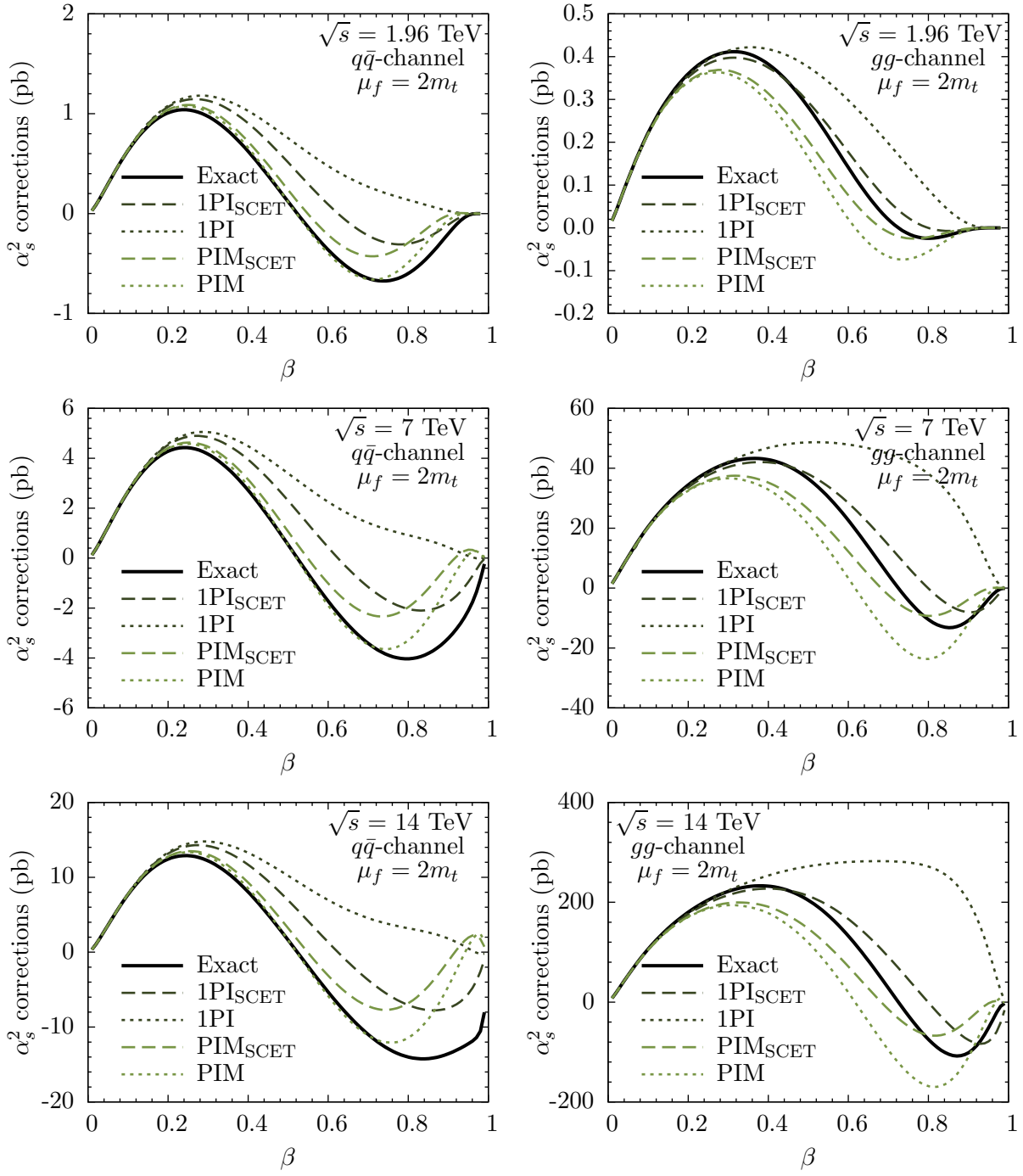

Figure 10.3.: The α_s^2 corrections to $d\sigma/d\beta$ obtained by dropping the scale-independent piece $f^{(2,0)}$ in (8.6), for $\mu_f = 2m_t$. The exact result is the black line, the dashed red line 1PI$_{\rm SCET}$, the dotted red line 1PI, the dashed blue line PIM$_{\rm SCET}$, and the dotted blue line PIM.

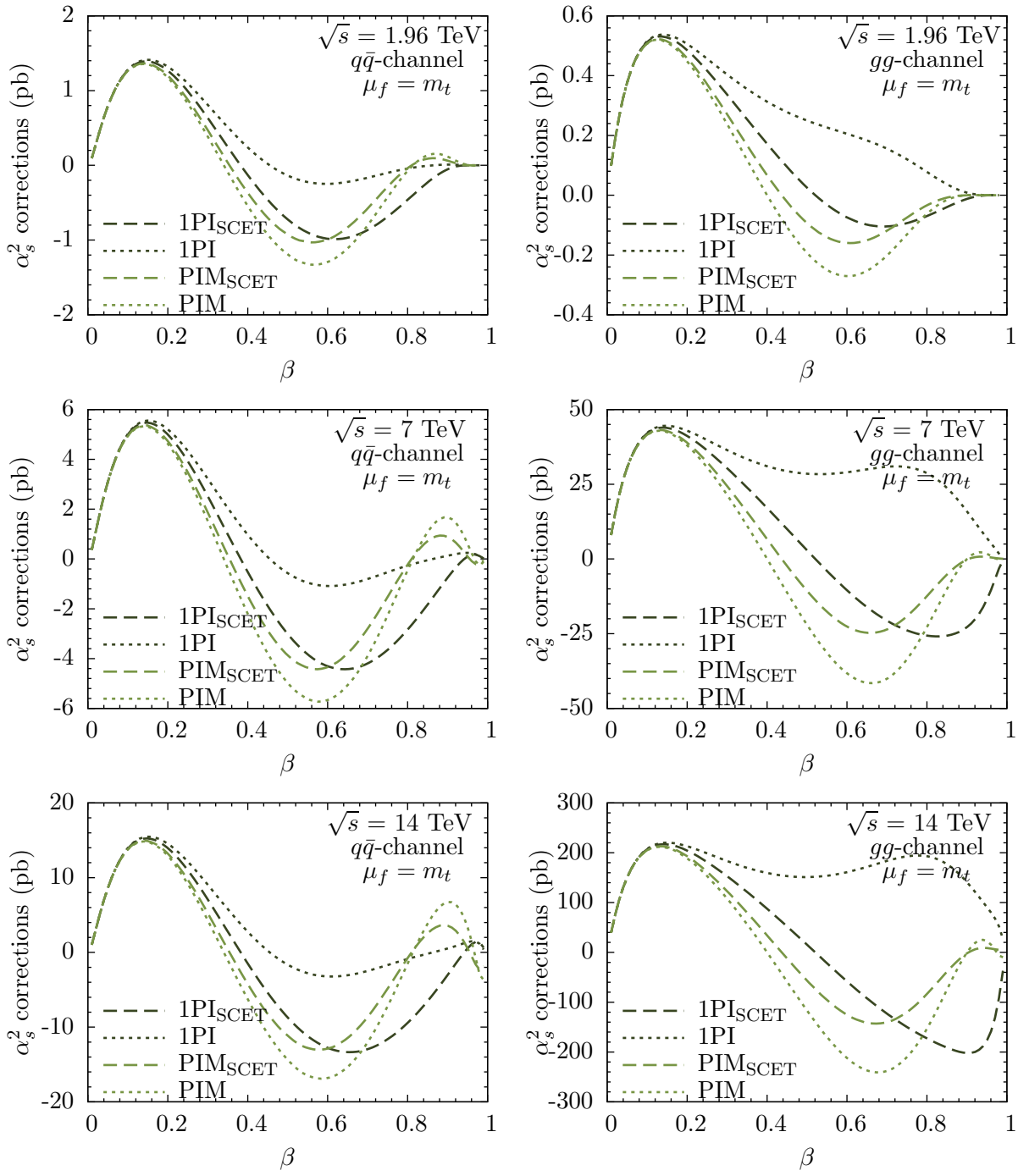

Figure 10.4.: The α_s^2 corrections to $d\sigma/d\beta$ arising from the scale-independent piece, for $\mu_f = m_t$.

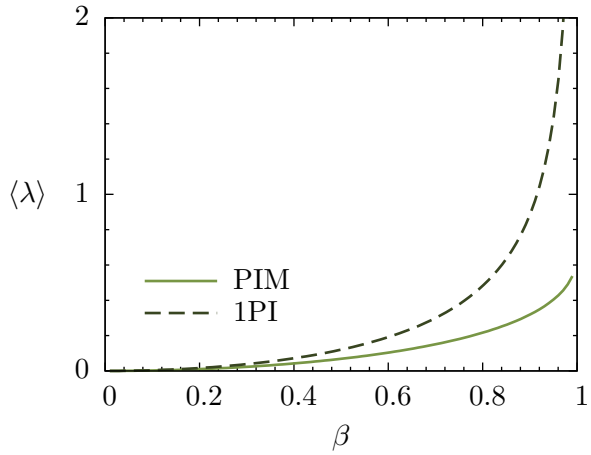

Figure 10.5.: Mean value of the "small" parameter λ, where $\lambda = (1-z)/(2\sqrt{z})$ in PIM and $\lambda = s_4/(2m_t\sqrt{m_t^2+s_4})$ in 1PI kinematics.

and the analogous expression

$$\langle\lambda\rangle_{\text{PIM}} = \int_{4m_t^2/\hat{s}}^1 dz \left(\frac{1-z}{2\sqrt{z}}\right) \Bigg/ \int_{4m_t^2/\hat{s}}^1 dz \tag{10.5}$$

in PIM kinematics. The results are shown in Figure 10.5. In the 1PI scheme, there is a sharp growth in the average value of the "small" parameter λ with increasing β. The expansion parameter in the PIM scheme also increases as a function of β, but not as quickly. Note that this behavior of the partonic expansion parameter λ does not translate directly into correspondingly large corrections to the threshold expansion for the physical cross sections. The singular distributions in s_4 or $(1-z)$ still enhance the region where λ is small, even if the integration range covers regions where it is not, and the regions of β closer to the endpoint are damped by the parton luminosities. However, given the results of the figure, it is not surprising that the power corrections are generally larger in 1PI than in PIM kinematics, and that they are especially important at the LHC, where the parton luminosities are larger at higher values of β.

So far, we have focused on the agreement of the corrections in 1PI or PIM kinematics with the exact QCD results or with each other. We can gain more information by looking at the contributions of the individual terms in the decomposition (6.12) in the 1PI scheme and also at the analogous contributions in the PIM scheme (6.8). The assumption of dynamical threshold enhancement is that contributions from regions of phase space where the partonic expansion parameter λ is large, as shown for example in Figure 10.5, are suppressed due to the properties of the PDFs, so one can expect to see a hierarchy between the different terms in the expansion. In particular, one would expect that the plus-distributions contribute more than the δ-function and of course the power-suppressed contributions contained in R.

			P_3	P_2	P_1	P_0	δ	R	sum
Tevatron	1PI_{SCET}	$\delta\sigma^{(1)}_{q\bar{q}}$			1.1	0.30	−0.06	−0.38	0.94
		$\delta\sigma^{(2)}_{q\bar{q}}$	0.57	0.39	−0.09	−0.19	−0.37	−0.31	0.01
		$\delta\sigma^{(1)}_{gg}$			0.32	0.08	−0.11	−0.06	0.45
		$\delta\sigma^{(2)}_{gg}$	0.39	0.18	−0.07	−0.14	−0.12	−0.12	0.14
	PIM_{SCET}	$\delta\sigma^{(1)}_{q\bar{q}}$			1.2	−0.67	−0.11	0.20	0.64
		$\delta\sigma^{(2)}_{q\bar{q}}$	0.64	−0.24	−0.26	−0.16	−0.08	0.11	0.02
		$\delta\sigma^{(1)}_{gg}$			0.48	−0.24	0.12	0.03	0.38
		$\delta\sigma^{(2)}_{gg}$	0.60	−0.31	−0.11	−0.11	−0.08	0.04	0.10
LHC14	1PI_{SCET}	$\delta\sigma^{(1)}_{q\bar{q}}$			18	1	−2	−9	7
		$\delta\sigma^{(2)}_{q\bar{q}}$	8.1	2.9	−1.6	−0.6	−5.4	−4.6	−1.1
		$\delta\sigma^{(1)}_{gg}$			280	14	124	−125	292
		$\delta\sigma^{(2)}_{gg}$	296	83	−20	−35	−160	−149	16
	PIM_{SCET}	$\delta\sigma^{(1)}_{q\bar{q}}$			11	−9	−1	5	6
		$\delta\sigma^{(2)}_{q\bar{q}}$	5.5	−2.8	−1.7	−1.0	−1.3	1.1	−0.1
		$\delta\sigma^{(1)}_{gg}$			250	−189	120	60	240
		$\delta\sigma^{(2)}_{gg}$	287	−194	−41	−60	−10	37	19

Table 10.1.: Corrections in pb from the different types of distributions at NLO and NNLO, for $\mu_f = m_t$.

The exact structure of contributions to the total cross section from the different terms are shown in Table 10.1, for the choice $\mu_f = m_t$. Generally speaking, the P_i distributions are indeed enhanced compared to the other terms. In fact, the NNLO contributions from P_3 can be as large as the NLO contributions from P_1. However, in both 1PI and PIM kinematics, there are large cancellations between the different terms, so that the total NNLO correction turns out to be small. In PIM kinematics, this happens at the level of the distributions, and to a lesser extent between the δ-function and R terms, which seem to be generically smaller than the other terms. In 1PI kinematics, the δ-function terms and especially the power-suppressed terms in R are relatively larger than in PIM. We emphasize that the results for the coefficients of the P_i distributions are exact, so a full NNLO calculation will change only the δ-function and R pieces, moreover in such a way that the cross section from both types of kinematics agrees exactly. The numbers above suggest that these terms are relatively small in PIM kinematics, because of threshold enhancement, so in order to preserve the good agreement between the two types of kinematics they would also need to be small in 1PI kinematics. In that case the terms already included in our calculation are the dominant ones at NNLO, although this can only be confirmed through the full NNLO results.

10.1.2. Combined Cross Sections in the Pole Scheme

In this section we give results for the total cross section coming from a combination of our PIM and 1PI calculations. This will merge the present state of the art knowledge about higher-order QCD corrections to the production cross section. When combining 1PI and PIM results, the numerical difference between NLO+NNLL and approximate NNLO is rather small. We will focus on the approximate NNLO results in this section for concreteness.

Until now all equations were written for the case where the factorization and renormalization scales are set equal, $\mu_f = \mu_r$. Later on we will consider the case where the running coupling is instead evaluated at an arbitrary renormalization scale μ_r. To derive such expressions we use

$$\alpha_s(\mu_f) = \alpha_s(\mu_r)\left[1 + \frac{\alpha_s(\mu_r)}{\pi}\frac{23}{12}L_{rf} + \left(\frac{\alpha_s(\mu_r)}{\pi}\right)^2\left(\frac{529}{144}L_{rf}^2 + \frac{29}{12}L_{rf}\right)\right], \tag{10.6}$$

with $L_{rf} = \ln(\mu_r^2/\mu_f^2)$, and re-expand the formulas to NNLO in powers of $\alpha_s(\mu_r)$.

To estimate the uncertainties associated with scale variations, we view the cross section as a function of the renormalization and factorization scales, which by default are chosen as $\mu_f = \mu_r = m_t$. We then consider two methods of scale variations: correlated variations with $\mu_f = \mu_r$ varied up and down by a factor of two from the default value, and independent variations of μ_f and μ_r by factors of two, with the uncertainties added in quadrature. We use as our final answer the larger uncertainty from these two methods.

To combine the results from PIM and 1PI kinematics, we first compute the cross sections and scale uncertainties in the PIM_{SCET} and 1PI_{SCET} schemes separately, and obtain six quantities σ_{PIM}, $\Delta\sigma^+_{\text{PIM}}$, $\Delta\sigma^-_{\text{PIM}}$, σ_{1PI}, $\Delta\sigma^+_{\text{1PI}}$, $\Delta\sigma^-_{\text{1PI}}$. The central value and perturbative uncertainties for the combined results are then determined by

$$\begin{aligned}
\sigma &= \frac{1}{2}\left(\sigma_{\text{PIM}} + \sigma_{\text{1PI}}\right), \\
\Delta\sigma^+ &= \max\left(\sigma_{\text{PIM}} + \Delta\sigma^+_{\text{PIM}}, \sigma_{\text{1PI}} + \Delta\sigma^+_{\text{1PI}}\right) - \sigma\,, \\
\Delta\sigma^- &= \min\left(\sigma_{\text{PIM}} + \Delta\sigma^-_{\text{PIM}}, \sigma_{\text{1PI}} + \Delta\sigma^-_{\text{1PI}}\right) - \sigma\,.
\end{aligned} \tag{10.7}$$

In this way, the central value is the average of the two, and the perturbative uncertainties reflect both the variation of the scales and the difference between the two types of kinematics. The PDF uncertainties are estimated as usual by evaluating the average of the 1PI and PIM results using the PDF error sets at a particular confidence level.

We quote in Table 10.2 the approximate NNLO predictions obtained with the above procedure at $m_t = 173.1$ GeV, using the sets of the MSTW2008 NNLO PDFs. To investigate the convergence of the perturbative series, we also list the LO and NLO results, obtained using MSTW2008 LO and NLO PDFs, respectively. In the pole scheme, the scale uncertainties are generally determined by the correlated scale variations with $\mu_r = \mu_f$. The one exception is the upper error at the Tevatron, which is instead determined by the

LO		
	MSTW	CTEQ
Tev.	$6.66^{+2.95+(0.34)}_{-1.87-(0.27)}$	$5.45^{+2.16+0.33(0.29)}_{-1.42-0.27(0.24)}$
LHC7	$122^{+49+(6)}_{-32-(7)}$	$100^{+35+9(7)}_{-24-8(7)}$
LHC14	$681^{+228+(26)}_{-159-(34)}$	$552^{+157+25(18)}_{-115-25(19)}$

NLO		
	MSTW	CTEQ
Tev.	$6.72^{+0.41+0.47(0.37)}_{-0.76-0.45(0.24)}$	$6.77^{+0.40+0.50(0.43)}_{-0.74-0.40(0.34)}$
LHC7	$159^{+20+14(8)}_{-21-13(9)}$	$148^{+18+13(11)}_{-19-12(10)}$
LHC14	$889^{+107+66(31)}_{-106-58(32)}$	$829^{+97+41(27)}_{-96-40(28)}$

NNLO approx.		
	MSTW	CTEQ
Tev.	$6.63^{+0.07+0.63(0.33)}_{-0.41-0.48(0.25)}$	$6.91^{+0.09+0.53(0.46)}_{-0.44-0.43(0.36)}$
LHC7	$155^{+8+14(8)}_{-9-14(9)}$	$153^{+8+13(11)}_{-8-12(10)}$
LHC14	$855^{+52+60(30)}_{-38-59(31)}$	$842^{+51+40(26)}_{-37-40(28)}$

Table 10.2.: Total cross sections in pb for $m_t = 173.1$ GeV with MSTW2008 and CTEQ6.6 PDFs. The first error results from the perturbative uncertainty from both scale variations and the difference between PIM and 1PI kinematics, the second one accounts for the combined PDFs+α_s uncertainty. The numbers in parenthesis show the PDF uncertainty only.

independent variations of μ_r and μ_f added in quadrature. Even though the perturbative uncertainty in the approximate NNLO result includes both scale variations and an estimate of power corrections to the soft limit through the difference of 1PI and PIM kinematics, it is still reduced compared to that in the NLO calculation, which by definition is due only to scale variations. We note that the central value and uncertainties of the approximate NNLO results are well contained within the uncertainty range predicted by the NLO results, so that the perturbative series to this order is well behaved in the pole scheme. The NNLO results are also within the uncertainties of the LO calculation, although the NLO results are slightly higher than the LO ones in the case of the LHC.

For comparison, we also include the results using CTEQ6.6 PDFs [147] in Table 10.2. Since the CTEQ PDFs are based on a NLO fit, the same set is used at LO, NLO and approximate NNLO. The statements based on the analysis with MSTW PDFs above,

including those concerning the moderate size of the NNLO corrections, are also true for the analysis with CTEQ PDFs. In this case, however, the LO results at the LHC are significantly lower than the NLO and NNLO results. To a certain extent, this shows the potential benefit of switching PDFs as appropriate to the order of perturbation theory. On the other hand, LO calculations are usually considered unreliable, so the more important observation for the perturbative convergence is the modest size of the NNLO correction.

The perturbative uncertainties in the approximate NNLO predictions are about the same size at both the Tevatron and the LHC. An additional source of uncertainty is related to the experimental value of $\alpha_s(M_Z)$ (where M_Z denotes the Z-boson mass), which is an input parameter for the running of the strong coupling constant. We estimate this uncertainty in combination with the PDF one by employing the method proposed in [139,148]. Table 10.2 shows that the uncertainty on $\alpha_s(M_Z)$ adds an error of $\pm(3-4)\%$ to the pair-production cross section when the calculation is carried out with MSTW2008 PDFs. The error is somewhat smaller, $\pm(1-2)\%$, when CTEQ6.6 PDFs are used. The reason is that CTEQ6.6 assigns a 90% CL error of ± 0.002 to $\alpha_s(M_Z)$, while for MSTW2008 it is ± 0.003. One can conclude that the $\alpha_s(M_Z)$ induced uncertainty is of the same order of magnitude as the perturbative and PDF uncertainties, and should not be neglected.

For an extraction of the top-quark mass through a comparison with the experimental cross section, we also provide our results as a function of m_t. We parametrize the mass dependence of the approximate NNLO cross section using the simple polynomial fit

$$\sigma(m_t) = c_0 + c_1 x + c_2 x^2 + c_3 x^3 + c_4 x^4 \,, \tag{10.8}$$

where $x = m_t/\text{GeV} - 173$, and c_i are fit coefficients which depend on the collider and the PDF set. The results for the fit coefficients including upper and lower errors due to perturbative uncertainties are shown in Table 10.3, again using MSTW2008 NNLO PDFs. A `Mathematica` implementation of the fit coefficients can be found with the electronic version of our publication [5], where the combined PDF and α_s uncertainties as well as the fit coefficients using CTEQ6.6 PDFs are also included. These fits reproduce the approximate NNLO calculations to 1 permille or better in the range $m_t \in [150, 180]$ GeV. For simplicity the uncertainties on fit coefficients are not displayed in Table 10.3. When these uncertainties are measured in percent of the central value of the cross section, they appear to be roughly independent of m_t in the range $m_t \in [150, 180]$ GeV, differing by no more than a percent from those at $m_t = 173.1$ GeV shown in Table 10.2.

10.1.3. Combined Cross Sections in the $\overline{\text{MS}}$ and 1S Schemes

The pole mass of a quark cannot be defined unambiguously in QCD due to confinement. The perturbatively defined pole mass is sensitive to long-distance physics and suffers from renormalon ambiguities of order Λ_{QCD}. This is an example of infrared renormalons. In general these are connected to the fact that an observable $O(\alpha_s)$ is approximated by a divergent sum $O(\alpha_s) \sim \sum_n c_n \alpha_s^n$ [3], see [149] for details.

[3] In the case of the pole mass the coefficients c_n are proportional to $n!$, leading to a divergent sum.

		c_0 [pb]	c_1 [pb]	c_2 [pb]	c_3 [pb]	c_4 [pb]
Tevatron	σ	6.647×10^{0}	-2.072×10^{-1}	3.617×10^{-3}	-4.304×10^{-5}	8.943×10^{-7}
	σ_+	6.722×10^{0}	-2.091×10^{-1}	3.629×10^{-3}	-5.009×10^{-5}	6.994×10^{-7}
	σ_-	6.233×10^{0}	-1.945×10^{-1}	3.401×10^{-3}	-4.034×10^{-5}	8.176×10^{-7}
LHC7	σ	1.555×10^{2}	-4.665×10^{0}	8.076×10^{-2}	-9.931×10^{-4}	1.753×10^{-5}
	σ_+	1.633×10^{2}	-4.924×10^{0}	8.504×10^{-2}	-1.136×10^{-3}	1.668×10^{-5}
	σ_-	1.468×10^{2}	-4.402×10^{0}	7.517×10^{-2}	-1.033×10^{-3}	1.481×10^{-5}
LHC14	σ	8.576×10^{2}	-2.299×10^{1}	3.653×10^{-1}	-4.027×10^{-3}	7.415×10^{-5}
	σ_+	9.088×10^{2}	-2.446×10^{1}	3.895×10^{-1}	-4.482×10^{-3}	8.142×10^{-5}
	σ_-	8.195×10^{2}	-2.203×10^{1}	3.543×10^{-1}	-3.819×10^{-3}	6.252×10^{-5}

Table 10.3.: Fit coefficients in (10.8) for the total cross sections with perturbative uncertainties at approximate NNLO, using MSTW2008 NNLO PDFs.

In perturbative calculations, the renormalon ambiguity is associated with large higher-order corrections to the pole mass, and thus to any observable calculated in this scheme. Therefore, it is worth investigating short-distance mass definitions which are free from these shortcomings. In this section, we analyze the cross section as a function of the running top-quark mass defined in the $\overline{\text{MS}}$ scheme, and of the threshold top-quark mass defined in the 1S scheme [150].

It is possible to calculate the cross section using the $\overline{\text{MS}}$ mass from the beginning, by performing mass renormalization in that scheme. However, since we already have the cross section in the pole scheme from the last section, it is simpler to convert from one scheme to another using the perturbative relation between the pole mass and $\overline{\text{MS}}$ mass. This relation is currently known to three-loop order [151]. To perform the conversion to the $\overline{\text{MS}}$ scheme, we take that result for QCD with five active flavors and write it in the form

$$m_t = \overline{m}(\bar{\mu}) \left[1 + \frac{\alpha_s(\mu_r)}{\pi} d^{(1)} + \frac{\alpha_s^2(\mu_r)}{\pi^2} d^{(2)} + \mathcal{O}(\alpha_s^3) \right], \tag{10.9}$$

where

$$d^{(1)} = \frac{4}{3} + L_m \,, \qquad d^{(2)} = 8.23656 + \frac{379}{72} L_m + \frac{37}{24} L_m^2 + \frac{23}{12} d^{(1)} L_r \,, \tag{10.10}$$

with $L_m = \ln(\bar{\mu}^2/\overline{m}^2(\bar{\mu}))$ and $L_r = \ln(\mu_r^2/\bar{\mu}^2)$. We then decompose the NNLO cross section in the pole scheme as

$$\sigma_{\text{NNLO}}(m_t) = \left[\frac{\alpha_s(\mu_r)}{\pi}\right]^2 \sigma^{(0)}(m_t, \mu_r) + \left[\frac{\alpha_s(\mu_r)}{\pi}\right]^3 \sigma^{(1)}(m_t, \mu_r) + \left[\frac{\alpha_s(\mu_r)}{\pi}\right]^4 \sigma^{(2)}(m_t, \mu_r) \,, \tag{10.11}$$

eliminate m_t through the relation (10.9), and re-expand the result in powers of $\alpha_s(\mu_r)$. The resulting cross section in the $\overline{\rm MS}$ scheme can be written as

$$\begin{aligned}\bar{\sigma}_{\rm NNLO}(\overline{m}) &= \left[\frac{\alpha_s(\mu_r)}{\pi}\right]^2 \bar{\sigma}^{(0)}(\overline{m}(\bar{\mu}),\bar{\mu},\mu_r) + \left[\frac{\alpha_s(\mu_r)}{\pi}\right]^3 \bar{\sigma}^{(1)}(\overline{m}(\bar{\mu}),\bar{\mu},\mu_r) \\ &+ \left[\frac{\alpha_s(\mu_r)}{\pi}\right]^4 \bar{\sigma}^{(2)}(\overline{m}(\bar{\mu}),\bar{\mu},\mu_r)\,,\end{aligned} \tag{10.12}$$

where

$$\begin{aligned}\bar{\sigma}^{(0)}(\overline{m}(\bar{\mu}),\bar{\mu},\mu_r) &= \sigma^{(0)}(\overline{m}(\bar{\mu}),\mu_r)\,, \\ \bar{\sigma}^{(1)}(\overline{m}(\bar{\mu}),\bar{\mu},\mu_r) &= \sigma^{(1)}(\overline{m}(\bar{\mu}),\mu_r) + \overline{m}(\bar{\mu})\, d^{(1)} \left[\frac{d\sigma^{(0)}(m_t,\mu_r)}{dm_t}\right]_{m_t=\overline{m}(\bar{\mu})}\,, \\ \bar{\sigma}^{(2)}(\overline{m}(\bar{\mu}),\bar{\mu},\mu_r) &= \sigma^{(2)}(\overline{m}(\bar{\mu}),\mu_r) + \overline{m}(\bar{\mu}) \left[d^{(1)} \frac{d\sigma^{(1)}(m_t,\mu_r)}{dm_t} + d^{(2)} \frac{d\sigma^{(0)}(m_t,\mu_r)}{dm_t} \right. \\ &\left. + \frac{\left(d^{(1)}\right)^2 \overline{m}(\bar{\mu})}{2} \frac{d^2\sigma^{(0)}(m_t,\mu_r)}{dm_t^2} \right]_{m_t=\overline{m}(\bar{\mu})}\,.\end{aligned} \tag{10.13}$$

The derivatives can be taken either at the level of the hadronic cross section, using fits such as the one in (10.8), or at the level of the differential cross section before carrying out the phase-space integrations. We have checked our calculations by verifying the agreement between the two methods. We note that our method of converting results from the pole scheme to the $\overline{\rm MS}$ scheme is similar to that used in [43, 152]. Indeed, our approximate NNLO results in the $\overline{\rm MS}$ scheme for the choice $\bar{\mu} = \overline{m}$ agree with those in the HATHOR program [152], apart from the piece related to the NNLO correction $\sigma^{(2)}$, which is of course different since we are not working in the $\hat{s} \to 4m_t^2$ limit of the partonic cross section.

Our procedure for combining the results from 1PI and PIM kinematics in the $\overline{\rm MS}$ scheme is analogous to that for the pole scheme described above. In the present case, we use by default $\mu_f = \mu_r = \overline{m}(\overline{m})$. We must also specify the scale in the running top-quark mass, for which we use $\bar{\mu} = \overline{m}$.[4] We provide results for the cross sections as a function of $\overline{m}(\overline{m})$ using the fit

$$\sigma(\overline{m}) = \bar{c}_0 + \bar{c}_1\bar{x} + \bar{c}_2\bar{x}^2 + \bar{c}_3\bar{x}^3 + \bar{c}_4\bar{x}^4\,, \tag{10.14}$$

where $\bar{x} = \overline{m}/\text{GeV} - 164$. The fit coefficients for the different colliders using the MSTW2008 NNLO PDFs can be found in Table 10.4; those including combined PDF and α_s uncertainties also with CTEQ6.6 PDFs are included in the `Mathematica` notebook mentioned above.

[4] Variations of $\bar{\mu}$ around values close to $\overline{m}$, which would correspond to sampling over different mass definitions, could potentially be used as an additional means of estimating systematic uncertainties. However, a numerical analysis shows that our approximate NNLO results are very stable for variations of $\bar{\mu}$ around the default value.

		$\bar{c}_0$ [pb]	$\bar{c}_1$ [pb]	$\bar{c}_2$ [pb]	$\bar{c}_3$ [pb]	$\bar{c}_4$ [pb]
Tevatron	σ	6.667×10^{0}	-2.178×10^{-1}	3.959×10^{-3}	-5.144×10^{-5}	1.099×10^{-6}
	σ_+	6.777×10^{0}	-2.211×10^{-1}	4.047×10^{-3}	-5.094×10^{-5}	1.116×10^{-6}
	σ_-	6.262×10^{0}	-2.052×10^{-1}	3.811×10^{-3}	-3.887×10^{-5}	1.285×10^{-6}
LHC7	σ	1.574×10^{2}	-4.941×10^{0}	9.009×10^{-2}	-9.385×10^{-4}	2.977×10^{-5}
	σ_+	1.664×10^{2}	-5.200×10^{0}	9.482×10^{-2}	-1.045×10^{-3}	2.813×10^{-5}
	σ_-	1.483×10^{2}	-4.627×10^{0}	8.266×10^{-2}	-1.063×10^{-3}	2.220×10^{-5}
LHC14	σ	8.645×10^{2}	-2.423×10^{1}	3.980×10^{-1}	-4.899×10^{-3}	8.447×10^{-5}
	σ_+	9.207×10^{2}	-2.598×10^{1}	4.342×10^{-1}	-5.006×10^{-3}	1.029×10^{-4}
	σ_-	8.0350×10^{2}	-2.214×10^{1}	3.608×10^{-1}	-4.199×10^{-3}	7.849×10^{-5}

Table 10.4.: Fit coefficients (10.14) for the cross section with perturbative uncertainties at approximate NNLO in the $\overline{\text{MS}}$ scheme, using MSTW2008 NNLO PDFs.

The results for $\overline{m}(\overline{m}) = 164.1$ GeV, which corresponds to $m_t = 173.1$ GeV when using the two-loop conversion between the pole and $\overline{\text{MS}}$ masses, are shown in Table 10.5 for MSTW2008 and CTEQ6.6 PDFs. As in the pole scheme, we switch the order of the MSTW PDFs according to the order of perturbation theory at which we are working, while the CTEQ PDFs are the same in both cases. In the $\overline{\text{MS}}$ scheme, the uncertainties from scale variations are dominated by the scheme where μ_f and μ_r are varied independently, rather than the scheme with correlated $\mu_r = \mu_f$ variations, as was the case in the pole scheme.

We observe that the results obtained from the approximate NNLO formulas are quite close to those in the pole scheme shown in Table 10.2, both in the central values and in the errors. Given this good agreement, which is roughly independent of the exact value of the top-quark mass as shown by the fits, it makes little practical difference whether one extracts the pole mass using the approximate NNLO results, and then determines the $\overline{\text{MS}}$ mass using the perturbative conversion (10.9), or whether one determines the $\overline{\text{MS}}$ mass directly, using the experimental results along with the fits at approximate NNLO. This statement would not be true at very high orders in perturbation theory, since the renormalon ambiguity inherent to the pole mass would lead to large corrections not present in a short-distance scheme such as the $\overline{\text{MS}}$ scheme. But given the present accuracy of perturbative calculations and experimental measurements, this does not yet appear to be an issue.

It is of course still interesting to study whether even at low orders the perturbative expansion is better behaved in the $\overline{\text{MS}}$ scheme than in the pole scheme. We observe that the perturbative uncertainties at NLO are generally smaller in the $\overline{\text{MS}}$ scheme than in the pole scheme, and that the central values are relatively higher compared to the approximate NNLO calculation. For this reason, the overlap between the NLO and approximate NNLO results is actually better in the pole scheme than in the $\overline{\text{MS}}$ scheme.[5] These results differ

[5]The overlap between LO and NLO is worse at the Tevatron and improved at the LHC compared to the pole scheme, but as mentioned earlier we consider the more important issue the overlap between the

LO		
	MSTW	CTEQ
Tev.	$8.82^{+3.91+(0.44)}_{-2.48-(0.35)}$	$7.24^{+2.86+0.46(0.40)}_{-1.89-0.38(0.32)}$
LHC7	$160^{+64+(8)}_{-42-(9)}$	$131^{+45+11(9)}_{-31-10(8)}$
LHC14	$875^{+291+(32)}_{-204-(43)}$	$705^{+199+30(21)}_{-145-30(23)}$

NLO		
	MSTW	CTEQ
Tev.	$7.33^{+0.11+0.50(0.40)}_{-0.49-0.47(0.25)}$	$7.39^{+0.10+0.57(0.50)}_{-0.48-0.45(0.39)}$
LHC7	$179^{+11+15(10)}_{-19-14(10)}$	$167^{+10+15(12)}_{-17-13(11)}$
LHC14	$991^{+79+71(35)}_{-96-62(36)}$	$925^{+71+44(29)}_{-87-43(31)}$

NNLO approx.		
	MSTW	CTEQ
Tev.	$6.64^{+0.11+0.58(0.33)}_{-0.40-0.43(0.23)}$	$6.92^{+0.12+0.52(0.46)}_{-0.43-0.42(0.37)}$
LHC7	$157^{+9+13(8)}_{-9-13(9)}$	$154^{+9+13(11)}_{-9-12(10)}$
LHC14	$862^{+56+54(30)}_{-61-53(32)}$	$848^{+56+37(26)}_{-61-38(28)}$

Table 10.5.: Total cross sections in pb in the $\overline{\text{MS}}$ scheme, for $\overline{m}(\overline{m}) = 164.1$ GeV. The first error results from the perturbative uncertainty from both scale variations and the difference between PIM and 1PI kinematics, the second one accounts for the combined PDFs+α_s uncertainty. The numbers in parenthesis show the PDF uncertainty only.

from those obtained in the $\hat{s} \to 4m_t^2$ limit, where the approximated NNLO corrections and the perturbative uncertainties at that order are significantly smaller in the $\overline{\text{MS}}$ scheme than in the pole scheme [43].

To elaborate further on these results, we note that the re-organization of the perturbative expansion in the $\overline{\text{MS}}$ scheme compared to the pole scheme is accomplished by the terms in square brackets in (10.13). To understand whether these terms are expected to cancel against unphysically large corrections in the pole scheme, we note that the main source of mass dependence in the Born level cross section is due to phase-space factors: the lower limit of integration in (8.4), and an overall factor of $\sqrt{1-4m_t^2/\hat{s}}$ in the partonic cross section related to two-body phase space and multiplying the Born-level matrix element. The

NLO and approximate NNLO results.

derivatives contained in the terms in square brackets are mainly sensitive to those sources of m_t dependence. However, the phase space of the pair production is more indicative of the pole mass than of an $\overline{\text{MS}}$ mass. Indeed, we are calculating the cross section for on-shell quarks according to the narrow width approximation. If the cross section is instead calculated in the $\overline{\text{MS}}$ scheme, the terms in the square brackets of the NLO and NNLO pieces of (10.13) give sizable negative corrections, which are accounted in the pole scheme by using a numerically higher value of the mass in the LO and NLO cross sections. Since the most appropriate mass scheme for a given process is the one where the higher-order corrections are expected to be smallest on physical grounds, it does not seem to us that the $\overline{\text{MS}}$ scheme is the optimal choice for this case.

LO		
	MSTW	CTEQ
Tev.	$6.83^{+3.02+(0.35)}_{-1.92-(0.28)}$	$5.59^{+2.21+0.34(0.30)}_{-1.46-0.28(0.24)}$
LHC7	$124^{+50+(6)}_{-33-(7)}$	$103^{+35+9(7)}_{-24-8(7)}$
LHC14	$696^{+223+(26)}_{-163-(34)}$	$564^{+160+25(18)}_{-117-25(19)}$

NLO		
	MSTW	CTEQ
Tev.	$6.82^{+0.39+0.48(0.38)}_{-0.75-0.46(0.24)}$	$6.87^{+0.38+0.51(0.44)}_{-0.73-0.41(0.34)}$
LHC7	$162^{+19+14(9)}_{-21-13(9)}$	$150^{+17+14(11)}_{-19-12(10)}$
LHC14	$902^{+106+66(32)}_{-106-59(33)}$	$841^{+96+41(27)}_{-96-40(29)}$

NNLO approx.		
	MSTW	CTEQ
Tev.	$6.65^{+0.06+0.63(0.32)}_{-0.38-0.47(0.24)}$	$6.93^{+0.08+0.54(0.47)}_{-0.40-0.42(0.36)}$
LHC7	$156^{+7+14(9)}_{-8-14(8)}$	$154^{+7+13(11)}_{-8-12(10)}$
LHC14	$859^{+47+59(30)}_{-35-58(32)}$	$846^{+46+39(25)}_{-35-40(29)}$

Table 10.6.: Total cross sections in pb in the 1S scheme, for $m_t^{\text{1S}} = 172.3$ GeV. The first error results from the perturbative uncertainty from both scale variations and the difference between PIM and 1PI kinematics, the second one accounts for the combined PDFs+α_s uncertainty. The numbers in parenthesis show the PDF uncertainty only.

As an alternative to the $\overline{\text{MS}}$ mass, we consider the group of short-distance masses known as threshold masses [153]. At lower orders in perturbation theory, these are closer numeri-

cally to the pole mass, but they do not suffer from renormalon ambiguities at higher orders. The cross section in these schemes can be easily calculated from the pole-scheme results, using an analogous procedure to the $\overline{\text{MS}}$ scheme calculation. It is evident that at approximate NNLO the numerical difference between these results and the $\overline{\text{MS}}$ and pole-scheme results will be quite small once the numerical value of the mass is adjusted appropriately, but we nonetheless illustrate this with a specific example. In particular, we consider the cross section as a function of the 1S mass introduced in [150]. The 1S mass is defined through the perturbative contribution to the mass of a hypothetical $n = 1$, $^3S_1$ toponium bound state. To perform the conversion to this scheme, we write its relation with the pole mass in the form [150]

$$m_t = m_t^{\text{1S}} \Bigg\{ 1 + \frac{\alpha_s(\mu_r)}{\pi} \frac{2}{9} \pi \alpha_s(\mu_r) + \left(\frac{\alpha_s(\mu_r)}{\pi} \right)^2 \left[\frac{2}{9} \pi \alpha_s(\mu_r) \left(\frac{23}{3} \ln \frac{3\mu_r}{4\alpha_s(\mu_r) m_t^{\text{1S}}} + \frac{181}{18} + \frac{2}{9} \pi \alpha_s(\mu_r) \right) \right] + \mathcal{O}\left(\frac{\alpha_s^3}{\pi^3} \right) \Bigg\} \tag{10.15}$$

and follow the same procedure as for the $\overline{\text{MS}}$ scheme calculation with the appropriate replacements, cf. (10.9). Note that in the above relation $\pi\alpha_s$ is counted as $\mathcal{O}(1)$ and is not expanded. The results are listed in Table 10.6 for the value $m_t^{\text{1S}} = 172.3$ GeV, which corresponds to a pole mass of $m_t = 173.1$ GeV using the two-loop conversion above. The approximate NNLO results in this scheme are very similar to those in the pole and $\overline{\text{MS}}$ schemes, but the moderate size of the NNLO correction is more indicative of the pole scheme than of the $\overline{\text{MS}}$ scheme. This leads us to conclude once again that although at yet higher orders in perturbation theory the pole mass would be disfavored, at approximate NNLO accuracy this is not yet a problem.

10.1.4. Comparing to Measurements

In Figure 10.6 we show our combined results for the total cross section as a function of the top-quark mass m_t defined in the pole scheme, using MSTW2008 NNLO PDFs. The bands reflect the uncertainties coming from scale variation alone, and from scale variation in addition with PDF+α_s uncertainties. On the left side we compare these with the dependence of a D0 measurement on m_t at the Tevatron [146]. On the right side we present our predictions for the m_t-dependent cross section in combination with new measurements done by the CMS [72] and ATLAS [73] collaborations. Both analyses use a top-quark mass of 172.5 GeV, but we have set them aside in Figure 10.6 for clarity. Both for the Tevatron and LHC there is good agreement between theoretical predictions and measurements.

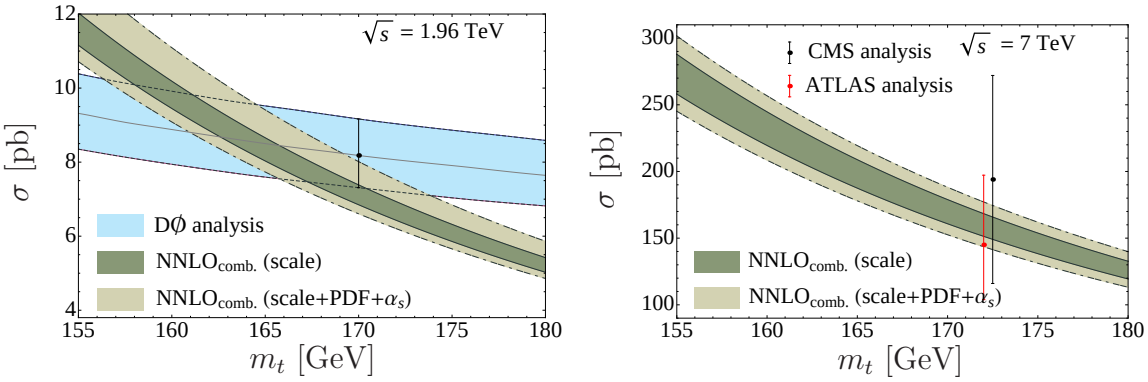

Figure 10.6.: Left: Dependence of the total cross section on the top-quark mass defined in the pole scheme. The bands reflect the uncertainties coming from scale variation alone, and from scale variation in addition with PDF+α_s uncertainties. The blue band shows the dependence of a D0 measurement of the total cross section on m_t [146]. Right: The same for the LHC but with a comparison to recent CMS [72] and ATLAS [73] measurements.

10.2. Forward-Backward Asymmetry

10.2.1. Introduction

The forward-backward asymmetry in top-quark pair production in proton-antiproton collisions is an observable which originates from the difference in the production rates for top quarks in the forward and backward hemispheres [15, 16]. As already mentioned in Section 1.3, the total FB asymmetry was measured by the CDF and D0 collaborations at the Tevatron [79–82]. The measurement can be carried out in the laboratory frame ($p\bar{p}$ frame) as well as in the center-of-mass frame of the top-quark pair ($t\bar{t}$ frame). The asymmetries in the two frames are defined as

$$A_{\text{FB}}^{i} = \frac{N(y_t^i > 0) - N(y_t^i < 0)}{N(y_t^i > 0) + N(y_t^i < 0)}\,, \tag{10.16}$$

where N is the number of events, $i = p\bar{p}\,(t\bar{t})$ indicates the laboratory frame ($t\bar{t}$ frame), and y_t^i is the top-quark rapidity in frame i. The measurements obtained by the CDF collaboration using 5.3 fb^{-1} of data are [82]

$$\begin{aligned} A_{\text{FB}}^{p\bar{p}} &= (15.0 \pm 5.5)\% \quad (p\bar{p}\text{ frame})\,, \\ A_{\text{FB}}^{t\bar{t}} &= (15.8 \pm 7.5)\% \quad (t\bar{t}\text{ frame})\,. \end{aligned} \tag{10.17}$$

The quoted uncertainties are derived from a combination of statistical and systematic errors.

At the Tevatron, the charge conjugation invariance of the strong interaction implies that the difference in the production of top quarks in the forward and backward hemispheres

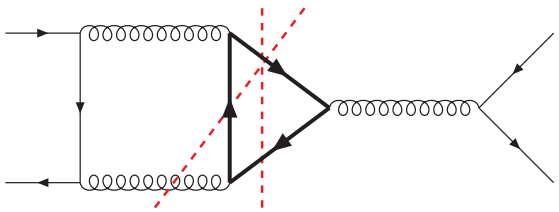

Figure 10.7.: Examples of interferences contributing to the charge-asymmetric cross section. The two-particle cut corresponds to the interference of a one-loop box with the tree-level diagram, while the three-particle cut corresponds to the interference of tree-level diagrams with a $t\bar{t}g$ final state.

is equivalent to the difference in the production of top and antitop quarks in the forward hemisphere. Therefore, in QCD the FB asymmetry is equivalent to the charge asymmetry.

At leading order in QCD ($\mathcal{O}(\alpha_s^2)$), the charge-asymmetric cross section vanishes. This quantity receives non-zero contributions starting at $\mathcal{O}(\alpha_s^3)$. These arise if, in the interference of one-loop and tree-level diagrams, the top-quark fermionic line and the light-quark fermionic line are connected by three gluons. The same observation applies also to the interference of two tree-level diagrams with three particles in the final state. In Figure 10.7 we show the interference of the planar box with the tree-level diagram and the corresponding interference of real emission diagrams. The other contribution to the asymmetry at $\mathcal{O}(\alpha_s^3)$ in the quark-annihilation channel originates from the interference of the crossed box and tree-level diagram (or from the corresponding real emission case). This can be visualized by imagining to cross the two gluons on the left side of the heavy-quark triangle in Figure 10.7. The color factors multiplying the structure in Figure 10.7 or its crossed counterpart are respectively

$$\mathcal{C}_{\text{planar}} = \frac{1}{16N^2}\left(f_{abc}^2 + d_{abc}^2\right), \qquad \mathcal{C}_{\text{crossed}} = \frac{1}{16N^2}\left(d_{abc}^2 - f_{abc}^2\right), \tag{10.18}$$

where $f_{abc}^2 = (N^2-1)N$ and $d_{abc}^2 = (N^2-1)(N^2-4)/N$. When the color factors are stripped off, the interference in Figure 10.7 and its crossed counterpart satisfy the relation

$$d\sigma_{\text{planar}}^{p\bar{p}\to t\bar{t}X} = -d\sigma_{\text{crossed}}^{p\bar{p}\to \bar{t}tX}. \tag{10.19}$$

This relation holds both for the three-particle and the two-particle cuts. Therefore, the charge-asymmetric cross section is proportional to d_{abc}^2. The interference of the one-loop box diagrams with the tree-level diagram gives a positive contribution to the asymmetry, which is partially canceled by the asymmetry originating from the interference of initial- and final-state radiation diagrams. An additional small contribution to the asymmetry at $\mathcal{O}(\alpha_s^3)$ originates from the flavor excitation channel $gq(\bar{q}) \to t\bar{t}X$ at tree level. The gluon-fusion channel does not contribute to the charge-asymmetric cross section, due to the fact that the gluon distribution is the same for protons and antiprotons. The study of

the charge-asymmetric cross section at $\mathcal{O}(\alpha_s^3)$ shows that top quarks (anti-top quarks) are preferably emitted of the direction of the incoming quark (anti-quark); consequently, in $p\bar{p}$ collisions top quarks are preferably emitted in the direction of the incoming proton [15,16].

The total FB asymmetry predicted by QCD at the first non-vanishing order (which, for reasons discussed later, we will indicate as next-to-leading order (NLO)) is lower than the one measured at the Tevatron. Applying the formulas of [16], we obtain the following values using MSTW2008 NLO PDFs,

$$A_{\rm FB}^{p\bar{p},\,\rm NLO} = (4.8^{+0.5}_{-0.4})\% \quad (p\bar{p}\text{ frame})\,,$$
$$A_{\rm FB}^{t\bar{t},\,\rm NLO} = (7.4^{+0.7}_{-0.6})\% \quad (t\bar{t}\text{ frame})\,. \tag{10.20}$$

The central values quoted in (10.20) refer to the choice $\mu_f = m_t$, and again $m_t = 173.1$ GeV. The errors originate from the standard scale variation. These choices will also be adopted in the rest of the section. Electroweak corrections enhance the prediction for the asymmetry by less than 10% of the central value [16, 154], and to separate uncertainties coming from electroweak calculations we do not include these corrections in our numerical results. As one can see, the discrepancy between the theory prediction and the experimental measurement in the $p\bar{p}$ frame is less than two standard deviations (2σ), while in the $t\bar{t}$ frame the two values agree within $\sim 1\sigma$, although the central value of the experimental measurement is a bit higher.

In [82], the CDF collaboration measured the FB asymmetry in the $t\bar{t}$ frame as a function of the top-pair invariant mass $M_{t\bar{t}}$. After grouping the events in two bins corresponding to $M_{t\bar{t}} \leq 450$ GeV and $M_{t\bar{t}} \geq 450$ GeV, they found the asymmetry in the latter bin to be

$$A_{\rm FB}^{t\bar{t}}\,(M_{t\bar{t}} \geq 450\,\text{GeV}) = (47.5 \pm 11.4)\%\,, \tag{10.21}$$

which is more than 3σ higher than the stated theoretical NLO prediction in [82] of $(8.8 \pm 1.3)\%$ obtained using the MCFM program [155]. A measurement of the FB asymmetry in two bins of the rapidity difference $y_t - y_{\bar{t}}$ was also performed and again in that case the higher bin shows a tension with the NLO QCD prediction, although with larger experimental errors. Many attempts to explain these results in terms of new physics scenarios have been made, see e.g. [156–166]. The task is complicated by the fact that the new physics contributions should not spoil the good agreement between theory and measurements for the total pair-production cross section and the differential distribution in the pair invariant mass.

In the previous chapters we had calculated the top-pair invariant-mass distribution and the top-quark rapidity and transverse-momentum distributions in RG improved perturbation theory. By integrating the differential distributions it is then straightforward to calculate the top-quark FB asymmetry both in the laboratory frame and in the $t\bar{t}$ frame. Starting from the double differential cross section in the pair invariant mass and scattering angle, we can also compute the $M_{t\bar{t}}$ and rapidity-dependent asymmetries, which can be compared to experimental measurements. The main goal of this section is to present the result of these calculations of the total and differential FB asymmetries in a systematic way.

At the Large Hadron Collider (LHC), the symmetry of the pp initial state dictates that the rapidity distributions of the top and antitop quarks are symmetric and that the FB asymmetry vanishes. However, it was observed in [16] that at the LHC top quarks are preferably produced at larger rapidities than antitop quarks in the laboratory frame. Like the FB asymmetry at the Tevatron, this rapidity-dependent charge asymmetry is generated at order α_s^3 in the squared amplitude, mainly through the asymmetric part of the quark-antiquark annihilation channel. Therefore, potential new physics contributions would effect these two quantities in a correlated way, and the higher collider energy at the LHC gives it better access to distortions at higher rapidities. As a final application of our formalism, we evaluate at NLO+NNLL order the partially integrated charge asymmetry at the LHC, giving results as a function of a lower cut-off on the top and antitop rapidities in the laboratory frame.

10.2.2. FB Asymmetry in the Laboratory Frame

Total Asymmetry

Using our results from Chapter 5, the FB asymmetry in the laboratory frame can be calculated starting from the top-pair production cross section differential with respect to the top-quark transverse momentum p_T and rapidity y_t. To do so, it is convenient to first define a total and differential asymmetric cross section via

$$\begin{aligned}\Delta\sigma_{\mathrm{FB}}^{p\bar{p}} &\equiv \int_0^{y_t^+} dy_t \left[\int_0^{p_T^{\max}} dp_T \, \frac{d^2\sigma^{p\bar{p}\to tX_{\bar{t}}}}{dp_T dy_t} - \int_0^{p_T^{\max}} dp_T \, \frac{d^2\sigma^{p\bar{p}\to tX_{\bar{t}}}}{dp_T d\bar{y}_t}\bigg|_{\bar{y}_t=-y_t}\right] \\ &\equiv \int_0^{y_t^+} dy_t \left[\left(\frac{d\sigma}{dy_t}\right)_F - \left(\frac{d\sigma}{dy_t}\right)_B\right] \equiv \int_0^{y_t^+} dy_t \frac{d\Delta\sigma_{\mathrm{FB}}^{p\bar{p}}}{dy_t}\,. \end{aligned} \tag{10.22}$$

Here

$$y_t^+ = \frac{1}{2}\ln\frac{1+\sqrt{1-4m_t^2/s}}{1-\sqrt{1-4m_t^2/s}} \quad \text{and} \quad p_T^{\max} = \frac{\sqrt{s}}{2}\sqrt{\frac{1}{\cosh^2 y_t} - \frac{4m_t^2}{s}}\,, \tag{10.23}$$

where s is again the square of the hadronic center-of-mass energy. To obtain the FB asymmetry in the laboratory frame one needs to calculate the ratio of the asymmetric cross section in (10.22) to the total cross section:

$$A_{\mathrm{FB}}^{p\bar{p}} = \frac{\Delta\sigma_{\mathrm{FB}}^{p\bar{p}}}{\sigma}\,. \tag{10.24}$$

In our phenomenological analysis we will consider two levels of perturbative precision for the asymmetric cross section and FB asymmetry. The first involves the differential cross section at NLO in fixed-order perturbation theory, the second the NLO calculation supplemented with soft-gluon resummation to NNLL order. In the laboratory frame, the

resummed calculations are carried out using the 1PI_{SCET} scheme. While in the fixed-order counting the asymmetric cross section first arises from the NLO calculation of the differential cross section, in the resummed counting it first appears at NLL order. The NLO+NNLL calculation is thus a refinement on the leading term, and will be considered our best prediction.

Before illustrating our results for the FB asymmetry, we need to clarify an important point concerning our convention for counting orders in the perturbative expansion. We calculate A_{FB} itself as a perturbative expansion in α_s, using a fixed-order or logarithmic counting as appropriate. For example, the first non-vanishing contribution to the asymmetry in fixed-order perturbation theory is obtained by calculating the numerator in (10.24) to order α_s^3 and the denominator to order α_s^2. The resulting asymmetry is of order α_s, which we will refer to as NLO, with reference to the order at which the differential distributions in (10.22) are calculated relative to α_s^2. Similarly, in RG-improved perturbation theory, the first non-vanishing contribution to A_{FB} is obtained by calculating both the numerator and the denominator at next-to-leading-logarithmic (NLL) order; the resulting asymmetry is then counted as NLL. There are two counting schemes in the literature (in fixed-order perturbation theory) which are different from ours. The first one also treats A_{FB} itself as a perturbative expansion, but counts the order α_s contribution as LO, and so on, as in [15, 16]. The second one treats the numerator and the denominator as separate perturbative series and does not further expand the ratio, as adopted in the quoted MCFM results in [82]. We note that while the first scheme differs from ours only by name, the second scheme leads to different numerical results. In general we find that the NLO+NNLL results are considerably more stable with respect to the choice of scheme than the NLO results.

	MSTW2008		CTEQ6.6		NNPDF2.1	
	$\Delta\sigma_{\text{FB}}^{p\bar{p}}$ [pb]	$A_{\text{FB}}^{p\bar{p}}$ [%]	$\Delta\sigma_{\text{FB}}^{p\bar{p}}$ [pb]	$A_{\text{FB}}^{p\bar{p}}$ [%]	$\Delta\sigma_{\text{FB}}^{p\bar{p}}$ [pb]	$A_{\text{FB}}^{p\bar{p}}$ [%]
NLO	$0.260^{+0.141+0.020}_{-0.084-0.014}$	$4.81^{+0.45+0.13}_{-0.39-0.13}$	$0.256^{+0.135}_{-0.082}$	$4.69^{+0.44}_{-0.38}$	$0.269^{+0.144}_{-0.086}$	$4.82^{+0.47}_{-0.38}$
Res.	$0.312^{+0.027+0.023}_{-0.035-0.019}$	$4.88^{+0.20+0.17}_{-0.23-0.18}$	$0.319^{+0.026}_{-0.037}$	$4.79^{+0.17}_{-0.25}$	$0.335^{+0.029}_{-0.039}$	$4.93^{+0.22}_{-0.24}$

Table 10.7.: The asymmetric cross section and FB asymmetry in the $p\bar{p}$ frame, at NLO order and at NLO+NNLL (Res.). The first error refers to perturbative uncertainties estimated through scale variations as explained in the text, and the second error in the MSTW2008 case is the PDF uncertainty.

Our results for the total FB asymmetry in the lab frame are shown in Table 10.7. As explained above, to calculate each entry in the table the numerator and the denominator in (10.24) are evaluated at the order indicated in the leftmost column, and then the ratio itself is expanded in powers of α_s up to the appropriate order. The central values are obtained by fixing the factorization scale at $\mu_f = m_t$, and the scale uncertainties are estimated by varying μ_f between $m_t/2$ and $2m_t$.[6] In the resummed calculations also the hard and

[6]Although we use $m_t = 173.1$ GeV throughout the analysis, the asymmetry is rather stable under the

soft scales are varied according to SUES with default values for μ_h and μ_s as given in Section 9.2.2. The effect of these variations is included in the scale uncertainty shown in the tables. In the first column of the table we use MSTW2008 PDFs and estimate the PDF uncertainties again by iterating through the 90% confidence level sets. Again we use PDFs as given by Table 7.1. The PDF uncertainties for the asymmetry, expressed as a percentage of the central values, are about half as large as those for the asymmetric cross section. This is due to cancellations in the ratio. In addition to results with MSTW2008 PDFs, we also show those obtained using CTEQ6.6 and NNPDF2.1 [167] PDFs. In those cases the PDFs are based on a NLO fit so that the same set is used in both the NLO and the NLO+NNLL calculations. We note that the results for the asymmetry obtained with the different PDF sets are well within the PDF uncertainties estimated through the MSTW2008 results.

Adding soft-gluon resummation at NNLL accuracy produces results for the asymmetric cross section which are numerically consistent with the NLO results for $\mu_f = m_t$, while the scale uncertainty is reduced by more than a factor of 2. The central value for the FB asymmetry does not change significantly with respect to the NLO predictions, and also in this case the scale uncertainties are reduced. We can therefore conclude that the discrepancy between theory and experiment cannot be explained with the effect of higher-order QCD corrections on the theory side, at least not those related to soft-gluon resummation.

The NLO+NNLL calculation represents the most accurate determination of the QCD contribution to the asymmetry that can be obtained at present. However, it is important to keep in mind the uncertainties related to yet higher-order corrections and how they could be reduced. The arguments based on the dynamical enhancement of the threshold region and the confirmation of this mechanism through the numerical results at NLO, imply that power corrections to the soft limit are small, so we expect the more important effect to be the calculation of the soft plus virtual corrections. We estimate uncertainties related to both types of corrections through the standard method of scale variations and the numerical results indicate that these higher-order effects are moderate. Again however, this statement can of course never be certain without the actual calculation of the higher-order pieces. Similar comments apply to all other quantities obtained in this section.

Rapidity-Dependent Asymmetry

As experimental measurements become more precise, differential quantities such as the rapidity-dependent asymmetry can be compared with theoretical predictions. Using quan-

exact choice of m_t. For instance, at $m_t = 160$ GeV the default value for the asymmetric cross section at NLO with MSTW2008 PDFs changes to $\Delta\sigma_{\rm FB}^{p\bar{p}} = 0.384$ pb, but the asymmetry itself changes only by a small amount to $A_{\rm FB}^{p\bar{p}} = 4.67\%$.

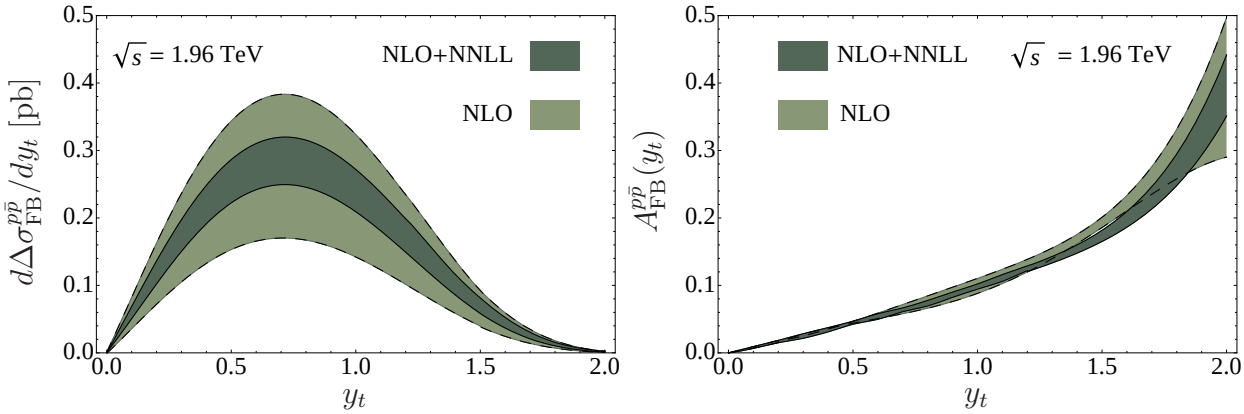

Figure 10.8.: Left: The asymmetric differential cross section $d\Delta\sigma^{p\bar{p}}_{\rm FB}/dy_t$. Right: The asymmetry $A^{p\bar{p}}_{\rm FB}(y_t)$. The bands show the uncertainties related to scale variation as explained in the text.

tities defined in (10.22), we can write this differential asymmetry as

$$A^{p\bar{p}}_{\rm FB}(y_t) = \frac{\left(\frac{d\sigma}{dy_t}\right)_F - \left(\frac{d\sigma}{dy_t}\right)_B}{\left(\frac{d\sigma}{dy_t}\right)_F + \left(\frac{d\sigma}{dy_t}\right)_B} = \frac{\frac{d\Delta\sigma^{p\bar{p}}_{\rm FB}}{dy_t}}{\left(\frac{d\sigma}{dy_t}\right)_F + \left(\frac{d\sigma}{dy_t}\right)_B}\,. \tag{10.25}$$

In Figure 10.8 we show results for the differential asymmetric cross section and the FB asymmetry as functions of the rapidity at NLO and NLO+NNLL order, using MSTW2008 PDFs. Here and below, the differential cross sections at NLO are obtained by the private NLO version of MadGraph. The bands refer to uncertainties associated with scale variations. One observes that the NLO+NNLL band for the asymmetric differential cross section displayed in the left-hand panel is contained within the NLO band over the entire range of y_t values shown in the figure, and that the scale uncertainty of the NLO+NNLL asymmetric cross section is smaller than the scale uncertainty obtained in the NLO calculation. On the other hand, the differences between the error bands in the NLO and NLO+NNLL results for the FB asymmetry shown in the right-hand panel are much smaller due to cancellations in the ratio which make the NLO FB asymmetry considerably more stable than the corresponding asymmetric cross section. We will encounter this feature repeatedly in the $t\bar{t}$-frame calculations which follow. One observes that the form of the rapidity-dependent asymmetry, which is an increasing function with respect to y_t, is very stable under higher-order corrections.

10.2.3. FB Asymmetry in the $t\bar{t}$ Frame

Total Asymmetry

For the studies of the FB asymmetry in the $t\bar{t}$ rest frame we use our results from Chapter 4. Thus, the fundamental quantity is the top-pair production cross section differential with respect to the pair invariant mass and the top-quark scattering angle in that frame. We define an asymmetric cross section as

$$\begin{aligned}\Delta\sigma_{\mathrm{FB}}^{t\bar{t}} &\equiv \int_{2m_t}^{\sqrt{s}} dM_{t\bar{t}} \left[\int_0^1 d\cos\theta \, \frac{d^2\sigma^{p\bar{p}\to t\bar{t}X}}{dM_{t\bar{t}}d\cos\theta} - \int_{-1}^0 d\cos\theta \, \frac{d^2\sigma^{p\bar{p}\to t\bar{t}X}}{dM_{t\bar{t}}d\cos\theta}\right] \\ &\equiv \int_{2m_t}^{\sqrt{s}} dM_{t\bar{t}} \left[\left(\frac{d\sigma}{dM_{t\bar{t}}}\right)_F - \left(\frac{d\sigma}{dM_{t\bar{t}}}\right)_B\right] \equiv \int_{2m_t}^{\sqrt{s}} dM_{t\bar{t}} \frac{d\Delta\sigma_{\mathrm{FB}}^{t\bar{t}}}{dM_{t\bar{t}}}, \end{aligned} \tag{10.26}$$

and the total FB asymmetry in the $t\bar{t}$ frame is then given by

$$A_{\mathrm{FB}}^{t\bar{t}} = \frac{\Delta\sigma_{\mathrm{FB}}^{t\bar{t}}}{\sigma} \,. \tag{10.27}$$

As in the previous section, we will study the FB asymmetry at both NLO and NLO+NNLL accuracy. In the $t\bar{t}$ frame, the resummed calculations are carried out using the $\mathrm{PIM}_{\mathrm{SCET}}$ scheme. The difference between the calculation of the asymmetry in the $t\bar{t}$ frame and the partonic center-of-mass frame is numerical negligible. The results in these two frames coincide in the threshold limit $z \to 1$, and differ by only about 1% at NLO, due to very small corrections from hard gluon emission.

	MSTW2008		CTEQ6.6		NNPDF2.1	
	$\Delta\sigma_{\mathrm{FB}}^{t\bar{t}}$ [pb]	$A_{\mathrm{FB}}^{t\bar{t}}$ [%]	$\Delta\sigma_{\mathrm{FB}}^{t\bar{t}}$ [pb]	$A_{\mathrm{FB}}^{t\bar{t}}$ [%]	$\Delta\sigma_{\mathrm{FB}}^{t\bar{t}}$ [pb]	$A_{\mathrm{FB}}^{t\bar{t}}$ [%]
NLO	$0.395^{+0.213+0.028}_{-0.128-0.021}$	$7.32^{+0.69+0.18}_{-0.59-0.19}$	$0.389^{+0.205}_{-0.123}$	$7.14^{+0.67}_{-0.54}$	$0.411^{+0.218}_{-0.131}$	$7.36^{+0.70}_{-0.58}$
Res.	$0.448^{+0.080+0.030}_{-0.071-0.026}$	$7.24^{+1.04+0.20}_{-0.67-0.27}$	$0.461^{+0.083}_{-0.073}$	$7.16^{+1.05}_{-0.68}$	$0.486^{+0.088}_{-0.078}$	$7.39^{+1.08}_{-0.69}$

Table 10.8.: The asymmetric cross section and FB asymmetry in the $t\bar{t}$ rest frame, at NLO order and at NLO+NNLL (Res.). The first error refers to perturbative uncertainties estimated through scale variations, and the second error in the MSTW2008 case is the PDF uncertainty.

Our numerical results for the total asymmetric cross section and FB asymmetry are summarized in Table 10.8. As was the case in the laboratory frame, the scale uncertainties in the asymmetric cross section are roughly halved at NLO+NNLL order compared to NLO. The scale uncertainties in the FB asymmetry, on the other hand, actually increase slightly after adding the resummation, while the central values are nearly unchanged. We note however that the resummed results are more stable with respect to the scheme for expanding the ratio defining the FB asymmetry, and in that sense are more reliable than the

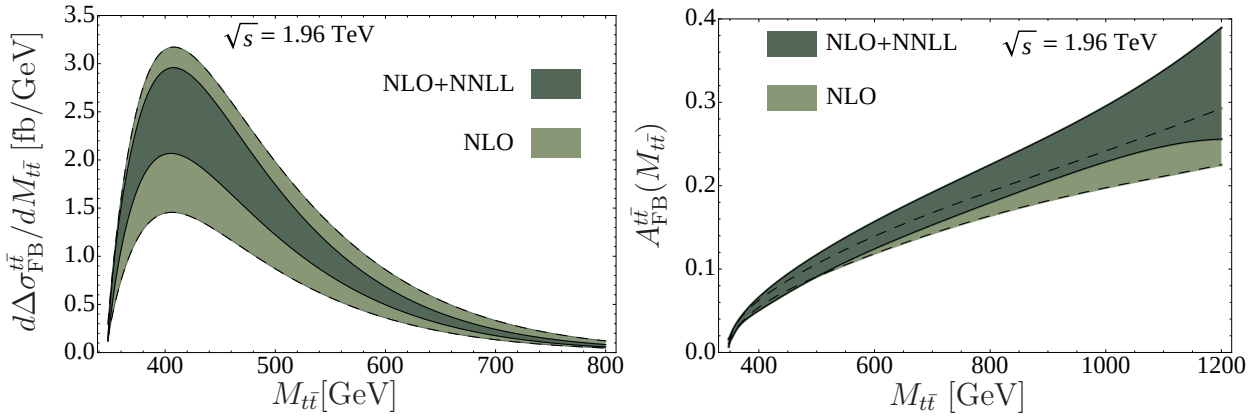

Figure 10.9.: Left: The asymmetric cross section $d\Delta\sigma^{t\bar{t}}_{\rm FB}/dM_{t\bar{t}}$ as a function of the invariant mass at NLO and NLO+NNLL order. Right: The asymmetry $A^{t\bar{t}}_{\rm FB}(M_{t\bar{t}})$. The bands show the uncertainties related to scale variation as explained in the text.

NLO predictions. Moreover, the resummed results for both the asymmetric and total cross sections are more stable under scale variations than their fixed-order counterparts. One should therefore be cautious of the rather small scale uncertainties in the NLO calculation of the FB asymmetry, which result from large cancellations in the ratio not observed in the resummed result. We again show the PDF uncertainties using the MSTW2008 PDFs at 90% CL, and the central values and scale uncertainties from the CTEQ6.6 and NNPDF2.1 sets. All comments from the previous section concerning the reduction of PDF errors in the FB asymmetry compared to the asymmetric cross section, and the good agreement between the different PDF sets, are also true in this case.

Invariant-Mass Dependent Asymmetry

As mentioned in the introduction, the recent measurement of the asymmetry at high values of the pair invariant mass shows a large deviation from the value predicted by QCD at NLO. In order to examine the effects of soft-gluon resummation on this observable, we first extract from (10.26) the invariant-mass dependent asymmetry as

$$A^{t\bar{t}}_{\rm FB}(M_{t\bar{t}}) = \frac{\left(\frac{d\sigma}{dM_{t\bar{t}}}\right)_F - \left(\frac{d\sigma}{dM_{t\bar{t}}}\right)_B}{\left(\frac{d\sigma}{dM_{t\bar{t}}}\right)_F + \left(\frac{d\sigma}{dM_{t\bar{t}}}\right)_B} = \frac{\frac{d\Delta\sigma^{t\bar{t}}_{\rm FB}}{dM_{t\bar{t}}}}{\frac{d\sigma}{dM_{t\bar{t}}}} \,. \tag{10.28}$$

Results for $A^{t\bar{t}}_{\rm FB}(M_{t\bar{t}})$ and $d\Delta\sigma^{t\bar{t}}_{\rm FB}/dM_{t\bar{t}}$ at NLO and NLO+NNLL order are shown in Figure 10.9, where the bands reflect uncertainties originating from scale variations. The figure shows that the asymmetry increases with the invariant mass and can reach nearly 40% at $M_{t\bar{t}} = 1200$ GeV. These results are obtained with the default MSTW2008 PDFs and do not

include PDF uncertainties. An analysis shows that the relative PDF error for $d\Delta\sigma^{t\bar{t}}_{\rm FB}/dM_{t\bar{t}}$ increases slightly with increasing $M_{t\bar{t}}$, from 7% (400 GeV) to 9% (1200 GeV). In contrast, the relative PDF error for $A^{t\bar{t}}_{\rm FB}(M_{t\bar{t}})$ is rather small and even decreases with $M_{t\bar{t}}$, from around 2% (400 GeV) to 1% (1200 GeV).

It is a well-known fact that electroweak corrections start to become more important for the differential cross section at high pair invariant mass, due to the presence of Sudakov logarithms. For instance, at $M_{t\bar{t}} \sim 1$ TeV, the electroweak corrections to the differential distribution at the Tevatron are roughly at the -5% level [168, 169], even though for the total cross section they are negligible. On the other hand, the electroweak corrections to the asymmetric cross section given in [16] do not contain Sudakov logarithms, and an estimate shows that their distortion of the QCD contribution is roughly independent of the invariant mass. We therefore do not expect the electroweak corrections to significantly alter our results for the FB asymmetry even at high values of pair invariant mass.

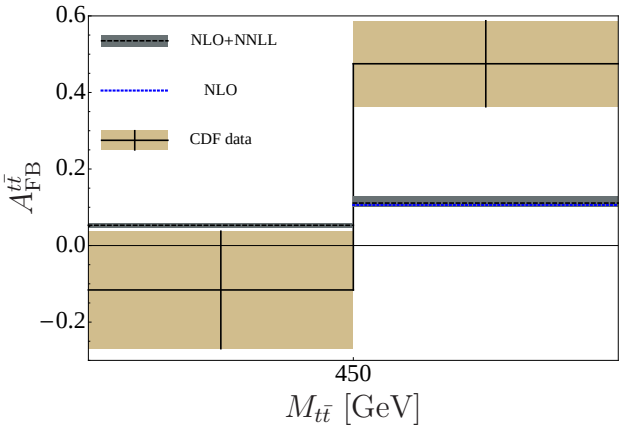

Figure 10.10.: The asymmetry in the high and low invariant-mass region as measured in [82], compared to our predictions at NLO+NNLL order. The bands in the NLO+NNLL results are related to uncertainties from scale variation, while the NLO result in the higher bin is evaluated at $\mu_f = m_t$.

We hope that better statistics can eventually lead to a detailed comparison of experimental results with the asymmetry curve in Figure 10.9. At present this is not possible, but the CDF collaboration has measured the invariant-mass dependent asymmetry by separating the events into a high invariant-mass bin ($M_{t\bar{t}} \geq 450$ GeV) and a low invariant-mass bin ($M_{t\bar{t}} \leq 450$ GeV) [82]. From Figure 10.9, one can see that this choice roughly divides the total asymmetric cross section equally between the two bins, although most of the asymmetric cross section in the high invariant-mass bin originates from the region close to 450 GeV. More precisely, the region $450 - 600\,(700)$ GeV captures more than $75\,(90)$% of the total asymmetric cross section in the high invariant-mass bin. To compare with the

	$M_{t\bar{t}} \leq 450$ GeV					
	$\Delta\sigma_{\rm FB}^{t\bar{t}}$ [pb]			$A_{\rm FB}^{t\bar{t}}[\%]$		
CDF				$-11.6^{+15.3}_{-15.3}$		
	MSTW	CTEQ	NNPDF	MSTW	CTEQ	NNPDF
NLO	$0.17^{+0.10}_{-0.05}$	$0.18^{+0.09}_{-0.05}$	$0.19^{+0.09}_{-0.06}$	$5.2^{+0.6}_{-0.2}$	$5.3^{+0.4}_{-0.4}$	$5.4^{+0.3}_{-0.4}$
NLO+NNLL	$0.21^{+0.04}_{-0.03}$	$0.22^{+0.04}_{-0.04}$	$0.23^{+0.04}_{-0.04}$	$5.2^{+0.9}_{-0.6}$	$5.2^{+0.8}_{-0.6}$	$5.4^{+0.7}_{-0.6}$

	$M_{t\bar{t}} > 450$ GeV					
	$\Delta\sigma_{\rm FB}^{t\bar{t}}$ [pb]			$A_{\rm FB}^{t\bar{t}}[\%]$		
CDF				$47.5^{+11.2}_{-11.2}$		
	MSTW	CTEQ	NNPDF	MSTW	CTEQ	NNPDF
NLO	$0.22^{+0.13}_{-0.07}$	$0.22^{+0.12}_{-0.07}$	$0.23^{+0.12}_{-0.07}$	$10.8^{+1.0}_{-0.8}$	$10.4^{+1.0}_{-0.6}$	$10.9^{+0.7}_{-0.6}$
NLO+NNLL	$0.24^{+0.04}_{-0.04}$	$0.25^{+0.05}_{-0.04}$	$0.26^{+0.04}_{-0.04}$	$11.1^{+1.7}_{-0.9}$	$10.8^{+1.7}_{-0.9}$	$11.4^{+1.3}_{-1.0}$

Table 10.9.: Comparison of the low- and high-mass asymmetry $A_{\rm FB}^{t\bar{t}}$ with CDF data [82], along with results for the asymmetric cross section. The errors in the QCD predictions refer to perturbative uncertainties related to scale variation.

CDF results, we evaluate the binned asymmetry

$$A_{\rm FB}^{t\bar{t}}(m_1, m_2) = \frac{\displaystyle\int_{m_1}^{m_2} dM_{t\bar{t}} \left(d\Delta\sigma_{\rm FB}^{t\bar{t}}/dM_{t\bar{t}} \right)}{\displaystyle\int_{m_1}^{m_2} dM_{t\bar{t}} \left(d\sigma/dM_{t\bar{t}} \right)} \,, \tag{10.29}$$

for $M_{t\bar{t}} \leq 450$ GeV and for $M_{t\bar{t}} \geq 450$ GeV. Our findings are given in Table 10.9, along with their visual representation in Figure 10.10, which shows the NLO+NNLL calculation with an error band from scale variations along with the default NLO number in the high invariant-mass bin. In both bins, the NLO+NNLL predictions for the asymmetric cross sections have considerably smaller scale uncertainties than the NLO ones, but the results for the FB asymmetries are essentially unchanged. As with all other results obtained in the $t\bar{t}$ frame, the scale uncertainties in the FB asymmetries are larger in the NLO+NNLL calculation that at NLO. However, if we had not expanded the ratio, the predicted FB asymmetry in the high invariant-mass bin would be 9.0% at NLO and 10.6% at NLO+NNLL order[7], showing the stability of the resummed results under this change of systematics.

We now turn to a discussion of the PDF uncertainties in the binned results, in this case deviating slightly from our usual procedure. The reason is that to compute the PDF uncertainties for the binned asymmetry at NLO+NNLL order, we need to run the Monte

[7]Using MSTW2008 PDFs as an example.

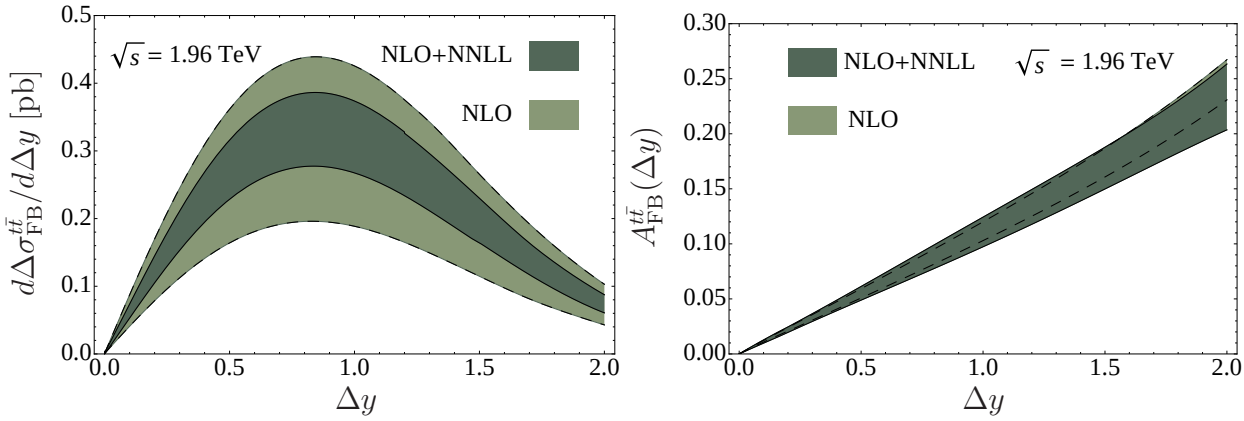

Figure 10.11.: Left: The asymmetric differential cross section $d\Delta\sigma^{t\bar{t}}_{\rm FB}/d\Delta y$. Right: The asymmetry $A^{t\bar{t}}_{\rm FB}(\Delta y)$. The bands show the errors related to scale variation as explained in the text.

Carlo program MadGraph at NLO for each of the PDFs in the error set, which is rather time consuming. As a compromise, we have estimated the PDF uncertainties using only the pieces of the NLO calculation which are leading in the threshold limit $M^2_{t\bar{t}}/\hat{s} \to 1$. Since these leading pieces alone account for the bulk of the NLO FB asymmetry, the relative PDF uncertainties obtained from these terms should provide a good approximation to those in the full NLO and NLO+NNLL results. For the MSTW2008 set, we find a relative PDF uncertainty of about 7% for the asymmetric cross section and about 2% for the FB asymmetry at 90% CL, in both the low and high invariant-mass bins.

Our calculations show that neither higher-order corrections from soft-gluon resummation nor the inclusion of a systematic uncertainty coming from PDF usage reduces in any significant way the current discrepancy between theory and experiment for the FB asymmetry in the high invariant-mass bin, which remains above the 3σ level when using our NLO+NNLL calculations.

Rapidity-Dependent Asymmetry

A further observable of interest is the rapidity dependence of the FB asymmetry in the $t\bar{t}$ frame. In practice, experiments measure the asymmetry as a function of the pair rapidity difference $\Delta y = y_t - y_{\bar{t}}$ [82]. We can calculate the differential cross section in this variable from the results in PIM kinematics by using that, up to power corrections which vanish in the soft limit,

$$\Delta y = \ln\left(\frac{1+\cos\theta\sqrt{1-4m_t^2/M_{t\bar{t}}^2}}{1-\cos\theta\sqrt{1-4m_t^2/M_{t\bar{t}}^2}}\right). \tag{10.30}$$

	$\Delta y < 1$		$\Delta y \geq 1$	
	$\Delta\sigma_{\rm FB}^{t\bar{t}}$ [pb]	$A_{\rm FB}^{t\bar{t}}$ [%]	$\Delta\sigma_{\rm FB}^{t\bar{t}}$ [pb]	$A_{\rm FB}^{t\bar{t}}$ [%]
CDF		$2.6^{+11.8}_{-11.8}$		$61.1^{+25.6}_{-25.6}$
NLO	$0.204^{+0.105}_{-0.064}$	$4.86^{+0.42}_{-0.35}$	$0.172^{+0.094}_{-0.057}$	$15.29^{+1.26}_{-1.11}$
NLO+NNLL	$0.230^{+0.040}_{-0.035}$	$4.77^{+0.39}_{-0.35}$	$0.196^{+0.035}_{-0.031}$	$14.59^{+2.16}_{-1.30}$

Table 10.10.: Comparison of $A_{\rm FB}^{t\bar{t}}$ for $\Delta y < 1$ and $\Delta y \geq 1$ with CDF data [82], along with the asymmetric cross section. The errors in the QCD predictions refer to the uncertainties related to scale variation.

After changing variables from the scattering angle to the pair rapidity difference, we express the asymmetric cross section as

$$\begin{aligned}\Delta\sigma_{\rm FB}^{t\bar{t}} &= \int_0^{\Delta y_+} d\Delta y \left[\int_{M_{t\bar{t}}^{\rm min}}^{\sqrt{s}} dM_{t\bar{t}} \frac{d^2\sigma^{p\bar{p}\to t\bar{t}X}}{dM_{t\bar{t}}d\Delta y} - \int_{M_{t\bar{t}}^{\rm min}}^{\sqrt{s}} dM_{t\bar{t}} \frac{d^2\sigma^{p\bar{p}\to t\bar{t}X}}{dM_{t\bar{t}}d\Delta\bar{y}}\bigg|_{\Delta\bar{y}=-\Delta y} \right] \\ &\equiv \int_0^{\Delta y_+} d\Delta y \left[\left(\frac{d\sigma}{d\Delta y}\right)_F - \left(\frac{d\sigma}{d\Delta y}\right)_B \right] \equiv \int_0^{\Delta y_+} d\Delta y \frac{d\Delta\sigma_{\rm FB}^{t\bar{t}}}{d\Delta y}\,, \end{aligned} \tag{10.31}$$

where

$$\Delta y_+ = \ln\left(\frac{1+\sqrt{1-4m_t^2/s}}{1-\sqrt{1-4m_t^2/s}}\right) \quad \text{and} \quad M_{t\bar{t}}^{\rm min} = 2m_t \cosh\left(\Delta y/2\right)\,. \tag{10.32}$$

Using these definitions, we can also introduce the Δy-dependent asymmetry

$$A_{\rm FB}^{t\bar{t}}(\Delta y) = \frac{\dfrac{d\Delta\sigma_{\rm FB}^{t\bar{t}}}{d\Delta y}}{\left(\dfrac{d\sigma}{d\Delta y}\right)_F + \left(\dfrac{d\sigma}{d\Delta y}\right)_B}\,, \tag{10.33}$$

and binned asymmetries analogous to (10.29), where the numerator and denominator of the above expression are integrated over a range in Δy. Note that the integration region above implies that higher values of Δy correspond to higher values of $M_{t\bar{t}}$. For example, the restriction $\Delta y > 1$ used in the binned analysis below corresponds to events with $M_{t\bar{t}} > 390$ GeV.

We show results related to the rapidity dependence of the FB asymmetry in Figures 10.11 and 10.12, and in Table 10.10. In all cases we use MSTW2008 PDFs. The more detailed results in the Figure 10.11 show the differential asymmetric cross section along with the pair-rapidity dependent FB asymmetry, in the form of bands related to uncertainties from scale variations. While resummation stabilizes the asymmetric cross section compared to NLO, there is little effect on the FB asymmetry. The results for the binned asymmetry are

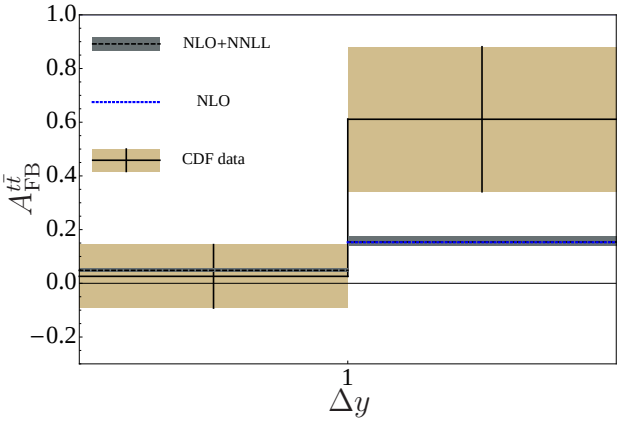

Figure 10.12.: The asymmetry for $\Delta y < 1$ and $\Delta y \geq 1$ as measured in [82], compared to our predictions at NLO+NNLL order. The bands in the NLO+NNLL results are related to uncertainties from scale variation, while the NLO result in the higher bin is evaluated at $\mu_f = m_t$.

given in Table 10.10, along with their visual representation in Figure 10.12, which shows the NLO+NNLL result with an error band from scale variations along with the default NLO number in the higher bin. For events where $\Delta y \leq 1$, the QCD prediction is in agreement with the CDF measurement [82]. In the bin where $\Delta y \geq 1$, the predicted asymmetry is lower than the measured one by $\sim 1.5\sigma$. Again in this case, soft-gluon resummation changes the NLO predictions only slightly.

10.2.4. Charge Asymmetry at the LHC

The Tevatron results for the FB asymmetry at high pair invariant mass and rapidity hint at a discrepancy with the Standard Model. It would of course be desirable to study the physics responsible for this effect through measurements at the LHC.

The total and differential FB asymmetries at the LHC vanish, because of the symmetric initial state. However, while charge conjugation invariance of the strong interaction implies that the rate for the forward production of top-quarks is equal to the rate for backward production of antitop quarks at the Tevatron, this is not the case at the LHC. At a proton-proton collider the total rate for top and antitop production in the forward or backward hemisphere is equal, but at a given rapidity the rates differ. In fact, at large (small) rapidities the rate for top-quark production is noticeably larger (smaller) than that for antitop production [16], so although there is no FB asymmetry at the LHC there is a differential charge asymmetry. Like the FB asymmetry at the Tevatron, this charge asymmetry at the LHC is related to the asymmetric part of the $q\bar{q}$ partonic cross section, implying a direct correlation between potential new physics contributions to the two measurements. The charge asymmetry at the LHC is generally smaller than the FB asymmetry at the Tevatron due to large contributions from the gg channel to the charge-symmetric part of

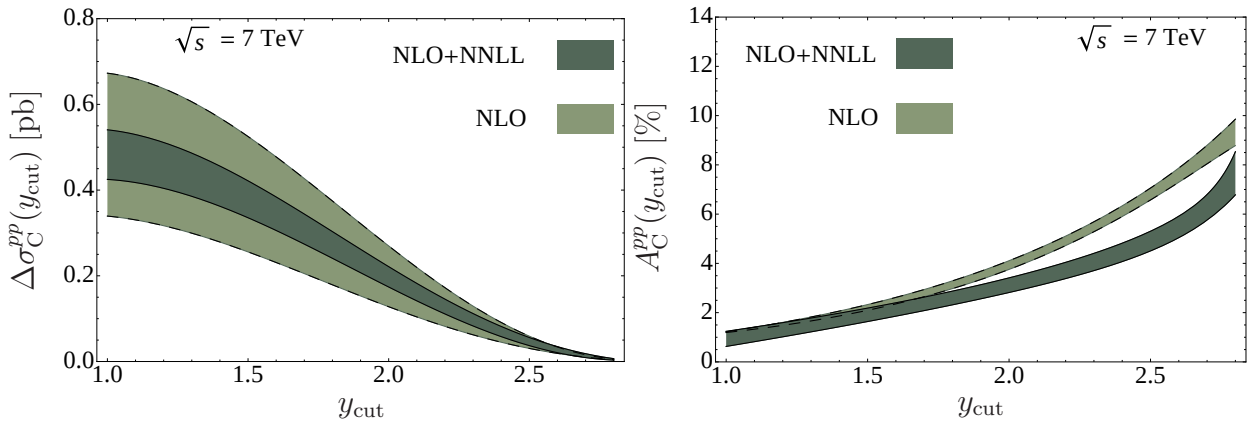

Figure 10.13.: Left: The partially integrated charge-asymmetric cross section $\Delta\sigma_{\mathrm{C}}^{pp}(y_{\mathrm{cut}})$. Right: The partially integrated charge asymmetry $A_{\mathrm{C}}^{pp}(y_{\mathrm{cut}})$. The bands show the uncertainties related to scale variation.

the differential cross section, but the rapidity reach at the LHC is larger and the charge asymmetry thus provides complementary information.

In this section we study the simplest realization of a charge asymmetry at the LHC, namely the rapidity-dependent quantity in the laboratory (pp) frame. In particular, we focus on the partially integrated charge asymmetry and charge-asymmetric cross section, where we impose the restriction $y > y_{\mathrm{cut}}$ on the differential cross section. We define these through

$$\begin{aligned} A_{\mathrm{C}}^{pp}(y_{\mathrm{cut}}) &= \frac{\displaystyle\int_{y_{\mathrm{cut}}}^{y_t^+} dy_t \left(\frac{d\sigma^{pp\to tX_{\bar{t}}}}{dy_t} - \left.\frac{d\sigma^{pp\to \bar{t}X_t}}{dy_{\bar{t}}}\right|_{y_{\bar{t}}=y_t} \right)}{\displaystyle\int_{y_{\mathrm{cut}}}^{y_t^+} dy_t \left(\frac{d\sigma^{pp\to tX_{\bar{t}}}}{dy_t} + \left.\frac{d\sigma^{pp\to \bar{t}X_t}}{dy_{\bar{t}}}\right|_{y_{\bar{t}}=y_t} \right)} \\ &\equiv \frac{\Delta\sigma_{\mathrm{C}}^{pp}(y_{\mathrm{cut}})}{\displaystyle\int_{y_{\mathrm{cut}}}^{y_t^+} dy_t \left(\frac{d\sigma^{pp\to tX_{\bar{t}}}}{dy_t} + \left.\frac{d\sigma^{pp\to \bar{t}X_t}}{dy_{\bar{t}}}\right|_{y_{\bar{t}}=y_t} \right)}, \end{aligned} \tag{10.34}$$

with y_t^+ as in (10.23).

We can study the partially integrated charge asymmetry and asymmetric cross section (10.34) at NLO and NLO+NNLL order using the results for the differential cross section in 1PI kinematics. The results generated with MSTW2008 PDFs are shown in Figure 10.13, where the bands reflect uncertainties related to scale variations carried out with the same procedure as at the Tevatron. For the charge-asymmetric cross section shown in the left-hand panel of the figure, the main effect of the resummation is to decrease the scale de-

pendence of the result to a relatively small region of the NLO error band. For the partially integrated asymmetry shown in the right-hand panel of the figure, the resummation is a mild effect up to $y_{\rm cut} \sim 1.5$, but substantially reduces the asymmetry at higher values of the cut. However, due to large K factors in the gluon channel at the LHC, the uncertainty band for the NLO curve is very sensitive to whether one consistently expands the asymmetry ratio in (10.34). If we had deviated from our normal procedure and had not expanded the ratio, instead evaluating the denominator at NLO order, the NLO band would actually overlap quite well with the NLO+NNLL results shown in figure. The NLO+NNLL result is largely insensitive to this change of systematics–the result where both the numerator and denominator are evaluated at NLO+NNLL order is within the error band shown in the figure.

The partially integrated charge asymmetry vanishes for $y_{\rm cut} = 0$, and becomes progressively larger at higher values of the cut. However, the charge asymmetric cross section shown in the left-hand side of the figure is very small at higher rapidity values and the experimental measurement is difficult. A reasonable way to compare theory and experiment in this case would be to perform a measurement in a high-rapidity bin with $y > y_{\rm cut} \sim$ 1-1.5. In such a bin the Standard Model charge asymmetry is predicted to be only slightly different from zero, less than 2% depending on the exact choice of the cut, so any appreciable charge asymmetry in an experimental measurement would be a clear sign of a new physics contribution to the high-rapidity region of the distribution, which is already hinted at by the Tevatron measurements.

Part IV.

Conclusions

11. Summary and Outlook

Summary

Top-quark physics is a very important area for the search for new physics at the Tevatron and the LHC. Detailed theoretical knowledge about $t\bar{t}$ production is a crucial input for searches for new physics at these facilities. Not only the total cross section is of interest but also differential properties such as the invariant mass, the rapidity and the transverse-momentum distributions. It is thus not surprising that a lot of effort from the theoretical side has been made to describe these observables.

In this thesis we have added to this effort by extending existing results to full NNLL order. Using techniques from effective field theories such as SCET and HQET, we were able to give a factorized formula for the double differential cross section with respect to the invariant mass M, and the top-quark scattering angle θ for the case of pair-invariant mass kinematics. Those results are valid in the threshold $M^2/\hat{s} \to 1$, where $\sqrt{\hat{s}}$ is the partonic center-of-mass energy. By using renormalization group equations, we were able to resum large logarithms of the form $\ln(1-z)$ to NNLL accuracy. As this was done directly in momentum-space, we were able to match these resummed results to the exact ones at NLO in fixed-order perturbation theory in a straightforward way. Similarly, working in single-particle inclusive kinematics, we were able to give a factorized formula for the double differential cross section with respect to the rapidity y and the transverse-momentum p_T of the top-quark. In addition we achieved resummation of large logs, this time in the threshold $s_4 \to 0$, to full NNLL order. In both kinematics we differed to existing resummation schemes by including formally subleading terms, we called our approaches PIM_{SCET} and 1PI_{SCET} respectively. Those terms have been known to be present in the fixed-order expansion of the hard-scattering kernel in other processes. Later, we showed on the level of the β distribution that the PIM_{SCET} and 1PI_{SCET} schemes indeed better approximates exact results compared to traditional approaches. Using the ingredients of our NNLL resummation formulas we showed in detail how to obtain approximate NNLO results for the case of PIM, and for the case of 1PI kinematics. Concerning PIM we went beyond the current accuracy by completely determining the coefficient of the $[1/(1-z)]_+$ distribution. Our analytical expressions for approximate NNLO in 1PI kinematics give explicit results for the $[1/s_4]_+$ coefficient for the first time.

We used our analytical results to make detailed phenomenological studies. We presented the invariant mass distribution at NLO+NNLL order for the first time. The advantages of resummation were clearly seen through the reduction of scale dependence and the better convergence of the perturbative series as can be seen from Figure 8.7. Furthermore we made predictions for the rapidity and transverse-momentum distributions at NLO+NNLL

accuracy. Again, the inclusion of higher order terms lead to a stability of the results with respect to scale variation, as can bee seen from Figure 9.5 and Figure 9.6.

Using the different distributions we made detailed predictions for the total cross section. For both kinematics the resummed results showed a decrease of the scale uncertainties by a factor of two compared to the fixed-order NLO predictions. This can be seen from Table 8.3 for the PIM case, and from Table 9.2 for the 1PI case. The total cross section coming from PIM or 1PI differs solely due to subleading terms in the threshold limits $z \to 1$, and $s_4 \to 0$ respectively. We compared the size of these subleading contributions to the total cross section coming from the two kinematics in Section 10.1.1. In general we observed that the SCET approaches PIM_{SCET} and 1PI_{SCET} are closer to the exact answer than the traditional ones, which can be seen from Figures 10.1 and 10.3. In addition to this we observed that subleading contributions in 1PI are generally larger than in PIM. Furthermore, we compared previous calculations working in the $\beta \to 0$ limit to our PIM_{SCET} results. We found that our predictions give a much better description of the exact answer (as can be seen from Figure 8.13), leading to the fact that subleading terms in β are not generally small.

Having studied the total cross section separately in the two kinematics, we than merged our PIM and 1PI results into a combined prediction. In this way we consolidated the current knowledge about higher order QCD corrections to $t\bar{t}$ production. We gave detailed predictions for the total cross section as a function of the top-quark mass at the LHC and Tevatron at NNLO order. As the pole mass has a renormalon ambiguity we also gave results using the $\overline{\text{MS}}$ and $1S$ mass scheme. Here, despite earlier claims, we did not find a poor convergence of the perturbative series up to NNLO in the pole scheme compared to the $\overline{\text{MS}}$ scheme.

In Section 10.2 we made predictions for the forward-backward asymmetry in the laboratory and the $t\bar{t}$ frame, and compared these results to recent measurements. This was done at NLO+NNLL accuracy, representing the most accurate determination of QCD contribution to the asymmetry to date. In both frames we gave results for the total asymmetry and the asymmetric cross section. From Table 10.7 and Table 10.8 one can see that the impact of higher order corrections to the asymmetry is very modest. From that we concluded that higher order QCD corrections do not account for the current discrepancy between experiment and theory.

In the laboratory frame we also made predictions for the FB asymmetry as a function of the the top-quark rapidity, as shown in Figure 10.8. Here we observed a stark reduction of the scale dependence of the asymmetric cross section compared to the fixed-order NLO prediction, but not so for the asymmetry itself. This feature, coming from large cancellations in the ratio not observed in the resummed result, was also present in $t\bar{t}$-frame calculations. Working in the $t\bar{t}$-frame we made predictions for the invariant-mass dependent asymmetry. We compared our binned results for this quantity to recent measurements, which can be seen in Figure 10.10. We pointed out that neither the inclusion of higher order QCD corrections nor of systematic PDF uncertainties account for the difference between theory and experiment in the high-mass bin, which remains above 3σ. Again in the $t\bar{t}$-frame we compared our predictions for the asymmetry as a function of the rapidity difference

$\Delta y = y_t - y_{\bar{t}}$ to measurement. From Figure 10.12 one can see that also in this case, soft gluon-resummation does change the NLO prediction only slightly. This leaves the discrepancy between experiment and theory in the $\Delta y \geq 1$ bin at the $\sim 1.5\sigma$ level. As a last phenomenological application of our results we made predictions for a charge asymmetry at the LHC coming from a lower cut-off on the top and antitop rapidities in the laboratory frame, see Figure 10.13.

In conclusion, we obtained NLO+NNLL predictions for the invariant mass, the rapidity and the transverse-momentum distribution. This was done using our PIM_{SCET} and 1PI_{SCET} schemes. We made detailed comparisons between our and previous approaches, which showed that the SCET-based approach provides the more reliable prediction. By integrating the differential results we made predictions for the total cross section as a function of the top-quark mass at approximate NNLO order. This was done applying the pole, the $\overline{\text{MS}}$, and the $1S$ mass scheme. Concerning the forward-backward asymmetry at the Tevatron we gave NLO+NNLL predictions for the first time. Numerical results were presented for the total, the invariant-mass, the rapidity, and the rapidity-difference dependent asymmetry. In all cases, when compared to recent measurements, the inclusion of higher order QCD corrections did not account for any discrepancy between experiment and theory, which leaves the experimental results as a possible sign for new physics. As a last application of our analytical expressions, we made predictions for a certain kind of charge asymmetry at the LHC.

The results presented in this work represent the most accurate predictions of higher order QCD corrections to $t\bar{t}$ production so far.

Outlook

Regarding the work presented in this thesis, there are two classes of future extensions. The first is related to an improvement of the methods and results obtained in this work, while the second class deals with using the general methods described here and applying them to other processes.

Connected to the first class is the already mentioned validity of our assumed scale hierarchy in PIM. There, the factorization process was based on the following setup

$$\hat{s}, M^2, |\, \hat{t}_1 \,|, |\, \hat{u}_1 \,|, m_t^2 \gg \hat{s}(1-z) \gg \Lambda^2_{\text{QCD}} \,. \tag{11.1}$$

In the case of very high invariant mass the situation is changed, and one has to consider

$$\hat{s}, M^2, |\, \hat{t}_1 \,|, |\, \hat{u}_1 \,| \gg m_t^2, \hat{s}(1-z) \gg \Lambda^2_{\text{QCD}} \,. \tag{11.2}$$

In this case our approach is not reliable anymore, and one should also resum logs of the ratio M^2/m_t^2. A scale hierarchy as in (11.2) was considered in [178], and in principle we can extend the methods in that paper to the case of hadron-hadron collisions. From a phenomenological point of view this would enable us to investigate the interesting area of

boosted tops. Similarly, our factorization in 1PI depended on the assumption $m_t^2 \gg s_4$, which breaks down for high p_T. With the method mentioned above one should be able to extend our 1PI results to the high p_T area.

There are several examples regarding the second class of extensions. For instance, the stop-antistop production can be calculated along the lines of this work. The overall factorization and resummation techniques are not changed. In addition to that, many input parameters as the soft-function and most of the anomalous dimensions, could be reused. A second example would be gluino-pair production which also can be addressed with the same approach presented here. In both cases the calculation of the one-loop hard function might be the biggest challenge as many massive objects have to be considered in the loop diagrams.

A. Appendix

.1. RG-Evolution Factors and Anomalous Dimensions

Here we collect the expressions of the perturbative solutions to NNLL order for the RG factors S, a_γ as in (4.85), and $\boldsymbol{u}$ as in (4.86) and (5.34), which appear in the solution of the evolution matrix $\boldsymbol{U}$ in the final resummed results (4.94) (PIM) and (5.35) (1PI) . We also collect the expansion coefficients of the anomalous dimensions and QCD β-function needed at this order.

We first define expansion coefficients of the anomalous dimensions and QCD β-function as

$$\begin{aligned}\Gamma_{\text{cusp}}(\alpha_s) &= \Gamma_0 \frac{\alpha_s}{4\pi} + \Gamma_1 \left(\frac{\alpha_s}{4\pi}\right)^2 + \Gamma_2 \left(\frac{\alpha_s}{4\pi}\right)^3 + \dots\,, \\ \beta(\alpha_s) &= -2\alpha_s \left[\beta_0 \frac{\alpha_s}{4\pi} + \beta_1 \left(\frac{\alpha_s}{4\pi}\right)^2 + \beta_2 \left(\frac{\alpha_s}{4\pi}\right)^3 + \dots\right],\end{aligned} \tag{A.1}$$

and similarly for the other anomalous dimensions (recall that $\Gamma_{\text{cusp}} = C_F \gamma_{\text{cusp}}$ for the $q\bar{q}$ channel, and $\Gamma_{\text{cusp}} = C_A \gamma_{\text{cusp}}$ for the gg channel). In terms of these quantities, the function a_Γ is given by [124, 170]

$$a_\Gamma(\nu,\mu) = \frac{\Gamma_0}{2\beta_0}\left\{\ln\frac{\alpha_s(\mu)}{\alpha_s(\nu)} + \left(\frac{\Gamma_1}{\Gamma_0} - \frac{\beta_1}{\beta_0}\right)\frac{\alpha_s(\mu)-\alpha_s(\nu)}{4\pi}\right\}, \tag{A.2}$$

and the result for the Sudakov factor S reads

$$\begin{aligned}S(\nu,\mu) = \frac{\Gamma_0}{4\beta_0^2}\Bigg\{&\frac{4\pi}{\alpha_s(\nu)}\left(1-\frac{1}{r}-\ln r\right) + \left(\frac{\Gamma_1}{\Gamma_0}-\frac{\beta_1}{\beta_0}\right)(1-r+\ln r) + \frac{\beta_1}{2\beta_0}\ln^2 r \\ &+ \frac{\alpha_s(\nu)}{4\pi}\Bigg[\left(\frac{\beta_1\Gamma_1}{\beta_0\Gamma_0}-\frac{\beta_2}{\beta_0}\right)(1-r+r\ln r) + \left(\frac{\beta_1^2}{\beta_0^2}-\frac{\beta_2}{\beta_0}\right)(1-r)\ln r \\ &- \left(\frac{\beta_1^2}{\beta_0^2}-\frac{\beta_2}{\beta_0}-\frac{\beta_1\Gamma_1}{\beta_0\Gamma_0}+\frac{\Gamma_2}{\Gamma_0}\right)\frac{(1-r)^2}{2}\Bigg]\Bigg\},\end{aligned} \tag{A.3}$$

where $r = \alpha_s(\mu)/\alpha_s(\nu)$.

A. Appendix

The matrix equation for $\boldsymbol{u}$ can be evaluated using the techniques described in [171,172]. To this end, we first define the matrix $\boldsymbol{V}$ which diagonalizes $\boldsymbol{\gamma}^{h(0)}$ as

$$\boldsymbol{\gamma}_D^{h(0)} = \boldsymbol{V}^{-1}\boldsymbol{\gamma}^{h(0)}\boldsymbol{V}\,. \tag{A.4}$$

We also define the vector $\vec{\gamma}^{h(0)}$ consisting of the diagonal elements of $\boldsymbol{\gamma}_D^{h(0)}$. Then the solution at NNLL reads

$$\boldsymbol{u}(M, m_t, \cos\theta, \mu_h, \mu) = \boldsymbol{V}\left(1 + \frac{\alpha_s(\mu)}{4\pi}\boldsymbol{K}\right)\left(\left[\frac{\alpha_s(\mu_h)}{\alpha_s(\mu)}\right]^{\frac{\vec{\gamma}^{h(0)}}{2\beta_0}}\right)_D\left(1 - \frac{\alpha_s(\mu_h)}{4\pi}\boldsymbol{K}\right)\boldsymbol{V}^{-1}, \tag{A.5}$$

where the matrix elements of $\boldsymbol{K}$ are

$$K_{IJ} = \delta_{IJ}\vec{\gamma}_I^{h(0)}\frac{\beta_1}{2\beta_0^2} - \frac{\left[\boldsymbol{V}^{-1}\boldsymbol{\gamma}^{h(1)}\boldsymbol{V}\right]_{IJ}}{2\beta_0 + \vec{\gamma}_I^{h(0)} - \vec{\gamma}_J^{h(0)}}\,. \tag{A.6}$$

Finally, we collect the expansion coefficients of the anomalous dimensions and QCD β-function needed in this work. The cusp anomalous dimension to three-loop order is [173]

$$\begin{aligned}
\gamma_0^{\text{cusp}} &= 4\,,\\
\gamma_1^{\text{cusp}} &= \left(\frac{268}{9} - \frac{4\pi^2}{3}\right)C_A - \frac{80}{9}T_F n_f\,,\\
\gamma_2^{\text{cusp}} &= C_A^2\left(\frac{490}{3} - \frac{536\pi^2}{27} + \frac{44\pi^4}{45} + \frac{88}{3}\zeta_3\right) + C_A T_F n_f\left(-\frac{1672}{27} + \frac{160\pi^2}{27} - \frac{224}{3}\zeta_3\right)\\
&\quad + C_F T_F n_f\left(-\frac{220}{3} + 64\zeta_3\right) - \frac{64}{27}T_F^2 n_f^2\,.
\end{aligned} \tag{A.7}$$

For the anomalous dimensions entering $\boldsymbol{\gamma}^h$, we have [126,130]

$$\begin{aligned}
\gamma_0^q &= -3C_F\,,\\
\gamma_1^q &= C_F^2\left(-\frac{3}{2} + 2\pi^2 - 24\zeta_3\right) + C_F C_A\left(-\frac{961}{54} - \frac{11\pi^2}{6} + 26\zeta_3\right) + C_F T_F n_f\left(\frac{130}{27} + \frac{2\pi^2}{3}\right),\\
\gamma_0^g &= -\frac{11}{3}C_A + \frac{4}{3}T_F n_f\,,\\
\gamma_1^g &= C_A^2\left(-\frac{692}{27} + \frac{11\pi^2}{18} + 2\zeta_3\right) + C_A T_F n_f\left(\frac{256}{27} - \frac{2\pi^2}{9}\right) + 4C_F T_F n_f\,,\\
\gamma_0^Q &= -2C_F\,,
\end{aligned}$$

$$\gamma_1^Q = C_F C_A \left(-\frac{98}{9} + \frac{2\pi^2}{3} - 4\zeta_3\right) + \frac{40}{9} C_F T_F n_f \,, \tag{A.8}$$

as well as [126, 131, 174–177]

$$\begin{aligned}
\gamma_0^{\rm cusp}(\beta) &= \gamma_0^{\rm cusp} \beta \coth\beta \,, \\
\gamma_1^{\rm cusp}(\beta) &= \gamma_1^{\rm cusp} \beta \coth\beta + 8 C_A \Bigg\{ \frac{\pi^2}{6} + \zeta_3 + \beta^2 \\
&\quad + \coth^2\beta \left[{\rm Li}_3(e^{-2\beta}) + \beta {\rm Li}_2(e^{-2\beta}) - \zeta_3 + \frac{\pi^2}{6}\beta + \frac{\beta^3}{3} \right] \\
&\quad + \coth\beta \left[{\rm Li}_2(e^{-2\beta}) - 2\beta \ln(1 - e^{-2\beta}) - \frac{\pi^2}{6}(1+\beta) - \beta^2 - \frac{\beta^3}{3} \right] \Bigg\} , \\
g_0(\beta) &= 0, \\
g_1(\beta) &= \coth\beta \left[\beta^2 + 2\beta \ln(1 - e^{-2\beta}) - {\rm Li}_2(e^{-2\beta}) + \frac{\pi^2}{6} \right] - \beta^2 - \frac{\pi^2}{6} \,.
\end{aligned} \tag{A.9}$$

The anomalous dimensions of the PDFs are given by

$$\begin{aligned}
\gamma_0^{\phi_q} &= 3 C_F \,, \\
\gamma_1^{\phi_q} &= C_F^2 \left(\frac{3}{2} - 2\pi^2 + 24\zeta_3 \right) + C_F C_A \left(\frac{17}{6} + \frac{22\pi^2}{9} - 12\zeta_3 \right) - C_F T_F n_f \left(\frac{2}{3} + \frac{8\pi^2}{9} \right) , \\
\gamma_0^{\phi_g} &= \frac{11}{3} C_A - \frac{4}{3} T_F n_f \,, \\
\gamma_0^{\phi_g} &= C_A^2 \left(\frac{32}{3} + 12\zeta_3 \right) - \frac{16}{3} C_A T_F n_f - 4 C_F T_F n_f \,,
\end{aligned} \tag{A.10}$$

and for the QCD β-function to three-loop order we have

$$\begin{aligned}
\beta_0 &= \frac{11}{3} C_A - \frac{4}{3} T_F n_f \,, \\
\beta_1 &= \frac{34}{3} C_A^2 - \frac{20}{3} C_A T_F n_f - 4 C_F T_F n_f \,, \\
\beta_2 &= \frac{2857}{54} C_A^3 + \left(2 C_F^2 - \frac{205}{9} C_F C_A - \frac{1415}{27} C_A^2 \right) T_F n_f + \left(\frac{44}{9} C_F + \frac{158}{27} C_A \right) T_F^2 n_f^2 \,.
\end{aligned} \tag{A.11}$$

.2. Integrals for the Soft Functions

Here we give some detail about the calculation of the soft functions appearing in the calculation of the factorization formulas. In Sections 4.2.4 and 5.2.1 we found that the relevant integrals for the PIM and 1PI soft functions are of the general form

$$\mathcal{I}(v_i, v_j) = -\frac{(4\pi\mu^2)^\epsilon}{\pi^{2-\epsilon}}\, v_i \cdot v_j \int d^d k\, \frac{e^{-ik^0 x_0}}{v_i \cdot k\, v_j \cdot k}\, (2\pi)\, \delta(k^2)\, \theta(k^0)\,. \tag{A.12}$$

In both kinematics $v_{i,j}$ can either be a light-like vector n or a space-like vector v. Thus, there are several combinations of v_i with v_j to consider, and we will do this in the following. The outcome of the integrals are general valid for PIM and 1PI kinematics, and we specify when we give results for a special case.

We can write (A.12) as

$$\mathcal{I}(v_i, v_j) = \frac{(4\pi)^\epsilon e^{-\epsilon\gamma_E}}{\pi\epsilon} \qquad \Gamma(1-\epsilon) e^{-\epsilon\gamma_E} (i/2\mu x_0 e^{\gamma_E})^{2\epsilon}$$
$$v_i \times v_j \times \begin{cases} \mathcal{I}^{(1,1)}(a,b,A,B,C)\,; & v_i \neq v_j \\ \mathcal{I}^{(2,0)}(a,b)\,; & v_i = v_j \end{cases}, \tag{A.13}$$

where we take $v_i = (a, 0, 0, -b)$ and $v_j = (A, 0, -C, -B)$. The integrals $\mathcal{I}^{(k,l)}$ are defined by[1]

$$\begin{aligned} \mathcal{I}^{(k,l)}(a,b,A,B,C) &= \int_0^\pi \sin^{d-3}\theta_1 d\theta_1 \int_0^\pi \sin^{d-4}\theta_2 d\theta_2 \\ &\times \quad (a + b\cos\theta_1)^{-k} (A + B\cos\theta_1 + C\sin\theta_1\cos\theta_2)^{-l}\,. \end{aligned} \tag{A.14}$$

In the following we will normalize light-like vectors as $n \cdot \bar{n} = 2$, and normalize time-like vectors as $v^2 = 1$.

1: $\mathbf{v_i = n_1}$, $\mathbf{v_j = n_2}$

We consider now v_i and v_j being two different light-like vectors n_1 and n_2 which we parametrize as

$$n_1 = (1,0,0,1)\,, \quad n_2 = (1,0,\sin\theta,\cos\theta)\,, \quad n_1 \cdot n_2 = 1 - \cos\theta\,. \tag{A.15}$$

Using a special case of the integral $\mathcal{I}^{(k,l)}$

$\mathcal{I}^{(k,l)}(1,-1,1,-\cos\theta,-\sin\theta)$

[1] This form of integrals was already used in [9].

$$= 2^{1-k-l}\pi \frac{\Gamma(1-2\epsilon)\Gamma(1-\epsilon-k)\Gamma(1-\epsilon-l)}{\Gamma^2(1-\epsilon)\Gamma(2-2\epsilon-k-l)}\, {}_2F_1\left(k,l,1-\epsilon,\cos^2\frac{\theta}{2}\right) . \quad \text{(A.16)}$$

One obtains

$$\begin{aligned}\mathcal{I}^{(k,l)}(1,-1,1,-\cos\theta,-\sin\theta) &= -\frac{\pi}{\epsilon}\, {}_2F_1\left(1,1,1-\epsilon,\cos^2\frac{\pi}{2}\right) \\ &= -\frac{\pi}{\epsilon}\left(\frac{n_1\cdot n_2}{2}\right)^{-1-\epsilon}\left[1+\epsilon^2 \mathrm{Li}_2(1-\frac{n_1\cdot n_2}{2})+\mathcal{O}(\epsilon^3)\right] .\end{aligned} \quad \text{(A.17)}$$

With this we one gets

$$\begin{aligned}\mathcal{I}(n_1,n_2) = -(4\pi)^\epsilon e^{-\epsilon\gamma_E}[&\frac{2}{\epsilon^2}+\frac{2}{\epsilon}\left(L_0-\ln\frac{n_1\cdot n_2}{2}\right)+\left(L_0-\ln\frac{n_1\cdot n_2}{2}\right)^2 \\ &+\frac{\pi^2}{6}+2\mathrm{Li}_2\left(1-\frac{n_1\cdot n_2}{2}\right)\Bigg] .\end{aligned} \quad \text{(A.18)}$$

- Special case $n_2=\bar{n}_1$ so that $n_1\cdot n_2=2$:

$$\mathcal{I}(n,\bar{n}) = -(4\pi)^\epsilon e^{-\epsilon\gamma_E}\left[\frac{2}{\epsilon^2}+\frac{2}{\epsilon}L_0+L_0^2+\frac{\pi^2}{6}\right] . \quad \text{(A.19)}$$

- Special case $n_1\cdot n_2 = 2\hat{s}m_t^2/(\hat{t}_1\hat{u}_1)$:

$$\begin{aligned}\mathcal{I}(n_1,n_2) = -(4\pi)^\epsilon e^{-\epsilon\gamma_E}\Bigg[&\frac{2}{\epsilon^2}+\frac{2}{\epsilon}\left(L_0-\ln\frac{\hat{s}m_t^2}{\hat{t}_1\hat{u}_1}\right) \\ &+L_0^2-2L_0\ln\frac{\hat{s}m_t^2}{\hat{t}_1\hat{u}_1}+\ln^2\frac{\hat{s}m_t^2}{\hat{t}_1\hat{u}_1}+\frac{\pi^2}{6}+2\mathrm{Li}_2\left(1-\frac{\hat{s}m_t^2}{\hat{t}_1\hat{u}_1}\right)\Bigg] .\end{aligned} \quad \text{(A.20)}$$

2: $\mathbf{v_i}=\mathbf{v_j}=\mathbf{v}$

We now set v_i and v_j to be the same time-like vector $v=(a,0,0,b)$ with $v^2=1$. With this one obtains

$$\begin{aligned}\mathcal{I}(v,v) &= -\frac{2(4\pi)^\epsilon\mu^{2\epsilon}}{\Gamma(1-\epsilon)}(1-\beta^2)\int_0^\infty dk^0\int_{-k^0}^{k^0}dk^3\,\frac{e^{-ik^0x_0}}{(k^0+\beta k^3)^2}\left((k^0)^2-(k^3)^2\right)^{-\epsilon} \\ &= -\frac{2(4\pi)^\epsilon\mu^{2\epsilon}}{\Gamma(1-\epsilon)}(1-\beta^2)\,\frac{(ix^0)^{2\epsilon}\Gamma(1-2\epsilon)}{-2\epsilon}\,\frac{\pi^{1/2}\Gamma(1-\epsilon)}{\Gamma(3/2-\epsilon)}\, {}_2F_1\left(1,\frac{3}{2},\frac{3}{2}-\epsilon,\beta^2\right) \\ &= \frac{2(4\pi)^\epsilon e^{-\epsilon\gamma_E}}{\epsilon}\left(\frac{i}{2}\mu x_0 e^{\gamma_E}\right)^{2\epsilon}\frac{1-\beta^2}{1-2\epsilon}\, {}_2F_1\left(1,\frac{3}{2},\frac{3}{2}-\epsilon,\beta^2\right) .\end{aligned} \quad \text{(A.21)}$$

Expanding in ϵ, we obtain

$$\begin{aligned}\mathcal{I}(v,v) &= \frac{2(4\pi)^\epsilon e^{-\epsilon\gamma_E}}{\epsilon}\left(\frac{i}{2}\mu x_0 e^{\gamma_E}\right)^{2\epsilon}\left[1+\frac{\epsilon}{\beta}\ln\frac{1+\beta}{1-\beta}\right]\\ &= (4\pi)^\epsilon e^{-\epsilon\gamma_E}\left[\frac{2}{\epsilon}+2L_0+\frac{2}{\beta}\ln\frac{1+\beta}{1-\beta}\right]\\ &= (4\pi)^\epsilon e^{-\epsilon\gamma_E}\left[\frac{2}{\epsilon}+2L_0-\frac{2}{\beta}\ln x\right], \end{aligned} \tag{A.22}$$

where $x=(1-\beta)/(1+\beta)$.

- Special case $\beta\to 0$:

$$\mathcal{I}_0(v,v) = (4\pi)^\epsilon e^{-\epsilon\gamma_E}\left[\frac{2}{\epsilon}+2L_0+4\right]. \tag{A.23}$$

3: $\mathbf{v_i}=\mathbf{v}$, $\mathbf{v_j}=\bar{\mathbf{v}}$

Next we consider $v_i=v=(a,0,0,b)$ and $v_j=\bar{v}=(a,0,0,-b)$ with $v\cdot\bar{v}=(1+\beta^2)/(1-\beta^2)$, where $\beta=b/a$.

$$\begin{aligned}\mathcal{I}(v,\bar{v}) &= -\frac{2(4\pi)^\epsilon\mu^{2\epsilon}}{\Gamma(1-\epsilon)}(1+\beta^2)\int_0^\infty dk^0\int_{-k^0}^{k^0}dk^3\frac{e^{-ik^0x_0}}{(k^0-\beta k^3)(k^0+\beta k^3)}\left((k^0)^2-(k^3)^2\right)^{-\epsilon}\\ &= \frac{2(4\pi)^\epsilon e^{-\epsilon\gamma_E}}{\epsilon}\left(\frac{i}{2}\mu x_0 e^{\gamma_E}\right)^{2\epsilon}\frac{1+\beta^2}{1-\beta^2}\,{}_2F_1\left(1/2,1,3/2-\epsilon,\beta^2\right)\\ &= -(4\pi)^\epsilon e^{-\epsilon\gamma_E}\frac{1+x^2}{1-x^2}\Big[\left(\frac{2}{\epsilon}+2L_0\right)\ln(x)\\ &+4\mathrm{Li}_2(x)+4\ln(x)\ln(1-x)-\ln^2(x)-2\pi^2/3\Big] \end{aligned} \tag{A.24}$$

- Special case $\beta\to 0$:

$$\begin{aligned}\mathcal{I}_0(v,\bar{v}) &= -\frac{2(4\pi)^\epsilon e^{-\epsilon\gamma_E}}{\epsilon}\left(\frac{i}{2}\mu x_0 e^{\gamma_E}\right)^{2\epsilon}(1+2\epsilon)\\ &= -(4\pi)^\epsilon e^{-\epsilon\gamma_E}\left[\frac{2}{\epsilon}+2L_0+4\right]. \end{aligned} \tag{A.25}$$

4: $\mathbf{v_i = n}$, $\mathbf{v_j = n}$

We now consider we set $v_i = n = (1,0,0,1)$ and $v_j = v = (A,0,C,B)$, again $v^2 = 1$. Defining $\beta = \sqrt{B^2+C^2}/A$ and using

$$\begin{aligned}\mathcal{I}^{(1,1)}(1,-1,&A,-B,-C) = \frac{\pi}{A-B}\Big\{-\frac{1}{\epsilon} + \ln\frac{(A-B)^2}{A^2-B^2-C^2} \\ &- \epsilon\Big[\ln^2\frac{A-\sqrt{B^2+C^2}}{A-B} - \frac{1}{2}\ln^2\frac{A+\sqrt{B^2+C^2}}{A-\sqrt{B^2+C^2}} \\ &+ 2\mathrm{Li}_2\left(-\frac{-B+\sqrt{B^2+C^2}}{A-\sqrt{B^2+C^2}}\right) - 2\mathrm{Li}_2\left(-\frac{-B-\sqrt{B^2+C^2}}{A-B}\right)\Big]\Big\} \qquad \text{(A.26)}\end{aligned}$$

Using this in combination with (A.13) one finally arrives at

$$\begin{aligned}\mathcal{I}(n,v) = -(4\pi)^\epsilon e^{-\epsilon\gamma_E}\Big[&\frac{1}{\epsilon^2} + \frac{1}{\epsilon}[L_0 - 2\ln(v\cdot n)] + \frac{1}{2}[L_0 - 2\ln(v\cdot n)]^2 \\ &+ \frac{\pi^2}{12} + 2\mathrm{Li}_2\left(1 - \frac{v\cdot n}{x^{1/2}}\right) + 2\mathrm{Li}_2(1 - v\cdot n\, x^{1/2})\Big]\,. \qquad \text{(A.27)}\end{aligned}$$

In top quark pair production we will need, for example,

$$n\cdot v = \frac{-\hat{t}_1}{\sqrt{\hat{s}}m} = \frac{-\hat{t}_1}{\hat{s}}\frac{1+x}{\sqrt{x}} \quad \text{or} \quad (\hat{t}_1 \leftrightarrow \hat{u}_1). \qquad \text{(A.28)}$$

- Special case $\beta \to 0$:

$$\begin{aligned}\mathcal{I}_0(n,v) &= -\frac{(4\pi)^\epsilon e^{-\epsilon\gamma_E}}{\epsilon^2}\,\Gamma(1-\epsilon)e^{-\epsilon\gamma_E}\left(\frac{i}{2}\mu x_0 e^{\gamma_E}\right)^{2\epsilon} \\ &= -(4\pi)^\epsilon e^{-\epsilon\gamma_E}\left[\frac{1}{\epsilon^2} + \frac{1}{\epsilon}L_0 + \frac{1}{2}L_0^2 + \frac{\pi^2}{12}\right]. \qquad \text{(A.29)}\end{aligned}$$

5: $\mathbf{v_i = v_1}$; $\mathbf{v_j = v_2}$

This integral has only to be considered in 1PI kinematics as PIM works in the partonic center-mass-frame. Consider $v_1 = (1,0,0,0)$, $v_2 = (a,0,0,-b)$ with $v_2^2 = 1$. Defining $\bar{\beta} = b/a$ and $\bar{x} = (1-\bar{\beta})/(1+\bar{\beta})$. We have

$$\begin{aligned}\mathcal{I}(v_1,v_2) &= -\frac{2(4\pi)^\epsilon\mu^{2\epsilon}}{\Gamma(1-\epsilon)}\int_0^\infty dk^0\int_{-k^0}^{k^0}dk^3\,\frac{e^{-ik^0x_0}}{k^0(k^0+\bar{\beta}k^3)}\left((k^0)^2-(k^3)^2\right)^{-\epsilon} \\ &= -\frac{2(4\pi)^\epsilon\mu^{2\epsilon}}{\Gamma(1-\epsilon)}\,\frac{(ix^0)^{2\epsilon}\Gamma(1-2\epsilon)}{-2\epsilon}\,\frac{\pi^{1/2}\Gamma(1-\epsilon)}{\Gamma(3/2-\epsilon)}\,{}_2F_1\left(\frac{1}{2},1,\frac{3}{2}-\epsilon,\bar{\beta}^2\right)\end{aligned}$$

$$= \frac{2(4\pi)^\epsilon e^{-\epsilon\gamma_E}}{\epsilon} \left(\frac{i}{2}\mu x_0 e^{\gamma_E}\right)^{2\epsilon} \frac{1}{1-2\epsilon}\, {}_2F_1\left(\frac{1}{2}, 1, \frac{3}{2}-\epsilon, \bar{\beta}^2\right). \tag{A.30}$$

Expanding in ϵ, we have

$$\mathcal{I}(v_1, v_2) = -(4\pi)^\epsilon e^{-\epsilon\gamma_E} \frac{1}{2\bar{\beta}} \left[\left(\frac{2}{\epsilon} + 2L_0\right) \ln \bar{x} \right.$$
$$\left. - \ln^2 \bar{x} + 4 \ln \bar{x} \ln(1-\bar{x}) + 4\mathrm{Li}_2(\bar{x}) - \frac{2\pi^2}{3}\right]. \tag{A.31}$$

Writing $\bar{\beta} = 2\beta/(1+\beta^2)$ and defining $x = (1-\beta)/(1+\beta)$, we find $\bar{x} = x^2$, and

$$\mathcal{I}(v_1, v_2) = -(4\pi)^\epsilon e^{-\epsilon\gamma_E} \frac{1+\beta^2}{2\beta} \left[\left(\frac{2}{\epsilon} + 2L_0\right) \ln x \right.$$
$$\left. - 2\ln^2 x + 4 \ln x \ln(1-x^2) + 2\mathrm{Li}_2(x^2) - \frac{\pi^2}{3}\right]. \tag{A.32}$$

.3. Comparing NNLL vs. NNLO

In our numerical analysis we considered two different ways of including higher-order perturbative corrections to the hard-scattering kernels: constructing approximate expansions to NNLO in fixed order, and all-orders resummation to NNLL accuracy. We emphasized that for a fixed numerical value of μ_s, the truncation of the NNLL series to NNLO in α_s contains a different structure of corrections than the approximate NNLO formula. Here we explain this statement in more detail, and show explicitly what types of higher-order corrections the master formulas (4.94) and (5.35) resum. The following discussion is equally valid for resummation in PIM and in 1PI but also applies to other processes than those described in this thesis.

To start, let us note that it is sufficient to ignore the matrix structure of the RG equations, and just consider hard and soft functions which are simple functions of their arguments. Then the treatment of the hard function is straightforward, and the complication for the soft function is its non-locality. To explain the issue, it is simplest to start with the hard function. Ignoring its matrix structure and dependence on kinematic invariants, its RG equation is of the form

$$\mu\frac{d}{d\mu} H(L_h, \alpha_s(\mu)) = \left(2\Gamma_{\text{cusp}} \ln\frac{M^2}{\mu^2} + 2\gamma^h\right) H(L_h, \alpha_s(\mu)), \tag{A.33}$$

where $L_h \equiv \ln(M^2/\mu^2)$. The parameter M is to be understood as a generic hard scale; in the specific case of 1PI and PIM kinematics, it would be $M = \sqrt{\hat{s}}$. The RG equation can

be used to generate higher-order terms in the perturbative expansion of H. For instance, we can solve the equation as a fixed-order series in α_s using the ansatz

$$H(L_h, \alpha_s(\mu)) = \alpha_s^2(\mu) \left[h^{(0,0)} + \frac{\alpha_s(\mu)}{4\pi} \sum_{n=0}^{2} h^{(1,n)} L_h^n + \dots \right]. \tag{A.34}$$

In terms of the lowest-order coefficient and the anomalous dimensions and β-function, whose expansions we define as

$$\begin{aligned} \Gamma_{\text{cusp}}(\alpha_s) &= \Gamma_0 \frac{\alpha_s}{4\pi} + \Gamma_1 \left(\frac{\alpha_s}{4\pi}\right)^2 + \Gamma_2 \left(\frac{\alpha_s}{4\pi}\right)^3 + \dots , \\ \beta(\alpha_s) &= -2\alpha_s \left[\beta_0 \frac{\alpha_s}{4\pi} + \beta_1 \left(\frac{\alpha_s}{4\pi}\right)^2 + \beta_2 \left(\frac{\alpha_s}{4\pi}\right)^3 + \dots \right], \end{aligned} \tag{A.35}$$

and similarly for γ^h, the expansion coefficients at NLO can be constructed as

$$H(L_h, \alpha_s(\mu)) = \alpha_s^2(\mu) \left\{ h^{(0,0)} + \frac{\alpha_s(\mu)}{4\pi} \left[-h^{(0,0)} \left(\frac{\Gamma_0}{2} L_h^2 + (\gamma_0^h + 2\beta_0) L_h \right) + h^{(1,0)} \right] + \dots \right\}. \tag{A.36}$$

One can obviously generalize this to any order in α_s and calculate the coefficients of the logarithms at a given order in terms of the anomalous dimensions and lower-order matching coefficients. This is the method used in constructing approximate fixed-order expansions.

In the effective-theory analysis, one assumes the presence of a second, widely separated scale $\mu_s \ll M$ and uses the counting of RG-improved perturbation theory, i.e. $\ln(\mu_s/M) \sim 1/\alpha_s$. Then the higher-order corrections contain large logarithms, which can be resummed to all-orders by using the exact solution to the RG equation. This solution reads [179]

$$H(L_h, \alpha_s(\mu)) = e^{4S(\mu_h,\mu) - 2a_{\gamma^h}(\mu_h,\mu)} H\left(\ln \frac{M^2}{\mu_h^2}, \alpha_s(\mu_h) \right) \left(\frac{M}{\mu_h} \right)^{-2\eta_h}, \tag{A.37}$$

where $\eta_h = 2a_\Gamma(\mu_h, \mu)$. The Sudakov exponent and normal anomalous exponent are the same as in (4.85)

$$S(\mu_h, \mu) = -\int_{\alpha_s(\mu_h)}^{\alpha_s(\mu)} d\alpha \, \frac{\Gamma_{\text{cusp}}(\alpha)}{\beta(\alpha)} \int_{\alpha_s(\mu_h)}^{\alpha} \frac{d\alpha'}{\beta(\alpha')}, \qquad a_\Gamma(\mu_h, \mu) = -\int_{\alpha_s(\mu_h)}^{\alpha_s(\mu)} d\alpha \, \frac{\Gamma_{\text{cusp}}(\alpha)}{\beta(\alpha)}, \tag{A.38}$$

and similarly for a_{γ^h}.

The all-orders solution does not actually depend on μ_h, as indicated by the notation. The same is true if the matching coefficient and the exponentials are consistently re-expanded as a series in $\alpha_s(\mu)$ in fixed order, in which case one just gets back the approximate formulas above. In practice, however, one must truncate the result at a given level of accuracy (e.g. NNLL), and beyond that level a residual dependence on μ_h remains. To avoid large logarithms in the matching coefficients, one chooses $\mu_h \sim M$ and runs to the scale μ_f

using the all-orders solution. Then the exponential factors resum logarithms which count as $\ln(M^2/\mu_f^2)$ and are large for $\mu_f \sim \mu_s$. To see this explicitly, we get rid of $\alpha_s(\mu_h)$ everywhere by using (with $a(\mu_f) \equiv \alpha_s(\mu_f)/4\pi$)

$$a(\mu_h) = \frac{a(\mu_f)}{X} - \frac{a(\mu_f)^2}{X^2}\frac{\beta_1}{\beta_0}\ln X + \dots\,; \qquad X = 1 + \beta_0\, a(\mu_f)\,\ln\frac{\mu_h^2}{\mu_f^2}\,, \tag{A.39}$$

and re-expand the solution in (A.37) as a series in $a(\mu_f)$. For reference, the expansion of the Sudakov factor and anomalous exponent to NNLO read

$$S(\mu_h,\mu_f) = -a(\mu_f)\,\frac{\Gamma_0}{8}\,L_{hf}^2 + a(\mu_f)^2\left(\frac{\beta_0\Gamma_0}{24}L_{hf}^3 - \frac{\Gamma_1}{8}L_{hf}^2\right) + \dots\,, \tag{A.40}$$

$$a_\Gamma(\mu_h,\mu_f) = a(\mu_f)\,\frac{\Gamma_0}{2}\,L_{hf} + a(\mu_f)^2\left(-\frac{\beta_0\Gamma_0}{4}L_{hf}^2 + \frac{\Gamma_1}{2}L_{hf}\right) + \dots\,, \tag{A.41}$$

where $L_{hf} \equiv \ln(\mu_h^2/\mu_f^2)$. The expansion of a_γ is identical to the one in (A.41), with the replacements $\Gamma_i \to \gamma_i$.

Using the above equations to expand (A.37) to NLO, one recovers the NLO solution (A.36). All the dependence on μ_h drops out to that order, as long as we keep the one-loop matching correction. However, this is *not* the case if we expand our NLL approximation of the resummed hard function to NLO. In that case, the NLO matching coefficient is of higher-order in the counting and not included in the formula, so after expansion to NLO dependence on the scale μ_h remains. The direct expansion of our NLL formula at NLO in fixed order reads

$$\alpha_s^2(\mu_f)\,a(\mu_f)\left\{-h^{(0,0)}\ln\frac{\mu_h^2}{\mu_f^2}\left[\frac{\Gamma_0}{2}\ln\frac{\mu_h^2}{\mu_f^2} + \Gamma_0\ln\frac{M^2}{\mu_h^2} + (\gamma_0^h + 2\beta_0)\right]\right\}. \tag{A.42}$$

This is necessarily different than the "approximate NLO" formula one would deduce by dropping the coefficient $h^{(1,0)}$ from (A.36), because it depends on μ_h, but if we set $\mu_h = M$ it is the same, and it is for this reason that one can still say the NLL solution "resums logarithms of the form $\ln(M/\mu_f)$ to all orders", although a more accurate statement would be that it "resums logarithms of the form $\ln(\mu_h/\mu_f)$ to all orders", which includes the possibility of other choices such as $\mu_h = m_t$. Given this fact, it makes little sense to construct an approximate formula for a quantity such as the hard function: if there are large logarithms, it is just as easy to sum them to all orders as it is to construct the fixed-order expansion, and if the logarithms are not large, there is no reason to include that subset of the higher-order corrections without the full answer.

We can repeat the analysis above to compare the structure of approximate fixed-order expansions and resummed formulas for the soft function. In this case the RG equation is non-local, and to solve for the momentum-space soft function we used the technique of Laplace transforms [123]. The solution for the resummed momentum-space soft function is

$$S(\omega,\mu_f) = e^{-4S(\mu_s,\mu_f)+2a_{\gamma^s}(\mu_s,\mu_f)}\,\tilde{s}\,(\partial_\eta,\mu_s)\,\frac{1}{\omega}\left(\frac{\omega}{\mu_s}\right)^{2\eta}\frac{e^{-2\gamma_E\eta}}{\Gamma(2\eta)}\,, \tag{A.43}$$

where $\eta = 2a_\Gamma(\mu_s, \mu_f)$, and $\tilde{s}$ is the Laplace-transformed function, which satisfies the local RG equation

$$\frac{d}{d\ln\mu}\,\tilde{s}\left(\ln\frac{M^2}{\mu^2}, \alpha_s(\mu)\right) = -\left(2\Gamma_{\text{cusp}}\ln\frac{M^2}{\mu^2} + 2\gamma_s\right)\tilde{s}\left(\ln\frac{M^2}{\mu^2}, \alpha_s(\mu)\right). \tag{A.44}$$

In this case, approximate formulas in fixed order are obtained by first constructing the solution to $\tilde{s}$ using the local RG equation. To NNLO, we use the ansatz

$$\tilde{s}(L, \alpha_s(\mu)) = 1 + \frac{\alpha_s(\mu)}{4\pi}\sum_{n=0}^{2} s^{(1,n)}L^n + \left(\frac{\alpha_s(\mu)}{4\pi}\right)^2\sum_{n=0}^{4} s^{(2,n)}L^n + \dots, \tag{A.45}$$

where we set $s^{(0,0)} = 1$ for simplicity. The explicit solution to NNLO reads

$$\begin{aligned}\tilde{s}(L, \alpha_s(\mu)) = 1 &+ \frac{\alpha_s(\mu)}{4\pi}\left[\frac{\Gamma_0}{2}L^2 + L\gamma_0^s + s^{(1,0)}\right] \\ &+ \left(\frac{\alpha_s(\mu)}{4\pi}\right)^2\left[\frac{\Gamma_0^2}{8}L^4 + \left(-\frac{\beta_0\Gamma_0}{6} + \frac{\Gamma_0\gamma_0^s}{2}\right)L^3 + \frac{1}{2}\left(\Gamma_1 - \beta_0\gamma_0^s + (\gamma_0^s)^2 + \Gamma_0 s^{(1,0)}\right)L^2\right. \\ &\left. + (\gamma_1^s - \beta_0 s^{(1,0)} + \gamma_0^s s^{(1,0)})L + s^{(2,0)}\right].\end{aligned} \tag{A.46}$$

To turn this into an approximate NNLO formula for the momentum-space soft function $S(\omega, \mu_f)$, one must take the limit $\mu_s = \mu_f$ and derive replacement rules analogous to (10.9). This is readily done using the expansion

$$\frac{1}{\omega}\left(\frac{\omega}{\mu_s}\right)^{2\eta} = \frac{1}{2\eta}\,\delta(\omega) + \sum_{n=0}^{\infty}\frac{2^n}{n!}\,D_n(\omega)\,\eta^n, \tag{A.47}$$

where the D_n here are defined as

$$D_n(\omega) = \left[\frac{1}{\omega}\,\ln^n\frac{\omega}{\mu_f}\right]_+. \tag{A.48}$$

As was the case with the hard function, the all-orders solution for the resummed soft function does not actually depend on the scale μ_s, but its truncation to a given logarithmic order (e.g. NNLL) introduces residual scale dependence. As explained earlier in this thesis, our method is to choose μ_s to be close to the numerical value where the corrections from the soft function to the (differential) cross section are minimal. We then adopt the parametric counting $\mu_s \sim \omega$ and apply RG-improved perturbation theory with $\ln\mu_s/\mu_f \sim 1/\alpha_s$, and the exponential factors resum logarithms of the form $\ln\mu_s/\mu_f$ to all orders. Since the scale μ_s is dynamically generated through the numerical analysis, it does not appear in the fixed-order calculation, so the resummation formula deals with different types of corrections than

the approximate fixed-order formulas.[2] For this reason, the structure of D_n distributions appearing at a given order is not the same in the two approaches.

We now show this in more detail, working first to NLO. In this case, the "approximate NLO" formula derived from the solution (A.46) reads

$$S(\omega,\mu_f) \approx 1 + a(\mu_f)\left[4\Gamma_0 D_1(\omega) + 2\gamma_0^s D_0(\omega) - \frac{\pi^2}{3}\Gamma_0\,\delta(\omega)\right]. \tag{A.49}$$

This should be compared with the expansion of the NLL formula to NLO in fixed order, for which the NLO correction reads (with $L_s \equiv \ln \mu_s^2/\mu_f^2$)

$$a(\mu_f)\left[2\Gamma_0 L_s D_0(\omega) + \left(\frac{1}{2}\Gamma_0 L_s^2 + \gamma_0^s L_s\right)\delta(\omega)\right] + \dots\,. \tag{A.50}$$

The "approximate NLO" formula has D_1 distributions, while the NLO expansion of our NLL formula has only D_0 distributions. In the counting of RG-improved perturbation theory, however, $D_0 \ln(\mu_s/\mu_f) \sim D_1$, so the tower of logarithms produced by the expansion of the NLL formulas is of course correct. The analogous formula at NNLO is rather lengthy, but to illustrate its structure, we focus on the leading correction in the logarithmic power counting, which reads

$$a(\mu_f)^2\Gamma_0^2\left[12 L_s D_2(\omega) - 6L_s^2 D_1(\omega) + L_s^3 D_0 - \frac{1}{8}L_s^4\,\delta(\omega)\right], \tag{A.51}$$

while the leading term of the "approximate NNLO" formula is

$$a(\mu_f)^2\, 8\Gamma_0^2\, D_3(\omega)\,. \tag{A.52}$$

Again, for $\omega \sim \mu_s$ the terms in the two equations are of the same parametric order but contain different types of distributions: the resummed formulas generate at most D_2 distributions, while the approximate NNLO formulas generate D_3 distributions.

From the discussion above it should be obvious that our formula does not literally resum the highest tower of D_n distributions to all orders, but rather terms which count that way in RG-improved perturbation theory, when the dynamically generated soft scale satisfies $\mu_s \sim \omega$. In the case of the hard function, we noted that the fixed-order corrections produced by expanding the resummed formula were equal to those in the approximate formula for the special choice $\mu_h = M$. For the soft function, there is no numerical value of μ_s for which this would be true, but the two are equal if we replace $L_s \to \partial_\eta$ and take the derivatives before re-expanding η in $\alpha_s(\mu_f)$. This procedure can be generalized to all orders by evaluating the formula

$$S(\omega,\mu_f) = \left\{\left[e^{-4S(\mu_s,\mu_f)+2a_{\gamma^s}(\mu_s,\mu_f)}\,\tilde{s}\,(0,\alpha_s(\mu_s))\right]\Big|_{\ln(\mu_s^2/\mu_f^2)\to\partial\eta}\right\}\frac{1}{\omega}\left(\frac{\omega}{\mu_f}\right)^{2\eta}\frac{e^{-2\gamma_E\eta}}{\Gamma(2\eta)}\Big|_{\eta\to 0}, \tag{A.53}$$

[2] In [106] it was shown that the soft scale decreases as the PDFs fall off more quickly away from values of x where $\omega \sim 0$, so the formulas effectively resum logarithms of the slopes of the PDFs.

where the factor in the curly brackets is understood to be expanded to all orders as a series in $\alpha_s(\mu_f)$ and so is a function only of $\ln(\mu_s^2/\mu_f^2)$. In this way, we exponentiate the derivatives with respect to η, which are what generate the highest-order distributions, and the expansion of the above formula to any given accuracy in fixed-order reproduces the approximate formulas. For instance, if we include the exact one-loop matching (which is just $s^{(1,0)}$) and the two-loop anomalous dimensions, the expansion of the above object gives back our approximate NNLO formula for the soft function, plus higher-order terms that resum all the higher-order D_n distributions at NNLL order, after converting the derivatives with respect to η with replacement rules. While this procedure generalizes choosing $\mu_h = M$ in the hard function, it is by no means the same conceptually. The exact hard function is independent of μ_h, so varying it around values $\mu_h \sim M$ gives a way of estimating the higher-order terms. However, it would make no sense to replace, for instance, $\ln(\mu_s^2/\mu_f^2) \to c_0\partial_\eta$ in (A.53), with $c_0 \neq 1$, since the derivatives generate both μ-independent and μ-dependent terms.

The conclusion of this discussion is that results based on approximate NNLO formulas contain different information than those based on NLO+NNLL resummation. This is not just due to a truncation of the NNLL series to NNLO, but also to the fact that the resummation formula exponentiates logarithms depending on the ratio $\ln \mu_s/\mu_f$ in combination with higher-order logarithmic plus-distributions, with μ_s a dynamically generated numerical soft scale. Such logarithms do not appear in the fixed-order calculation, which is independent of μ_s. Therefore, the choice between using approximate NNLO and NLO+NNLL amounts to whether one takes seriously the improved convergence of the soft function at a numerically small soft scale. If so, one should use the resummed formulas, if not, one should use the approximate fixed-order calculations. In practice, this question can only be answered after a numerical analysis.

Bibliography

[1] K. Nakamura et al., JPG 37, 075021 (2010) (http://pdg.lbl.gov).

[2] V. Ahrens, A. Ferroglia, M. Neubert, B. D. Pecjak, L. L. Yang, JHEP **1009**, 097 (2010). [arXiv:1003.5827 [hep-ph]].

[3] V. Ahrens, A. Ferroglia, M. Neubert, B. D. Pecjak, L. L. Yang, [arXiv:1103.0550 [hep-ph]].

[4] V. Ahrens, A. Ferroglia, M. Neubert, B. D. Pecjak and L. L. Yang, Phys. Lett. B **687** (2010) 331 [arXiv:0912.3375 [hep-ph]].

[5] V. Ahrens, A. Ferroglia, B. D. Pecjak and L. L. Yang, arXiv:1105.5824 [hep-ph].

[6] V. Ahrens, A. Ferroglia, M. Neubert, B. D. Pecjak and L. L. Yang, arXiv:1106.6051 [hep-ph].

[7] J. C. Collins, D. E. Soper and G. Sterman, Adv. Ser. Direct. High Energy Phys. **5**, 1 (1988) [arXiv:hep-ph/0409313].

[8] P. Nason, S. Dawson and R. K. Ellis, Nucl. Phys. B **303**, 607 (1988).

[9] W. Beenakker, H. Kuijf, W. L. van Neerven and J. Smith, Phys. Rev. D **40**, 54 (1989).

[10] W. Beenakker, W. L. van Neerven, R. Meng, G. A. Schuler and J. Smith, Nucl. Phys. B **351**, 507 (1991).

[11] M. Czakon and A. Mitov, Nucl. Phys. B **824**, 111 (2010) [arXiv:0811.4119 [hep-ph]].

[12] P. Nason, S. Dawson and R. K. Ellis, Nucl. Phys. B **327**, 49 (1989) [Erratum-ibid. B **335**, 260 (1990)].

[13] M. L. Mangano, P. Nason and G. Ridolfi, Nucl. Phys. B **373**, 295 (1992).

[14] S. Frixione, M. L. Mangano, P. Nason and G. Ridolfi, Phys. Lett. B **351**, 555 (1995) [arXiv:hep-ph/9503213].

[15] J. H. Kühn and G. Rodrigo, Phys. Rev. Lett. **81**, 49 (1998) [arXiv:hep-ph/9802268].

[16] J. H. Kühn and G. Rodrigo, Phys. Rev. D **59**, 054017 (1999) [arXiv:hep-ph/9807420].

[17] M. Czakon, A. Mitov and S. Moch, Phys. Lett. B **651**, 147 (2007) [arXiv:0705.1975 [hep-ph]].

[18] M. Czakon, A. Mitov and S. Moch, Nucl. Phys. B **798**, 210 (2008) [arXiv:0707.4139 [hep-ph]].

[19] M. Czakon, Phys. Lett. B **664**, 307 (2008) [arXiv:0803.1400 [hep-ph]].

[20] R. Bonciani, A. Ferroglia, T. Gehrmann, D. Maitre and C. Studerus, JHEP **0807**, 129 (2008) [arXiv:0806.2301 [hep-ph]].

[21] R. Bonciani, A. Ferroglia, T. Gehrmann and C. Studerus, JHEP **0908**, 067 (2009) [arXiv:0906.3671 [hep-ph]].

[22] R. Bonciani, A. Ferroglia, T. Gehrmann, A. Manteuffel, C. Studerus, JHEP **1101**, 102 (2011). [arXiv:1011.6661 [hep-ph]].

[23] J. G. Korner, Z. Merebashvili and M. Rogal, Phys. Rev. D **77**, 094011 (2008) [arXiv:0802.0106 [hep-ph]].

[24] C. Anastasiou and S. M. Aybat, Phys. Rev. D **78**, 114006 (2008) [arXiv:0809.1355 [hep-ph]].

[25] B. Kniehl, Z. Merebashvili, J. G. Korner and M. Rogal, Phys. Rev. D **78**, 094013 (2008) [arXiv:0809.3980 [hep-ph]].

[26] S. Dittmaier, P. Uwer and S. Weinzierl, Phys. Rev. Lett. **98**, 262002 (2007) [arXiv:hep-ph/0703120].

[27] S. Dittmaier, P. Uwer, S. Weinzierl, Nucl. Phys. Proc. Suppl. **183**, 196-201 (2008). [arXiv:0807.1223 [hep-ph]].

[28] G. Bevilacqua, M. Czakon, C. G. Papadopoulos, M. Worek, Phys. Rev. Lett. **104**, 162002 (2010). [arXiv:1002.4009 [hep-ph]].

[29] K. Melnikov, M. Schulze, Nucl. Phys. **B840**, 129-159 (2010). [arXiv:1004.3284 [hep-ph]].

[30] M. Czakon, Phys. Lett. **B693**, 259-268 (2010). [arXiv:1005.0274 [hep-ph]].

[31] M. Czakon, [arXiv:1101.0642 [hep-ph]].

[32] G. Sterman, Nucl. Phys. B **281**, 310 (1987).

[33] S. Catani and L. Trentadue, Nucl. Phys. B **327**, 323 (1989).

[34] E. Laenen, J. Smith and W. L. van Neerven, Nucl. Phys. B **369**, 543 (1992).

[35] E. Laenen, J. Smith and W. L. van Neerven, Phys. Lett. B **321**, 254 (1994) [arXiv:hep-ph/9310233].

[36] E. L. Berger and H. Contopanagos, Phys. Lett. B **361**, 115 (1995) [arXiv:hep-ph/9507363].

[37] E. L. Berger and H. Contopanagos, Phys. Rev. D **54**, 3085 (1996) [arXiv:hep-ph/9603326].

[38] E. L. Berger and H. Contopanagos, Phys. Rev. D **57**, 253 (1998) [arXiv:hep-ph/9706206].

[39] S. Catani, M. L. Mangano, P. Nason and L. Trentadue, Phys. Lett. B **378**, 329 (1996) [arXiv:hep-ph/9602208].

[40] R. Bonciani, S. Catani, M. L. Mangano and P. Nason, Nucl. Phys. B **529**, 424 (1998) [Erratum-ibid. B **803**, 234 (2008)] [arXiv:hep-ph/9801375].

[41] S. Moch and P. Uwer, Phys. Rev. D **78**, 034003 (2008) [arXiv:0804.1476 [hep-ph]].

[42] M. Czakon and A. Mitov, Phys. Lett. B **680**, 154 (2009) [arXiv:0812.0353 [hep-ph]].

[43] U. Langenfeld, S. Moch and P. Uwer, Phys. Rev. D **80**, 054009 (2009) [arXiv:0906.5273 [hep-ph]].

[44] M. Beneke, P. Falgari and C. Schwinn, Nucl. Phys. B **828**, 69 (2010) [arXiv:0907.1443 [hep-ph]].

[45] M. Czakon, A. Mitov and G. Sterman, Phys. Rev. D **80**, 074017 (2009) [arXiv:0907.1790 [hep-ph]].

[46] M. Beneke, M. Czakon, P. Falgari, A. Mitov and C. Schwinn, arXiv:0911.5166 [hep-ph].

[47] M. Beneke, P. Falgari and C. Schwinn, Nucl. Phys. B **842**, 414 (2011) [arXiv:1007.5414 [hep-ph]].

[48] N. Kidonakis and G. Sterman, Phys. Lett. B **387**, 867 (1996).

[49] N. Kidonakis and G. Sterman, Nucl. Phys. B **505**, 321 (1997) [arXiv:hep-ph/9705234].

[50] A. Banfi and E. Laenen, Phys. Rev. D **71**, 034003 (2005) [arXiv:hep-ph/0411241].

[51] L. G. Almeida, G. Sterman and W. Vogelsang, Phys. Rev. D **78**, 014008 (2008) [arXiv:0805.1885 [hep-ph]].

[52] N. Kidonakis, Phys. Rev. D **64**, 014009 (2001) [arXiv:hep-ph/0010002].

[53] N. Kidonakis, E. Laenen, S. Moch and R. Vogt, Phys. Rev. D **64**, 114001 (2001) [arXiv:hep-ph/0105041].

[54] N. Kidonakis and R. Vogt, Phys. Rev. D **68**, 114014 (2003) [arXiv:hep-ph/0308222].

[55] N. Kidonakis and R. Vogt, Phys. Rev. D **78**, 074005 (2008) [arXiv:0805.3844 [hep-ph]].

[56] E. Laenen, G. Oderda and G. Sterman, Phys. Lett. B **438**, 173 (1998) [arXiv:hep-ph/9806467].

[57] N. Kidonakis, Phys. Rev. **D82**, 114030 (2010). [arXiv:1009.4935 [hep-ph]].

[58] M. Kobayashi and T. Maskawa, Prog. Theor. Phys. **49** (1973) 652.

[59] F. Abe *et al.* [CDF Collaboration], Phys. Rev. Lett. **74**, 2626 (1995) [arXiv:hep-ex/9503002].

[60] V. M. Abazov *et al.* [D0 Collaboration], Phys. Rev. Lett. **103** (2009) 092001 [arXiv:0903.0850 [hep-ex]].

[61] T. Aaltonen *et al.* [CDF Collaboration], Phys. Rev. Lett. **103**, 092002 (2009) [arXiv:0903.0885 [hep-ex]].

[62] T. E. W. Group [CDF and D0 Collaboration], arXiv:0908.2171 [hep-ex].

[63] S. Chatrchyan *et al.* [CMS Collaboration], arXiv:1106.3052 [hep-ex].

[64] ATLAS-CONF-2011-101

[65] V. M. Abazov *et al.* [D0 Collaboration], arXiv:1105.5384 [hep-ex].

[66] CDF Collaboration, CDF Public Report No.9890

[67] V. M. Abazov *et al.* [D0 Collaboration], Phys. Rev. D **84** (2011) 012008 [arXiv:1101.0124 [hep-ex]].

[68] CDF Collaboration, CDF Public Report No.10137

[69] T. Aaltonen *et al.* [CDF Collaboration], Phys. Rev. D **76** (2007) 072009 [arXiv:0706.3790 [hep-ex]].

[70] V. M. Abazov *et al.* [D0 Collaboration], Phys. Rev. D **82** (2010) 032002 [arXiv:0911.4286 [hep-ex]].

[71] CDF Collaboration, CDF Public Report No. 9913 (2009).

[72] V. Khachatryan *et al.* [CMS Collaboration], Phys. Lett. B **695**, 424 (2011) [arXiv:1010.5994 [hep-ex]].

[73] G. Aad *et al.* [ATLAS Collaboration], arXiv:1012.1792 [hep-ex].

[74] ATLAS-CONF-2011-100

[75] CMS-PAS-TOP-11-007

[76] CMS-PAS-TOP-11-006

[77] T. Aaltonen *et al.* [CDF Collaboration], Phys. Rev. Lett. **102**, 222003 (2009) [arXiv:0903.2850 [hep-ex]].

[78] V. M. Abazov *et al.* [D0 Collaboration], Phys. Lett. B **693**, 515 (2010) [arXiv:1001.1900 [hep-ex]].

[79] V. M. Abazov *et al.* [D0 Collaboration], Phys. Rev. Lett. **100**, 142002 (2008) [arXiv:0712.0851 [hep-ex]].

[80] V. M. Abazov *et al.* [D0 Collaboration], arXiv:1107.4995 [hep-ex].

[81] T. Aaltonen *et al.* [CDF Collaboration], Phys. Rev. Lett. **101**, 202001 (2008) [arXiv:0806.2472 [hep-ex]].

[82] T. Aaltonen *et al.* [CDF Collaboration], arXiv:1101.0034 [hep-ex].

[83] ATLAS-CONF-2011-106

[84] CMS-PAS-TOP-11-014

[85] B. Lillie, L. Randall and L. T. Wang, JHEP **0709** (2007) 074 [arXiv:hep-ph/0701166].

[86] L. M. Sehgal and M. Wanninger, Phys. Lett. B **200** (1988) 211.

[87] A. Leike, Phys. Rept. **317** (1999) 143 [arXiv:hep-ph/9805494].

[88] T. Aaltonen *et al.* [CDF Collaboration], arXiv:1107.3574 [hep-ex].

[89] T. Aaltonen *et al.* [The CDF Collaboration], Phys. Rev. Lett. **106** (2011) 141803 [arXiv:1101.5728 [hep-ex]].

[90] T. Aaltonen *et al.* [CDF Collaboration], Phys. Rev. Lett. **100** (2008) 161803 [arXiv:0801.3877 [hep-ex]].

[91] V. M. Abazov *et al.* [D0 Collaboration], arXiv:1104.4522 [hep-ex].

[92] V. M. Abazov *et al.* [D0 Collaboration], Phys. Lett. B **682** (2009) 278 [arXiv:0908.1811 [hep-ex]].

[93] V. M. Abazov *et al.* [D0 Collaboration], Phys. Lett. B **674** (2009) 4 [arXiv:0901.1063 [hep-ex]].

[94] ATLAS-CONF-2011-087

[95] ATLAS-CONF-2011-070

[96] ATLAS-CONF-2011-070

[97] CMS-PAS-TOP-10-007

[98] A. V. Manohar, arXiv:hep-ph/9606222.

[99] W. D. Goldberger, arXiv:hep-ph/0701129.

[100] W. Skiba, arXiv:1006.2142 [hep-ph].

[101] K. G. Wilson and J. B. Kogut, Phys. Rept. **12** (1974) 75.

[102] C. W. Bauer, S. Fleming and M. E. Luke, Phys. Rev. D **63** (2000) 014006 [arXiv:hep-ph/0005275].

[103] C. W. Bauer, S. Fleming, D. Pirjol and I. W. Stewart, Phys. Rev. D **63**, 114020 (2001) [arXiv:hep-ph/0011336].

[104] C. W. Bauer, D. Pirjol and I. W. Stewart, Phys. Rev. D **65**, 054022 (2002) [arXiv:hep-ph/0109045].

[105] M. Beneke, A. P. Chapovsky, M. Diehl and T. Feldmann, Nucl. Phys. B **643** (2002) 431 [arXiv:hep-ph/0206152].

[106] T. Becher, M. Neubert and G. Xu, JHEP **0807**, 030 (2008) [arXiv:0710.0680 [hep-ph]].

[107] V. Ahrens, T. Becher, M. Neubert and L. L. Yang, Eur. Phys. J. C **62**, 333 (2009) [arXiv:0809.4283 [hep-ph]].

[108] V. Ahrens, T. Becher, M. Neubert and L. L. Yang, Phys. Rev. D **79**, 033013 (2009) [arXiv:0808.3008 [hep-ph]].

[109] T. Becher and M. D. Schwartz, JHEP **0807** (2008) 034 [arXiv:0803.0342 [hep-ph]].

[110] C. W. Bauer and M. D. Schwartz, Phys. Rev. D **76** (2007) 074004 [arXiv:hep-ph/0607296].

[111] C. W. Bauer and M. D. Schwartz, Phys. Rev. Lett. **97** (2006) 142001 [arXiv:hep-ph/0604065].

[112] M. Baumgart, C. Marcantonini and I. W. Stewart, Phys. Rev. D **83** (2011) 034011 [arXiv:1007.0758 [hep-ph]].

[113] M. Beneke and T. Feldmann, Phys. Lett. B **553** (2003) 267 [arXiv:hep-ph/0211358].

[114] C. W. Bauer, S. Fleming, D. Pirjol, I. Z. Rothstein and I. W. Stewart, Phys. Rev. D **66** (2002) 014017 [arXiv:hep-ph/0202088].

[115] T. Becher, R. J. Hill, B. O. Lange and M. Neubert, Phys. Rev. D **69** (2004) 034013 [arXiv:hep-ph/0309227].

[116] A. V. Manohar, Phys. Rev. D **68** (2003) 114019 [arXiv:hep-ph/0309176].

[117] M. Neubert, Phys. Rept. **245** (1994) 259 [arXiv:hep-ph/9306320].

[118] A. V. Manohar and M. B. Wise, Camb. Monogr. Part. Phys. Nucl. Phys. Cosmol. **10** (2000) 1.

[119] T. Becher and M. Neubert, Phys. Lett. B **633** (2006) 739 [arXiv:hep-ph/0512208].

[120] T. Aaltonen *et al.* [CDF Collaboration], Phys. Rev. Lett. **105** (2010) 232003 [arXiv:1008.3891 [hep-ex]].

[121] N. Kidonakis, G. Oderda and G. Sterman, Nucl. Phys. B **525**, 299 (1998) [arXiv:hep-ph/9801268].

[122] N. Kidonakis, G. Oderda and G. Sterman, Nucl. Phys. B **531**, 365 (1998) [arXiv:hep-ph/9803241].

[123] T. Becher and M. Neubert, Phys. Rev. Lett. **97**, 082001 (2006) [arXiv:hep-ph/0605050].

[124] T. Becher, M. Neubert and B. D. Pecjak, JHEP **0701**, 076 (2007) [arXiv:hep-ph/0607228].

[125] T. Becher and M. D. Schwartz, JHEP **1002**, 040 (2010) [arXiv:0911.0681 [hep-ph]].

[126] T. Becher and M. Neubert, Phys. Rev. D **79**, 125004 (2009) [Erratum-ibid. D **80**, 109901 (2009)] [arXiv:0904.1021 [hep-ph]].

[127] T. Becher, R. J. Hill and M. Neubert, Phys. Rev. D **69**, 054017 (2004) [arXiv:hep-ph/0308122].

[128] S. Catani and M. H. Seymour, Phys. Lett. B **378**, 287 (1996) [arXiv:hep-ph/9602277].

[129] S. Catani and M. H. Seymour, Nucl. Phys. B **485**, 291 (1997) [Erratum-ibid. B **510**, 503 (1998)] [arXiv:hep-ph/9605323].

[130] T. Becher and M. Neubert, JHEP **0906**, 081 (2009) [arXiv:0903.1126 [hep-ph]].

[131] A. Ferroglia, M. Neubert, B. D. Pecjak and L. L. Yang, JHEP **0911**, 062 (2009) [arXiv:0908.3676 [hep-ph]].

[132] J. A. M. Vermaseren, arXiv:math-ph/0010025.

[133] G. P. Korchemsky and G. Marchesini, Phys. Lett. B **313**, 433 (1993).

[134] S. Frixione, M. L. Mangano, P. Nason and G. Ridolfi, Nucl. Phys. B **412**, 225 (1994) [arXiv:hep-ph/9306337].

[135] V. N. Gribov and L. N. Lipatov, Sov. J. Nucl. Phys. **15**, 438 (1972) [Yad. Fiz. **15**, 781 (1972)].

[136] G. Altarelli and G. Parisi, Nucl. Phys. B **126**, 298 (1977).

[137] Y. L. Dokshitzer, Sov. Phys. JETP **46**, 641 (1977) [Zh. Eksp. Teor. Fiz. **73**, 1216 (1977)].

[138] S. W. Bosch, B. O. Lange, M. Neubert and G. Paz, Nucl. Phys. B **699**, 335 (2004) [arXiv:hep-ph/0402094].

[139] A. D. Martin, W. J. Stirling, R. S. Thorne and G. Watt, Eur. Phys. J. C **64**, 653 (2009) [arXiv:0905.3531 [hep-ph]].

[140] J. M. Campbell and R. K. Ellis, Phys. Rev. D **62**, 114012 (2000) [arXiv:hep-ph/0006304].

[141] A. Czarnecki and K. Melnikov, Phys. Rev. Lett. **80**, 2531 (1998) [arXiv:hep-ph/9712222].

[142] M. Beneke, A. Signer and V. A. Smirnov, Phys. Lett. B **454**, 137 (1999) [arXiv:hep-ph/9903260].

[143] A. Czarnecki and K. Melnikov, Phys. Rev. D **65**, 051501 (2002) [arXiv:hep-ph/0108233].

[144] J. Alwall *et al.*, JHEP **0709**, 028 (2007) [arXiv:0706.2334 [hep-ph]].

[145] R. Frederix, S. Frixione, F. Maltoni and T. Stelzer, JHEP **0910**, 003 (2009) [arXiv:0908.4272 [hep-ph]].

[146] V. M. Abazov *et al.* [D0 Collaboration], Phys. Rev. D **80**, 071102 (2009) [arXiv:0903.5525 [hep-ex]].

[147] P. M. Nadolsky, H. -L. Lai, Q. -H. Cao, J. Huston, J. Pumplin, D. Stump, W. -K. Tung, C. -P. Yuan, Phys. Rev. **D78**, 013004 (2008). [arXiv:0802.0007 [hep-ph]].

[148] H. -L. Lai, J. Huston, Z. Li, P. Nadolsky, J. Pumplin, D. Stump, C. -P. Yuan, Phys. Rev. **D82**, 054021 (2010). [arXiv:1004.4624 [hep-ph]].

[149] M. Beneke, Phys. Rept. **317** (1999) 1 [arXiv:hep-ph/9807443].

[150] A. H. Hoang, T. Teubner, Phys. Rev. **D60**, 114027 (1999). [hep-ph/9904468].

[151] K. G. Chetyrkin, M. Steinhauser, Phys. Rev. Lett. **83**, 4001-4004 (1999). [hep-ph/9907509].

[152] M. Aliev, H. Lacker, U. Langenfeld, S. Moch, P. Uwer, M. Wiedermann, Comput. Phys. Commun. **182**, 1034-1046 (2011). [arXiv:1007.1327 [hep-ph]].

[153] A. H. Hoang, M. Beneke, K. Melnikov, T. Nagano, A. Ota, A. A. Penin, A. A. Pivovarov, A. Signer *et al.*, Eur. Phys. J. direct **C2**, 1 (2000). [hep-ph/0001286].

[154] W. Bernreuther and Z. G. Si, arXiv:1003.3926 [hep-ph].

[155] J. M. Campbell and R. K. Ellis, Phys. Rev. D **60** 113006 (1999) [arXiv:hep-ph/9905386].

[156] K. Cheung, T. -C. Yuan, Phys. Rev. **D83**, 074006 (2011). [arXiv:1101.1445 [hep-ph]].

[157] Y. Bai, J. L. Hewett, J. Kaplan, T. G. Rizzo, JHEP **1103**, 003 (2011). [arXiv:1101.5203 [hep-ph]].

[158] E. L. Berger, Q. -H. Cao, C. -R. Chen, C. S. Li, H. Zhang, Phys. Rev. Lett. **106**, 201801 (2011). [arXiv:1101.5625 [hep-ph]].

[159] B. Bhattacherjee, S. S. Biswal, D. Ghosh, Phys. Rev. **D83**, 091501 (2011). [arXiv:1102.0545 [hep-ph]].

[160] V. Barger, W. -Y. Keung, C. -T. Yu, Phys. Lett. **B698**, 243-250 (2011). [arXiv:1102.0279 [hep-ph]].

[161] K. M. Patel, P. Sharma, JHEP **1104**, 085 (2011). [arXiv:1102.4736 [hep-ph]].

[162] Z. Ligeti, M. Schmaltz, G. M. Tavares, JHEP **1106**, 109 (2011). [arXiv:1103.2757 [hep-ph]].

[163] B. Grinstein, A. L. Kagan, M. Trott, J. Zupan, [arXiv:1102.3374 [hep-ph]].

[164] M. I. Gresham, I. -W. Kim, K. M. Zurek, [arXiv:1103.3501 [hep-ph]].

[165] S. Jung, A. Pierce, J. D. Wells, [arXiv:1103.4835 [hep-ph]].

[166] J. Shu, K. Wang, G. Zhu, [arXiv:1104.0083 [hep-ph]].

[167] R. D. Ball, V. Bertone, F. Cerutti, L. Del Debbio, S. Forte, A. Guffanti, J. I. Latorre, J. Rojo *et al.*, Nucl. Phys. **B849**, 296-363 (2011). [arXiv:1101.1300 [hep-ph]].

[168] W. Bernreuther, M. Fuecker, Z. -G. Si, Phys. Rev. **D74**, 113005 (2006). [hep-ph/0610334].

[169] J. H. Kuhn, A. Scharf, P. Uwer, Eur. Phys. J. **C51**, 37-53 (2007). [hep-ph/0610335].

[170] M. Neubert, Eur. Phys. J. C **40**, 165 (2005) [arXiv:hep-ph/0408179].

[171] A. J. Buras, M. Jamin, M. E. Lautenbacher and P. H. Weisz, Nucl. Phys. B **370**, 69 (1992) [Addendum-ibid. B **375**, 501 (1992)].

[172] G. Buchalla, A. J. Buras and M. E. Lautenbacher, Rev. Mod. Phys. **68**, 1125 (1996) [arXiv:hep-ph/9512380].

[173] S. Moch, J. A. M. Vermaseren and A. Vogt, Nucl. Phys. B **688**, 101 (2004) [arXiv:hep-ph/0403192].

[174] A. Ferroglia, M. Neubert, B. D. Pecjak and L. L. Yang, Phys. Rev. Lett. **103**, 201601 (2009) [arXiv:0907.4791 [hep-ph]].

[175] G. P. Korchemsky and A. V. Radyushkin, Nucl. Phys. B **283**, 342 (1987).

[176] G. P. Korchemsky and A. V. Radyushkin, Phys. Lett. B **279**, 359 (1992) [arXiv:hep-ph/9203222].

[177] N. Kidonakis, Phys. Rev. Lett. **102**, 232003 (2009) [arXiv:0903.2561 [hep-ph]].

[178] S. Fleming, A. H. Hoang, S. Mantry and I. W. Stewart, Phys. Rev. D **77**, 074010 (2008) [arXiv:hep-ph/0703207].

[179] S. W. Bosch, R. J. Hill, B. O. Lange and M. Neubert, Phys. Rev. D **67**, 094014 (2003) [arXiv:hep-ph/0301123].